Topological Photonics with Anisotropic Materials

Robert Mc Guinness

A thesis submitted for the degree of
Doctor of Philosophy

in the

Quantum Light and Matter Group
School of Physics
Trinity College Dublin

February 4, 2020

Declaration

I declare that this thesis has not been submitted as an exercise for a degree at this or any other university and it is entirely my own work.

I agree to deposit this thesis in the University's open access institutional repository or allow the library to do so on my behalf, subject to Irish Copyright Legislation and Trinity College Library conditions of use and acknowledgement.

I consent to the examiner retaining a copy of the thesis beyond the examining period, should they so wish (EU GDPR May 2018).

Robert Mc Guinness

Summary

In this thesis we discuss and explore several different aspects of the topological classification of light propagating through matter, or topological photonics. In particular we will focus on anisotropic materials where the optical response is dependent on the polarisation and direction of propagation of the incoming light. We will consider both homogeneous dielectric media and periodically patterned optical materials known as photonic crystals. These explorations will consider either the weak-coupling regime, where the solutions of the wave equation describe photons, or the strong-coupling regime, where the solutions describe mixed light-matter quasiparticles called polaritons.

Our first subject is examining the topological characterisation of the refractive index surfaces of homogeneous optical materials. We do this by computing a topological invariant known as a Chern number in the case of different materials. The materials we consider are biaxial dielectrics with optical activity. In the absence of optical activity the refractive index surfaces of biaxial materials feature polarisation degeneracies. The introduction of optical activity lifts these degeneracies. We explore whether in combination biaxiality and either of two possible forms of optical activity can produce optical topological order. We find that the refractive index surfaces of chiral biaxial materials can have non-zero Chern numbers. We additionally derive an effective Hamiltonian which paraxially evolves light through a biaxial optically active material in directions close to a lifted degeneracy.

Next we turn to periodically patterned optical materials. We adapt the derived Hamiltonian to describe anisotropic, optically active two dimensional photonic crystals of two differing patterning geometries. The two geometries which we consider are either a square or a triangular arrangement of the dielectric constituents. For each geometry we examine the topological phase diagrams for each of the two forms of optical activity as we vary relevant parameters. We find that, for each geometry and either form of optical activity, topologically non-trivial iso-frequency surfaces can be achieved. The results of the studies for each form of patterning is compared and contrasted with each other and with the homogeneous material. We additionally explore the possibility of topological edge states for these anisotropic photonic crystals when they are considered in a finite geometry.

Our final subject concerns the strong-coupling regime of light and matter

in semiconductors. We focus on bulk direct band-gap semiconductors with the zincblende crystal structure. When these semiconductors are subjected to a magnetic field the dielectric function becomes anisotropic and multiply-resonant. We find that, in this situation, there is a complicated polariton dispersion relation which exhibits many topological degeneracies, both in the absence and presence of non-radiative decay.

Acknowledgements

Firstly I would like to thank my supervisor, Prof. Paul Eastham, for all his guidance and support. I have enjoyed the many lengthy and stimulating discussions we have had over the past four years. I am thoroughly indebted to him for what depth of understanding I have accrued during my postgraduate studies. Paul is a brilliant supervisor and it has been a privilege to work with him.

I am also thankful to the wider academic, technical and administrative community within the school of physics. It has been a great place to carry out both undergraduate and postgraduate studies. In particular I would like to thank Prof. David O'Regan, Prof. John Donegan, Prof. David McCloskey and Prof. John Goold for helpful discussions over the course of my postgraduate studies.

The writing up process for this thesis has proved an acutely stressful experience. I was lucky to have resources and supports like the Student Learning Development and the Student Counselling Service to help me during this tough time.

Attempting to distill the innumerable fugacious interactions that shaped my impression of Trinity College Dublin into a coherent few lines will be unfairly reductive. I must however try. I have spent eight of the past nine years as a student growing up in Trinity College Dublin and have loved nearly every day. Trinity is a place of amazing dynamism and flux and I will miss it immensely. Much of what made Trinity so special to me has been the people I have met, the conversations I have had and the friends I have made. My undergraduate theoretical physics coursemates were central; we had an incredible four years and I treasure all my friends dearly. During the postgraduate years many people have been integral to making my experience so overwhelmingly positive. In my office mates I was lucky to have a community committed to creating and maintaining a fun atmosphere during the day-to-day grind. In particular I would like to acknowledge João, Jane, Stephen P., Sonia, Matthias, Kasia, Akshara, Kiril, Chuan and Gaurav with whom I shared CRANN 4.22 for the majority of my four years. I was also fortunate to have supportive and engaging friends and postgrads within our academic group, the wider optics group and the school of physics at large. In particular Conor, John, Brian, Killian, Stephen O'B, Marlon, Dualta and Emmet among many many others. I reserve a special mention for Chris, Laura H. and Colin with whom I shared much of my time in Trinity. It wasn't the same without them for

the final months. Finally there is Laura M. who has been the best thing about my last nine months in Trinity. She has believed in me when I've found it hard to myself.

Although my tether to the campus is passing I will never be able to de-couple my feelings for Trinity from the friends with whom I shared the campus. As long as I hold on to them my personal Trinity will live on.

I am especially thankful for my non-physics friends and my family. My friends were a constant support throughout and their company was a tremendous comfort when I wished to escape the thesis obsession of the final months. Of my wider family I wish to particularly acknowledge my uncle Cormac who always encouraged my interest in physics. Last and most importantly of all I am indebted to my immediate family: my sister Lizzi and my wonderful parents Anne and Diarmaid. It would not have been possible without them. I hope my parents will not have to endure such a surly, irritable and withdrawing lodger going forward.

Contents

List of Figures

List of Tables

List of Symbols

$\underline{\underline{A}}_q$	Q-th exciton oscillator strength matrix	J
$\underline{\underline{\tilde{A}}}_q$	Directionally dependent q-th exciton oscillator strength matrix	J
$\mathbf{A}_{c,v}$	Reciprocal space exciton envelope function	$m^{\frac{3}{2}}$
a	Lattice spacing of photonic crystal	m
a_0	Exciton Bohr radius	m
$\mathbf{a}_i$	Direct lattice basis vector	m
A	Cone semi-angle of biaxial material	$^\circ$
$\mathbf{A}$	Envelope function of displacement field	$C\ m^{-2}$
$\mathbf{b}_i$	Reciprocal lattice basis vector	m^{-1}
$\underline{\underline{B}}_{\blacksquare}$	Paraxial wave equation Hamiltonian for light propagating through a square photonic crystal	
$\underline{\underline{B}}_{\blacktriangle}$	Paraxial wave equation Hamiltonian for light propagating through a triangular photonic crystal	
$\mathbf{B}$	Magnetic field	T
$\mathbf{b}_{\blacksquare}$	Vector of constituent functions of $\underline{\underline{B}}_{\blacksquare}$	
$\mathbf{b}_{\blacktriangle}$	Vector of constituent functions of $\underline{\underline{B}}_{\blacktriangle}$	
$b_{\blacksquare 0}$	Polarisation averaged contribution to $\underline{\underline{B}}_{\blacksquare}$	
$b_{\blacktriangle 0}$	Polarisation averaged contribution to $\underline{\underline{B}}_{\blacktriangle}$	
C	The first Chern number	
$\mathbf{D}$	Electric displacement field	$C\ m^{-2}$
$\mathbf{E}$	Electric field	$V\ m^{-1}$
$\mathbf{E}_\perp$	Transverse electric field	$V\ m^{-1}$
E_g	Semiconductor band-gap energy	J
$\underline{\underline{f}}$	Faraday effect tensor	rad T^{-1}
$\mathbf{F}_{c,v}$	Real space exciton envelope function	$m^{-\frac{3}{2}}$
$\underline{\underline{G}}$	Symmetric chirality tensor	rad
$\underline{\underline{\tilde{G}}}$	Scaled symmetric chirality tensor	
$\tilde{G}_a$	Anisotropic contribution to chirality from $\underline{\underline{\tilde{G}}}$	
$\tilde{G}_i$	Isotropic contribution to chirality $\underline{\underline{\tilde{G}}}$	
g^*	Semiconductor conduction electron g-factor	
$\underline{\underline{H}}$	Propagation Hamiltonian	
$\mathbf{H}$	Magnetizing field	$\mathrm{A\,m^{-1}}$
$\mathbf{h}$	Magnetic field	T

$H_{\pm}$	Dimensionless propagation constant corresponding to higher or lower refractive index	
h	Magnetic field strength	T
$\underline{\underline{J_i}}$	Angular momentum $J = \frac{3}{2}$ matrices	
$\mathbf{j}_f$	Free current density	$\mathrm{A\,m^{-2}}$
$\mathbf{k}$	Wavevector	m^{-1}
$\tilde{\mathbf{k}}$	Scaled wavevector $\frac{\mathbf{k}}{k_0}$	
$\hat{\mathbf{k}}_\theta$	Unit vector perpendicular to $\mathbf{k}$	
$\hat{\mathbf{k}}_\phi$	Different unit vector perpendicular to $\mathbf{k}$	
k_0	Free space wavenumber	m^{-1}
k	Wavenumber along optic axis of biaxial material $(= \sqrt{\epsilon_2} k_0)$	m^{-1}
$\underline{\underline{M}}$	3×3 matrix for displacement field wave equation	
$\underline{\underline{m}}$	2×2 matrix for displacement field wave equation	
$\underline{\underline{\mathcal{M}}}$	On-site finite geometry block	
m_e^*	Semiconductor conduction electron effective mass	
m_s	Projection of conduction electron angular momentum	
m_h	Projection of valence hole angular momentum	
$n_{\pm}$	The two refractive indices for light propagating in an anisotropic dielectric	
$\underline{\underline{P}}$	Permutation matrix	
$\mathbf{p}$	Relative-off-optic-axis momenta	
P	Kane's parameter	$J\ m$
q	Semiconductor hole anisotropic g-factor	
$\mathbf{r}$	Position	m
$\underline{\underline{R}}$	Rotation matrix	
$\underline{\underline{R}}_C$	Another rotation matrix	
R_0	Exciton Rydberg energy	J
$\underline{\underline{S}}$	Transformation matrix	
$\hat{\mathbf{s}}$	Unit wavevector	
$\underline{\underline{\mathcal{T}}}$	Inter-site finite geometry block	
t	Time	s
$\underline{\underline{V}}$	Eigenvector matrix	
V	Verdet constant	$\mathrm{rad}\ T^{-1}\ m^{-1}$
$\underline{\underline{\alpha}}$	Bi-anisotropic coupling tensor	
α	One measure of spread of principal dielectric constants.	
α_x	Adjustable parameter	
α_y	Another adjustable parameter	
$\underline{\underline{\beta}}$	Other bi-anisotropic coupling tensor	
β	Another measure of spread of principal dielectric constants	
Γ_q	Linewidth broadening associated with transitions between a particular pair of bands	J

γ	Ratio of cyclotron energy to exciton Rydberg energy	
γ_C	Dimensionless specific rotation	
γ_i	Semiconductor valence hole effective mass parameters	
Δ	Discriminant of polariton equation	m^{-4}
$\underline{\underline{\epsilon}}$	Dielectric permittivity tensor	
ϵ_b	Semiconductor background dielectric	
ϵ_i	ith component of principal dielectric constant of biaxial material, $i \in (1,2,3)$	
$\underline{\underline{\eta}}$	Inverse permittivity tensor	
κ	Valence hole g-factor	
λ_0	Free space wavelength	m
λ	In medium wavelength	m
$\underline{\underline{\mu}}$	Permeability tensor (Tellgen representation)	
$\underline{\underline{\nu}}$	Permeability tensor (Boys-Post representation)	
$\boldsymbol{\pi}$	Canonical momentum	$m\ s^{-1}$
ρ_C	Optical specific rotation	rad m^{-1}
ρ_f	Free charge density	$C\ m^{-3}$
$\underline{\underline{\sigma}}_i$	The i-th Pauli matrix $(\underline{\underline{\mathbb{1}}}, \underline{\underline{\sigma_1}}, \underline{\underline{\sigma_2}}, \underline{\underline{\sigma_3}})$	
$\underline{\underline{\chi}}$	Susceptibility tensor	
$\underline{\underline{\tilde{\chi}}}$	Directionally dependent susceptibility tensor	
ω	Angular frequency	rad s^{-1}
ω_g	Band gap frequency of semiconductor	rad s^{-1}
ω_{R_0}	Exciton Rydberg frequency	rad s^{-1}
(θ, ϕ)	Magnetic field application direction (Propagation direction in Chapters 2 and 6)	

Chapter 1

Introduction & Motivation

1.1 Introduction

A primary focus of science is to classify by comparing and contrasting properties of distinct systems. In the context of material science this approach allows us to sort matter into phases which display markedly different behaviour; solids and liquids, magnetic and non-magnetic. This work is important as it allows understanding of the behaviour of individual materials by appreciating the divisions into which they have been sorted rather than necessarily having to conduct an independent investigation into every case. Many of these classifications are understandable within the Landau theory of symmetry breaking. This theory essentially states that each phase of matter has a distinct way in which its constituent parts organise themselves and a transition between two phases is accompanied by a re-organisation of its constituent parts. This re-organisation changes some symmetry that the previous phase held; for instance in the liquid to solid phase change the continuous translation symmetry of the liquid becomes a discrete translation symmetry of the solid. This approach has however proved unable to categorise all materials, with some phases which possess the same symmetry yet display qualitatively different behaviour requiring a new framework to be understood.

These anomalies of classification can be reconciled within the framework of topology. There are integer topological invariants which can distinguish phases which have different global arrangements yet look the same locally [1, 2]. The integer quantum Hall state [3] is an example of a topologically non-trivial phase. In this phase the non-zero invariant is linked to a quantised Hall conductance [4]. Topological phases can exhibit significant protection against disorder as many of the possible deformations induced by the disorder will affect the local organisation but not the global one [5]. Due to these integer invariants interesting effects occur when materials of differing topological order are placed into contact including the dissipation-less transport of charge or spin along the interfaces [6]. For these reasons there is considerable interest in exploring topologically non-trivial systems.

A particular focus in this area has been on the assignation of topological

invariants to the electronic band structures of solids [7]. In this context the periodic nature of the solid results in Bloch form solutions [8] of the Schrödinger equation, for which topological invariants can be calculated [1, 2]. Although formally the set of invariants is attributable to the Hamiltonian, which provides the mapping between the periodic Brillouin zone and the Bloch states, one can loosely think of the integers being attributable to individual bands, provided one holds certain rules in mind [7]. In particular, the sum of the invariants of any pairs of bands is conserved across those bands becoming degenerate.

Rather than being intrinsically reliant on electronic systems the concepts of topological band theory are generally applicable. Far from being a hindrance, the broad relevance of topology has allowed the discovery of topologically non-trivial bandstructures in many types of system, such as in optical [9, 10] and acoustical [11, 12] systems. This is the case as the understanding of the underlying mechanisms which produce a non-zero topological invariant in one setting can be effectively replicated in other settings.

In this thesis we will examine several aspects of the topological characterisation of light propagating through matter, or topological photonics [6]. The fundamental starting point for such examinations are Maxwell's equations and the wave equations which follow [13, 14]. We will assess the topological characteristics of the solutions of the wave equation for various anisotropic optical media. We will consider both homogeneous dielectric materials and periodically patterned photonic crystals for which there are photonic band structures [15, 16]. These studies will be set in either the weak-coupling regime, where the solutions describe photons, or the strong-coupling regime, where the solutions represent mixed light-matter quasiparticles called polaritons [17, 18].

The first problem we address is the topological characterisation of the refractive index surfaces of homogeneous optical materials. The materials we consider are anisotropic and optically active. We consider two distinct types of optical activity and assess whether it is possible to realise optical topological order for either case. We also derive a Hamiltonian which paraxially evolves light through one of these materials in directions close to a special optical axis.

In the two following chapters we make use of this derived Hamiltonian, adapting it to provide an effective description of two dimensional photonic crystals of two different patterning geometries. The two geometries which we consider are square patterned and triangularly patterned. For each geometry we examine the topological phase diagrams for either form of optical activity. We compare and contrast the results of these investigations with each other and with the case of the homogeneous material.

One of the important properties of topologically non-trivial systems is the appearance of edge states when those bulk systems are considered in a finite geometry. In chapter 5 we investigate the survival and changing characteristics of these edge states in systems as the bulk band gaps are closed. Within this examination we explore the role played by the boundary conditions and whether choosing a particular termination of the structures allows partial edge states to form. We apply these insights to assess the prospects of edge states for the photonic crystal models previously studied.

In the final investigation we explore the strong-coupling of light and matter in bulk semiconductors. The semiconductors that we consider are zincblende structures with direct band-gaps. When a magnetic field is applied to one of these materials the dielectric function becomes anisotropic and multiply-resonant close to the band-edge. The polariton dispersion relations for light propagating in such materials are complicated and exhibit many topologically protected degeneracies, both in the absence and presence of dissipation.

In the balance of this chapter we introduce concepts which are relevant to the developments to follow and survey the state of the art of the fields as they stand. This will begin with a general introduction to topology, Berry phases and Chern numbers. We shall then explain how these concepts apply to topologically non-trivial phases in two dimensions, three dimensions and non-Hermitian systems. Interleaved in these discussions we will introduce the existing theories and realisations of such phases. From there we will lay some more specific foundations on which this thesis will build. We will particularly focus on the role that iso-frequency surfaces play in describing the propagation of light through materials and on the polaritons that result from the strong-coupling of light to matter excitations in semiconductors. In each instance we will detail how the previously introduced topological concepts have become relevant in these areas and the further directions which will be explored in this thesis.

1.2 Topology, Berry Phase and Chern Numbers

1.2.1 General Introduction

Topology is the study of the properties of geometrical objects that are preserved under smooth continuous deformations of the object. The allowable continuous deformations consist of, among others, bending, stretching, twisting and compressing but do not include processes which tear the object or join it to other objects. Those properties which are preserved by the permissible deformations are topological properties. These topological properties can be captured by appropriate topological

invariants which allow objects to be distinguished.

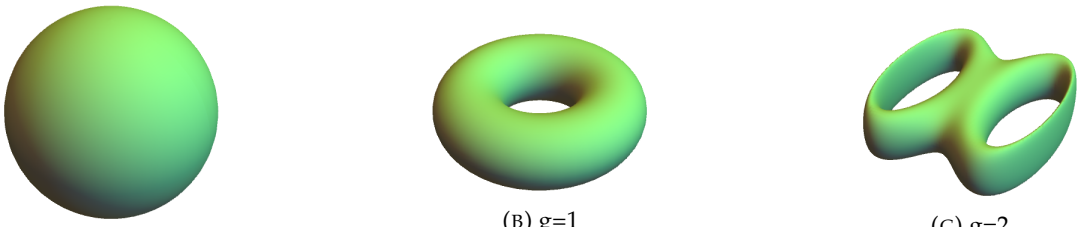

(A) g=0 (B) g=1 (C) g=2

FIGURE 1.1: Three surfaces with different values of the genus invariant, g.

A familiar example of a topological invariant is the genus, g, of a surface, which equals the number of holes an object has. In figure 1.1 we show three surfaces of different genera. The sphere, which has no holes, is topologically distinct from the torus and both are topologically distinct from the double torus. One could imagine, by smooth deformations, transforming the sphere into any topologically equivalent object, for instance a cube, but the only way to transform the sphere into a torus would involve discontinuous processes.

This global topological property of these surfaces, the number of holes, can be related to local geometric properties of the surfaces themselves. In this case the relation is known as the Gauss-Bonnet theorem [4]. It relates the Gaussian curvature $\mathbf{K}$, a local geometric property, to the genus by an area integral over the surface considered M:

$$\frac{1}{2\pi}\int_M \mathbf{K}\cdot d\mathbf{A} = (2-2g). \tag{1.1}$$

1.2.2 Berry Phase

The Gauss-Bonnet theorem is not unique in linking local geometric quantities to global topological properties - there are further examples in which topological quantities are expressible in terms of integrals over suitable local quantities. One such example is that of the Berry phase [19]. The Berry phase is relevant when a Hamiltonian depends on a parameter which undergoes adiabatic cyclic evolution in parameter space. Under these circumstances the wavefunction can accrue an additional geometric phase in addition to the familiar dynamical phase. This Berry phase can be expressed as an integral of local quantities, either the so-called Berry connection or Berry curvature, as we shall shortly address. In this instance the geometry of the wavefunctions dependence on the parameters determines whether the phase is non-zero. In particular if we consider a Hamiltonian which depends on some set of parameters $\mathbf{R}$ then clearly the eigenvalues and eigenvectors will also depend on

those parameters according to

$$H(\mathbf{R})|n(\mathbf{R})\rangle = E_n(\mathbf{R})|n(\mathbf{R})\rangle. \tag{1.2}$$

If we consider the parameters $\mathbf{R}$ to vary in time then the time-dependent wave function can be written as

$$|n(\mathbf{R}(t))\rangle = \exp\{i\gamma_n(t)\}\exp\{-\frac{i}{\hbar}\int_0^t E_n(\mathbf{R}(t'))dt'\}|n(\mathbf{R}(0))\rangle. \tag{1.3}$$

In the equation (1.3) above $\gamma_n(t)$ is the Berry phase and is determined by

$$\gamma_n(t) = i\int_0^t \langle n(\mathbf{R}(t'))|\frac{\partial}{\partial t'}|n(\mathbf{R}(t'))\rangle dt' = i\int_{R(0)}^{R(t)}\langle n(\mathbf{R})|\nabla_{\mathbf{R}}|n(\mathbf{R})\rangle\cdot d\mathbf{R}. \tag{1.4}$$

Under cyclic parameter evolution $\mathbf{R}(0) = \mathbf{R}(t)$ and the Berry phase is

$$\gamma_n = \oint_C \mathbf{A}_n(\mathbf{R})\cdot d\mathbf{R} = \int_S \mathbf{F}_n(\mathbf{R})\cdot d\mathbf{S}. \tag{1.5}$$

In equation (1.5) we have introduced the Berry connection, $\mathbf{A}_n(\mathbf{R}) = i\langle n(\mathbf{R})|\nabla_{\mathbf{R}}|n(\mathbf{R})\rangle$, and the Berry curvature, $\mathbf{F}_n(\mathbf{R}) = \nabla_{\mathbf{R}}\times\mathbf{A}_n(\mathbf{R})$, which are the previously mentioned local quantities. The second equivalence in equation (1.5) follows via Stokes' theorem. The Berry phase is only non-zero in cases where the parameter evolution encloses a point where the phase of the wavefunction is indeterminate. Such points are known as singularities of the wavefunction. Consequently, there is a link between non-zero Berry phases and Hamiltonians which feature degeneracies in their eigenvalue spectra [19, 20]. To illustrate this point we shall consider the Hamiltonian of a continuum massless Dirac fermion of the form:

$$\underline{\underline{H}}(\mathbf{k}) = k_x\underline{\underline{\sigma}}_x + k_y\underline{\underline{\sigma}}_y. \tag{1.6}$$

This Hamiltonian has a degeneracy, known as a Dirac point, at $\mathbf{k} = 0$. The eigenstates of the Hamiltonian are

$$|\pm\rangle = \frac{1}{\sqrt{2}}(\exp\{-i\phi(\mathbf{k})\}, \pm 1)^T \tag{1.7}$$

where $\phi(\mathbf{k}) = \arctan\left(\frac{k_y}{k_x}\right)$ and the superscript T indicates that the row vector should be transposed. The Berry phase, by equation (1.5), is then given by $\gamma = \frac{1}{2}\oint \nabla_{\mathbf{k}}\phi(\mathbf{k})\cdot d\mathbf{k}$. This integral takes the value π and for this reason Dirac points are said to have a topological index of $\frac{1}{2}$.

1.2.3 Chern Numbers

In a periodic medium the eigenstates take the form of modulated plane-waves known as Bloch wavefunctions: $\psi_{\mathbf{k}}(\mathbf{r}) = \exp\{i\mathbf{k}\cdot\mathbf{r}\}u_{\mathbf{k}}(\mathbf{r})$, where $u_{\mathbf{k}}(\mathbf{r})$ has the same

periodicity as the material. In this context one can regard the wavevector $\mathbf{k}$ as an external parameter, and consider the Berry phase acquired around loops in reciprocal space. One special possible loop in reciprocal space is that around the first Brillouin zone, which is the fundamental area of wavevector space for a periodic system. For a two dimensional periodic system a topological invariant known as the first Chern number is obtained when the Berry curvature is integrated over the first Brillouin zone:

$$2\pi C_n = \int F_n(\mathbf{k}) d\mathbf{k}. \tag{1.8}$$

This topological invariant counts up the number of phase windings of the Bloch states over the first Brillouin zone. It is zero whenever the Bloch functions do not feature any singularities over this domain [21].

Chern numbers are, in general, difficult to calculate however. They are usually calculated in one of two ways - directly or indirectly. Direct calculation techniques include either low energy continuum expansions around each inequivalent degenerate point [6] or judicious numerical integration [22]. Indirect calculation techniques infer a non-zero Chern number from the presence of edge states when considering a finite geometry.

For a two-band system a method for calculating the Chern number is provided in a work by Sticlet et al. [23]. This approach applies to insulators which can be treated by an effective Hamiltonian model. Any two band Hermitian Hamiltonian can be decomposed into the sum of products of functions times the identity matrix and the three Pauli spin matrices. The functions multiplying the Pauli matrices can be considered as an effective magnetic field, $\mathbf{h}(\mathbf{k})$, due to the equivalence of such a Hamiltonian to that of an electron in a magnetic field. Sticlet et al. [23] showed a way to determine the Chern number from the sum of the topological index associated with the Dirac points of a truncated Hamiltonian:

$$C = \frac{1}{2} \sum_{\mathbf{k} \in \mathbf{D}_i} \text{sign}(\partial_{k_x} \mathbf{h} \times \partial_{k_y} \mathbf{h})_i \text{sign}(h_i). \tag{1.9}$$

Here $\mathbf{D}_i$ are the inequivalent Dirac points, which are determined by the $\mathbf{k}$ for which $\mathbf{h}(\mathbf{k}) = 0$ having already set an arbitrary one of the components $h_i(\mathbf{k}) = 0$. Each topological index is then the Berry phase divided by 2π times the sign of the "mass term", which gaps that Dirac point. The mass term is the $h_i(\mathbf{k})$ that has been chosen. It was emphasised in Sticlet et al. [23] that, due to the periodicity of these lattice models, the sum of the Berry phases (or circulations) over the first Brillouin zone will always be zero. This means that to achieve a non-zero Chern number the mass term must change sign over the Brillouin zone in a manner that separates Dirac points with net circulation. We will now detail the solution of a toy model which shows how this can be done and the implications of non-zero topological invariants.

1.3 Topological Insulators in Two Dimensions

To further explore this concept of a topologically non-trivial material we shall consider a representative model. The model we consider is a lattice generalisation of the continuum massive Dirac Hamiltonian [6]. This model describes an insulator with spinless fermions arranged in a square lattice geometry. We consider two orbitals on each site, with the two orbitals possessing different parities (for instance these could be an s-type orbital and a p-type orbital). Given that the orbitals differ in parity the coupling between them must be an $L = 1$ angular momentum coupling. The lowest order coupling in $\mathbf{k}$ of the appropriate form is $\sin(k_x) \pm i \sin(k_y)$. In this model we additionally allow intra-orbital dispersion that is even in $\mathbf{k}$. The Hamiltonian of the model is

$$\underline{\underline{H}}(\mathbf{k}) = \sin(k_x)\underline{\underline{\sigma}}_x + \sin(k_y)\underline{\underline{\sigma}}_y + \big(2 + m - \cos(k_x) - \cos(k_y)\big)\underline{\underline{\sigma}}_z, \tag{1.10}$$

where $m \in \mathbb{R}$ is taken to be an adjustable parameter.

1.3.1 Bulk Topological Invariants

Following the approach of Sticlet et al. [23] to determine the Chern number we initially focus on the case when $h_3(\mathbf{k}) = 0$. In this instance the reduced Hamiltonian represents a system with four degeneracies in the first Brillouin zone. These degeneracies are located at the points in reciprocal space where the $h_1(\mathbf{k})$ and $h_2(\mathbf{k})$ components vanish simultaneously. These points occur at $(k_x, k_y) = \{(0,0),\ (\pi,0),\ (0,\pi),\ (\pi,\pi)\}$. The local behaviour of the reduced Hamiltonian around each of these points is that of a Dirac fermion, meaning each of these points has a Berry phase of $\pm\pi$. The Chern number is then calculated by summing up the product of the vorticity and the sign of $h_3(\mathbf{k})$ for each Dirac point. This procedure results in a Chern number of:

$$C = \frac{1}{2}\big\{(+1)[\mathrm{sgn}(m)] + 2(-1)[\mathrm{sgn}(2+m)] + (+1)[\mathrm{sgn}(4+m)]\big\}. \tag{1.11}$$

Examining equation (1.11) we see that the topological phase diagram as a function of the parameter m is partitioned into four regions. The boundaries between these regions are the values $m = -4$, $m = -2$ and $m = 0$. At each of these values the band structure closes at some point in the Brillouin zone. As m is tuned through these values the band structure closes and re-opens which can result in a change of Chern number [7]. These three values of m are the only values at which the band structure closes and hence the only locations of topological phase transitions. Using equation (1.9) we determine the Chern numbers in each of the four regions to be:

$$C = \begin{cases} 0 & m < -4 \\ 1 & -4 < m < -2 \\ -1 & -2 < m < 0 \\ 0 & m > 0 \end{cases} \tag{1.12}$$

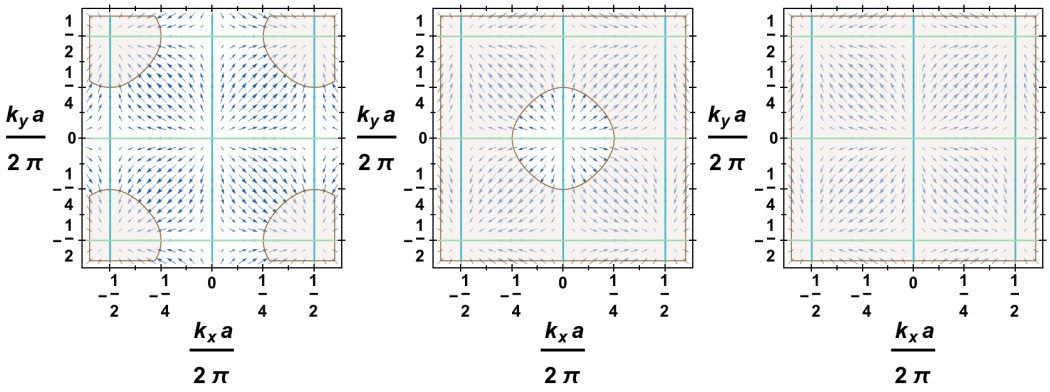

FIGURE 1.2: Three plots showing the zero contour lines of each component of $\mathbf{h}(\mathbf{k})$ over an enlarged Brillouin zone. Each plot considers a different value of m. In the left plot $m = -3$, in the central plot $m = -1$ and in the right plot $m = 1$. Within each plot the zero contour lines are each a different colour; the zero contour line of $h_1(\mathbf{k})$ is displayed in turquoise, that of $h_2(\mathbf{k})$ is displayed in light green and that of $h_3(\mathbf{k})$ is brown. The shaded regions are those in which $h_3(\mathbf{k}) > 0$. The vector field $(h_1(\mathbf{k}), h_2(\mathbf{k}))$ is overlaid in blue.

To better appreciate the origin of these topologically non-trivial phases we can examine plots of the components of $\mathbf{h}(\mathbf{k})$ over the first Brillouin zone for different values of m. In figure 1.2 we examine plots showing the zero contour lines of each of the three components of $\mathbf{h}(\mathbf{k})$. Each plot considers a distinct value of m which are chosen so that we are in three distinct phases. In the left plot $m = -3$, in the central plot $m = -1$ and in the right plot $m = 1$. In each plot the light brown shaded region corresponds to the areas for which $h_3(\mathbf{k}) > 0$. Furthermore we display the vector field $(h_1(\mathbf{k}), h_2(\mathbf{k}))$ in blue. Equation (1.9) tells us that the Chern number depends on the vorticity around each of the distinct Dirac points as well as the sign of the mass term at each of those points. The vorticity of each Dirac point is independent of the value of m. The zone centre and zone corner Dirac points have a positive vorticity, while those at the face centres have negative vorticity. This net zero vorticity follows from the version of the Poincaré-Hopf theorem [24] applicable to the Brillouin zone torus. The value of m does affect the sign of the mass term at each of the lifted Dirac point degeneracies. In the rightmost plot the sign of $h_3(\mathbf{k})$ is the same across all of the Brillouin zone and hence the sum of the products of the vorticities and masses of each Dirac point is zero. In the other two cases $h_3(\mathbf{k})$ changes sign over the Brillouin zone in such way that the zero contour line separates Dirac points of opposite circulations. This is the origin of the non-zero Chern number in each of these phases.

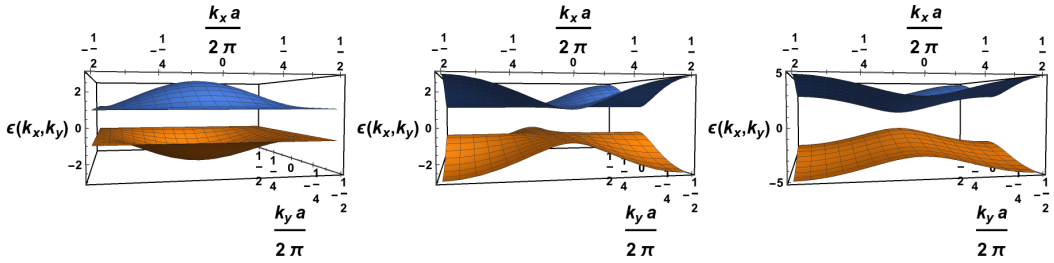

FIGURE 1.3: Three plots showing the bulk band structure of the Chern insulator over the first Brillouin zone. Each plot considers a different value of m. In the left plot $m = -3$, in the central plot $m = -1$ and in the right plot $m = 1$.

It is not possible to infer the topological phase from the bulk band-structures of the Hamiltonian (1.10). Figure 1.3 shows the bulk band structure of the Hamiltonian for each of the values of m considered in figure 1.2. These band structures are the eigenvalues of the Hamiltonian (1.10) whereas it is the eigenvectors that determine the Chern number. The morphology of the bulk bands does play some role in the understanding of the finite geometry band structures as we shall now explore.

1.3.2 Edge States

One of the hallmarks of topologically non-trivial materials is the bulk-boundary correspondence [25, 26]. When two materials with a different value of a topological invariant are put into contact then there must be a degeneracy to reconcile this difference. As this degeneracy is enforced by the boundary it therefore describes low-energy states bound locally to the edge [27]. In the case of our idealised Chern insulator these edge states propagate chirally and without diminishing in intensity.

In order to examine the prospect for edge state formation one has to mathematically incorporate the boundary into these Chern insulator models. The introduction of the boundary means that one of the wavevector components can no longer characterise the solutions. Instead one must perform a discrete Fourier transform on this component and move to a mixed real space and wavevector space representation [6]. The result of this is a large matrix to diagonalise. The matrix is tri-diagonal, representing on site and nearest neighbour hopping, with each entry itself a two-by two block, representing the two orbitals on that site. If one chooses to consider a finite system with N sites along the y direction (say), then the resulting finite geometry Hamiltonian is a $2N \times 2N$ matrix.

In figure 1.4 we display the finite geometry band structure resulting from diagonalising the Hamiltonian for 20 sites along y. In each case we consider a distinct value of m which correspond with those used in figures 1.2 and 1.3. In each instance we can understand most of the finite geometry band structure as a

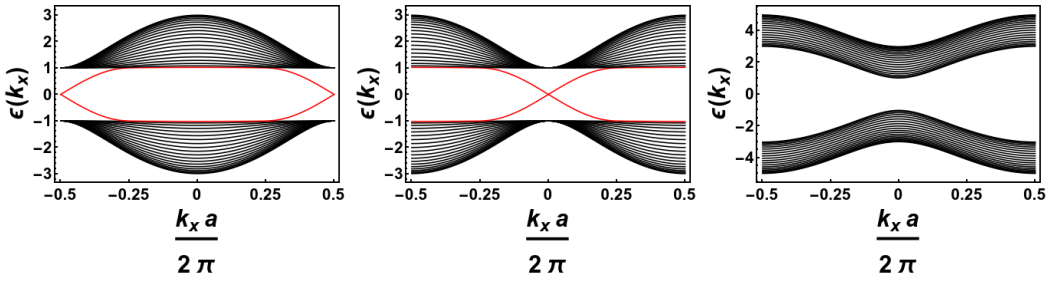

FIGURE 1.4: Three plots showing the finite geometry band structure of the Chern insulator when a termination is introduced along the y direction. Each plot considers a different value of m. For the left plot $m = -3$, for the central plot $m = -1$ and for the right plot $m = 1$. In each case we have terminated the structure after 20 sites. The bulk states are coloured black while the edge states are displayed in red.

projection of the bulk band structures of figure 1.3 onto a single direction. There are however notable exceptions. In the two cases that are topologically non-trivial we see bands which cross the bulk band-gap. These are the edge solutions associated with the non-zero topological invariant. The group velocity of the edge states, $\partial_{k_x}\epsilon$, is either positive or negative for each mini-band. The eigenvectors from the finite geometry calculation give additional information regarding the distribution of the edge states in the mixed real and reciprocal space.

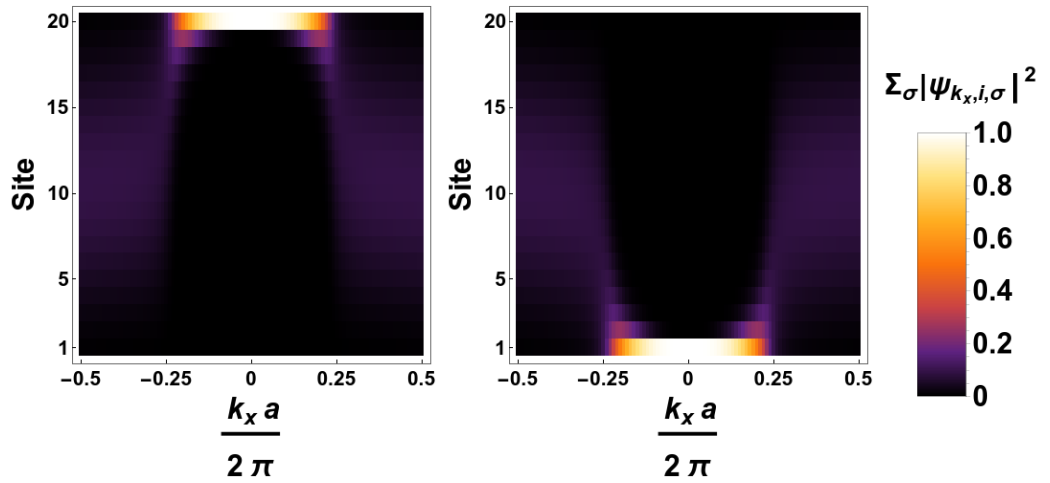

FIGURE 1.5: Two density plots showing the spin-summed squared magnitude of the eigenvectors $\psi_{k_x,\, i,\sigma}$ for each of the Chern insulator edge states. For this plot we have considered a finite system of 20 sites along y and we have considered the case $m = -1$.

In figure 1.5 we examine the eigenvectors for the two red coloured mini-bands in the central plot of figure 1.4. Here we show density plots of the spin-summed squared magnitude of the eigenvectors $\psi_{k_x,i,\sigma}$. Along the y-axis we display the real space sites along the y direction while along the x axis we display the k_x wavevector component. We see that the two red mini-bands do indeed correspond to edge localised solutions; which reside on the top and bottom edges of the material

respectively. The combination of the always positive or negative group velocity and the spatial profile of the edge solutions means that we have chiral edge states.

1.3.3 Physical Realisations

The Chern insulator model explored in the previous subsections is an idealisation, designed to exemplify the essential features of systems with non-zero Chern numbers. Nevertheless there are related proposals and experimental observations that have essentially the same features. The first example was the theoretical model of Haldane [28]. In this work a honeycomb lattice tight-binding model is adopted which consists of two inter-penetrating triangular lattices of different atomic species, A and B. There is coupling both between the sub-lattices and within each sub-lattice. There is also an on-site energy difference between the two sub-lattices, which breaks inversion symmetry. Additionally there are phase factors attached to the hopping between sites on the same sub-lattice. These phase factors mimic the effect of a magnetic field in breaking time-reversal symmetry, but there is no overall flux. As this theory is defined on a hexagonal lattice there can be Dirac points at the two inequivalent zone corners, as in graphene [29]. Haldane showed that, when these Dirac points are gapped, the Chern number of the model is $C \in \{-1, 0, 1\}$ [28]. Which of these Chern numbers is realised then depends on the hopping strengths, the on-site energy difference and the phase factors. Within the space of these parameters there exist finite areas (or volumes) for each of the three possible Chern numbers. The boundaries between these areas of different Chern numbers correspond to a set of parameters for which the gap closes at one or both of the Dirac points.

The theoretical proposal by Haldane [28] has much in common with the Chern insulator model previously addressed. In both cases there are locations in the first Brillouin zone at which the band gap of the models can close. In both cases tuning the parameters of the model through these degeneracies can result in a change of the topological phase. The only major difference between the two models is the number of tunable parameters and hence how complicated the topological phase diagram is.

Although realising the Haldane model [28] in an electronic context has proved difficult, the model provided the basis for a proposal for topologically non-trivial electromagnetic states [9, 10]. In this proposal a two dimensional photonic crystal was arranged in a triangular geometry resulting in zone corner Dirac points for the transverse electric modes. These degeneracies were then lifted by considering a Faraday effect term which breaks time-reversal symmetry. The resulting split bands have Chern numbers of ± 1. This work ignited interest in optical topological order resulting in more proposals for [30, 31] and experimental realisations of [32, 33]

topologically non-trivial photonic systems. In most of these systems the decoupling of the polarisation states and the wavevector within the two dimensional Brillouin zone was relied upon.

Beyond optics this proposal also set a typical course towards achieving topological order in myriad settings. This conventional developmental route relies on a triangular patterning of the system in order to produce Dirac points in the band-structure. Having achieved these Dirac points the idea is to introduce a perturbation so as to lift the degeneracies resulting in bands with non-zero Chern numbers. This approach has been used in, among others, acoustic [11, 12], polaritonic [34–36], magnonic [37] and mechanical [38] settings.

The Chern number is not the only kind of topological invariant possible for two dimensional insulators. Systems that have a non-zero Z_2 topological invariant are also possible [2]. The first model proposed for such an occurrence was again focused on graphene, this time with the addition of a spin-orbit effect [39]. This minimal model is essentially two copies of the Haldane insulator model, one for each electronic spin. The 4×4 matrix model consists of de-coupled 2×2 blocks. Due to time-reversal symmetry the Chern number of each of these blocks sum to zero, but their difference is linked to this Z_2 invariant. These Z_2 insulators also exhibit a bulk-boundary correspondence. For these materials the edge states are helical rather than chiral. This means that electrons of each spin travel in opposite directions around the boundary of these materials. A more realistic proposal for a system that realises a non-zero Z_2 invariant was set in semiconductor quantum well heterostructures [40] which have a stronger spin-orbit interaction. In this instance the effective Hamiltonian consists of two time-reversal partner versions of the Chern insulator model introduced earlier. For such systems this Z_2 invariant was quickly confirmed by edge transport measurements [41]. Photonic systems which realise polarisation-resolved helical edge states due to a non-zero Z_2 invariant have also been proposed [42]. In that proposal the authors suggested designing a two dimensional lattice of metamaterials which possess a bi-anisotropic response designed to mimic the spin-orbit coupling of electronic systems. This scheme was implemented experimentally under similar conditions resulting in the desired photonic Z_2 insulator [43].

1.4 Topological Features in Three Dimensional Dispersions

In three dimensions there are several classes of topologically non-trivial materials. These classes can be divided into the topological insulators, which have a complete bulk band gap, and the topological semi-metals, which do not. In the former category is a three dimensional generalisation of the Z_2 topological insulator [44–46]

that was introduced in the previous sections while in the latter there are systems which exhibit topologically robust degeneracy structures [47, 48].

The proposals for $3D$ Z_2 topological insulators [44–46] have considered both cases where the insulator is built from coupled layers of $2D$ Z_2 topological insulators and those for which the $3D$ topological insulator has no obvious $2D$ counterpart. The former type of three dimensional topological insulator is known as a weak topological insulator while the latter is a strong topological insulator [6]. Three dimensional Z_2 topological insulators have been theorised [49, 50] and realised [51, 52] in several electronic settings. Beyond electronic settings weak $3D$ Z_2 topological insulators have also been proposed [53] and experimentally observed [54] in photonic systems. In this context the original $2D$ photonic Z_2 insulator [42] was essentially extended to $3D$ again using the bi-anisotropic metamaterials this time arranged in a $3D$ hexagonal lattice.

Topological semi-metal phases are a fast emerging research area [55]. These semi-metal phases exhibit degeneracies which can be either isolated or extended. There are three principal variants of these gap-less phases; the Weyl semi-metal [56], the Dirac semi-metal [57, 58] and the nodal line semi-metal [48]. In the first two cases the degeneracies are isolated points in the $3D$ Brillouin zone, while in the latter case the degeneracies are extended lines in reciprocal space. The difference between the Weyl and Dirac semi-metal phases is in the number of bands coming into contact at the degenerate point; in the former case there are two while in the latter case there are four. In both the Weyl and Dirac semi-metal phases the low-energy dispersion around the degeneracies is linear and thus the dispersion resembles that of a Weyl or Dirac fermion respectively. These phases were experimentally realised in various $3D$ electronic systems [59–62].

The $3D$ topological phases which we will be most concerned with in this thesis are gap-less phases which feature emergent Weyl points. The Weyl points are robust degeneracies in two senses. Firstly their presence is immune to the smooth variation of parameters of the underlying material and secondly the points themselves carry a topological charge of ± 1. The topological charge must be distributed throughout the Brillouin zone such that the net charge is zero and hence there must always be a matching number of positive and negatively charged degeneracies. These Weyl points can locally be described by the Hamiltonian $\underline{\underline{H}}(\mathbf{k}) = k_i \nu_{ij} \sigma_j$ with the topological charge of each point determined by $\mathrm{sgn}(\det(\nu_{ij}))$. The momentum space Berry curvature associated with each Weyl point is that of a monopole. Owing to this the charge can alternatively be understood as the Chern number obtained by integrating the curvature over a chosen momentum space surface which encloses the degeneracy.

In three dimensional Weyl semi-metal phases, as in gapped $2D$ and $3D$ topological phases, there is a bulk-boundary correspondence. In this instance when the system is terminated in an appropriate direction open momentum space arcs connecting Weyl points of opposite charge are observed in the surface Brillouin zone. These open contours are known as Fermi arcs. Three dimensional Weyl semimetals along with their surface states have been proposed and realised in optical [63–68] and acoustic [69–71] settings also.

To explore these Weyl semi-metals we can consider a model Hamiltonian [72]. The Hamiltonian we consider describes a $3D$ tight-binding model of spinless fermions. The lattice is made of layers of two inter-penetrating square lattices each of a different species, A or B. The Hamiltonian is

$$\begin{aligned}\underline{\underline{H}}(\mathbf{k}) = 2t_1 \sin\left[\frac{1}{2}(k_x + k_y)\right] \underline{\underline{\sigma}}_x + 2t_1 \sin\left[\frac{1}{2}(k_x - k_y)\right] \underline{\underline{\sigma}}_y + \\ + \left[\Delta - 2t_2\big(\cos(k_x) + \cos(k_y)\big) + 2t_3 \cos(k_z)\right] \underline{\underline{\sigma}}_z,\end{aligned} \tag{1.13}$$

where t_1 represents the strength of hopping between the A and B sub-lattices in the same layer, t_2 represents the strength of hopping between atoms of the same species in the same layer, t_3 represents the strength of hopping between atoms of the same species in adjacent layers and Δ represents the sub-lattice energy difference. The lattice spacing has been chosen as $a_x = a_y = a_z = 1$. Degeneracies occur at points in reciprocal space where each component $h_i(\mathbf{k})$ of the Hamiltonian (1.13) vanish simultaneously. Clearly the $h_1(\mathbf{k})$ and $h_2(\mathbf{k})$ components both vanish at $(k_x, k_y) = (0, 0)$ and $(k_x, k_y) = (\pi, \pi)$. The solutions of $h_3(\mathbf{k}) = 0$ for each of these (k_x, k_y) pairs leads to two equations:

$$\cos(k_z) = -\left(\frac{\Delta}{2t_3} - \frac{2t_2}{t_3}\right), \tag{1.14}$$

$$\cos(k_z) = -\left(\frac{\Delta}{2t_3} + \frac{2t_2}{t_3}\right). \tag{1.15}$$

The values of the quantities $\Delta/2t_3$ and $2t_2/t_3$ determine if there are solutions to $h_3(\mathbf{k}) = 0$ at all . If there are solutions each of the equations contributes a pair of Weyl points at $\pm k_z$ of opposite helicity.

Figure 1.6 shows the topological phase diagram of the Hamiltonian (1.13). There are two distinct gapped insulator phases and three Weyl semi-metal phases. The two insulator phases are a normal topologically trivial insulator and a quantum hall insulator, respectively. The three Weyl semi-metal phases represent solving either of the two equations (1.14) and (1.15) individually or both simultaneously.

We shall focus on the phase WSM1; where the two Weyl points occur at $(k_x, k_y) = (0, 0)$. We shall fix $\Delta/2t_3 = 1 = 2t_2/t_3$ such that the two Weyl points

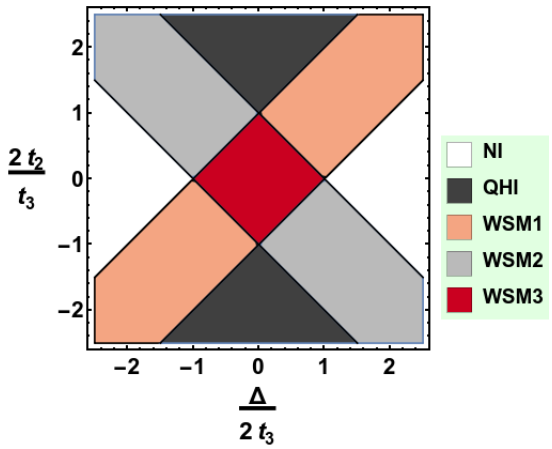

FIGURE 1.6: A phase diagram representing the topological phases of the Hamiltonian (1.13). The phases are displayed in the accompanying legend. The phases NI and QHI represent normal insulators and quantum Hall insulators respectively. The phases labeled WSM represent one of three different Weyl semi-metal phases. In the phase WSM1 there are two Weyl points which appear along the line $k_x = k_y = 0$. In the phase WSM2 there are two Weyl points which appear along the line $k_x = k_y = \pi$. In the phase WSM3 there are four Weyl points which appear at each of the locations of the WSM1 phase and the WSM2 phase.

occur at $k_z = \pm\pi/2$ as shown in the figure 1.7.

The expansion of the Hamiltonian around the points $(0, 0, \pm\pi/2)$ results in the local behaviour:

$$\underline{\underline{H}}(\mathbf{k}) \simeq t_1(k_x + k_y)\underline{\underline{\sigma}}_x + t_1(k_x - k_y)\underline{\underline{\sigma}}_y \mp 2t_3(k_z \mp \frac{\pi}{2})\underline{\underline{\sigma}}_z. \tag{1.16}$$

From this expansion we can determine that the charges of these two Weyl points are $c = \pm\text{sgn}(t_3)$. As the ratios of $\Delta/2t_3$ and $2t_2/t_3$ depart from unity the Weyl points move along the line $k_x = k_y = 0$. Beyond certain critical values the Weyl points meet and annihilate, either at $k_z = 0$ or $k_z = \pi$, and we reach one of the gapped insulator phases.

Introducing terminations of the system in two surfaces parallel to either the xz or yz planes will result in Fermi arc surface states which join the projections of the two Weyl points in the surface Brillouin zone. Figure 1.8 shows a portion of the surface band structure which results from introducing terminations to the bulk Hamiltonian (1.13) in the xz plane. In this chosen finite geometry k_x and k_z remain good quantum numbers but k_y can no longer characterise the solutions. In this figure we can see the open curve degeneracy joining the two Weyl points. In this case if the Fermi energy is assumed to be zero then the Fermi surface will just consist of this open arc joining the two Weyl points. The local colouring of the surface bands indicates that these Fermi arcs are an edge feature.

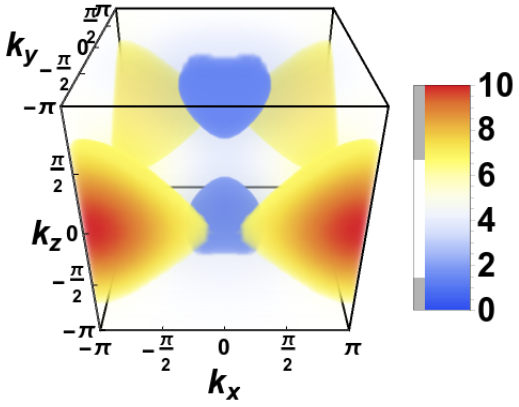

FIGURE 1.7: Density plot representing the magnitude of the vector $\mathbf{h}(\mathbf{k})$ over the three dimensional Brillouin zone. The magnitude of this vector represents half the splitting between the two bands of the band structure. The parameters have been chosen so that we are in the phase WSM1. The two Weyl points, for these parameters, occur at $(0, 0, \pm\frac{\pi}{2})$

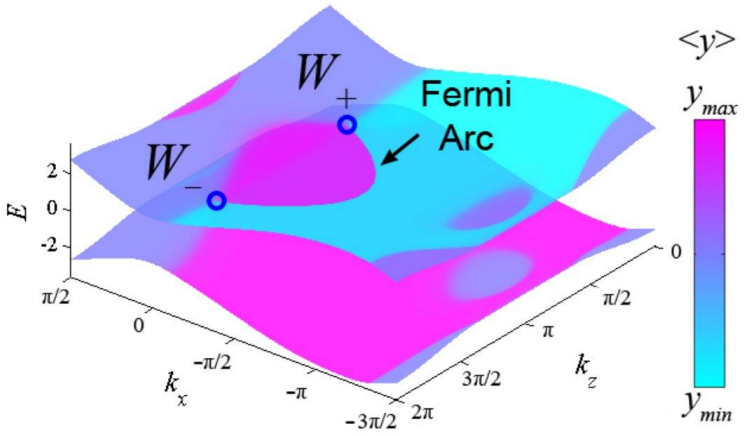

FIGURE 1.8: A plot taken from Delplace et al. [72] showing two of the surface bands of the WSM1 phase plotted over a shifted surface Brillouin zone. In Delplace et al. [72] terminations of the bulk Hamiltonian (1.13) in the xz plane were considered. The surface band structure shows the open Fermi arc degeneracy joining the projections of the bulk Weyl points which are indicated by W_- and W_+. The surfaces are coloured according to the legend and represent the average position $\langle y \rangle$ of the corresponding states.

1.5 Topological Features of Dissipative Systems

The systems we have considered up to this point have been Hermitian and therefore all possess real eigenvalue spectra. There is however a growing interest in aspects of non-Hermitian systems which exhibit gain and loss. This began with the work of Bender and Boettcher who noticed that PT symmetric systems have real eigenvalue spectra [73]. A PT symmetric Hamiltonian is one which is invariant under the

combined action of the parity, P, and time reversal, T, operators. In quantum mechanics the Hamiltonian is usually assumed to be Hermitian resulting in real eigenvalues and unitary time evolution which conserves the overall probability. An interesting aspect of non-Hermitian PT symmetric Hamiltonians is that they can also display unitary time evolution and hence could describe new classes of complex quantum theories [74].

Beyond PT symmetry there is interest in systems that display dissipation and amplification more generally. In these systems the eigenvalues can be complex with unconventional consequences. Many of these curiosities are linked to the presence of exceptional points - locations in parameter space where two or more complex eigenvalues and their associated eigenvectors coalesce. These exceptional points often, but not always, occur at points in parameter space where PT symmetry is broken [75]. Initially it was believed that one such unconventional aspect is that as exceptional points are encircled once in parameter space the modes are swapped, and thus it requires twice encircling the exceptional point in order to return to the original state [76]. Even then the states have accumulated a Berry phase of π, so it would therefore take four circuits to return fully to the original situation [77]. Such a perspective of state-flips and geometric phases however requires the instantantaneous eigenstates to be followed upon the encircling evolution. The non-Hermitian nature of these systems however can lead to a breakdown of the adiabatic theorem [78, 79]. Recently it was shown that the effect of the breakdown of the adiabatic theorem is that the direction of encircling of the exceptional point completely determine the eigenvalue sheet which one ends up on [80]. The presence of exceptional points also gives rise to novel edge features as discussed by Leykam et al. [81]. In Leykam et al. [81] the authors discovered that there are two types of topological charges associated with exceptional points, one a generalisation of the Berry phase and a second one with no Hermitian counterpart, which in combination can produce myriad diverse edge theories.

These ideas have a natural relevance to optics where there is a ubiquitous presence of both gain and loss due to, for example, stimulated emission and material absorption [75]. Recognition of this has sparked interest in designing PT symmetric optical systems, for instance coupled waveguides one with gain and the other with matching loss [82]. In this system there is a change in behaviour between the PT symmetric phase, with real eigenvalues, and the broken PT phase, where the eigenvalues are complex. In the unbroken PT phase a symmetric exchange of input light intensity between the two waveguides occurs while in the broken phase intensity is confined to, and amplified in, the gain waveguide irrespective of which waveguide it was incident upon. The transition point between these two regimes is an exceptional point. There has been much interest in recognising exceptional points in optical systems [83]. Some of this interest has focused on steering optical

systems to exceptional points, allowing mode selection [84], and on going through exceptional points, resulting in unconventional behaviour in laser systems [85]. Beyond marked behaviour changes achieved by traversing through exceptional points there is interest in exploiting the topological structure of the eigenvalue sheets around the exceptional points in optical systems [86].

The type of systems which exhibit exceptional points need not be especially complicated, in either a mathematical or physical sense. As an example we shall consider a simple model of coupled lossy modes that exhibits exceptional point physics:

$$\underline{\underline{H}} = \begin{pmatrix} \omega_1 - i\gamma_1 & \mu \\ \mu & \omega_2 - i\gamma_2 \end{pmatrix}. \tag{1.17}$$

In equation (1.17) ω_1 and ω_2 are two distinct mode frequencies and γ_1 and γ_2 are the corresponding loss rates. The coupling strength between the modes is μ. The eigenvalues of this model are

$$E_\pm = \frac{\omega_1 + \omega_2}{2} - i\frac{\gamma_1 + \gamma_2}{2} \pm \sqrt{\mu^2 + \left(\frac{\omega_1 - \omega_2}{2} + i\frac{\gamma_1 - \gamma_2}{2}\right)^2}. \tag{1.18}$$

The difference of the two eigenvalues only depends on the difference of the two mode frequencies and the differences of the two loss rates and not the average of the mode frequencies and loss rates. As such to find exceptional points we need only examine the difference in these quantities for a chosen fixed coupling μ.

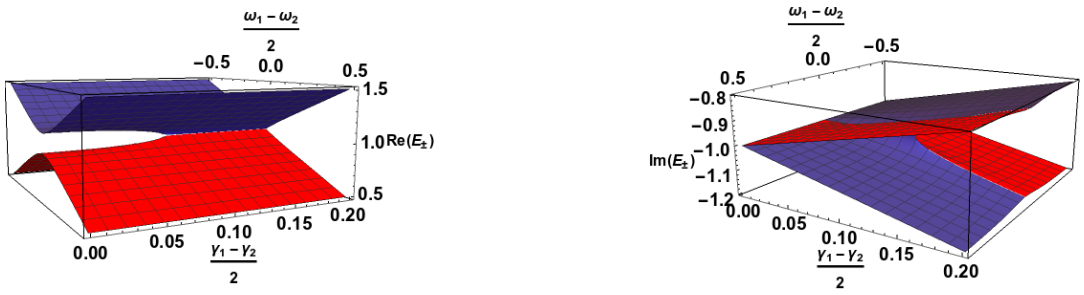

FIGURE 1.9: The real and imaginary parts of the eigenvalues of the Hamiltonian (1.17). For this plot we have considered $\omega_{\text{av}} = 1$ and $\gamma_{\text{av}} = 1$. The chosen coupling strength is $\mu = 0.1$.

Figure 1.9 shows the real and imaginary parts of the eigenvalues as a function of the difference in mode frequencies and difference in loss rates. We see that an exceptional point occurs at $(\delta\omega, \delta\gamma) = (0, 0.1)$, corresponding to the difference in loss rates matching the strength of coupling.

In figure 1.10 we examine the local dispersion of the real (continuous lines) and imaginary (dashed lines) parts of the eigenvalues around the exceptional point. For this picture we fix the two mode frequencies to be equal. We see that

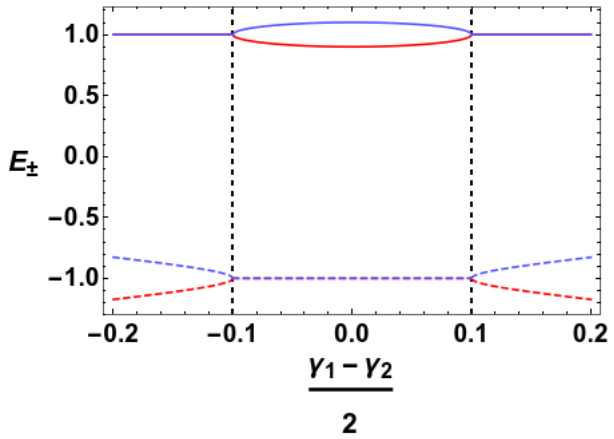

FIGURE 1.10: The real (continuous) and imaginary (dashed) parts of the eigenvalues of the Hamiltonian (1.17) along the line $\omega_1 = \omega_2$.

there are extended degeneracies in the real parts and in the imaginary parts of the eigenvalues. These extended degeneracies are non-overlapping except at the two exceptional points locations at $\delta\gamma = \pm\mu = \pm 0.1$ indicated by the black dashed gridlines. The dispersion away from the exceptional points for both the real and imaginary parts exhibit square-root dependence, a hallmark of the lowest order exceptional point.

1.6 Iso-Frequency Surfaces

The previous sections have considered the topological classification of band structures, i.e. assigning topological invariants to the surfaces $\omega(\mathbf{k})$, where $\mathbf{k}$ is either (effectively) a two dimensional or three dimensional wavevector. It is also possible however to characterise a different surface: the iso-frequency surface of a material. This construction is a closed surface in wavevector space representing all the wavevectors that a wave of a given frequency can propagate with. In electronic settings a well known example of one of these surfaces is the Fermi surface which is the surface of all wavevectors that can propagate at the Fermi frequency. In optical systems the analogous surface is set by the frequency of the incoming light. The iso-frequency surface is then an important descriptor of the refraction and polarisation behaviour of the material in optical contexts.

These iso-frequency surfaces, when gapped, can also be characterised by a Chern number. This characterisation has been done for two diverse optical systems, in either a direct or implicit manner. In the first the iso-frequency surfaces of a homogeneous uniaxial hyperbolic material with chirality are shown to be topologically non-trivial [87]. In the second system the authors considered the related Floquet "quasi-energy" surface of a two dimensional photonic crystal [88].

This first approach, by Gao et al. [87], studies the iso-frequency surfaces of effectively homogeneous uniaxial hyperbolic metamaterials with chirality. In this context, prior to the introduction of chirality, the iso-frequency surface has three sheets and features two isolated degeneracies between pairs of the sheets. For a chosen frequency the sheets of this surface represent the allowed wavevectors that light of a given polarisation can propagate in the uniaxial hyperbolic material with. The degeneracies of the surface are quadratic intersections rather than the linear Dirac point crossings in section 1.2. In this instance the quadratic degeneracies have a topological index of ± 1 rather than the $\pm\frac{1}{2}$ of Dirac points. The introduction of chirality then lifts both degeneracies resulting in non-zero Chern numbers for each sheet of the iso-frequency surface. The distinction between the topological indices of linear and quadratic degeneracies can have global consequences on the allowable Chern numbers of the surfaces, as we shall later explore.

It is worth examining the work of Gao et al. [87] in relation to the Chern insulator model presented in section 1.3. One difference is in the work of Gao et al. [87] the relevant reciprocal space is not the Brillouin zone torus but rather the sphere of propagation directions. This is a noteworthy distinction as in the work of Gao et al. [87] the degeneracies are not generated by lattice effects but rather by the anisotropy of the optical material. A second difference is that the authors here are considering the polarisation texture in reciprocal space [89] as generating the topologically non-trivial result rather than some complicated orbital hybridisation behaviour in reciprocal space. In this context the Dirac points and zeroes of the mass terms, discussed in section 1.3, are then polarisation features known as C-points and L-lines [90, 91]. C-points are directions in reciprocal space where the polarisation state is purely circularly polarised, either left-handed or right-handed. L-lines are directions in reciprocal space along which the polarisation state is linear. In the language of polarisation optics a non-zero Chern number results from the L-lines separating C-points of different handedness [89].

The second relevant proposal to discuss, by Rechtsman et al. [88], considers a paraxial wave equation describing light propagating out of the plane of a two dimensional photonic crystal. In this case the two-dimensional photonic crystal is formed by a triangular arrangement of evanescently coupled waveguides in the xy plane. Each waveguide is extended along the z-direction, forming a helix. By transforming the coordinates into ones which follow these helices Rechtsman et al. [88] showed that an effective external field appears in the paraxial wave equation. A tight-binding adaptation of this paraxial wave equation was implemented and analysed using Floquet theory. Within this framework the authors calculated the Floquet "quasi-energy" band structures and inferred a non-zero Chern number from finite geometry calculations and experiment. The work in Rechtsman et al. [88] follows a similar approach to the conventional developmental route outlined in

subsection 1.3.3. In particular, a triangular geometry was considered in Rechtsman et al. [88] so as to produce Dirac point degeneracies in the bandstructure and a perturbation, the effective external field induced by the helical waveguides, lifts the degeneracies producing a topologically non-trivial result.

Although not explicitly stated, focusing on these Floquet "quasi-energies" is similar to analysing iso-frequency surfaces of photonic crystals. Rechtsman et al. [88] are looking at the form of the quasi-invariants which evolve the field along the structure. The "quasi-energy" surface is in fact a closed surface in wavevector space meaning that the surface is more accurately described as a quasi iso-frequency surface. The Floquet quasi-invariants are therefore similar to the iso-frequency surface if one thinks of the latter as a surface of $k_z(k_x, k_y)$. In the work of Rechtsman et al. [88] a scalar wave equation was employed, implicit in which is an assumption that the polarisation state is completely decoupled from the direction of propagation. This assumption is generally not the case; for instance polarisation mixing occurs for light propagating in anisotropic materials.

In this thesis we shall present work which is complementary to these two diverse realisations of optical topological order. As in the work of Gao et al. [87] we will eschew the reliance on a particular form of lattice patterning to produce degeneracies and instead rely on the intrinsic polarisation degeneracies of anisotropic dielectrics. We will consider both homogeneous materials, as was done in Gao et al. [87], and periodic structures. In the former instance the distinction between our work and that of Gao et al. [87] is that we will consider several different forms of biaxial anisotropy rather than uniaxial anisotropy. In the latter case the distinction, as well as considering more general anisotropic materials, is that the topology of the Brillouin zone torus differs compared to the sphere of propagation directions. Such a difference in topology will require a different polarisation texture in reciprocal space and will therefore have a different topological phase diagram to that of the homogeneous material. The work we present will be complementary to that of Rechtsman et al. [88] in the sense that we will also consider light propagating out of the periodic plane of a two dimensional photonic crystal. The distinction for us is that we will exploit the effective optical spin-orbit coupling of anisotropic materials rather than considering the decoupling of the polarisation and the direction of propagation in reciprocal space.

1.7 Light-Matter Coupling in Semiconductors & Topological Polaritons

The concepts introduced in the previous sections do not belong to any one branch of physics. They principally emerged in electronic settings but are being rapidly

appropriated by many other diverse settings. In the previous sections we primarily focused on the relevance of topological concepts to optical systems as that shall be one of the two primary settings of the work presented in this thesis. The other setting we shall be considering is that of exciton-polariton systems.

An exciton is an elementary excitation of a semiconductor. This excitation comprises a valence band hole and a conduction band electron which are bound by their Coulomb attraction [17]. There are in fact a number of discrete exciton energy levels just below the semiconductor band-gap as well as the continuum of unbound yet interacting electron and holes above the electronic band-gap [92]. For light impinging upon a semiconductor, with a frequency just below that of the band-gap frequency, the excitons make a significant contribution to the optical response of the material [93]. The effect of the excitons is to heavily modify the linear photonic dispersion resulting in mixed light-matter modes known as polaritons [17].

These polaritons have proved an interesting platform to study myriad phenomena. In particular microcavity polaritons resulting from the coupling of heavy-hole quantum-well excitons to photonic cavity modes have allowed polariton condensation [94] and consequently polariton lasing [95], among many other effects. Within the microcavity polariton setting there has also been several proposals [34–36] and a realisation [96] of various topological insulators in two dimensions characterised by non-zero Chern numbers. These schemes have considered the implementation of triangular two dimensional lattice potentials for either the excitonic [34, 36] or the photonic component [35] of the polaritons so as to produce Dirac point in the polaritonic band-structure. The degeneracies at the Dirac points were then lifted due to the Zeeman splitting of the bright excitons arising from the introduction of a magnetic field. The result of this is to achieve the desired set of topologically non-trivial bands.

The study of topological effects in polaritonic systems is however not as mature as in electronic and optical settings. The topological features of three dimensional dispersion relations of polaritons have yet to be explored. Similarly the possibility of polaritons as a platform to study non-Hermitian topological effects has yet to be fully examined. One of the intentions of this thesis is to focus on these inchoate areas. We shall do this by considering the dispersion relations of the magneto-exciton-polaritons of bulk semiconductors. In comparison to the spectrum of quantum well excitons, the exciton spectrum of bulk semiconductors is more complex. This is the case as the excitons formed between the light-hole valence band and the conduction band electrons need to be included for the bulk semiconductor. The resulting dispersions therefore promise to be rich in structure and consequently an interesting platform to study for three dimensional topological features and, when dissipation is included, non-Hermitian effects also.

1.8 Outline of Thesis

In this thesis we consider the topological characteristics, both in terms of topological invariants and topologically protected degeneracies, of various photonic systems. This work leads to new theoretical understanding of the topological characteristics of bulk homogeneous dielectrics, patterned two dimensional photonic crystals and bulk magneto-exciton-polaritons.

In chapter 2 we examine the topological invariants that can be assigned to the refractive index surfaces of anisotropic optically active bulk dielectric media. We examine specifically the L-lines and C-points for light propagating through biaxial dielectrics and how these polarisation degeneracies can lead to non-zero Chern numbers once gyromagnetic effects are introduced. In this chapter we also derive an effective Hamiltonian which paraxially evolves the field along one of the optic axis directions of the biaxial dielectric.

In chapters 3 and 4 we make use of the Hamiltonian derived in chapter 2, adapting it to describe light propagating through two dimensional photonic crystals with two different lattice geometries. In chapter 3 we consider square patterned photonic crystals while in chapter 4 we consider triangularly patterned photonic crystals. In each chapter we determine the Chern number of the iso-frequency surface for crystals primarily composed of biaxial materials with one of two possible forms of optical activity. For all combinations of form of lattice and optical activity we examine the topological phase diagrams. We compare the topological phase diagrams achieved in each geometry and contrast them with those of the homogeneous materials considered in chapter 2.

In chapter 5 we examine the bulk-boundary correspondence of topologically non-trivial materials. We investigate this correspondence for two different boundary conditions; one of which explicitly includes the adjacent material. For each type of boundary condition we explore the fate of the edge states as the bulk band gap is closed. We also explore the role that the orientation of the boundary plays in the emergence of edge states. Using these insights we address the question of edge states for the bulk photonic crystal models developed in the previous chapters.

In chapter 6 we investigate the topological features that are present in the three dimensional dispersion relations of magneto-exciton-polaritons. The multiple conduction and valence states participating in the exciton ground state result, when a magnetic field is applied, in an anisotropic and multiply resonant dielectric response. The polariton dispersions that follow host a wealth of topologically protected degeneracies both in the absence of dissipative effects and when dissipation is included. We examine this plethora of topologically protected features for the

representative case of gallium arsenide.

Chapter 2

Propagation of Light Through Anisotropic Optically Active Materials

2.1 Introduction

In this chapter we study the propagation of light through homogeneous anisotropic materials which additionally exhibit gyrotropic effects. The anisotropy we consider is that of an optically biaxial crystal resulting from low crystal symmetry [13]. In these materials double refraction is the norm, with the two refractive indices as well as the natural polarisation state of the light varying with the direction of propagation through the material [97]. These refractive indices coalesce and come apart four times over all possible propagation directions. These points of contact in direction space are the conical intersections of the refractive index surfaces and shall be of primary interest in this chapter.

We shall see that the introduction of optical activity can cause these conical intersections to disappear resulting in two distinct refractive indices for light travelling in any direction [14]. With this addition the polarisation state is in general that of elliptic polarisation, with departures from this general state worthy of attention. These departures are in the form of either C-points or L-lines, the former being points in direction space at which the polarisation is circular and the latter being contours in direction space along which the polarisation is linear [91].

The totality of refractive indices in direction space defines two closed surfaces, each of which has an associated polarisation state in every direction. A topological invariant can be associated with the polarisation states defined over these surfaces. Whether this invariant is non-zero or not is determined by the nature of the optical activity considered. We study the invariants of the surfaces corresponding to biaxial optically active materials within the framework developed by Berry and Dennis [91]. As discussed in chapter 1, this work is a complementary study of the topological invariants of the refractive index surfaces of homogeneous materials to

that conducted by Gao et al. [87].

As well as assessing these surfaces in their entirety we are also interested in the behaviour of the refractive indices locally to one of the conical intersections. We will pursue this interest by deriving a Hamiltonian which evolves the displacement field through an arbitrary biaxial optically active material in the paraxial limit. This Hamiltonian shall extend that of Jeffrey [98], including higher order terms in the local dispersion. The derived Hamiltonian shall be a central result of this chapter and will be used extensively in the following chapters 3 and 4. In these chapters we shall re-adapt this Hamiltonian in order to describe periodic anisotropic optically active media patterned in two different geometries.

To this end we begin with, in section 2.2, an introduction to Maxwell's equations and the constitutive relations in a general sense. We shall then proceed to the particular constitutive relations of biaxial materials featuring either of two forms of optical activity. With the nature of the induced response in biaxial gyrotropic materials established we move onto examining the propagation of disturbances through these materials in section 2.3. This is done through a 2×2 matrix eigenvalue problem for the transverse displacement field, as developed by Berry and Dennis [91]. The eigenvalues of this problem are related to the refractive indices, while the eigenvectors determine the polarisation state of the displacement field both of which are examined in section 2.4. The polarisation structure additionally has an associated topological invariant which we discuss in subsection 2.4.3. Having discussed these surfaces in generality we then move to the aforementioned local paraxial approximation approach in section 2.5. This approach facilitates the derivation of a Hamiltonian that evolves the field along an optic axis direction, which we consider in section 2.6.

2.2 The Constitutive Relations of Anisotropic Optically Active Materials

Maxwell's equations are the fundamental description of the propagation of light. They are a set of coupled differential equations describing the temporal and spatial evolution of the electric and magnetic field of a disturbance as the disturbance moves through space. The equations can be written in an arbitrary medium as

$$\boldsymbol{\nabla} \cdot \mathbf{D} = \rho_f, \tag{2.1}$$

$$\boldsymbol{\nabla} \cdot \mathbf{B} = 0, \tag{2.2}$$

$$\boldsymbol{\nabla} \times \mathbf{E} = -\partial_t \mathbf{B}, \tag{2.3}$$

$$\boldsymbol{\nabla} \times \mathbf{H} = \mathbf{j}_f + \partial_t \mathbf{D}. \tag{2.4}$$

In the above eqs. (2.1) to (2.4), $\mathbf{E}$ and $\mathbf{B}$ are the free space electric and magnetic fields, $\mathbf{D}$ and $\mathbf{H}$ are the induced electric and magnetic fields in the material considered and ρ_f and $\mathbf{j}_f$ are the free charge density and current density respectively. In what follows we shall be exclusively interested in describing the spatial and temporal evolution of the fields in the situation where the charge and current densities are zero, thus $p_f = 0$ and $\mathbf{j}_f = \mathbf{0}$ henceforth.

The description of the medium under consideration is fully accounted for by a set of constitutive equations that relate the free space electric and magnetic fields $(\mathbf{E}, \mathbf{B})$ to those induced in the material $(\mathbf{D}, \mathbf{H})$. The induced fields can be expanded as a power series in the free fields and in most circumstances it is sufficient to retain only the linear terms in this expansion. The response may however be non-local in either space and/or time:

$$\mathbf{D}(\mathbf{r},t) = \int dt' \int d\mathbf{r}' \left[\underline{\underline{\epsilon}}(\mathbf{r}',t')\mathbf{E}(\mathbf{r}-\mathbf{r}',t-t') + \underline{\underline{\alpha}}(\mathbf{r}',t')\mathbf{B}(\mathbf{r}-\mathbf{r}',t-t') \right], \tag{2.5}$$

$$\mathbf{H}(\mathbf{r},t) = \int dt' \int d\mathbf{r}' \left[\underline{\underline{\beta}}(\mathbf{r}',t')\mathbf{E}(\mathbf{r}-\mathbf{r}',t-t') + \underline{\underline{\nu}}(\mathbf{r}',t')\mathbf{B}(\mathbf{r}-\mathbf{r}',t-t') \right]. \tag{2.6}$$

Spatial non-locality will only be important when considering light whose wavelength is of the scale of the structure probed. This situation will not be treated in this chapter so we can take the response to be local. The temporal non-locality can be dealt with by taking the Fourier transform and using the convolution theorem to arrive at the constitutive relations

$$\mathbf{D}(\mathbf{r},\omega) = \underline{\underline{\epsilon}}_{\mathrm{BP}}(\mathbf{r},\omega)\mathbf{E}(\mathbf{r},\omega) + \underline{\underline{\alpha}}_{\mathrm{BP}}(\mathbf{r},\omega)\mathbf{B}(\mathbf{r},\omega), \tag{2.7}$$

$$\mathbf{H}(\mathbf{r},\omega) = \underline{\underline{\beta}}_{\mathrm{BP}}(\mathbf{r},\omega)\mathbf{E}(\mathbf{r},\omega) + \underline{\underline{\nu}}_{\mathrm{BP}}(\mathbf{r},\omega)\mathbf{B}(\mathbf{r},\omega). \tag{2.8}$$

This is the so-called Boys-Post representation of the constitutive relations in which the induced fields are expressed in terms of the free fields [99]. There is another representation, the Tellgen representation [99], which expresses $(\mathbf{D}, \mathbf{B})$ in terms of $(\mathbf{E}, \mathbf{H})$:

$$\mathbf{D}(\mathbf{r},\omega) = \underline{\underline{\epsilon}}_{\mathrm{T}}(\mathbf{r},\omega)\mathbf{E}(\mathbf{r},\omega) + \underline{\underline{\alpha}}_{\mathrm{T}}(\mathbf{r},\omega)\mathbf{H}(\mathbf{r},\omega), \tag{2.9}$$

$$\mathbf{B}(\mathbf{r},\omega) = \underline{\underline{\beta}}_{\mathrm{T}}(\mathbf{r},\omega)\mathbf{E}(\mathbf{r},\omega) + \underline{\underline{\mu}}_{\mathrm{T}}(\mathbf{r},\omega)\mathbf{H}(\mathbf{r},\omega). \tag{2.10}$$

The Tellgen representation will be the one used throughout, however they are entirely equivalent descriptions and (all being well-behaved) are related by an inversion. In this chapter we shall be concerned with non-magnetic materials i.e., $\underline{\underline{\mu}}(\mathbf{r},\omega) = \mu_0 \underline{\underline{\mathbb{1}}}$ which are not bi-responsive ($\underline{\underline{\alpha}}(\mathbf{r},\omega) = \underline{\underline{0}} = \underline{\underline{\beta}}(\mathbf{r},\omega)$). The response of these materials will then be entirely determined by their permittivity tensors $\underline{\underline{\epsilon}}(\mathbf{r},\omega)$, or alternatively by their inverse permittivity, or impermeability, tensor $\underline{\underline{\eta}}(\mathbf{r},\omega)$. We shall consider the tensor $\underline{\underline{\eta}}(\mathbf{r},\omega)$ as this neatly facilitates working with

the transverse displacement field **D**, which will prove advantageous. In doing this we have made a choice as to how to include chirality in the constitutive relations; we have followed the approach used by Landau and Lifshitz [97]. In this approach chirality is included by adding the simplest non-trivial non-local contribution to the electric field **E** which is proportional to $\boldsymbol{\nabla} \times \mathbf{D}$. There are alternative ways to include chirality through a bianisotropic response [99] however they can be related with the approach of Landau and Lifshitz [97] thorough Faraday's law (2.3). We do not expect the conclusions of this or subsequent chapters to be dependent on the way in which chirality is included in the constitutive relations. Additionally in this chapter and the work which follows in chapters 3, 4 and 5 we shall consider materials which are non-dispersive. As such in these subsequent chapters when we consider frequency variation we are not strictly referring to a single material but rather to an abstract material which at each wavelength considered has the allotted properties. We shall now move to examining the form of the inverse permittivity tensors of anisotropic optically active dielectrics.

2.2.1 Biaxial Faraday Effect Material

In the case of a transparent biaxial Faraday effect material the inverse permittivity tensor is of Hermitian form, i.e. $\eta_{ij} = \eta_{ji}^*$ [97]. In the absence of an external magnetic field this tensor becomes real symmetric. In this instance there is a coordinate system, known as the the principal dielectric axes, in which this symmetric tensor is diagonal, with real distinct eigenvalues $\frac{1}{\epsilon_i}$ [98]. We shall consider the inverse permittivity in this coordinate system initially and refer to this as the 123 coordinate system henceforth. These optically biaxial dielectrics occur in crystal systems with the lowest degree of symmetry; those of the orthorhombic, monoclinic and triclinic varieties [13]. We now turn to the effect of introducing an external magnetic field.

Upon introduction of a static external magnetic field the permittivity tensor is no longer diagonal, acquiring, to the leading order in the external field **h**, imaginary off-diagonal components according to

$$(-\eta_{23}, \eta_{13}, -\eta_{12})^T = i\underline{\underline{f}}\,\mathbf{h} \tag{2.11}$$

where $\underline{\underline{f}}$ is a general rank two tensor [97] and **h** is measured in Tesla. The next order correction in the magnetic field is a real symmetric contribution to the off-diagonal terms of the inverse permittivity tensor. This contribution is responsible for the Cotton-Mouton effect. The Faraday effect occurs in many transparent materials and causes a small discrepancy in the refractive indices experienced by left and right circularly polarised light [97]. This discrepancy results in the material rotating the direction of polarisation of linearly polarised light as it passes through a Faraday effect material subjected to a magnetic field. The scale of this optical rotation

is captured in a quantity called the Verdet constant. The Verdet constant gives the rotation in radians per meter per Tesla. A typical value for this quantity is $V = 9.25\,\mathrm{rad\,T^{-1}\,m^{-1}}$ (for quartz at $\lambda = 435.8\,\mathrm{nm}$ [100]). In a similar vein we now introduce chiral materials.

2.2.2 Chiral Biaxial Material

Just like materials exhibiting the Faraday effect, chiral materials do not affect the two circular polarisations of light in the same way. In chiral materials, however, the asymmetry arises from intrinsic material properties, rather than the effect of an external magnetic field [97]. For chiral materials the inverse permittivity tensor is again Hermitian. As for the Faraday effect the chiral contributions appear on the off-diagonal of the inverse permittivity tensor according to

$$(-\eta_{23}, \eta_{13}, -\eta_{12})^T = i\underline{\underline{G}}\,\mathbf{s} \tag{2.12}$$

where $\mathbf{s}$ is the unit propagation direction and $\underline{\underline{G}}$ is the chirality tensor, which may be taken to be real symmetric [97]. The equation (2.12) is for weak spatial dispersion, a regime in which the chiral contributions to the permittivity tensor can be expanded in powers of the unit propagation direction $\mathbf{s}$. This expansion starts linearly in $\mathbf{s}$ with each successive term smaller by a factor of a/λ, where a is the lattice spacing and λ is the wavelength. We choose to omit the higher-order terms as at optical and longer wavelengths the higher-order terms are considerably smaller in magnitude than the leading term. If we were to have additionally considered metamaterial structures it would be possible to have more complicated gyromagnetic tensors however we have chosen to focus solely on dielectric crystals. The number of the six components of $\underline{\underline{G}}$ which are non-zero depends on the crystal system considered. In crystals which possess a centre of symmetry all six of the components are zero. In optically biaxial systems there are eight different possible crystal point groups. Of these eight point groups only five lack a centre of symmetry and hence exhibit chirality. For each of these five possible crystal point groups, there are different forms of the chirality tensor $\underline{\underline{G}}$ which are listed in table 2.1.

Name	Schönflies Notation	Crystal System	Non-Zero Components of $\underline{\underline{G}}$
Pedial	C_1	Triclinic	All non-zero
Sphenoidal	C_2	Monoclinic	G_{aa}, G_{bb}, G_{cc}, G_{ac}
Domatic	C_s	Monoclinic	G_{ab}, G_{bc}
Rhombic Disphenoidal	D_2	Orthorhombic	G_{aa}, G_{bb}, G_{cc}
Rhombic Pyramidal	C_{2v}	Orthorhombic	G_{ab}

TABLE 2.1: The non-zero components of the chirality tensor $\underline{\underline{G}}$ for all non-centrosymmetric biaxial crystals [101].

The relationship between the non-zero chirality components in the standard crystallographic basis *abc* and those in the principal dielectric basis 123 depends on both the system of crystal considered and the material itself within that system.

For orthorhombic crystals the three principal axes coincide with the crystallographic axes in some permutation. The chirality tensor for orthorhombic crystals in the principal axes basis is then

$$\underline{\underline{G}}_{123} = \underline{\underline{P}}\, \underline{\underline{G}}_{abc}\, \underline{\underline{P}}^{T} \tag{2.13}$$

where $\underline{\underline{P}}$ is the appropriate 3×3 permutation matrix that describes how the *abc* and the 123 bases relate. The necessary permutation can be found by looking up the considered material in the Handbook of Mineralogy [102]. In the case of rhombic pyramidal structures (C_{2v}) any of the permutations will result in a symmetric chirality tensor with one of the off-diagonals terms being non-zero and all other terms zero. For the case of rhombic disphenoidal structures (D_2) the result of any of the permutations will produce a diagonal chirality tensor matrix, with distinct entries on the diagonal.

For monoclinic crystals one of the principal axes coincides with the *b* crystallographic axis while the other two have no fixed correspondence with the *a* and the *c* crystallographic axes. In this instance the chirality tensor in the principal axes basis is again related to that stated in table 2.1 by a material specific permutation. This relationship is given by

$$\underline{\underline{G}}_{123} = \underline{\underline{P}}\, \underline{\underline{G}}_{abc}\, \underline{\underline{P}}^{T} \tag{2.14}$$

where $\underline{\underline{P}}$ is the appropriate permutation matrix, which can again be determined from the Handbook of Mineralogy [102]. For domatic crystal systems (C_s) any of the permutations will result in a symmetric chirality tensor possessing two distinct off-diagonal terms with zeroes on the diagonal. In the case of sphenoidal crystals (C_2) any permutation will produce a symmetric chirality tensor with three distinct diagonal entries and one off-diagonal entry unrelated to any of those on the diagonal.

In triclinic crystal systems there is no relationship between the crystallographic axes and the principal dielectric axes. As such all components of the chirality tensor in the principal dielectric basis are non-zero and have no relationship to each other.

In biaxial crystals it is rare that the precise values of all the components of the chirality tensor are known. This is because the effect, in comparison to biaxiality, is weak. Owing to this it is difficult to measure the strength of the chirality away from an optic axis [101]. A typical scale for these components is set by the optical specific rotation ρ_C, which is the angle in radians that the polarisation direction of linearly

polarised light is rotated by per meter in travelling through a chiral medium. In quartz, a uniaxial material, this quantity is $\rho_C \simeq 840\,\mathrm{rad\,m^{-1}}$ (at $\lambda_0 = 400\,\mathrm{nm}$) [100]. The quantity ρ is defined as $\rho_C = \frac{\pi}{\lambda_0}\Delta n$ and this equation shall be used to set the scale for the chirality tensor components in later chapters.

We note that it is entirely possible that a biaxial dielectric can exhibit both the Faraday effect and chirality. Were this the case we would expect that, due to linearity, these effects should be additive. In the work to follow we have not however considered the possibility of the simultaneous presence of both. Thus from this point on when we refer to biaxial Faraday effect materials it should be assumed that we are referring to a biaxial material which is centrosymmetric and hence does not exhibit chirality.

Now that the nature of the relationship between the applied and induced field in each of these anisotropic optically active materials has been established we can look at describing the propagation of light through them.

2.3 The Wave Equation as a 2×2 Matrix Eigenvalue Problem

To examine the propagation of light through biaxial optically active materials we shall initially work with a wave equation for the displacement field $\mathbf{D}$. We will follow the approach of Berry and Dennis [91] and of Jeffrey [98] where they express the wave equation as a 2×2 matrix eigenvalue problem. In this approach the matrix describes the propagation direction and the material characteristics. As our work will build on this approach we shall spend some time explicitly introducing how this 2×2 matrix eigenvalue problem emerges.

The decoupled wave equation is obtained as an extension to Maxwell's equations. The wave equation follows upon taking the curl of Faraday's law (2.3), using Ampere's law (2.4) to re-write the right hand side and expressing the electric field $\mathbf{E}$ in terms of the displacement field $\mathbf{D}$ through the impermeability tensor $\underline{\underline{\eta}}$. The resulting wave equation for the displacement field is

$$\boldsymbol{\nabla} \times \boldsymbol{\nabla} \times (\underline{\underline{\eta}}\mathbf{D}) = -\frac{1}{c^2}\partial_t^2 \mathbf{D}. \tag{2.15}$$

If we are interested in plane-wave solutions of the wave equation of the form

$$\exp\{i(k_0 n(\mathbf{s})\mathbf{s}\cdot\mathbf{r} - \omega t)\}\mathbf{d}(\mathbf{s}) \tag{2.16}$$

then the wave equation (2.15) becomes

$$-k_0^2 n^2(\mathbf{s})\left[\mathbf{s}\times\mathbf{s}\times(\underline{\underline{\eta}}\mathbf{d}(\mathbf{s}))\right] = \frac{\omega^2}{c^2}\mathbf{d}(\mathbf{s}). \tag{2.17}$$

Using the dispersion relation, the equation (2.17) can be re-written as an eigenvalue problem for the inverse squared refractive indices. This eigenvalue problem takes the form

$$-\left[\mathbf{s}\times\mathbf{s}\times(\underline{\underline{\eta}}\mathbf{d}(\mathbf{s}))\right] = \frac{1}{n^2(\mathbf{s})}\mathbf{d}(\mathbf{s}). \tag{2.18}$$

It is worth noting that the operator $-\mathbf{s}\times\mathbf{s}\times$ acting on a vector is a projector, which picks out the part of the vector which is transverse to $\mathbf{s}$. Henceforth we shall regard the part of the left hand side of equation (2.18) which acts on the displacement field $\mathbf{d}(\mathbf{s})$ as a 3×3 matrix operator, denoted $\underline{\underline{M}}$:

$$\underline{\underline{M}}(\mathbf{s},\underline{\underline{\eta}})\mathbf{D} = \lambda\mathbf{D}. \tag{2.19}$$

The form that $\underline{\underline{M}}$ takes follows from the material considered; in particular from the relevant constitutive relations. As such, for a biaxial material the matrix $\underline{\underline{M}}$ is real symmetric, while upon introduction of either form of optical activity considered in section 2.2 the matrix $\underline{\underline{M}}$ becomes complex Hermitian [91].

The matrix $\underline{\underline{M}}$ is constrained by one of Maxwell's equation (2.1). The transverse nature of the displacement field $\mathbf{d}(\mathbf{s})$ ($\mathbf{s}\cdot\mathbf{d}(\mathbf{s}) = 0$) dictates that $\underline{\underline{M}}$ must have a zero eigenvalue. The other two eigenvalues correspond to the inverse squares of the directionally dependent refractive indices of an anisotropic material. The zero eigenvalue of $\underline{\underline{M}}$ must have a corresponding eigenvector which is directed along the propagation direction $\mathbf{s}$ considered. This information allows us to reduce the equation (2.19) to a 2×2 matrix eigenvalue problem.

To accomplish this reduction we shall change the basis of $\underline{\underline{M}}$ such that one of the coordinate axes points along the propagation direction $\mathbf{s}$. This procedure is carried out by writing the unit propagation direction $\mathbf{s}$ in spherical polar coordinates $\mathbf{s} = (\sin\theta\cos\phi, \sin\theta\sin\phi, \cos\theta)$ and then implementing the transformation

$$\underline{\underline{M}}_{R\theta\phi} = \underline{\underline{R}}\,\underline{\underline{M}}_{xyz}\,\underline{\underline{R}}^{-1} \tag{2.20}$$

where the transformation matrix $\underline{\underline{R}}$ is given by

$$\underline{\underline{R}} = \begin{pmatrix} \sin\theta\cos\phi & \sin\theta\sin\phi & \cos\theta \\ \cos\theta\cos\phi & \cos\theta\sin\phi & -\sin\theta \\ -\sin\phi & \cos\phi & 0 \end{pmatrix}. \tag{2.21}$$

This transformation allows us to easily extract the part of the operator $\underline{\underline{M}}$ which is transverse to $\mathbf{s}$. This transverse part is the 2×2 matrix $\underline{\underline{m}}$:

$$\underline{\underline{m}}_{\theta\phi} = \begin{pmatrix} m_{\theta\theta} & m_{\theta\phi} \\ m_{\phi\theta} & m_{\phi\phi} \end{pmatrix}. \tag{2.22}$$

For later convenience we shall proceed to transform the basis of $\underline{\underline{m}}$ (equation (2.22)) to a circular polar basis by affecting the transformation:

$$\underline{\underline{m}}_{RL} = \underline{\underline{R}}_C \, \underline{\underline{m}}_{\theta\phi} \, \underline{\underline{R}}_C^{-1}. \tag{2.23}$$

In this instance the transformation matrix $\underline{\underline{R}}_C$ is given by the equation

$$\underline{\underline{R}}_C = \frac{1}{\sqrt{2}} \begin{pmatrix} 1 & -i \\ 1 & i \end{pmatrix}. \tag{2.24}$$

As a final step we shall re-express $\mathbf{s}$ in Cartesian coordinates, arriving at a final equation of the form

$$\underline{\underline{m}}_{RL}(\mathbf{s}, \underline{\underline{\eta}}) \mathbf{d}_{RL} = \frac{1}{n^2(\mathbf{s})} \mathbf{d}_{RL}. \tag{2.25}$$

To study the intricacies of the resulting matrix $\underline{\underline{m}}$ we shall decompose it into factors proportional to the identity matrix and each of the three Pauli matrices $\underline{\underline{\sigma}}_i$

$$\underline{\underline{m}}(\mathbf{s}, \underline{\underline{\eta}}) = A(\mathbf{s}, \underline{\underline{\eta}}) \underline{\underline{\mathbb{1}}} + B(\mathbf{s}, \underline{\underline{\eta}}) \underline{\underline{\sigma}}_z + C(\mathbf{s}, \underline{\underline{\eta}}) \underline{\underline{\sigma}}_x + D(\mathbf{s}, \underline{\underline{\eta}}) \underline{\underline{\sigma}}_y. \tag{2.26}$$

When decomposed in this fashion the functions A, B, C and D are polynomials in the unit wavevector direction $\mathbf{s}$. These functions additionally depend linearly on the components of the impermeability tensor $\underline{\underline{\eta}}$. The functions are

$$A(\mathbf{s}, \underline{\underline{\eta}}) = \frac{(s_1^2 s_3^2 + s_2^2)}{2(s_1^2 + s_2^2)} \eta_{11} + \frac{(s_2^2 s_3^2 + s_1^2)}{2(s_1^2 + s_2^2)} \eta_{22} + \frac{(s_1^2 + s_2^2)}{2} \eta_{33}, \tag{2.27}$$

$$B(\mathbf{s}, \underline{\underline{\eta}}) = i(s_3 \eta_{12} - s_2 \eta_{13} + s_1 \eta_{23}), \tag{2.28}$$

$$C(\mathbf{s}, \underline{\underline{\eta}}) = \frac{(s_1^2 s_3^2 - s_2^2)}{2(s_1^2 + s_2^2)} \eta_{11} + \frac{(s_2^2 s_3^2 - s_1^2)}{2(s_1^2 + s_2^2)} \eta_{22} + \frac{(s_1^2 + s_2^2)}{2} \eta_{33}, \tag{2.29}$$

$$D(\mathbf{s}, \underline{\underline{\eta}}) = \frac{s_1 s_2 s_3}{(s_1^2 + s_2^2)} (\eta_{22} - \eta_{11}). \tag{2.30}$$

The off-diagonal terms of the impermeability tensor $\underline{\underline{\eta}}$, those responsible for optical activity, only appear in the polynomial (2.28). For the two variants of optical activity detailed in section 2.2 the resultant forms of polynomial (2.28) are

$$B_F(\mathbf{s}) = \mathbf{s}^T \underline{\underline{f}} \mathbf{h}, \tag{2.31}$$

$$B_C(\mathbf{s}) = \mathbf{s}^T \underline{\underline{G}} \mathbf{s}. \tag{2.32}$$

2.4 Refractive Index Surfaces and Their Polarisation Structure

The refractive indices $n_{\pm}(\mathbf{s}, \underline{\underline{\eta}})$ which follow from the eigenvalues $\lambda_{\pm}(\mathbf{s}, \underline{\underline{\eta}})$ of the matrix $\underline{\underline{m}}_{RL}$ are then

$$n_{\pm}(\mathbf{s}, \underline{\underline{\eta}}) = \frac{1}{\sqrt{\lambda_{\pm}(\mathbf{s}, \underline{\underline{\eta}})}} = \frac{1}{\sqrt{A(\mathbf{s}, \underline{\underline{\eta}}) \pm \sqrt{B(\mathbf{s}, \underline{\underline{\eta}})^2 + C(\mathbf{s}, \underline{\underline{\eta}})^2 + D(\mathbf{s}, \underline{\underline{\eta}})^2}}} \tag{2.33}$$

The refractive indices (2.33) can be visualised by plotting two surfaces whose magnitude in a given direction is the refractive index for light propagating in that direction. When done over all directions of the unit wavevector $\mathbf{s}$ this procedure defines two closed surfaces in direction space. These plots are known as refractive index surfaces and the two sheets are associated with the two polarisation states for light propagating in that direction. There is a related construction, which is known as the optical indicatrix or index ellipsoid, which also describes the two refractive indices as well as the vibration direction of $\mathbf{D}$ over all directions $\mathbf{s}$. We have chosen to work exclusively with the refractive index surface rather than the index ellipsoid in this thesis however it could be an interesting complimentary approach to instead consider the index ellipsoid.

2.4.1 Refractive Index Surfaces of Biaxial Materials

In a biaxial material, that does not exhibit optical activity, the refractive index surfaces are two ellipsoids. These ellipsoids intersect at four points in direction space which are joined by two optic axes. Each of the four points represent a direction in which the refractive indices are degenerate. These degeneracies shall be the primary focus of the balance of this chapter and shall feature prominently in chapters 3 and 4. We now discuss why these points are worthy of such attention.

The left plot of figure 2.1 shows a section of the refractive index surfaces of a general homogeneous biaxial material. Throughout this thesis we shall be adopting the convention that $\epsilon_1 < \epsilon_2 < \epsilon_3$ where ϵ_i is the i-th principal dielectric constant of a biaxial material. With this convention the aforementioned degeneracies all appear in the plane $s_2 = 0$.

The accompanying plot on the right of figure 2.1 shows a close up of one of these degeneracies, or conical intersections. We can see from this plot that the local dispersion of this degeneracy is linear and as such this degeneracy is equivalent to the celebrated Dirac points of condensed matter physics. This conical intersection is in fact one of the earliest examples of a Dirac point having been discovered by William Rowan Hamilton in Trinity College Dublin in 1832 [103]. The presence of

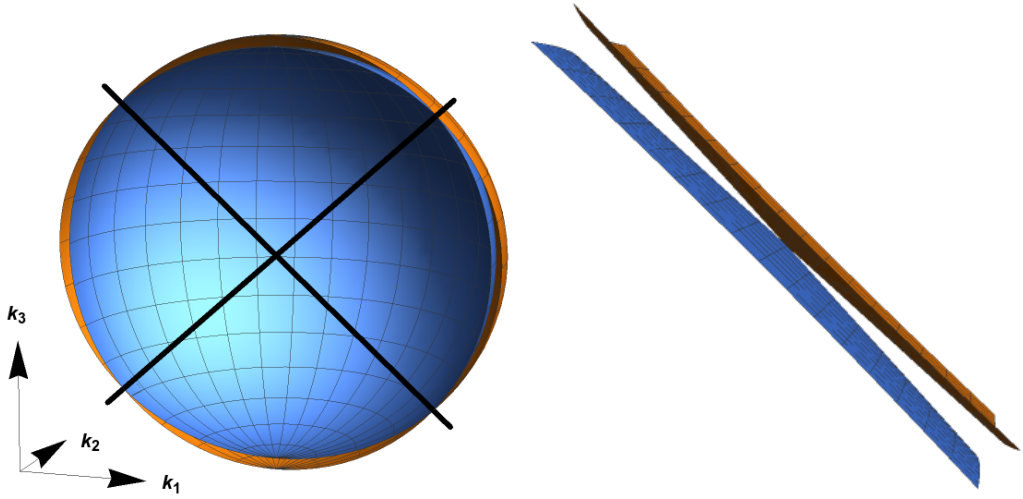

FIGURE 2.1: On the left is a figure showing a section of the refractive index surfaces of a biaxial material. The two surfaces represent, by radius in a given direction, the magnitude of the refractive index for light propagating in that direction. The black lines represent the two optic axes which join pairs of the four conical intersections in the $s_2 = 0$ plane. The figure on the right is a close up of one of these conical intersections. In these plots the principal dielectric constants were chosen to be $(\epsilon_1, \epsilon_2, \epsilon_3) = (2.25, 2.5, 2.75)$. We shall use this set of constants for the figures in the remainder of this chapter also.

this conical intersection is responsible for the phenomenon of conical refraction, which was observed by Humphrey Lloyd shortly after [104].

Each of the eigenvalues of equation (2.25) (and hence each point on each surface of the plots in figure 2.1) has an associated eigenvector $\mathbf{d}(\mathbf{s})$ describing the polarisation state of light travelling in a particular direction. In any chosen direction the two polarisations of light are orthogonal to each other, owing to the Hermiticity of $\underline{\underline{m}}_{RL}$. The polarisation associated with each surface varies as the direction of propagation is varied. We shall now study the polarisation structure of the refractive index surfaces of a biaxial material. Initially we shall consider a situation where there is no optical activity and then we shall examine the resulting polarisation structure following its introduction.

For a biaxial material which lacks any optical activity, each of the two refractive index surfaces are linearly polarised. The direction of the linear polarisation of each surface is dependent on the propagation direction $\mathbf{s}$. To assess the totality of directions of linear polarisation over each surface we can examine the ratio of the components of the eigenvectors $\mathbf{d}(\mathbf{s})$ in a given direction. If we define

$$z_{\pm}(\mathbf{s}) = \frac{d_{\pm R}(\mathbf{s})}{d_{\pm L}(\mathbf{s})} \tag{2.34}$$

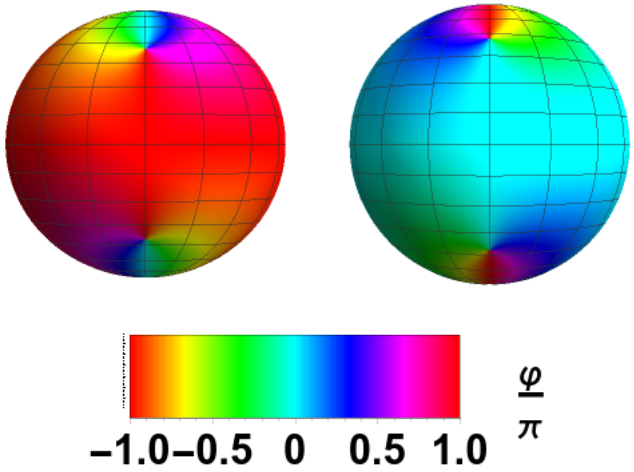

FIGURE 2.2: A view of each of the two index surfaces of a homogeneous biaxial material. The left plot is the outer index surface, i.e. that of larger refractive index, while the right is the inner surface. The surfaces are viewed from out along the positive s_1 axis. Each surface is coloured according to the argument of the ratio of the eigenvector components φ where $\frac{1}{2}\varphi$ represents the direction of the linear polarisation for light propagating in that direction. *varphi* is measured with respect to the direction of the local polar unit vector.

to be this ratio then the direction of linear polarisation can be accessed by examining the argument of this complex number $\varphi_{\pm}(\mathbf{s}) = \arg z_{\pm}(\mathbf{s})$. The phase represents twice the angle of linear polarisation. We can look at the polarisation behaviour by examining this phase over each of the refractive index surfaces of a biaxial material.

Figure 2.2 looks at the two refractive index surfaces separately with each surface coloured according to the phase $\varphi(\mathbf{s})$. This figure is viewed from out along the positive s_1 axis. We see that the phase difference $\Delta\varphi$ between each of the surfaces in any direction is π, reflecting the orthogonality of the two polarisation states.

Of greater interest than the orthogonality however is the behaviour of the direction of linear polarisation of each surface around each of the conical intersections. We can see in figure 2.2 that the phase φ completes a full cycle from $-\pi$ to π around the degeneracy. This means that the direction of linear polarisation turns by π as the degeneracy is encircled. A change of linear polarisation of π is equivalent to the original polarisation state a half cycle further along. This rotation of the direction of polarisation arises as these points are equivalent to the Dirac points introduced in subsection 1.2.2 and have a topological index of $\frac{1}{2}$ associated with them.

In figure 2.3 we look at a representation of the phase $\varphi(\mathbf{s})$ of each refractive index surfaces over all possible directions (θ, ϕ) of the unit wavevector. This figure allows us to assess the properties of all of the conical intersections. In particular we note that the sense of circulation of the phase φ around each of the degeneracies is

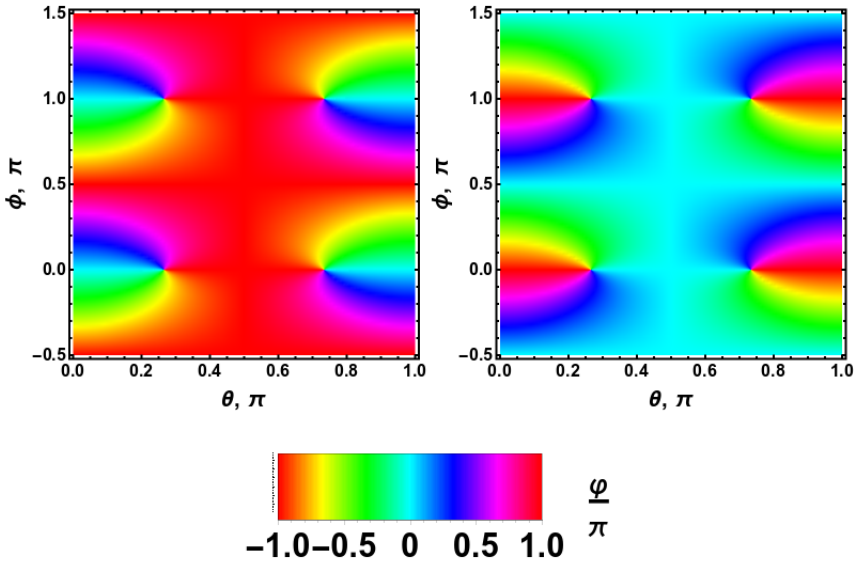

FIGURE 2.3: The direction of the linear polarisation for light propagating in a direction (θ, ϕ) through a biaxial material. The angle θ is the polar angle measured from the 3 principal dielectric axis and the angle ϕ is the azimuthal angle measured in the $s_3 = 0$ plane from the s_1 direction. The left figure corresponds to the outermost refractive index surface and the right figure to the inner one. The plots are coloured according to the argument of the ratio of the eigenvector components φ where $\frac{1}{2}\varphi$ represents the direction of the linear polarisation for light propagating in that direction.

the same. This reveals that the topological index of each of the degeneracies is $\frac{1}{2}$. The topological index is an additive quantity and hence the total topological index of each of the surfaces is 2. This is reflective of, and dictated by, the Poincaré-Hopf, or "hairy-ball" theorem [90] which states that the total vorticity of a tangent vector field on the surface of a sphere must be 2.

This analysis of the refractive index surfaces of biaxial materials should be considered as the necessary groundwork towards the understanding of these structures in the presence of optical activity. This is the case as, over most of the index surfaces, the addition of optical activity can be viewed as a perturbation.

2.4.2 Refractive Index Surfaces of Biaxial Optically Active Materials

The introduction of optical activity provides a weak modulation to the refractive index surfaces seen in subsection 2.4.1. The change in the refractive indices due to either form of optical activity discussed in section 2.2 is comparatively small in relation to biaxial anisotropy [97, 101]. This is not the case however along the directions of the degenerate conical intersections of the biaxial material. In these directions the addition of either form of optical activity, in a suitable manner, can lift

the degeneracies [14, 105].

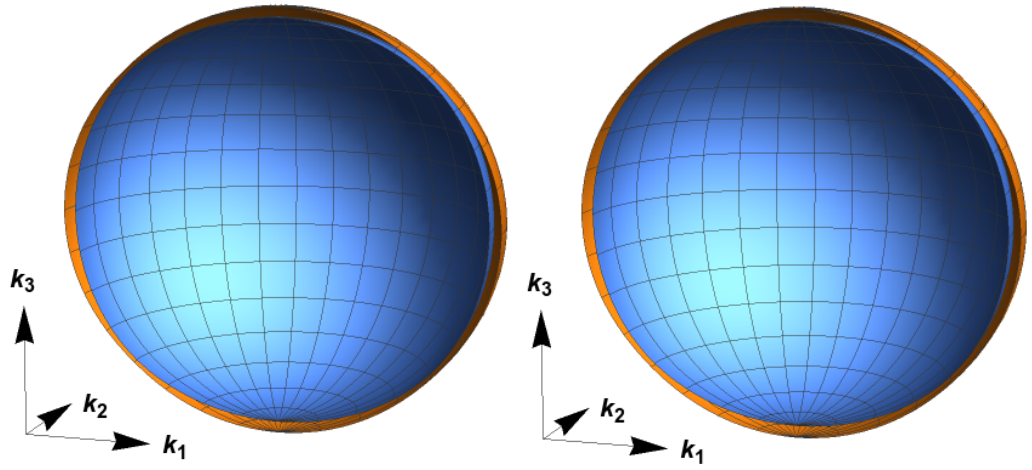

FIGURE 2.4: Figures showing sections of the index surfaces of a homogeneous biaxial material with two possible forms of optical activity. On the left we have considered the Faraday effect with a magnetic field of 1 T along the s_1 direction. On the right we have considered a chiral material. The Faraday effect and chirality tensors were taken to be $\underline{\underline{f}} = 0.01\underline{\underline{\mathbb{1}}}_3\ \mathrm{T}^{-1}$ and $\underline{\underline{G}} = 0.01\underline{\underline{\mathbb{1}}}_3$.

In figure 2.4 we look at the refractive index surfaces of biaxial materials with either form of optical activity. The left plot in figure 2.4 is the refractive index surface of a biaxial Faraday effect material. In this figure we have taken the Faraday effect tensor $\underline{\underline{f}} = 0.01\ \underline{\underline{\mathbb{1}}}_3\mathrm{T}^{-1}$ and a magnetic field $\mathbf{h}$ of 1 T along the s_1 direction. For the right plot in figure 2.4 we see the refractive index surface of a chiral biaxial material. For this figure we have considered an isotropic chirality $\underline{\underline{G}} = 0.01\ \underline{\underline{\mathbb{1}}}_3$. For each case in figure 2.4 we can see that there is now a small gap separating the surfaces along each of the optic axes. In each instance the strength of the optical activity is somewhat exaggerated in order to make the effect of the introduction manifest in figure 2.4. Owing to the small deviations from that of a biaxial material the introduction of the optical activity could be seen as of little importance however an examination of the resulting polarisation structure will dispel such a conclusion.

Upon introduction of either form of optical activity the refractive index surfaces are no longer linearly polarised for every direction as we saw was the case for biaxial materials in subsection 2.4.1. Generally the polarisation states of light are that of elliptic polarisation. In the presence of optical activity the phase $\frac{1}{2}\varphi(\mathbf{s})$ now determines the semi-major axis of the polarisation ellipse. There remains the possibility of linearly polarised states in some directions. This occurs along directions $\mathbf{s}'$ which satisfy either, in the case of the Faraday effect $\mathbf{s}'^{T}\underline{\underline{f}}\mathbf{h} = 0$, or in the case of chirality

$\mathbf{s}'^T \underline{\underline{G}} \mathbf{s}' = 0$. Alternatively, these directions can be determined by looking for directions $\mathbf{s}$ which satisfy

$$|z_{\pm}(\mathbf{s})| = 1. \tag{2.35}$$

This condition is in-fact usually satisfied along lines in directional space known as L-lines [90, 106]. The precise details of the optical activity that is introduced determines whether these lines appear at all, and, if so, what paths in directional space they follow. The L-lines (2.35) separate regions of left-handed elliptic polarisation ($|z_{\pm}(\mathbf{s})| < 1$) from regions of right handed elliptic polarisation ($|z_{\pm}(\mathbf{s})| > 1$). For light propagating along the directions of the previously degenerate conical intersections the two polarisation states are now circularly polarised having previously been ill-defined. These points are therefore known as C-points [90, 106]. We now explore these concepts with reference to the two kinds of optical activity.

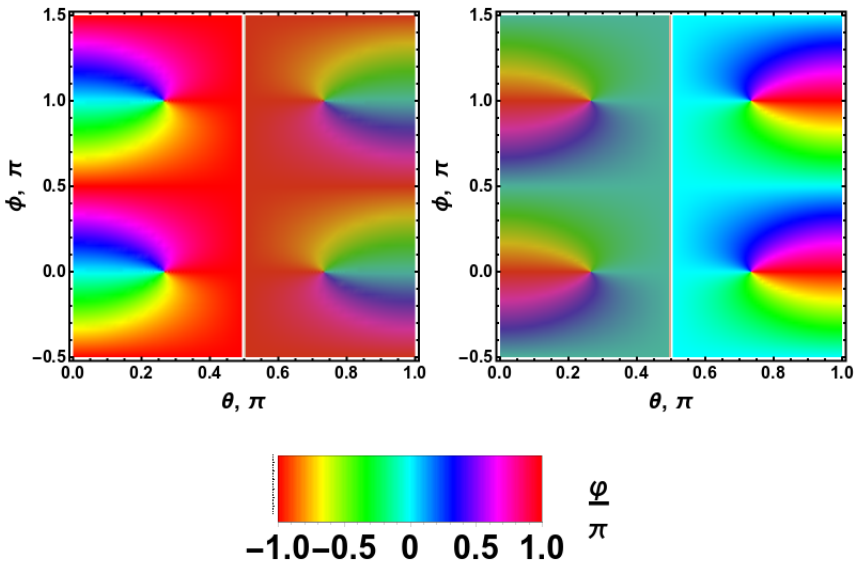

FIGURE 2.5: The polarisation structure for light propagating in a direction (θ, ϕ) through a biaxial Faraday effect material. The magnetic field is directed along the s_3 axis. The left figure corresponds to the outermost refractive index surface and the right figure to the inner one. The plots are coloured according to the argument of the ratio of the eigenvector components φ where $\frac{1}{2}\varphi$ represents the direction of the semi-major axis of the polarisation ellipse. The white contour lines are lines of linear polarisation. The brown shaded regions represent areas where the elliptic polarisation is left-handed.

Figure 2.5 shows the polarisation structure of the refractive index surfaces of a biaxial Faraday effect material. In this figure we have considered the magnetic field along the s_3 axis. For this orientation of the magnetic field we see that there is an L-line for propagation directions in the $s_3 = 0$ plane. This L-line separates regions of different handed elliptical polarisation, with the brown shaded region representing left-handed elliptical polarisation. The points where all the colours of

φ meet are C-points with a handedness determined by the shading of the figure. The orthogonality of the polarisation states of the two surfaces in a given direction is now reflected by the semi-major axes of the polarisation ellipses differing by $\frac{\pi}{2}$ as well as the two states having opposite handedness. Irrespective of the orientation of the magnetic field the regions of each handedness of the polarisation states for both refractive index surfaces will always be symmetric. This follows from the effective $\mathbf{h} \cdot \mathbf{s}$ contribution of the Faraday effect. This enforces the condition that each antipodal pair of degeneracies must have opposite handedness. We shall see the implications of this condition when we later discuss the topological invariants associated with these surfaces.

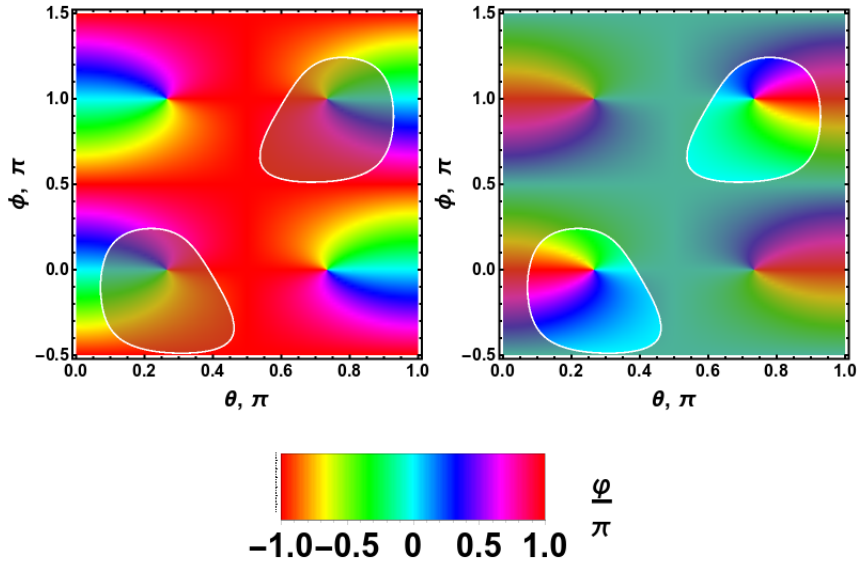

FIGURE 2.6: The polarisation structure for light propagating in a direction (θ, ϕ) through a chiral biaxial material. We have considered the pedial crystal point group. The left figure corresponds to the outermost refractive index surface and the right figure to the inner one. The plots are coloured according to the argument of the ratio of the eigenvector components φ where $\frac{1}{2}\varphi$ represents the direction of the semi-major axis of the polarisation ellipse. The white contour lines are lines of linear polarisation. The brown shaded regions represent areas where the elliptic polarisation is left-handed. The components of the symmetric chirality tensor $\underline{\underline{G}}$ were $G_{11} = 0.45$, $G_{12} = 0.13$, $G_{13} = -0.6$, $G_{22} = 0.15$, $G_{23} = 0.18$ and $G_{33} = 0.3$.

In figure 2.6 we study the polarisation structure of the refractive index surfaces of a chiral biaxial material. In this instance we consider a triclinic crystal of the pedial form. We have assigned random real numbers to each of the six components of $\underline{\underline{G}}$ which are given in the figure caption. We immediately note that for this form of optical activity there is no restriction of equal regions of each polarisation handedness on each surface, in contrast to what we saw for the Faraday effect. Besides this difference the polarisation structures are not dissimilar, with each surface featuring

C-points and L-Lines. As in figure 2.5 there are two C-points of each handedness, however as previously mentioned there is no antipodal symmetry. There being equal numbers of C-points of each handedness is, for chiral biaxial materials, not a requisite as we shall see.

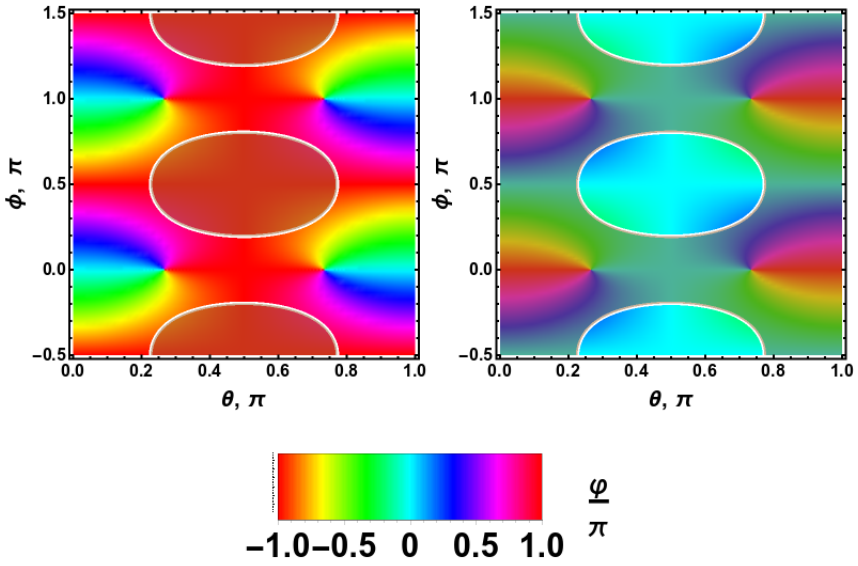

FIGURE 2.7: The polarisation structure for light propagating in a direction (θ, ϕ) through a chiral biaxial material. We have considered the rhombic disphenoidal crystal point group. The left figure corresponds to the outermost refractive index surface and the right figure to the inner one. The plots are coloured according to the argument of the ratio of the eigenvector components φ where $\frac{1}{2}\varphi$ represents the direction of the semi-major axis of the polarisation ellipse. The white contour lines are lines of linear polarisation. The brown shaded regions represent areas where the elliptic polarisation is left-handed.

Figure 2.7 shows just this. In this figure we consider a chiral biaxial material, with an orthorhombic crystal of the rhombic disphenoidal type. For the non-zero components of the chirality tensor $\underline{\underline{G}}$ we have chosen $G_{11} = -2G_{22} = 1.5G_{33}$. We can see that for each of the refractive index surfaces the four C-points have the same handedness.

2.4.3 Topological Invariants of Refractive Index Surfaces

The handedness of the C-points has a critical bearing on a topological invariant which is associated with each refractive index surface [89]. The appropriate topological invariant is the Chern number C which can be determined for each of these surfaces by examination of the plots of the polarisation structures in subsection 2.4.2. According to equation (1.9) since the topological index of each of the C-points is the same the Chern number is then completely determined by the handedness

of each of the C-points. If all of the signs of the handedness at the C-points are the same then the two surfaces have $C = \pm 2$, while if there are two C-points of each handedness then $C = 0$ for each surface.

For the figures in subsection 2.4.2 we can use this recipe to determine the Chern number associated with each of the refractive index surfaces. In the case of the refractive index surfaces in figure 2.5 we see that there are two C-points of each handedness, as such the Chern number $C = 0$. In fact, owing to the previously mentioned antipodal anti-symmetry of the Faraday effect contribution to the polarisation structure of these surfaces, a non-zero Chern number will not be possible for any field application direction. In chapters 3 and 4 we investigate two alternative geometries for this type of material, those of a two dimensional photonic crystal with two patterning arrangements, and see that non-zero Chern numbers for biaxial Faraday effect materials can be achieved in these arrangements.

In the case of the refractive index surfaces of the chiral biaxial material studied in subsection 2.4.2 there are less severe restrictions on the Chern number. In particular in figures 2.6 and 2.7 we observe two configurations corresponding to different values of this invariant. In figure 2.6 we observe that there are again two C-points of each handedness and hence the Chern number is 0 for both surfaces. However in figure 2.7 we are presented with a configuration that has each of the four C-points of each surface having the same handedness and hence the Chern number of the surfaces is $C = \pm 2$.

This survey of the polarisation structure of refractive index surfaces is complementary to that conducted by Gao et al. [87]. In this work we have considered materials with biaxial anisotropy and one of two possible forms of optical activity compared to the work of Gao et al. [87] where uniaxial hyperbolic materials with isotropic chirality were considered. In each case Chern numbers were determined for the refractive index surfaces of the anisotropic materials. As well as providing novel conclusions about the prospect of topological order in homogeneous, anisotropic and optically active materials this work also serves as a primer for corresponding studies of patterned materials in chapters 3 and 4.

2.5 The Paraxial Approximation to the Refractive Index Surfaces

We are also interested in the local behaviour of the dispersion around a single one of the C-points of the refractive index surface. Appropriately describing this behaviour will allow us to build theories of light travelling through periodic arrangements of biaxial optically active materials in directions close to one of the C-points in

subsequent chapters. Since we are interested in the structure of the refractive index surfaces locally to just one of the conical intersections we can then discard all non-pertinent parts of the polynomials eqs. (2.27) to (2.30). We do this in the hope that what remains is more physically transparent and easier to work with. This is the spirit of the paraxial approximation. In our case we shall consider the expansion of eqs. (2.27) to (2.30) to second order around the direction of a conical intersection. This expansion will be an extension of the work of Jeffrey [98] where the polynomials eqs. (2.27) to (2.29) were expanded to first order and the final polynomial (2.30) to zeroth order. To facilitate this expansion it will be useful to introduce a new set of coordinates.

The direction of an optic axes of a biaxial material is in the plane $s_2 = 0$ at an angle θ_{OA} from the s_3 direction such that

$$\cos\theta_{OA} = \sqrt{\frac{\beta}{\alpha+\beta}} \tag{2.36}$$

where α and β are measures of spread of the principal dielectric constants given by $\alpha = \epsilon_1^{-1} - \epsilon_2^{-1}$ and $\beta = \epsilon_2^{-1} - \epsilon_3^{-1}$. With this in mind we introduce a new set of coordinates with the z direction along an optic axis direction

$$\begin{pmatrix} s_1 \\ s_2 \\ s_3 \end{pmatrix} = \begin{pmatrix} \cos\theta_{OA} & 0 & \sin\theta_{OA} \\ 0 & 1 & 0 \\ -\sin\theta_{OA} & 0 & \cos\theta_{OA} \end{pmatrix} \begin{pmatrix} s_x \\ s_y \\ s_z \end{pmatrix}. \tag{2.37}$$

The relationship between these two coordinate systems is visualised in figure 2.8. The paraxial approximation then assumes that we are interested in highly directional beams primarily travelling along the s_z direction. This approximation of $\mathbf{s}$ to second order in transverse wavevector $\mathbf{p} = \frac{1}{\sqrt{\epsilon_2}k_0}(k_x, k_y)$ is then

$$(s_x, s_y, s_z) \simeq (p_x, p_y, 1 - \frac{1}{2}(p_x^2 + p_y^2)). \tag{2.38}$$

The paraxial approximation is then accomplished by re-writing eqs. (2.27) to (2.30) using (2.37) and (2.38) and dropping any terms higher than second order in $\mathbf{p}$. The result of this procedure is the paraxial approximation to the polynomials:

$$A(\mathbf{p}) = \frac{1}{\epsilon_2} - \frac{2A}{\epsilon_2}p_x + \frac{1}{2}(\alpha-\beta)(p_x^2 + p_y^2), \tag{2.39}$$

$$C(\mathbf{p}) = -\frac{2A}{\epsilon_2}p_x + \frac{1}{2}(\alpha-\beta)p_x^2 - \frac{1}{2}(\alpha+3\beta)p_y^2, \tag{2.40}$$

$$D(\mathbf{p}) = -\frac{2A}{\epsilon_2}p_y + (\alpha+\beta)p_x p_y. \tag{2.41}$$

In the above equations eqs. (2.39) to (2.41) $A = \frac{\epsilon_2}{2}\sqrt{\alpha\beta}$ is the biaxial cone semi-angle of the conical intersection. Depending on which form of optical activity is

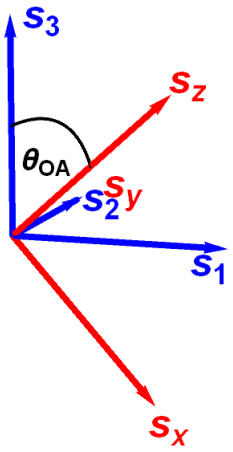

FIGURE 2.8: A plot showing the relationship between the natural basis of the dielectric tensor 123 and the xyz basis in which the z axis is oriented along an optic axis. The two bases are related by a rotation around the s_2/s_y axis.

being considered there are two possible forms that the paraxial approximation to the polynomial (2.28) can adopt:

$$B_F(\mathbf{p}) = f_{xi}h_i p_x + f_{yi}h_i p_y + f_{zi}h_i(1 - \frac{1}{2}(p_x^2 + p_y^2)), \tag{2.42}$$

$$B_C(\mathbf{p}) = G_{xx}p_x^2 + 2G_{xy}p_x p_y + G_{yy}p_y^2 + 2G_{xz}p_x + 2G_{yz}p_y + G_{zz}(1 - \frac{1}{2}(p_x^2 + p_y^2))^2. \tag{2.43}$$

In equations (2.42) and (2.43) we are assuming summation over repeated indices. These polynomials shall be integral to the following section where we derive a Hamiltonian that evolves the displacement field along the optic axis direction.

2.6 The Paraxial Hamiltonian Propagator

We can derive a Hamiltonian for a Schrödinger-like equation that evolves the displacement field along the optic axis direction $i\partial_z \mathbf{d} = \underline{\underline{H}}\mathbf{d}$. In this instance z plays the role of time t, and the displacement field $\mathbf{d}$ stands in for the quantum-mechanical wave function ψ [107]. In this analogy we are considering a spinor Schrödinger equation in order for the polarisation of light to be properly described. Thus $\underline{\underline{H}}$ is an operator in both spin (polarisation) and real space, with optical spin-orbit coupling terms as we now elaborate.

To derive this Hamiltonian we begin with the dispersion relation re-written for the propagation constant along the optic axis direction k_z

$$k_z = \pm k_0 \sqrt{n_\pm^2(\mathbf{s}) - \tilde{k}_x^2 - \tilde{k}_y^2} \tag{2.44}$$

where $\tilde{\mathbf{k}} = \frac{\mathbf{k}}{k_0}$. In the equation (2.44) above the two $\pm$ signs are independent, i.e. there are four possible k_z propagation constants. The $\pm$ outside the square root refers to solutions which propagate in either the positive or negative z direction while the $\pm$ inside the square root refers to the two possible refractive indices of an anisotropic material.

The two forward propagating k_z solutions are the eigenvalues of the matrix $\underline{\underline{H}}$ that we seek. These eigenvalues depend on the direction of propagation $\mathbf{s}$ considered, as well as the frequency of light ω. To proceed further we must relate $\tilde{\mathbf{k}}$ and $\mathbf{s}$. This relationship however is in general complicated. As we are considering highly directional beams along the optic axis we shall make the assumption that $\tilde{\mathbf{k}}$ and $\mathbf{s}$ are related by the optic axis refractive index $\sqrt{\epsilon_2}$ according to $\tilde{\mathbf{k}} = \sqrt{\epsilon_2}\mathbf{s}$. In the absence of optical activity this approximation is justified so long as deviations from the optic axis propagation are minor i.e. $s_x,\ s_y << 1$. Upon introduction of optical activity the approximation remains valid as the strength of optical activity is weak compared to the overall dispersion. This allows us to write the eigenvalues $H_\pm$ of the Hamiltonian $\underline{\underline{H}}$ in the paraxial regime as

$$H_\pm = k_0\sqrt{n_\pm^2(\mathbf{p}) - \epsilon_2 p_x^2 - \epsilon_2 p_y^2} \tag{2.45}$$

where the the paraxial approximation to the squared refractive indices is

$$n_\pm^2(\mathbf{p}) = \frac{1}{A(\mathbf{p}) \pm \sqrt{(B(\mathbf{p}))^2 + (C(\mathbf{p}))^2 + (D(\mathbf{p}))^2}}. \tag{2.46}$$

This equation can be re-written, through examination of eqs. (2.39) to (2.43), as

$$n_\pm^2(\mathbf{p}) = \frac{\epsilon_2}{(1 + \mu_\pm(\mathbf{p}))} \tag{2.47}$$

where $\mu_\pm(\mathbf{p}) = \epsilon_2(\Delta A(\mathbf{p}) \pm \sqrt{(B(\mathbf{p}))^2 + (C(\mathbf{p}))^2 + (D(\mathbf{p}))^2})$ and $\Delta A(\mathbf{p}) = (A(\mathbf{p}) - \frac{1}{\epsilon_2})$. Going further we can expand the equation (2.47) for $\mu(\mathbf{p}) << 1$ to obtain

$$n_\pm^2(\mathbf{p}) \simeq \epsilon_2(1 - \mu_\pm(\mathbf{p}) + \mu_\pm^2(\mathbf{p}) + \cdots). \tag{2.48}$$

Using equation (2.48) we can re-write the eigenvalues of the Hamiltonian $H_\pm$ and then expand the square root to obtain

$$H_\pm = \sqrt{\epsilon_2}k_0\sqrt{(1 - \mu_\pm(\mathbf{p}) + \mu_\pm^2(\mathbf{p}) + \cdots) - p_x^2 - p_y^2}, \tag{2.49}$$

$$\simeq k(1 - \frac{1}{2}\mu_\pm(\mathbf{p}) + \frac{3}{8}\mu_\pm^2(\mathbf{p}) - \frac{1}{2}p_x^2 - \frac{1}{2}p_y^2 + \cdots). \tag{2.50}$$

In the above equations we have introduced $k = \sqrt{\epsilon_2}k_0$ as the wavevector along the optic axis. The two eigenvalues $H_\pm$ give the paraxial Hamiltonian in its diagonal

basis.

$$\underline{\underline{H}}_D = \begin{pmatrix} H_+ & 0 \\ 0 & H_- \end{pmatrix}. \tag{2.51}$$

To obtain a general form of the Hamiltonian matrix $\underline{\underline{H}}$ we must transform out of the diagonal basis however. The necessary transformation matrix for achieving this follows from noting that the matrices $\underline{\underline{H}}$ and $\underline{\underline{m}}$ share a common eigenbasis. Therefore the transformation matrix $\underline{\underline{V}}$ can be expressed in terms of the paraxial polynomials of $\underline{\underline{m}}$, eqs. (2.39) to (2.43), as:

$$\underline{\underline{V}} = \begin{pmatrix} C(\mathbf{p}) - iD(\mathbf{p}) & C(\mathbf{p}) - iD(\mathbf{p}) \\ -B(\mathbf{p}) + \sqrt{B(\mathbf{p})^2 + C(\mathbf{p})^2 + D(\mathbf{p})^2} & -B(\mathbf{p}) - \sqrt{B(\mathbf{p})^2 + C(\mathbf{p})^2 + D(\mathbf{p})^2} \end{pmatrix}. \tag{2.52}$$

The general form of $\underline{\underline{H}}$ is then

$$\underline{\underline{H}} = \underline{\underline{V}}\,\underline{\underline{H}}_D\,\underline{\underline{V}}^{-1}, \tag{2.53}$$

$$= \frac{1}{2}\left((H_- + H_+)\underline{\underline{\mathbb{1}}} - \frac{(H_- - H_+)}{\sqrt{B(\mathbf{p})^2 + C(\mathbf{p})^2 + D(\mathbf{p})^2}}(C(\mathbf{p}), D(\mathbf{p}), B(\mathbf{p})) \cdot \underline{\underline{\boldsymbol{\sigma}}}\right). \tag{2.54}$$

The Hamiltonian is then finally completely determined by working out the sum and difference of the two eigenvalues (2.50). For the sum, which, when the pre-factor is included, represents the polarisation averaged contribution to the propagation constant k_z for light travelling in the direction $\mathbf{p}$, we have:

$$\begin{aligned} H_- + H_+ &= k(2 - \frac{1}{2}(\mu_+(\mathbf{p}) + \mu_-(\mathbf{p})) + \frac{3}{8}(\mu_+^2(\mathbf{p}) + \mu_-^2(\mathbf{p})) - p_x^2 - p_y^2), \\ &= k(2 - \epsilon_2(\Delta A(\mathbf{p})) + \frac{3}{4}\epsilon_2^2(\Delta A(\mathbf{p})^2 + B(\mathbf{p})^2 + C(\mathbf{p})^2 + D(\mathbf{p})^2)), \end{aligned} \tag{2.55}$$

whereas for the difference of the two eigenvalues (2.50), which affects the polarisation distinguishing contributions to the propagation constant k_z for light travelling in a direction $\mathbf{p}$, we have:

$$\begin{aligned} H_- - H_+ &= k\big(-\frac{1}{2}(\mu_-(\mathbf{p}) - \mu_+(\mathbf{p})) + \frac{3}{8}(\mu_-^2(\mathbf{p}) - \mu_+^2(\mathbf{p}))\big), \\ &= k\sqrt{B(\mathbf{p})^2 + C(\mathbf{p})^2 + D(\mathbf{p})^2}\big(\epsilon_2 - \frac{3}{2}\epsilon_2^2\Delta A(\mathbf{p})\big). \end{aligned} \tag{2.56}$$

We can re-arrange equation (2.56) to reflect how it appears in equation (2.54) resulting in:

$$\Longrightarrow \frac{H_- - H_+}{\sqrt{B(\mathbf{p})^2 + C(\mathbf{p})^2 + D(\mathbf{p})^2}} = k\big(\epsilon_2 - \frac{3}{2}\epsilon_2^2\Delta A(\mathbf{p})\big). \tag{2.57}$$

Using eqs. (2.55) to (2.57) we can express the Hamiltonian $\underline{\underline{H}}$ generally. For all that follows we shall be considering $\underline{\underline{H}}$ to second order in $\mathbf{p}$. The general form which this Hamiltonian takes is

$$\underline{\underline{H}} = h_0(\mathbf{p}, \underline{\eta})\underline{\underline{\mathbb{1}}} + h_x(\mathbf{p}, \underline{\eta})\underline{\underline{\sigma}}_x + h_y(\mathbf{p}, \underline{\eta})\underline{\underline{\sigma}}_y + h_z(\mathbf{p}, \underline{\eta})\underline{\underline{\sigma}}_z \tag{2.58}$$

where h_0, h_x, , h_y and h_z are polynomials in the relative transverse wavevector $\mathbf{p}$. In the absence of either form of optical activity the Hamiltonian describes a purely biaxial material and the polynomials are

$$\begin{aligned} h_{0,B}(\mathbf{p},\underline{\underline{\eta}}) =& -Ap_x + \frac{1}{4}\left[2+\epsilon_2(\alpha-\beta)-12A^2\right]p_x^2 + \\ &+ \frac{1}{4}\left[2+\epsilon_2(\alpha-\beta)-6A^2\right]p_y^2, \end{aligned} \tag{2.59}$$

$$h_{x,B}(\mathbf{p},\underline{\underline{\eta}}) = -Ap_x + \frac{1}{4}\left[\epsilon_2(\alpha-\beta)-12A^2\right]p_x^2 - \frac{1}{4}\epsilon_2(\alpha+3\beta)p_y^2, \tag{2.60}$$

$$h_{y,B}(\mathbf{p},\underline{\underline{\eta}}) = -Ap_y + \frac{1}{2}\left[\epsilon_2(\alpha+\beta)-6A^2\right]p_x p_y, \tag{2.61}$$

$$h_{z,B}(\mathbf{p},\underline{\underline{\eta}}) = 0. \tag{2.62}$$

Upon addition of the Faraday effect the polynomials $h_{0,B}$ and $h_{z,B}$ of the pure biaxial Hamiltonian become modified according to

$$\begin{aligned} h_{0,F} =& h_{0,B} - \frac{3}{8}\epsilon_2^2\Big((f_{zi}h_i f_{zj}h_j) + 2f_{zi}h_i(f_{xj}h_j\ p_x + f_{yj}h_j\ p_y) + 2f_{xi}h_i f_{yj}h_j\ p_x p_y + \\ &+ (f_{xi}h_i f_{xj}h_j - f_{zi}h_i f_{zj}h_j)p_x^2 + (f_{yi}h_i f_{yj}h_j - f_{zi}h_i f_{zj}h_j)p_y^2)\Big), \end{aligned} \tag{2.63}$$

$$\begin{aligned} h_{z,F} =& \frac{1}{2}\epsilon_2\Big(f_{zi}h_i + \left(f_{xi}h_i + 3Af_{zi}h_i\right)p_x + f_{yi}h_i p_y + 3Af_{yi}h_i p_x p_y \\ &- \frac{1}{2}\{f_{zi}h_i[1+\frac{3}{2}\epsilon_2(\alpha-\beta)] - 6Af_{xi}h_i\}p_x^2 - \frac{1}{2}\{f_{zi}h_i[1+\frac{3}{2}\epsilon_2(\alpha-\beta)]\}p_y^2\Big), \end{aligned} \tag{2.64}$$

where the repeated indices i, j are summed over. The tensor $\underline{\underline{f}}$ and the magnetic field $\mathbf{h}$ are expressed in the xyz coordinate system with the z axis oriented along the optic axis. They are related to the corresponding ones in the principle axis basis by $\underline{\underline{f}}_{xyz} = \underline{\underline{R}}\,\underline{\underline{f}}_{123}\,\underline{\underline{R}}^T$ and $\mathbf{h}_{xyz} = \underline{\underline{R}}\mathbf{h}_{123}$. Upon addition of chirality the polynomials $h_{0,B}$ and $h_{z,B}$ of the pure biaxial Hamiltonian become modified according to

$$\begin{aligned} h_{0,C} =& h_{0,B} - \frac{3}{8}\epsilon_2^2\Big(G_{zz}^2 + 4G_{xz}G_{zz}\ p_x + 4G_{yz}G_{zz}\ p_y + 4(G_{xy}G_{zz} + 2G_{xz}G_{yz})\ p_x p_y + \\ &+ 2\{2G_{xz}^2 + G_{zz}[G_{xx} - G_{zz}]\})p_x^2 + 2\{2G_{yz} + G_{zz}[G_{yy} - G_{zz}]\}p_y^2\Big), \end{aligned} \tag{2.65}$$

$$\begin{aligned} h_{z,C} =& \frac{1}{2}\epsilon_2\Big(G_{zz} + (2G_{xz} + 3AG_{zz})p_x + 2G_{yz}p_y + (2G_{xy} + 6AG_{yz})p_x p_y + \\ &+ \{G_{xx} + 6AG_{xz} - G_{zz}[1+\frac{3}{4}\epsilon_2(\alpha-\beta)]\}p_x^2 + \{G_{yy} - G_{zz}[1+\frac{3}{4}\epsilon_2(\alpha-\beta)]\}p_y^2\Big), \end{aligned} \tag{2.66}$$

where the tensor $\underline{\underline{G}}$ is expressed in the xyz basis. It is related to the corresponding one in the principal axis basis by $\underline{\underline{G}}_{xyz} = \underline{\underline{R}}\,\underline{\underline{G}}_{123}\,\underline{\underline{R}}^T$.

2.7 Conclusion

In this chapter we have examined the propagation of light through homogeneous anisotropic optically active materials within several frameworks and at varying degrees of generality. In particular, we considered dielectrics which are optically biaxial and additionally exhibit either the Faraday effect or chirality.

This examination began by developing the wave equation as a 2×2 matrix eigenvalue problem for the transverse displacement field. Within this framework we explored the refractive index surfaces of biaxial optically active materials, which characterise the retardation experienced by light of a particular polarisation travelling in a given direction in these materials. These surfaces have an associated polarisation texture, describing the natural vibrational state of the displacement field in the plane transverse to the propagation direction. In the presence of either form of optical activity, this natural vibrational state is generally that of elliptic polarisation. We have seen that there are, however, two noteworthy possible departures from this general state. These departures are directions in which the polarisation state is either that of circular or linear polarisation. The former occur in isolated directions in reciprocal space and are known as C-points. The C-points originate from the polarisation degeneracies of pure biaxial materials. The latter occur along lines in reciprocal space which are known as L-lines. L-lines are contours along which the optical activity effects vanish.

In tandem, these polarisation features allow us to understand the assignation of a value of a topological invariant to each of the refractive index surfaces. The invariant in question is the Chern number. The values of the Chern number of the refractive index surfaces can be read off from examination of the polarisation texture of each of the surfaces. The realisation of a non-zero value of this invariant relies on the topological index of each of the C-points combining rather than cancelling. To achieve this there has to be an asymmetry between the number of left and right circularly polarised C-points on each surface. Whether or not this occurs depends on both the variant of optical activity considered and the precise details within each variant. We saw that, for one of these optical activity variants, a non-zero Chern number is not possible due to the Faraday effect contribution being an odd function of the propagation direction. However, in the case of chiral biaxial materials, it is possible to have topologically non-trivial index surfaces. As well as being novel in and of themselves, these conclusions will be of interest for later comparative analysis.

We are additionally interested in the local behaviour of the refractive index around one of these C-points, rather than the global refractive index surfaces

themselves. To this end we pursued a Hamiltonian which describes the evolution of the field in directions close to an optic axis. This derivation was achieved within the framework of the paraxial approximation, an intrinsically local approach.

This Hamiltonian is a central result of this chapter and being to second order in the transverse wavevector it is therefore an extension of that derived by Jeffrey [98]. The Hamiltonian derived by Jeffrey [98] has already proved a powerful tool, being used to analyse the minutiae of the diffractive evolution of an incident field through homogeneous anisotropic optically active media [105, 108, 109]. Our motivation in extending the Hamiltonian of Jeffrey [98] shall become more transparent in the following chapters.

In these chapters we adapt the derived Hamiltonian to describe the propagation of light through periodic optical media, known as photonic crystals, which are composed of biaxial optically active materials. In these arrangements the vector field is defined on a torus rather than a sphere. In such a setting the Poincaré-Hopf theorem dictates that the total topological index of the vector field on the torus is null as compared to a total topological index of two on the sphere. This requirement therefore dictates equal numbers of degeneracies of positive and negative topological index on the torus of the Brillouin zone. The alternative consequence of the Poincaré-Hopf theorem, dictated by geometry, will have interesting implications when we look at the topological invariants of the iso-frequency surfaces of these materials. It is within this interplay between the Hamiltonian derived in this chapter and the geometric enforcement of the periodicity that the motivation for the extended Hamiltonian will become manifest, as we shall now explore.

Chapter 3

Square Patterned Photonic Crystals

3.1 Introduction

In this chapter we study periodic optical materials known as photonic crystals. These regular and repeating structures, which are periodic on the scale of the wavelength, can be patterned in one, two or three dimensions [15]. In figure 3.1 we show an illustration of forms of photonic crystals with varying dimensions of patterning. In these figures the different coloured blocks represent materials of distinct refractive indices. In the case of $1D$ photonic crystals, the patterning is restricted to repeating blocks along the patterning direction. For higher dimensional photonic crystals more complex patterning geometries are possible. The available patterning arrangements are linked to the possible Bravais lattices for that dimension. In figure 3.1 each of the photonic crystals features a simple Bravais lattice (linear, square and cubic) along with a two point basis specifying the placement of the two different dielectrics within each fundamental block of the structures.

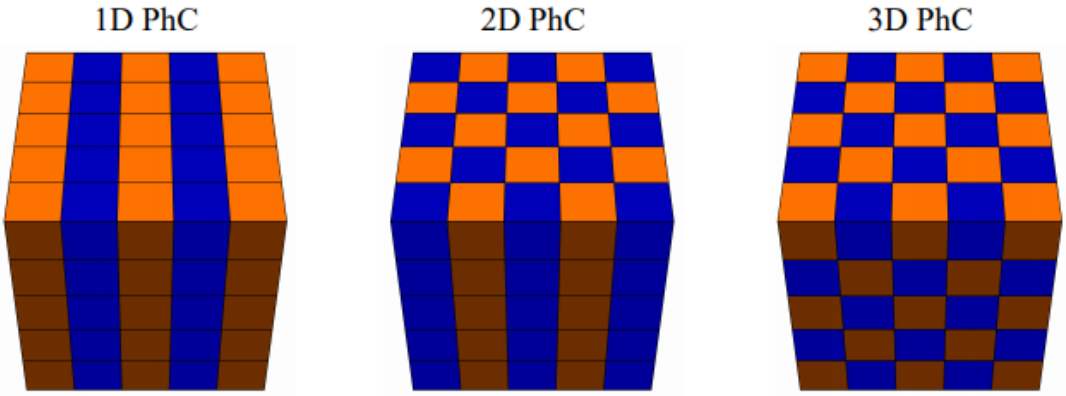

FIGURE 3.1: A cartoon showing the periodic dielectric function of one (left), two (middle) and three (right) dimensional photonic crystals (PhCs).

In any of the cases the dielectric function of the structure obeys the periodicity requirement

$$\underline{\underline{\epsilon}}(\mathbf{r}+\mathbf{R}) = \underline{\underline{\epsilon}}(\mathbf{r}), \tag{3.1}$$

where **R** is a translation by an integer number of fundamental blocks of the structure [110]. These possible translations **R** can be expressed in terms of sums of the minimal translations **a** as

$$\mathbf{R} = \sum_{i=1}^{D} n_i \mathbf{a}_i, \tag{3.2}$$

where $n_i \in \mathbb{Z}$, D is the number of dimensions of patterning and $\mathbf{a}_i$ determines the Bravais lattice geometry. In this chapter we will be concerned exclusively with $2D$ photonic crystals which are patterned in the simplest square geometry. In particular, we will consider photonic crystals composed primarily of anisotropic optically active materials. Figure 3.2 below shows the entrance face of a square-patterned $2D$ photonic crystal structure.

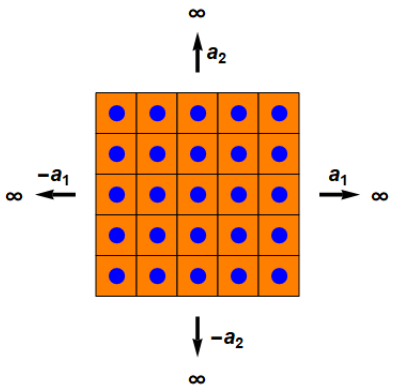

FIGURE 3.2: An illustration of a section of the entrance face of a square-patterned 2D photonic crystal.

Just as for periodic electronic systems these photonic crystals possess electromagnetic dispersion relations $\omega(\mathbf{k})$ describing the totality of possible frequencies and wavevectors at which light can travel through the material. Our focus in this chapter, and in chapter 4, will be to determine the topological invariants associated with the band-structures of $2D$ photonic crystals. In particular, we examine the iso-frequency surfaces of these photonic crystals, which are constant frequency slices of the full $\omega(\mathbf{k})$ dispersion relation. The iso-frequency surface is akin to a Fermi surface of a solid, and is the fundamental construct for analysing the refractive, reflective and diffractive properties of monochromatic light incident on a photonic crystal [16]. In this context a non-zero Chern number of a particular photonic crystal iso-frequency surface could indicate the presence of edge states for which incident light follows the boundary of the $2D$ patterned plane.

Two-dimensional photonic crystals with topologically non-trivial band structures have been theorised [9, 10, 31, 111] and realised [32, 111]. These realisations have commonly followed a conventional developmental route, set in scenarios where the propagation direction and polarisation degrees of freedom straightforwardly decouple, and are reliant on a specific patterning geometry so as to produce

Dirac points in the photonic band-structure. The decoupling of the propagation direction and polarisation degrees of freedom is by no means guaranteed, however, and generally does not hold. For instance, when one considers the propagation of light out of the periodic plane of a $2D$ photonic crystal, or light travelling in an anisotropic material, the propagation direction and polarisation state are coupled. Far from being a hindrance the optical spin-orbit coupling of anisotropic materials provides an opportunity to potentially eschew the conventional route to topological order in periodic optical systems. Rather than producing Dirac points in the band structures of the photonic crystals by adopting a triangular or hexagonal patterning we can harness the intrinsic polarisation singularities of homogeneous biaxial dielectrics to produce degenerate photonic band-structures. If the iso-frequency surfaces of photonic crystals composed of biaxial dielectrics possess degeneracies we will then address whether optical activity has the potential to lift these degeneracies and produce a topologically non-trivial system. The central question to be answered in this chapter is then whether it is possible to achieve optical topological order by utilising the intrinsic optical spin-orbit coupling of anisotropic optically active materials patterned in a square geometry?

To investigate this question we make use of the Hamiltonian eqs. (2.59) to (2.66) describing the paraxial evolution of light through an anisotropic optically active material. In section 3.2 we consider how to adapt this Hamiltonian to describe a square photonic crystal. We are particularly interested in the resulting degeneracy structure of the adapted Hamiltonian. In section 3.3 we assess the number and locations of C-points of the adapted Hamiltonian and compare the predictions of the model to numerical simulations of corresponding structures. From there we move to determining the topological phase diagrams of the iso-frequency surfaces of these photonic crystals. The photonic crystals we consider are composed of biaxial materials featuring one of two possible variants of optical activity. In section 3.4 we consider the Faraday effect while in section 3.5 we consider chirality. In both cases we compute the Chern number as the relevant material parameters are allowed to vary, allowing us to develop a full appreciation of the complicated topological phase diagrams. Finally we offer conclusions on the efficacy and merit of this approach in section 3.6.

3.2 Square Photonic Crystal Geometry

In this section we discuss how the paraxial Hamiltonian eqs. (2.59) to (2.66) derived in section 2.6 can be adapted to describe periodic media composed of anisotropic gyrotropic materials. We will be concerned with periodic media featuring a square patterning of the dielectric materials. The square patterning will be in the xy plane and the structures will be invariant along the z direction. The characteristic period in the xy plane is given by the lattice constant a and the geometry of the lattice is

captured by the two primitive lattice vectors $\mathbf{a}_1$ and $\mathbf{a}_2$:

$$\mathbf{a}_1 = a(1,0)\ ,\ \mathbf{a}_2 = a(0,1). \tag{3.3}$$

The real space lattice structure of the photonic crystal has a corresponding direction space lattice arrangement, from which follows the invariant translation vectors in wavevector space. These reciprocal lattice vectors, $\mathbf{b}$, are determined by solving $\mathbf{a}_i \cdot \mathbf{b}_j = 2\pi\delta_{ij}$. In the case of the square geometry (3.3), the corresponding reciprocal lattice vectors are

$$\mathbf{b}_1 = \frac{2\pi}{a}(1,0)\ ,\ \mathbf{b}_2 = \frac{2\pi}{a}(0,1). \tag{3.4}$$

We are free to orient the biaxial optically active inclusions in any manner of our choosing with regard to the xy patterning plane. The symmetries of the photonic crystal derive from those of both the patterning arrangement and of the dielectric structure of the material [112, 113]. In simple photonic crystals, composed of isotropic materials and patterned appropriately, the symmetry of the structure is effectively that of a square lattice. In the cases we choose to consider however this is not the case and the set of symmetries of the structure depend on the orientation of the anisotropic dielectric media [114]. In this chapter we choose to orient the anisotropic dielectric materials with their optic axis normal to the patterned planes. This choice is not necessary and therefore the freedom of orientation should be considered a parameter which we have decided to fix. Since we are orienting the optic axis, about which the paraxial approximation of section 2.6 was considered, along the invariant direction of the photonic crystal structure it is natural that we consider propagation primarily along this direction.

To realise the requisite periodic lattice model of the $2D$ photonic crystal structure we need to determine the lattice generalisation of the paraxial Hamiltonian of section 2.6. One way to achieve the lattice version of the Hamiltonian is to make the replacements

$$p_i = \frac{k_i}{k} \to \frac{1}{ak}\sin(k_i a) \tag{3.5}$$

$$p_i^2 = \frac{k_i^2}{k^2} \to \frac{2}{a^2k^2}[1-\cos(k_i a)] \tag{3.6}$$

to the Hamiltonian in section 2.6 [115], where in equation (3.6) $i \in \{x, y\}$. We shall denote the resulting lattice Hamiltonian $\underline{\underline{B}}_{\blacksquare}(\mathbf{k})$ which takes the form

$$\underline{\underline{B}}_{\blacksquare}(\mathbf{k}) = b_{\blacksquare 0}(\mathbf{k})\underline{\underline{\mathbb{1}}} + \mathbf{b}_{\blacksquare}(\mathbf{k}) \cdot \underline{\underline{\boldsymbol{\sigma}}}. \tag{3.7}$$

The matrix $\underline{\underline{B}}_{\blacksquare}(\mathbf{k})$ encodes the physics governing the propagation of light through square photonic crystals composed of biaxial optically active materials. This Hamiltonian matrix is the simplest lattice generalisation that both (i) reduces

to the paraxial Hamiltonian under small angle approximations of the trigonometric functions in equations (3.6) and (ii) is invariant under the addition of any integer number of reciprocal lattice vectors. The eigenvalues of this Hamiltonian describe the two polarisation-split bands of highest propagation constant k_z for a square photonic crystal composed of anisotropic optically active materials. These bands are plotted in figure 3.3 for a biaxial photonic crystal lacking optical activity. The parameters used in this figure were $(\epsilon_1, \epsilon_2, \epsilon_3) = (2.25, 2.5, 2.75)$ and $\frac{a}{\lambda} = 0.8$. These parameters correspond to a biaxial material with a cone-semi angle $A = 2.88°$, representing a biaxial material with quite strong birefringence. The parameters used for figure 3.3 shall be considered the default parameters and will be used throughout this chapter and chapters 4 and 5 unless otherwise stated. Since this model does not specifically include the lower refractive index material of the photonic crystal, we would expect it to perform best in situations where there is a large fraction of biaxial optically active material in the unit cell. Additionally since the higher refractive index materials act as a potential well for the electric field we will choose to use a lower index isotropic material, such as air, as the secondary unit cell material in more rigorous simulations of these materials. We should note that the simple replacements in (3.6) owes much to the square geometry; we shall see in chapter 4 that for alternative geometries the replacements are somewhat more complicated.

The elementary area of reciprocal space for a periodic system is the first Brillouin zone. For a square geometry with lattice spacing a the first Brillouin zone is also a square. This square is centred on the origin of reciprocal space and has side $\frac{2\pi}{a}$. The ratio of the lattice constant a to the operating wavelength λ thus sets the region of the index surfaces that are probed by the primary bands of the lattice Hamiltonian $\underline{\underline{B}}_{\blacksquare}(\mathbf{k})$. The higher this ratio the tighter a region of reciprocal space is explored in the primary bands.

In figure 3.4 we show the evolution of the iso-frequency surfaces of a homogeneous biaxial material (top left panel) upon adding either optical activity (moving from left panels to right panels in the figure) or periodicity (moving from top panels to bottom panels). Upon introduction of periodicity, irrespective of the lattice spacing to wavelength ratio, the resulting Hamiltonian will always inherit the conical intersection of the homogeneous biaxial material. Additionally there appear extra degeneracies towards the boundaries of the first Brillouin zone. The mathematical origin of these additional degeneracies is similar to that of fermion doubling [116] except in this case the extra conical intersections are an entirely real physical consequence of the periodic electromagnetic setting. They are a consequence of the periodic topology of the Brillouin zone, which requires the vector field $\mathbf{b}_{\blacksquare}(\mathbf{k})$ to have zero net circulation in the absence of optical activity.

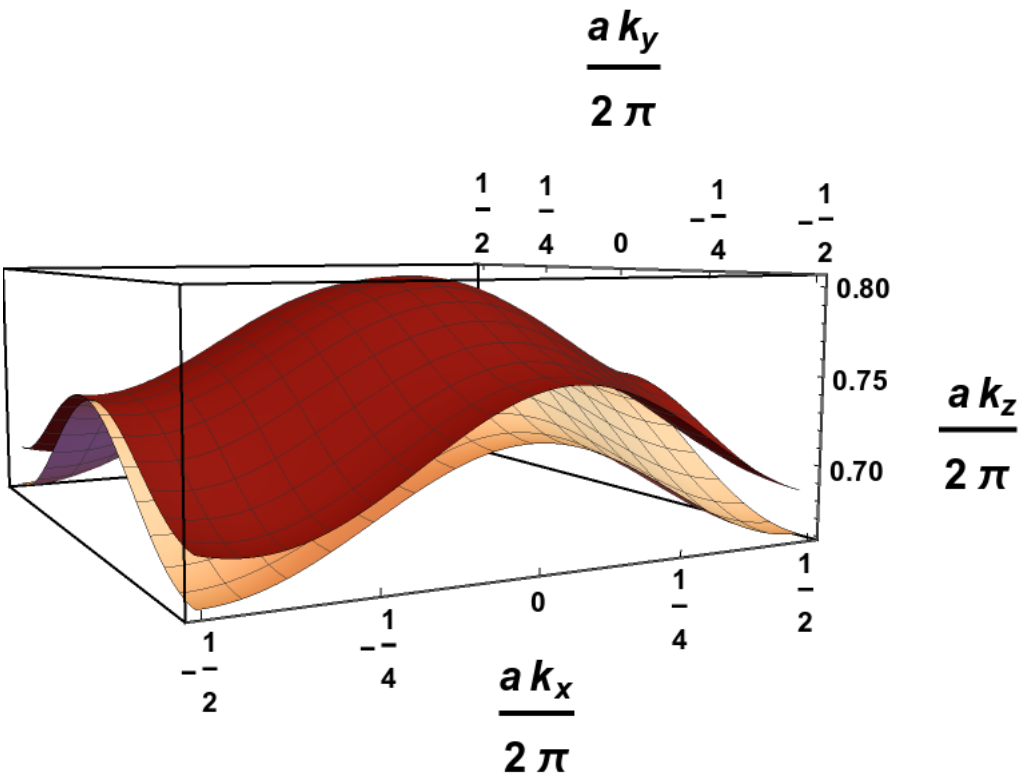

FIGURE 3.3: The iso-frequency surfaces of a square-patterned photonic crystal composed of biaxial material. The plot is generated from the lattice Hamiltonian model $\underline{\underline{B}}_{\blacksquare}(\mathbf{k})$. The surfaces are plotted over the first Brillouin zone and the parameters are $(\epsilon_1, \epsilon_2, \epsilon_3) = (2.25, 2.5, 2.75)$ for the principal dielectric constants and a lattice spacing to wavelength ratio of $\frac{a}{\lambda} = 0.8$.

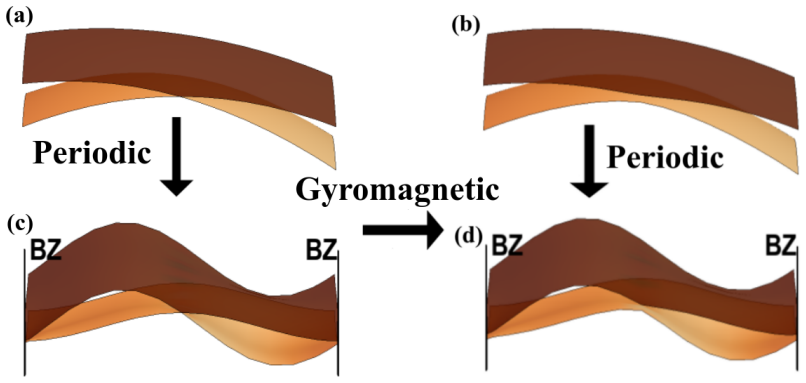

FIGURE 3.4: Illustration of the formation of topologically non-trivial iso-frequency surfaces in square two-dimensional photonic crystals. Each panel is a section of an iso-frequency surface for (a) a homogeneous biaxial dielectric, (b) a homogeneous biaxial dielectric with optical activity, (c) a periodic biaxial dielectric and (d) a periodic biaxial dielectric with optical activity. Each of these panels is centred on the the wavevector corresponding to the conical singularity in (a). The periodicity is taken to be in the plane perpendicular to this wavevector, forming a two-dimensional Brillouin zone (BZ).

Upon the addition of optical activity, seen in the bottom right panel of figure 3.4, the iso-frequency surfaces can become gapped generally. In this situation one can assign a Chern number to each of these bands, characterising the winding number of the vector field $\mathbf{b}_{\blacksquare}(\mathbf{k})$ over the Brillouin zone. The realisation of a non-zero Chern number for a photonic crystal places different stipulations on the nature of the optical activity compared to that of the homogeneous media investigated in subsection 2.4.3. The stipulation to achieve a non-zero Chern number in this case is that an odd number of L-lines separates C-points of different topological index. We shall see that, in this geometry, both forms of optical activity can achieve this, resulting in non-zero Chern numbers. This result is in contrary to what we saw for the homogeneous materials in subsection 2.4.3. Furthermore we shall see that in the case of chiral biaxial photonic crystals there is no restriction to even values of the Chern number as for the homogeneous material. To reach these conclusions we begin by determining the degeneracy structure of the lattice Hamiltonian $\underline{\underline{B}}_{\blacksquare}(\mathbf{k})$.

3.3 Degeneracy Structure of Square Photonic Crystals

We now examine the degeneracy structure of the iso-frequency surfaces of square photonic crystals. Initially, as in subsection 2.4.1, we focus on a situation where there is no optical activity. We carry out a preliminary assessment of the degeneracy structure through use of the lattice Hamiltonian $\underline{\underline{B}}_{\blacksquare}(\mathbf{k})$ describing these structures. This assessment will be concerned primarily with four factors: (i) the number of C-points of the iso-frequency surfaces, (ii) their locations in the first Brillouin zone, (iii) their local circulation and (iv) their motion in reciprocal space as the lattice spacing to wavelength ratio is varied. We shall then compare the results obtained from the lattice Hamiltonian to those from a frequency-domain plane-wave simulation of a corresponding structure.

3.3.1 Degeneracy Structure from Lattice Hamiltonian

For the lattice Hamiltonian C-points are locations in reciprocal space $\mathbf{k}'$ where $\mathbf{b}_{\blacksquare}(\mathbf{k}') = \mathbf{0}$. Since $b_{\blacksquare 3}(\mathbf{k}) = 0$ in all directions in the absence of optical activity we need only focus on the zeroes of the functions $b_{\blacksquare 1}(\mathbf{k})$ and $b_{\blacksquare 2}(\mathbf{k})$. These zeroes follow contours in the first Brillouin zone, with the intersections of these contours representing C-point locations. We can visualise these locations graphically by looking at appropriate plots of the vector field $(b_{\blacksquare 1}(\mathbf{k}), b_{\blacksquare 2}(\mathbf{k}))$.

Figure 3.5 shows two plots of the vector field $(b_{\blacksquare 1}(\mathbf{k}), b_{\blacksquare 2}(\mathbf{k}))$ along with the contours representing the zeroes of each of its components over an enlarged first Brillouin zone. Each of the two plots considers a different lattice spacing to

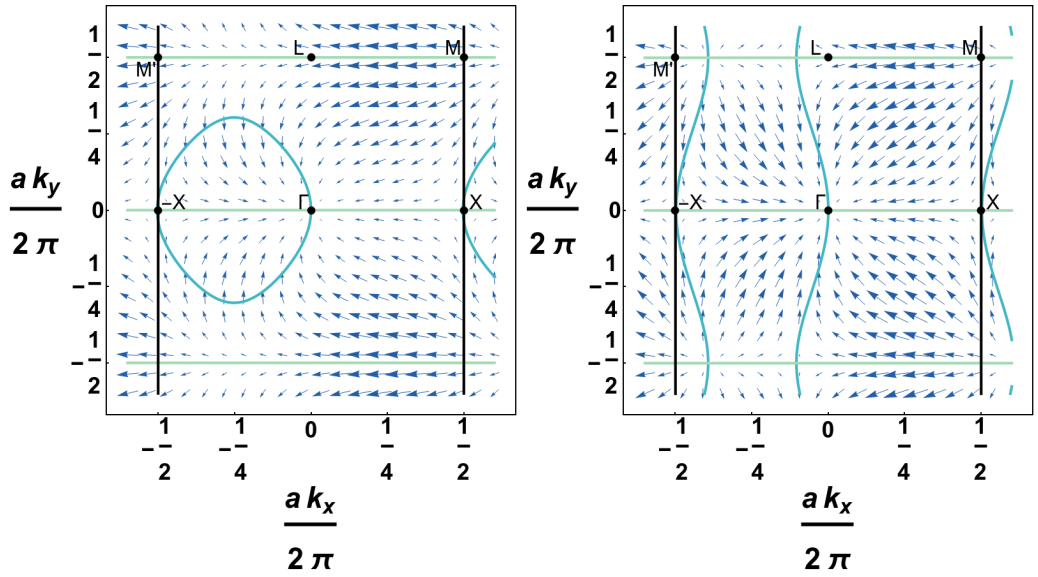

FIGURE 3.5: Two plots showing the zero contour lines of the polynomials $b_{\blacksquare 1}(\mathbf{k})$ (turquoise) and $b_{\blacksquare 2}(\mathbf{k})$ (green) over an enlarged area containing the first Brillouin zone. Each plot considers a distinct lattice spacing to wavelength ratio $\frac{a}{\lambda}$. In the left plot $\frac{a}{\lambda} = 0.8$ and in the right plot $\frac{a}{\lambda} = 2$. In the absence of any gyromagnetic perturbation the intersection of the zero contour lines represent C-points of the iso-frequency bandstructure. The vector field $(b_{\blacksquare 1}(\mathbf{k}), b_{\blacksquare 2}(\mathbf{k}))$ is overlaid in blue.

wavelength ratio. In the left figure $\frac{a}{\lambda} = 0.8$ and in the right figure $\frac{a}{\lambda} = 2$. In each figure the intersection of the turquoise and green contour lines represent C-points of the iso-frequency surfaces. We see that the number of C-points depends on the lattice spacing to wavelength ratio; in the left plot there are two C-points in the first Brillouin zone while in the right plot there are four. In addition to the C-point at Γ, which is that of the original Hamiltonian of the homogeneous material, both plots show an extra one just inside the $-X$ boundary along the line $k_y = 0$. In the rightmost figure there are further C-points along the boundary line of the first Brillouin zone $k_y = \pm\frac{\pi}{a}$. Since these extra C-points along the lines $k_y = \frac{\pi}{a}$ and $k_y = -\frac{\pi}{a}$ are related by a reciprocal lattice vector we need only consider the pair along one of these lines. Henceforth we shall count the pair of C-points along the line $k_y = \frac{\pi}{a}$. By studying the overlaid vector field we can assess the local circulation of each of these C-points. On studying the vector field we note that the sense of circulation is opposite for each pair of points along the lines $k_y = 0$ and $k_y = \frac{\pi}{a}$. The Berry phase corresponding to each of these singularities is $\pm\pi$, so that upon introduction of optical activity the Chern number can be $C \in \{-1, 0, 1\}$ for the left plot or $C \in \{-2, -1, 0, 1, 2\}$ in the right plot.

The appearance of the C-points along the high symmetry lines $k_y = 0$ and $k_y = \frac{\pi}{a}$ is of course no accident - and can be inferred from examination of $b_{\blacksquare 2}(\mathbf{k})$. We note from figure 3.5 that the number and locations of the C-points is clearly dependent

on the lattice spacing to wavelength ratio. This ratio essentially determines the relative importance of the linear and quadratic contributions to the Hamiltonian $\underline{\underline{B}}_{\blacksquare}(\mathbf{k})$. To assess the frequency dependence of the C-points we shall study their movement along the high symmetry lines as the lattice spacing to wavelength ratio is varied.

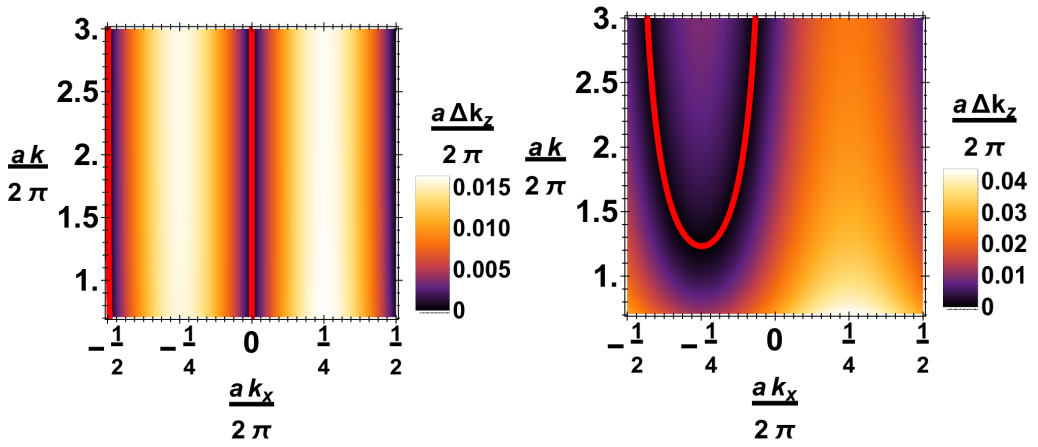

FIGURE 3.6: Two density plots representing the splitting of the bands of the iso-frequency surfaces. Each plot shows how the splitting of the bands varies with the lattice spacing to wavelength ratio. Each of these plots is along a high symmetry line of the first Brillouin zone. The high symmetry lines are $k_y = 0$ (left) and $k_y = \frac{\pi}{a}$ (right). Contour lines representing C-points are superposed on each plot in red.

Figure 3.6 shows two density plots examining the splitting of the iso-frequency surfaces along high symmetry lines in the first Brillouin zone as the lattice spacing to wavelength ratio is varied. Each of the two density plots has overlaid red contour lines showing conical intersections of the iso-frequency surfaces. In the left-hand figure we consider the line $k_y = 0$; along this line there are two C-points one of which is fixed at Γ and the other which starts close to the $-X$ boundary and increasingly tends towards that boundary as the ratio is increased. In the right-hand figure we observe that at low lattice spacing to wavelength ratio that there are no C-points but above a critical $\frac{a}{\lambda}$ an additional pair emerges.

The conical intersections of the iso-frequency surfaces are also affected by the variation of the principal dielectric constants of the biaxial material. As the biaxial cone semi-angle is increased the C-points tend to further displace from the zone corners and faces along the high symmetry lines.

This set of either two or four C-points represents the degeneracy structure of the iso-frequency surfaces following from the lattice Hamiltonian $\underline{\underline{B}}_{\blacksquare}(\mathbf{k})$. In either case there is an equal number of singularities of positive and negative topological

index, this is the opposite of what was seen in subsection 2.4.1 where all conical intersections had the same topological index. This difference is due to the differing topology of the space of wavevector direction which is that of a sphere in the homogeneous medium, and a torus in the periodic one. We shall now assess whether the Hamiltonian theory is a reasonable qualitative descriptor of one of these photonic crystals.

3.3.2 Comparison to Simulations of Square Photonic Crystal Structures

To test the validity of the lattice Hamiltonian $\underline{\underline{B}}_{\blacksquare}(\mathbf{k})$ we shall compare it to the results of a realistic numerical bandstructure calculation using the frequency-domain plane-wave method [117]. We focus on the number and locations of singularities in the absence of optical activity as these are the crucial quantities to determining the Chern number once optical activity is introduced. We specifically consider a biaxial dielectric in which cylindrical air holes are drilled to form a square lattice.

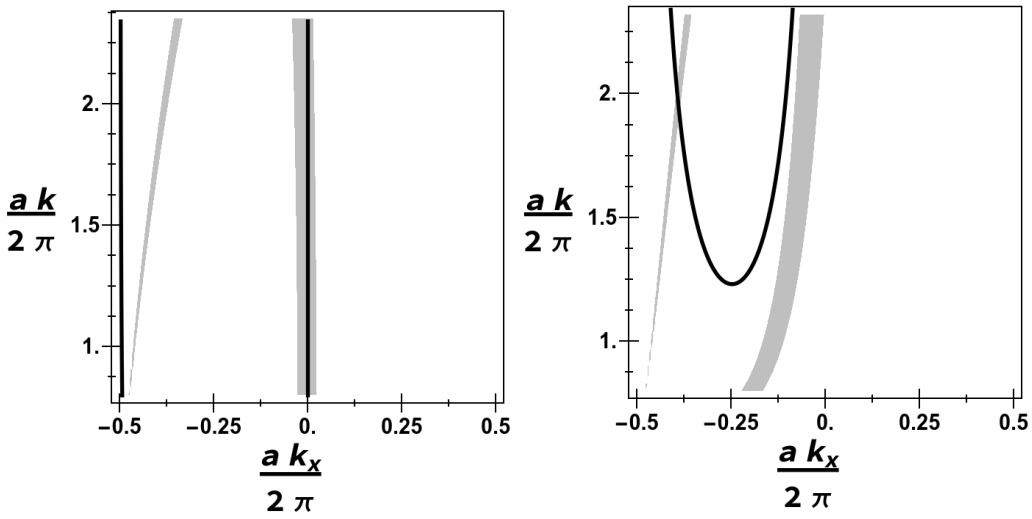

FIGURE 3.7: Comparison of the locations of the C-points given by the lattice Hamiltonian and a frequency-domain plane-wave simulation as k is varied. In both cases C-points occur along the lines $k_y = 0$ (left) and $k_y = \frac{\pi}{a}$ (right). Solid lines represent k_x locations of C-points from the lattice Hamiltonian while the shading represents bounds on k_x for the C-points from the plane-wave simulations. The chosen shading bounds are such that the magnitude of the splitting of the two most paraxial bands is less than $a\Delta k_z = 2\pi \times e^{-6}$. The plane-wave simulation has cylindrical air holes in the dielectric background. The radius of each of the air holes considered is $r = 0.15a$.

In figure 3.7 we examine how the locations of the C-points are affected by variation of the lattice spacing to wavelength ratio. The solid black contour lines give the locations predicted by $\underline{\underline{B}}_{\blacksquare}(\mathbf{k})$, while the shaded regions provide bounds on the C-point locations from the numerical simulation. We see that the $\underline{\underline{B}}_{\blacksquare}(\mathbf{k})$ gives

a reasonable qualitative account of the numerical results. Each picture considers the two previously mentioned high symmetry lines of the first Brillouin zone upon which the C-points appear. The left panel of figure 3.7 is along the high symmetry line $k_y = 0$ which features two C-points in both approaches at all values of lattice spacing to wavelength ratio considered. Both approaches have the zone centre C-point and agree that the second one is adjacent to the $-X$ boundary of the Brillouin zone. The right panel of figure 3.7 shows the C-point positions along the line $k_y = \frac{\pi}{a}$. There are some deviations between the two approaches along this high symmetry line, in particular, the numerics indicate two C-points at all lattice spacing to wavelength ratios considered while the extra two only emerge above a critical $\frac{a}{\lambda}$ for the lattice Hamiltonian $\underline{\underline{B}}_{\blacksquare}(\mathbf{k})$. We attribute this difference to the different treatment of scattering in the two methods, and perhaps also to higher-order terms neglected in the paraxial Hamiltonian of the homogeneous material. Figure 3.7 suggests that the theory represented by $\underline{\underline{B}}_{\blacksquare}(\mathbf{k})$ is a reasonable qualitative descriptor of the desired $2D$ photonic crystal structures, but to further confirm this we turn to comparing iso-frequency surfaces generated from each approach.

Figure 3.8 shows two iso-frequency diagrams plotted following a path along high symmetry lines in the first Brillouin zone. The top figure is that produced from the Hamiltonian $\underline{\underline{B}}_{\blacksquare}(\mathbf{k})$, and the bottom one the result of the numerical simulation. These surfaces are compared at $ka \simeq 4\pi$ such that we are in a regime towards the top of the scale in figure 3.7, where each approach predicts four C-points. We note the striking similarity between the surfaces generated by each approach, in terms of their overall morphology as well as the number and locations of the conical intersections of the surfaces. As expected from figure 3.7, we see that the extra C-point along the $k_y = 0$ line in each approach are slightly displaced from each other. In the lattice Hamiltonian model the additional C-point along the $k_y = 0$ line is just inside the $-X$ boundary, whereas in the numerical simulation this C-point is further inward along the $-X\Gamma$ line. We further note that the lattice Hamiltonian generally underestimates the overall dispersion of the surfaces as well as the polarisation splitting of the bands. A quantitative measure of the differences of the two methods could have been calculated. However, from a topological point of view, the important features of the iso-frequency surface are the number and locations of the degeneracies. As such, a quantitative measure was not calculated.

Given the overall reasonable correspondence between the two approaches we conclude that the Hamiltonian $\underline{\underline{B}}_{\blacksquare}(\mathbf{k})$ is a qualitatively accurate descriptor of $2D$ photonic crystals composed primarily of biaxial material. This conclusion is based on the two approaches showing

1. Agreement on the number of C-points of the iso-frequency surfaces over most lattice spacing to wavelength ratios.

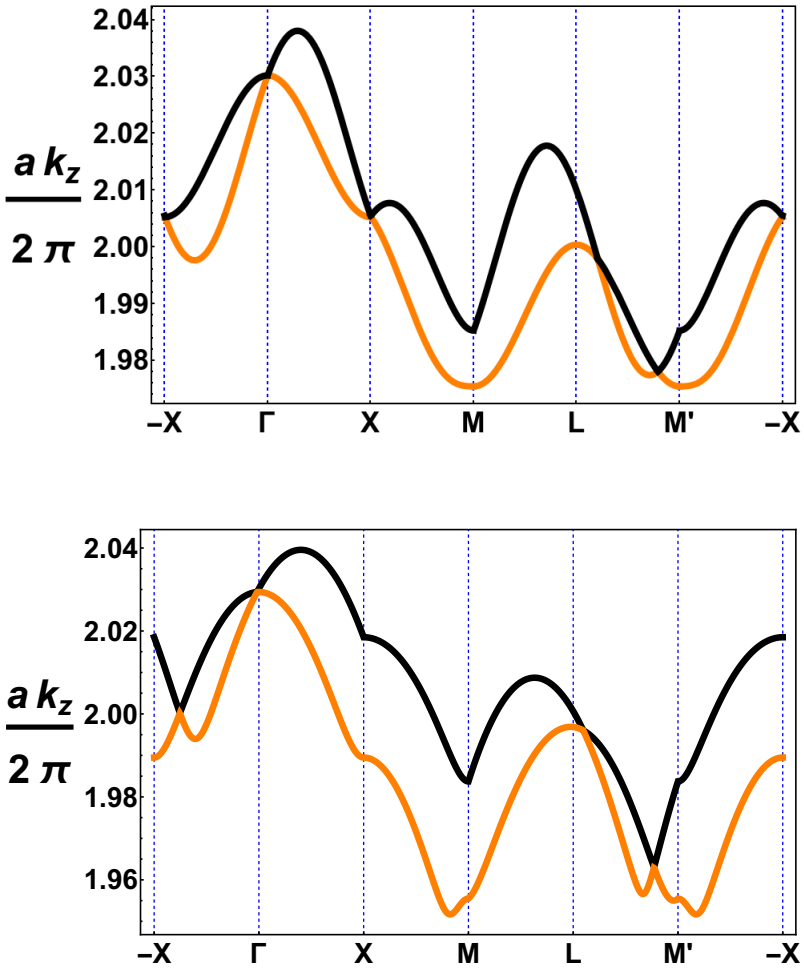

FIGURE 3.8: A comparison between the iso-frequency surfaces generated from the lattice Hamiltonian (top) and those generated from a frequency domain plane-wave simulation (bottom). The iso-frequency surfaces are plotted as a path along high-symmetry lines of the first Brillouin zone is followed. The high symmetry points are indicated in figure 3.3. These surfaces are compared at $ka \simeq 4\pi$.

2. Agreement on the pinning of those C-points to high symmetry lines of the first Brillouin zone.

3. Approximate agreement on the locations of the C-points along those high symmetry lines.

Owing to this we argue that the topological phase diagrams of the two models will be similar to each other. In the regime prior to the emergence of the extra C-points in $\underline{\underline{B}}_{\blacksquare}(\mathbf{k})$ the phase diagram of the numerical simulation will be richer than that of the lattice model. Having established that $\underline{\underline{B}}_{\blacksquare}(\mathbf{k})$ is an adequate qualitative descriptor of these structures we now turn to the introduction of each form of optical activity separately. These additions will allow us to examine the topological phase diagrams of $2D$ photonic crystals composed of anisotropic optically active materials.

3.4 Photonic Crystals Composed of Biaxial Faraday Effect Materials

The first form of optical activity we shall consider is the Faraday effect. Upon introduction of the non-zero magnetic field in a general direction the degeneracies of the iso-frequency surfaces are lifted and the polarisation states of each of the surfaces becomes generally elliptical. For some directions of the magnetic field L-lines can appear in the first Brillouin zone. These L-lines always appear in such a way that a translation identifying two sides of the Brillouin zone always crosses an even number of L-lines, enforcing the requirement that the polarisation state of each surface is the same under all reciprocal lattice translations. When L-lines appear in the Brillouin zone they can, depending on the field application directions, result in C-points of different index having different handedness. If this is the case then this is an orientation of the magnetic field which can produce a non-zero Chern number.

3.4.1 Examination of Topological Phase Diagrams

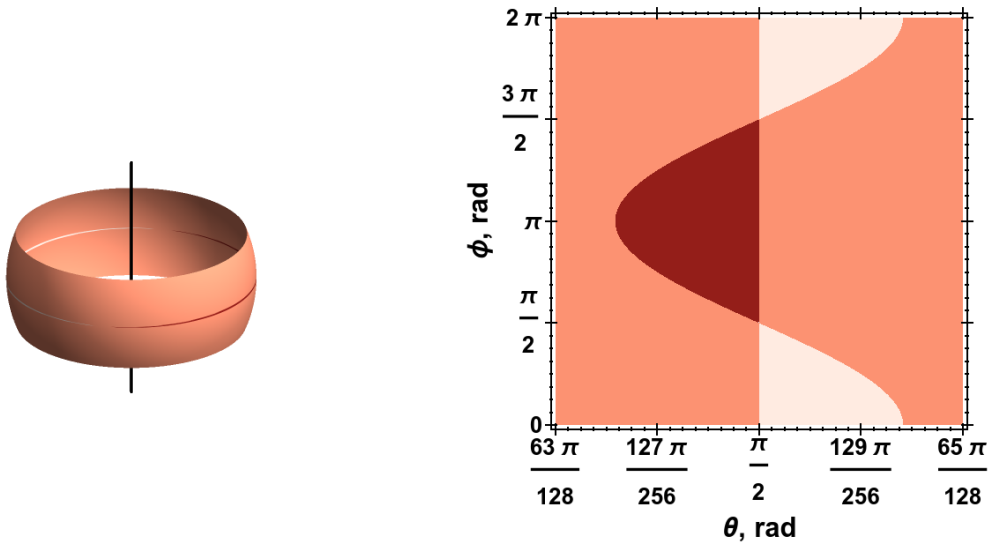

FIGURE 3.9: Phase diagrams representing the Chern number, C, by colour of a square patterned photonic crystal. The photonic crystal is composed of biaxial Faraday effect material. The phase diagrams are plotted in the space of the externally applied magnetic field direction (θ, ϕ). The colours represent $C = 0$ (mid pink) and $C = \pm 1$ (dark or light pink). The figure on the left is a wrapping of the figure on the right onto a section of the surface of a sphere. The black line in the left figure represents the optic axis direction of the biaxial material.

In figure 3.9 we see two plots showing the Chern number by colour of a square patterned photonic crystal composed of biaxial Faraday effect material. The plots are in the space of the direction of the externally applied magnetic field (θ, ϕ);

where θ is measured from the optic axis direction of the homogeneous material, i.e. $\theta = \frac{\pi}{2}$ corresponds to applying the magnetic field in a plane perpendicular to the optic axis direction. In figure 3.9 we see that non-zero Chern numbers (light and dark pink) are achievable. These non-zero Chern numbers occur for a range of field application directions close to perpendicular to the optic axis. In these figures we have considered a lattice spacing to wavelength ratio $\frac{a}{\lambda} = 0.8$ for which there are two C-points. The bounding contours of these non-zero Chern number regions then represent the gap closing at each of these two lifted degeneracies. The $\theta = \frac{\pi}{2}$ contour corresponds to the gap closing at the Γ point with the contour which weaves above and below the equator corresponding to the gap closure at the C-point towards the face centre. In these figures we have assumed, without loss of generality, that the Faraday effect tensor, which was introduced in subsection 2.2.1, is isotropic ($\underline{\underline{f}} = f\underline{\underline{\mathbb{1}}}$). Relaxation of this assumption will move around the features seen in figure 3.9 without introducing any new structure.

The existence of a finite region between the two contour lines along which the gaps of the individual C-points close and the Chern number is non-zero is by no means guaranteed. To understand the origin of this finite region we shall examine the Faraday effect contribution which is of the form

$$\begin{aligned} b_{\blacksquare z}(\mathbf{k}) =& \frac{1}{2}\epsilon_2 f|h|\Big(\cos\theta + \big(\sin\theta\cos\phi + 3A\cos\theta\big)\frac{1}{ak}\sin ak_x + \sin\theta\sin\phi\frac{1}{ak}\sin ak_y + \\ &+ 3A\sin\theta\sin\phi\frac{1}{a^2k^2}\sin ak_x\sin ak_y - \frac{1}{2}\big\{\cos\theta[1+\frac{3}{2}\epsilon_2(\alpha-\beta)] + \\ &- 6A\sin\theta\cos\phi\big\}\frac{4}{a^2k^2}\sin^2\frac{ak_x}{2} - \frac{1}{2}\big\{\cos\theta[1+\frac{3}{2}\epsilon_2(\alpha-\beta)]\big\}\frac{4}{a^2k^2}\sin^2\frac{ak_y}{2}\Big). \end{aligned} \tag{3.8}$$

In the case of the zone centre C-point equation (3.8) reduces to $b_{\blacksquare z} = \frac{1}{2}\epsilon_2 f|h|\cos\theta$, which has a zero at $\theta = \frac{\pi}{2}$. This zero, where the band gap closes at the zone centre and the Chern number changes, is therefore the equatorial contour in figure 3.9. The other contour of figure 3.9 represents the solution of $b_{\blacksquare z} = 0$ for the other C-point. In this case the equation takes the form

$$c_1\cos\theta + c_2\sin\theta\cos\phi = 0 \tag{3.9}$$

for some constants c_1 and c_2. The simultaneous solutions of equation (3.9) and that for the zone centre C-point represent field application directions for which the iso-frequency surface is degenerate at both locations in the Brillouin zone. These special field application directions occur for the antipodal pair $(\theta,\phi) = \big\{(\frac{\pi}{2},\frac{\pi}{2}),(\frac{\pi}{2},\frac{3\pi}{2})\big\}$ and correspond to the pinch points in the right-hand phase diagram of figure 3.9 where the $C = \pm 1$ phases come into contact. As these two special directions are antipodal there are an infinite family of geodesics connecting them. It is therefore interesting to determine whether the two bounding contours of the phase diagram

are members of this family of geodesics. As the zero contour of the zone centre C-point is the $\theta = \frac{\pi}{2}$ equatorial circle it is clearly a geodesic. For the other C-point we can manipulate the zero contour equation (3.9) into the form

$$\cot\theta = -\frac{c_2}{c_1}\cos\phi, \tag{3.10}$$

which is the equation of a geodesic. The geodesic corresponding to the zero-contour of the zone-centre C-point is the special case of equation (3.10) when $c_2 = 0$. The ratio c_2/c_1 determines how large the topologically non-trivial parameter regime is. The motivation for extending the Hamiltonian of Jeffrey [98] can now be properly appreciated; without the extension the equations for the zero contour lines of $b_{\blacksquare z}(\mathbf{k})$ at all of the C-points would be the same and hence there would be no topologically non-trivial area in parameter space.

We now wish to examine the evolution of these phase diagrams as the parameters of the photonic crystal are varied. We will consider variation of both the strength of biaxiality and the lattice spacing to wavelength ratio. For each of these variations the shrinking or increasing of the topologically non-trivial phase can be understood in the context of whether or not the variation increases the ratio c_2/c_1 in the geodesic equation (3.10).

3.4.2 Variation of Topological Phase Diagrams with Degree of Biaxiality

The first parameter we consider the variation of is the degree of biaxiality. Initially we shall examine four snapshots of the topological phase diagrams in the space of the magnetic field application direction. Each of these snapshots considers a different set of principal dielectric constants.

Figure 3.10 shows an array of topological phase diagrams representing the Chern number by colour. In each case the biaxial cone semi-angle, A, is stated above the plot. We see that the stronger the biaxiality the larger the region of non-zero Chern numbers. This enlargement of the topologically non-trivial phase results from the ratio c_2/c_1 of the geodesic equation (3.10) for the second C-point becoming larger with increasing biaxiality. The magnetic field directions for which the iso-frequency surfaces is degenerate at both C-point locations do not change as the biaxiality does. As such, the location of the pinch-points in the topological phase diagrams does not vary between the phase diagrams of figure 3.10.

Figure 3.11 examines the effect on the topological phase diagram of the continuous variation of two of the principal dielectric constants with the median one held fixed. The black overlaid contours represent constant values of the biaxial cone semi-angle in 2° increments from bottom to top of the figure. From this figure

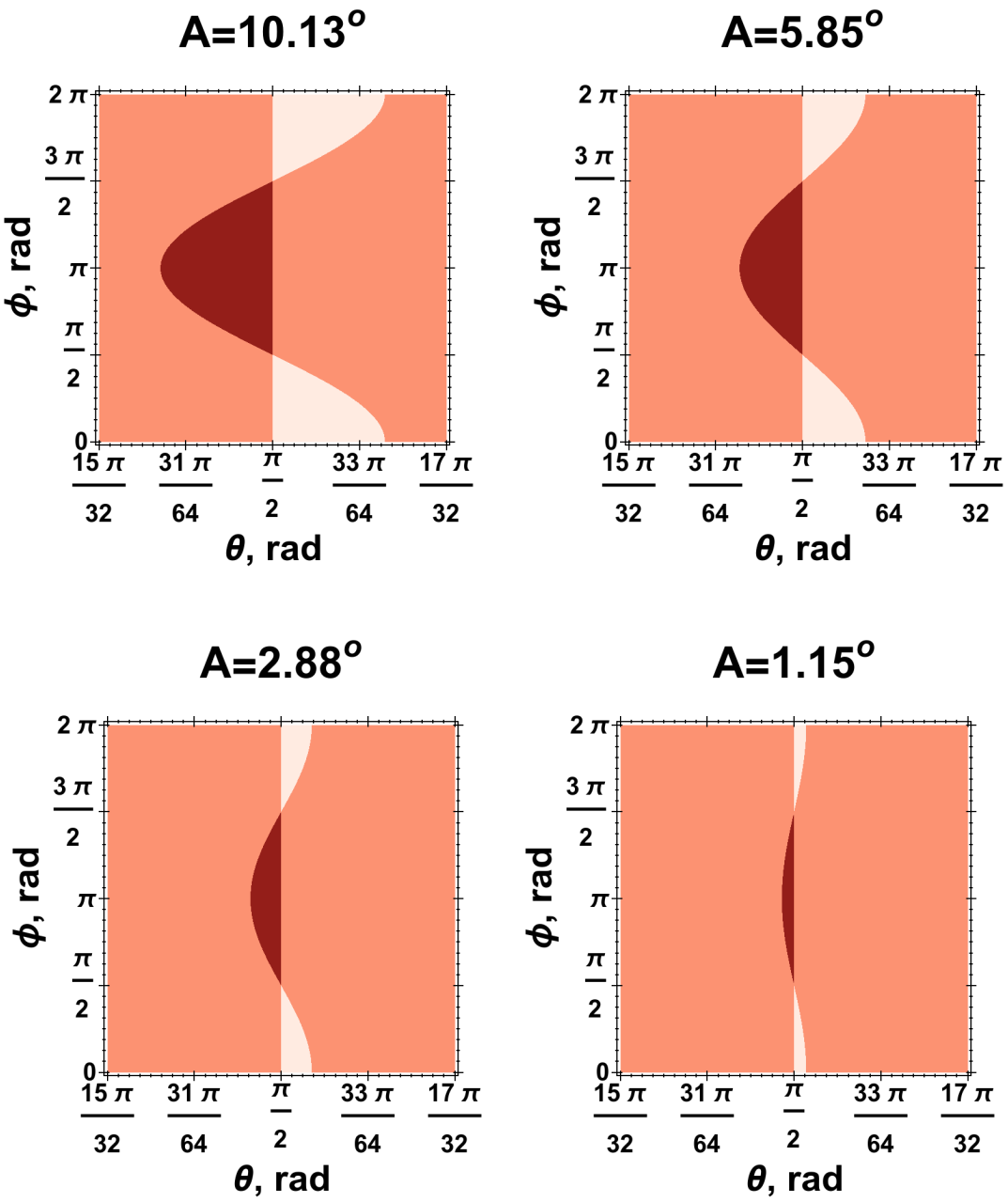

FIGURE 3.10: A panel of four phase diagrams representing the Chern number by colour of square patterned photonic crystals. The photonic crystals are composed of biaxial Faraday effect material. For each of the plots we consider a lattice spacing to wavelength ratio of $\frac{a}{\lambda} = 0.8$. The degree of biaxiality is different in each diagram. The principal dielectric constants $(\epsilon_1, \epsilon_2, \epsilon_3)$ are (from left to right and then top to bottom) (i) $(2, 3, 4)$, (ii) $(2, 2.5, 3)$, (iii) $(2.25, 2.5, 2.75)$ and (iv) $(2.4, 2.5, 2.6)$.

we can see the size of the topologically non-trivial phase increases with increasing strength of biaxiality. The boundary between the phases, for this set of parameters, approximately follows the yellow $\alpha = 1.4\beta$ contour.

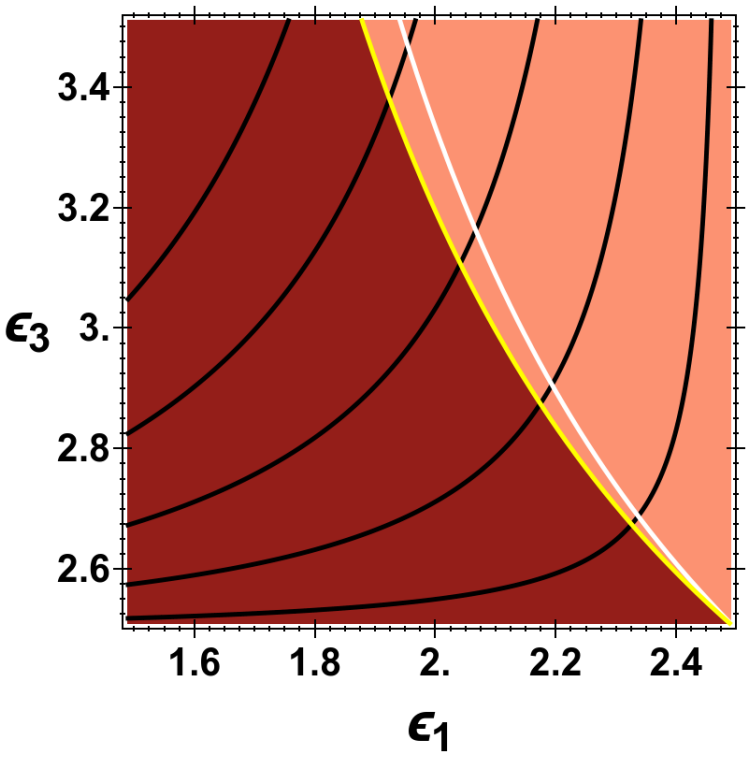

FIGURE 3.11: The Chern number at field application direction $(\theta, \phi) = (\frac{127\pi}{256}, \pi)$, of a square patterned photonic crystal. The photonic crystal is composed of biaxial Faraday effect material. The median principal dielectric constant is fixed at $\epsilon_2 = 2.5$ and the other two principal refractive indices (ϵ_1, ϵ_3) are allowed to vary. The black contours are curves along which the angle of the conical intersection, A, is constant. The lowest of these contours represents a cone semi-angle of $A = 2°$. Each higher black contour is a further increase of $2°$. The white contour represents $\alpha = \beta$, while the yellow one is $\alpha = 1.45\beta$. The lattice spacing to wavelength ratio is $\frac{a}{\lambda} = 0.8$.

3.4.3 Variation of Topological Phase Diagrams with Lattice Spacing to Wavelength Ratio

The other parameter we can vary is the lattice spacing to wavelength ratio. As before we study four snapshots of the topological phase diagram in the space of the magnetic field application direction. Each of these snapshots considers a different lattice spacing to wavelength ratio.

Figure 3.12 shows an array of topological phase diagrams representing the Chern number by colour. In each case the lattice spacing to wavelength ratio is stated above the plot. We see that the higher this ratio the smaller the region of non-zero Chern numbers. This diminishing of the topologically non-trivial phase results from the ratio of c_2/c_1 in the geodesic equation 3.10 for the second C-point decreasing with increasing lattice spacing to wavelength ratio. This occurs because the iso-frequency surface dispersion becomes increasingly dominated by

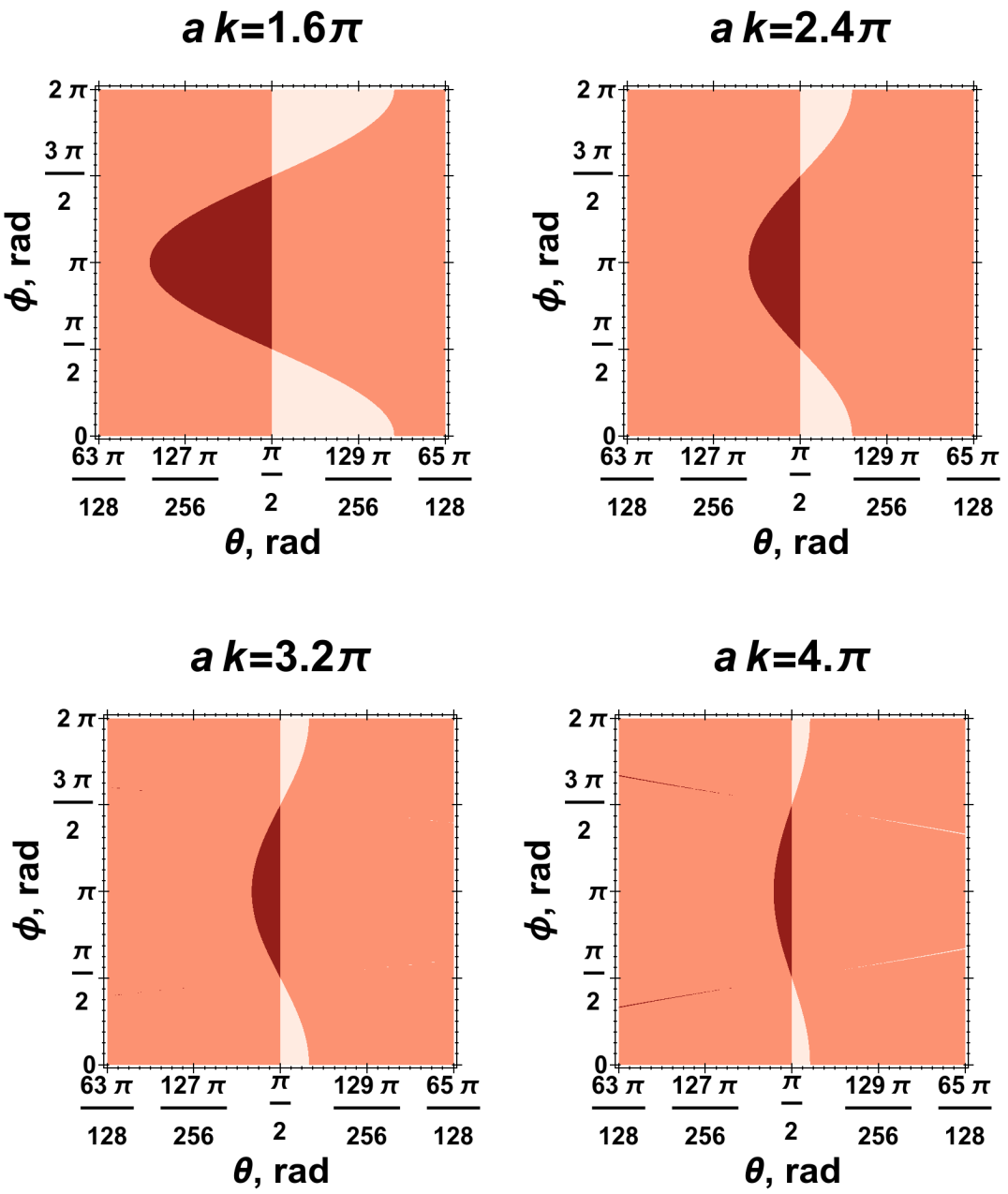

FIGURE 3.12: A panel of four phase diagrams representing the Chern number by colour of square patterned photonic crystals. The photonic crystals are composed of biaxial Faraday effect material. Each diagram in the panel is for a different lattice spacing to wavelength ratio. In each case the lattice spacing to wavelength ratio is stated above the diagram. The phase diagrams are plotted in the space of the direction (θ, ϕ) of the externally applied magnetic field.

the lower-order terms as $\frac{a}{\lambda}$ increases. Beyond a critical $\frac{a}{\lambda}$ a second pair of C-points emerge along the line $k_y = \frac{\pi}{a}$. The two extra C-points have opposite signs of the $\pm\frac{1}{2}$ topological index so as to maintain the net zero topological index over the Brillouin zone torus. The zero contour lines of $b_{\blacksquare z}(\mathbf{k})$ at each of the new C-points also represent geodesics of the form (3.10). As such, the topological phase diagram

results from the interplay of four geodesics joining the antipodal magnetic field directions. Although this emergence takes place for $\frac{a}{\lambda} \simeq 1.3$, we do not start to properly see the effect of these extra C-points over the range plotted until the bottom right phase diagram. The extra feature on the phase diagram is a thin region over all ϕ which is well displaced from the $\theta = \frac{\pi}{2}$ equator over much of this range. The sign of the Chern number of the new feature is opposite to that produced by the original two C-points at the same value of ϕ. This sign discrepancy results from the sign of the ratio c_2/c_1 for each of the new geodesics being opposite to that of the second C-point along the $k_y = 0$ line.

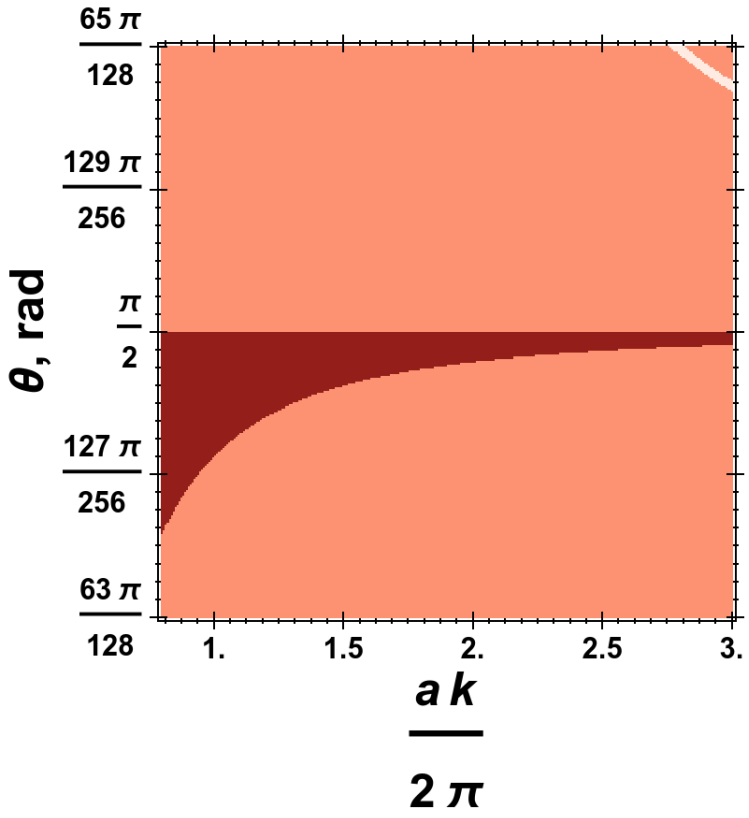

FIGURE 3.13: A phase diagram representing the Chern number by colour of a square patterned photonic crystal. The photonic crystal is composed of biaxial Faraday effect material. This phase diagram examines the effect of continuous variation of the lattice spacing to wavelength ratio. The lattice spacing to wavelength ratio is plotted against the magnetic field direction θ with $\phi = \pi$ held fixed.

Figure 3.13 examines the effect on the topological phase diagram of the continuous variation of the lattice spacing to wavelength ratio. From this figure we can see the size of the topologically non-trivial phase contracts with increasing $\frac{a}{\lambda}$. At large $\frac{a}{\lambda}$ we begin to see the effect of the extra two C-points on the topological phase diagram. We note that this feature begins at lower $\frac{a}{\lambda}$ than figure 3.13 suggests but is cut off due to the range of θ considered in the figure.

We have now developed a picture of the topological phase diagram of square patterned photonic crystals composed of biaxial Faraday effect dielectrics. This phase diagram depends on six parameters which together fix the locations of the C-points and L-lines of the iso-frequency surfaces. The topological phase diagram is therefore a complicated hypersurface in the space of these parameters, nonetheless we have developed an understanding of it by examining representative slices. The immediate conclusion, and one which differs from that of the corresponding homogeneous material seen in subsection 2.4.3, is that one can achieve a non-zero Chern number. This non-zero Chern number occurs when the magnetic field is applied for a band of directions almost perpendicular to the optic axis direction. Once the presence of a topologically non-trivial surface in this hyperspace has been established we look at studying how the volume of that surface varies in different directions in parameter space. This analysis has led us to conclude that, with regard to maximising the size of the topologically non-trivial region, the biaxiality should be as strong as possible and the lattice spacing to wavelength ratio as small as possible.

3.4.4 Implications for Numerical Studies of Topological Invariants

All of the topological phase diagrams presented for biaxial Faraday effect photonic crystals followed from analysis of the lattice Hamiltonian $\underline{\underline{B}}_{\blacksquare}(\mathbf{k})$. However we saw in subsection 3.3.2 that in the regime of low lattice spacing to wavelength ratio, which has been considered for most of the phase diagrams, there are two additional C-points in the numerical bandstructure calculations compared with the predictions of the lattice Hamiltonian. This means that there would be four rather than two zero contour lines of the Faraday effect contribution in the (θ, ϕ) space which represent the band-gap closing at each of the four C-points. These extra zero contours are likely to result in richer phase diagrams with an increase in the topologically non-trivial parameter areas. For instance in the bottom right panel of figure 3.12 we see a situation, at higher $\frac{a}{\lambda}$ where the lattice Hamiltonian features four C-points. Despite the higher lattice spacing to wavelength ratio meaning the overall topologically non-trivial area is somewhat diminished, we see that there is a richer structure to the phase diagram compared to those at lower $\frac{a}{\lambda}$. It is also possible that the numerical study will display somewhat different structure in the vicinity of the pinch-points of the topological phase diagrams from the lattice Hamiltonian model owing to the inclusion of higher order terms and scattering effects. For these reasons we argue that the topological phase diagram which would be produced from numerical bandstructure calculations would be richer than that obtained from the lattice Hamiltonian.

3.5 Photonic Crystals Composed of Chiral Biaxial Materials

We now consider $2D$ photonic crystals composed of chiral biaxial materials. The introduction of chirality has the potential to lift the degeneracies of the iso-frequency surfaces. If this proves to be the case the iso-frequency surfaces can be assigned a Chern number. Whether or not this invariant is non-zero depends on the parameters of the photonic crystal. Depending on the form of the chirality there are between five and ten parameters determining the Chern numbers of the iso-frequency surfaces. We shall initially focus on the simpler forms of chirality, those of the orthorhombic crystals, and then progress to those of increasing complexity.

Before looking at the different forms of chirality though it will be helpful to recall the function $b_{\blacksquare z}$,

$$\begin{aligned} b_{\blacksquare z}(\mathbf{k}) =& \frac{1}{2}\epsilon_2\gamma_C\Bigg(\tilde{G}_{zz} + \frac{1}{ak}(2\tilde{G}_{xz} + 3A\tilde{G}_{zz})\sin k_x a + \frac{2}{ak}\tilde{G}_{yz}\sin k_y a + \\ &+ \frac{1}{a^2k^2}(2\tilde{G}_{xy} + 6A\tilde{G}_{yz})\sin k_x a \sin k_y a + \frac{4}{a^2k^2}\Bigg\{\tilde{G}_{xx} + 6A\tilde{G}_{xz} + \\ &- \tilde{G}_{zz}[1 + \frac{3}{4}\epsilon_2(\alpha - \beta)]\Bigg\}\sin^2\frac{k_x a}{2} + \frac{4}{a^2k^2}\Bigg\{\tilde{G}_{yy} - \tilde{G}_{zz}[1 + \\ &+ \frac{3}{4}\epsilon_2(\alpha - \beta)]\Bigg\}\sin^2\frac{k_y a}{2}\Bigg), \end{aligned} \tag{3.11}$$

where the symmetric chirality tensor $\underline{\underline{G}}$ has been re-expressed as $\underline{\underline{G}} = \gamma_C\underline{\underline{\tilde{G}}}$. The pre-factor γ_C relates the overall scale of the gyromagnetic effect ρ_C to the effective operating wavenumber through $\gamma_C = \frac{2\rho_C}{\epsilon_2 k}$. In the tensor $\underline{\underline{\tilde{G}}}$ each non-zero component is allowed to vary from -1 to 1. The reason for this decomposition is that the Chern number depends on the sign of $b_{\blacksquare z}$ at the C-point locations which is determined by the ratios of the components of $\underline{\underline{G}}$; the overall scale of $b_{\blacksquare z}$ at these points is irrelevant in this regard. The component $\left(\tilde{G}_{xyz}\right)_{ij}$ in the optic axis coordinate system is related to that in the principal axes coordinate system by $\left(\tilde{G}_{xyz}\right)_{ij} = R_{ik}\left(\tilde{G}_{123}\right)_{kl}R^T_{lj}$. At low lattice spacing to wavelength ratio there are only two C-points which both feature along the line $k_y = 0$. Along this line the function (3.11) only depends on the components $\tilde{G}_{xx}$, $\tilde{G}_{xz}$ and $\tilde{G}_{zz}$ which in turn are expressible in terms of $\tilde{G}_{11}$, $\tilde{G}_{13}$ and $\tilde{G}_{33}$ in combinations. At higher lattice spacing to wavelength ratio, when the extra pair of C-points emerge along $k_y = \frac{\pi}{a}$, the handedness of these new C-points additionally depends on $\tilde{G}_{22}$. As such, within the lattice Hamiltonian model at least, the Chern number does not depend on the components $\tilde{G}_{12}$ and $\tilde{G}_{23}$. This immediately reduces the parameter space to be explored to a maximum of eight dimensions depending on the form of chirality considered.

3.5.1 Forms of Chirality

We now move to examine whether each of the different types of chirality allows non-zero Chern numbers. These conclusions shall be based on the lattice Hamiltonian $\underline{\underline{B}}_{\blacksquare}(\mathbf{k})$ exclusively. We shall address the implications for numerical studies of these structures later.

Rhombic Pyramidal

For rhombic pyramidal dielectrics there is one non-zero component of the symmetric chirality tensor $\underline{\underline{\tilde{G}}}_{abc}$ featuring on the off-diagonal. This tensor is related to that in the principal axes frame $\underline{\underline{\tilde{G}}}_{123}$ by a permutation to appropriately match up the crystallographic axes and the principal dielectric axes. Considering photonic crystals formed from these materials, under any of the possible permutations of axes, the resulting Chern number is zero. This zero Chern number is irrespective of whether we are in a regime with two or four C-points. There being only one non-zero component of $\underline{\underline{\tilde{G}}}$ simply does not give the flexibility to achieve different signs of $b_{\blacksquare z}$ at the different C-points.

Rhombic Disphenoidal

For rhombic disphenoidal structures the chirality tensor is diagonal with distinct entries. Considering photonic crystals patterned out of rhombic disphenoidal materials, it seems difficult to achieve a non-zero Chern number for the iso-frequency surfaces, at least within the lattice Hamiltonian model. This is the case irrespective of whether we are in a regime with two or four C-points. In this instance despite having three non-zero components of $\underline{\underline{\tilde{G}}}$ so that the sign of $b_{\blacksquare z}$ can change, the zero contours of the two C-points along the $k_y = 0$ are practically identical as are those for the two C-points along the $k_y = \frac{\pi}{a}$ line. This means that the signs of the C-points of opposite index change simultaneously.

Domatic

For domatic materials the symmetric chirality tensor features two non-zero distinct entries on the off-diagonals. Considering photonic crystals patterned out of domatic materials, it is not possible to achieve a non-zero Chern number for the iso-frequency surfaces. The zero Chern number in this case is irrespective of both whether we are in a regime with two or four C-points and which of the dielectric axes correspond to the b crystallographic axis. Since $\tilde{G}_{12}$ and $\tilde{G}_{23}$ do not contribute to equation (3.11) along the lines $k_y = 0$ and $k_y = \frac{\pi}{a}$ we are again effectively in a situation where only one component of $\underline{\underline{\tilde{G}}}$ is relevant. This case is then similar to

that of chirality of rhombic pyramidal form with one component of $\underline{\underline{\tilde{G}}}$ lacking the flexibility to achieve a non-zero Chern number.

Sphenoidal

For sphenoidal materials the symmetric chirality tensor features three distinct entries on the diagonal as well as one off-diagonal entry. Considering photonic crystals patterned out of sphenoidal materials, it is possible to achieve a non-zero Chern number for the iso-frequency surfaces. This occurs in the case where the 2 dielectric axis corresponds to the b crystallographic axis. For the other possible configurations the situation reduces to that of the rhombic disphenoidal materials and the Chern number is zero.

Pedial

All the previous cases represent subsets of what can be seen in pedial crystal structures. Owing to this the possibility of a non-zero Chern number for the iso-frequency surfaces of square patterned pedial materials follows from that of the sphenoidal structures.

3.5.2 Examination of Topological Phase Diagrams

Henceforth we will focus on dielectrics with either the sphenoidal or pedial point groups. This choice follows from the lattice model predicting that photonic crystals made of these type of dielectrics could exhibit a non-zero Chern number. In the low lattice spacing to wavelength ratio regime, the sign of the handedness of each of the C-points along the $k_y = 0$ line is determined by the three chirality tensor components $\tilde{G}_{11}$, $\tilde{G}_{33}$ and $\tilde{G}_{13}$. With this in mind we can examine the Chern number in the space of these three components.

Figure 3.14 plots the regions of non-zero Chern number in the space of the three aforementioned chirality tensor components. We immediately see the possibility of non-zero Chern number, which was theorised earlier, can be realised. This realisation occurs in regions where the two components $\tilde{G}_{11}$ and $\tilde{G}_{33}$ have the same sign as each other and a different sign to $\tilde{G}_{13}$.

We shall now turn to assessing the variation of the phase diagrams as the other parameters of the photonic crystal are changed. As in section 3.4 we consider the variation of the principal dielectric constants and the lattice spacing to wavelength ratio of the photonic crystal. To facilitate a more direct assessment of the effect of the parameter variation we shall consider the green $2D$ planar slice of the parameter

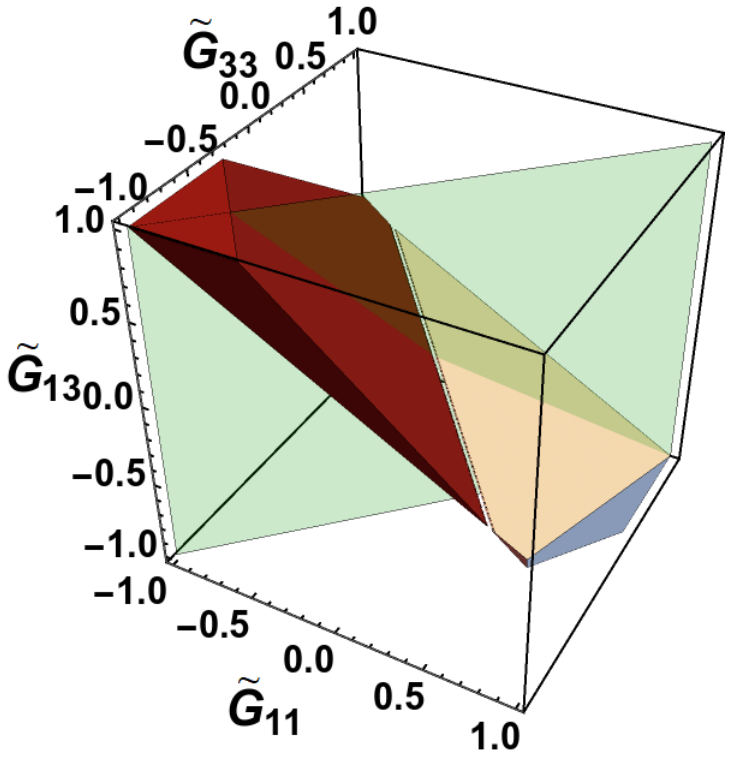

FIGURE 3.14: A 3D phase diagram representing the regions of non-zero Chern number by colour of a square patterned photonic crystal. The photonic crystal is composed of chiral biaxial material. The form of chirality is either that of a sphenoidal or pedial structure. In the case of a sphenoidal material we have taken the b crystallographic axis and the 2 dielectric axis to coincide. The darker (lighter) pink region represents a Chern number $C = 1$ ($C = -1$). The region of zero Chern number is left transparent. The plane $\tilde{G}_{11} = \tilde{G}_{33}$ is shown in green.

space shown in figure 3.14. The slice we consider is $\tilde{G}_{11} = \tilde{G}_{33} \equiv \tilde{G}_i$ which, although artificial, is likely the easiest to examine due to the observations that followed from the examination of figure 3.14 in the preceding paragraph. We additionally relabel $\tilde{G}_{13} \equiv \tilde{G}_a$. At higher lattice spacing to wavelength ratio, following the emergence of the additional two C-points, the component $\tilde{G}_{22}$ can also affect the Chern number. In this regime we consider the slice $\tilde{G}_{11} = \tilde{G}_{22} = \tilde{G}_{33} \equiv \tilde{G}_i$ of the four dimensional parameter space for analogous reasons.

3.5.3 Variation of Topological Phase Diagrams with Degree of Biaxiality

The first parameter we consider the variation of is the degree of biaxiality. Initially we shall examine four snapshots of the topological phase diagrams in the space of the isotropic chirality tensor components $\tilde{G}_i$ and anisotropic chirality tensor components $\tilde{G}_a$. Each of these snapshots considers a different set of principal dielectric constants.

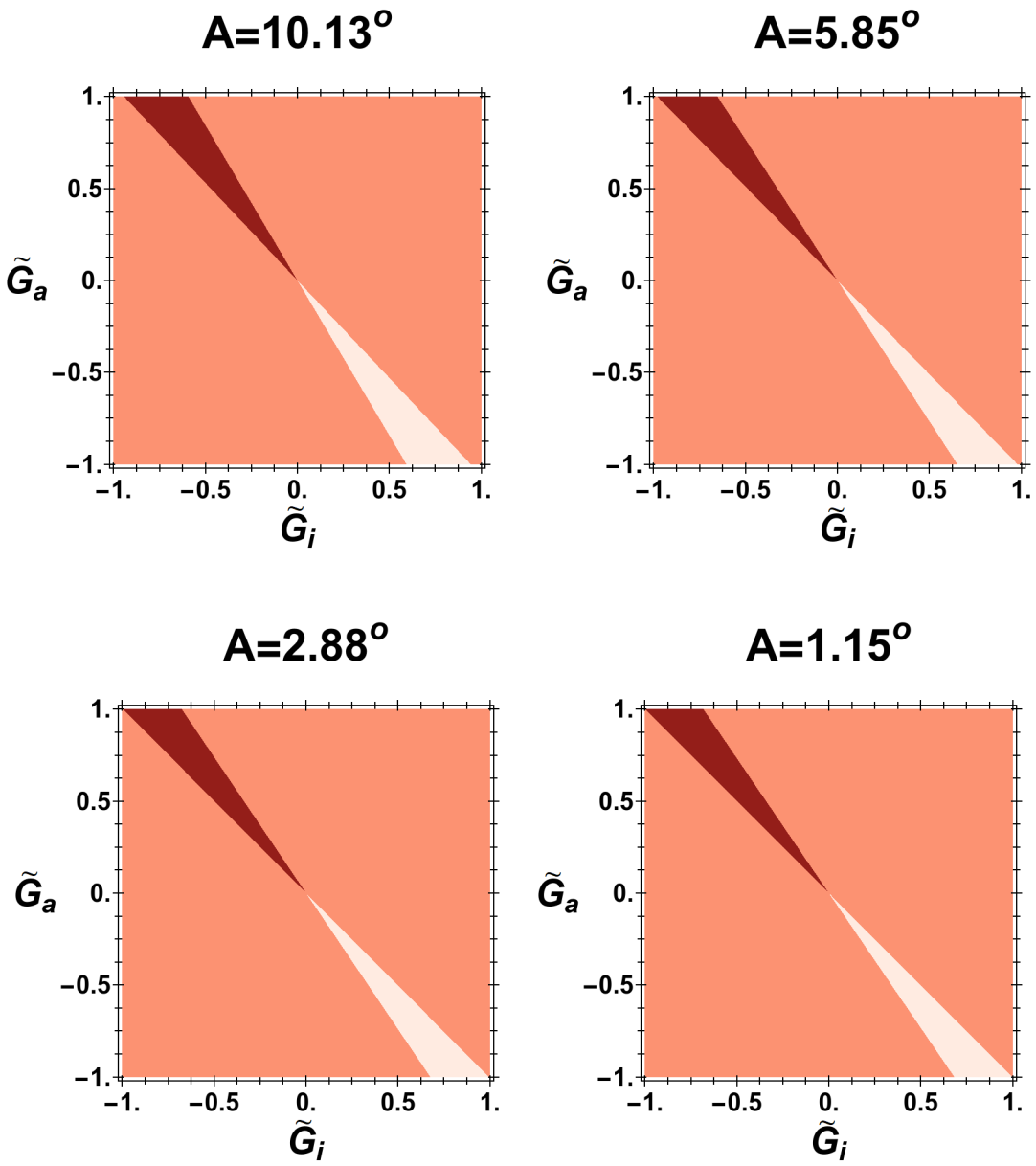

FIGURE 3.15: A panel of four phase diagrams representing the Chern number by colour of square patterned photonic crystals. Each photonic crystal considered is composed of chiral biaxial material of sphenoidal or pedial type. The degree of biaxiality is different in each diagram. The cone semi-angle of each diagram is stated above. The principal dielectric constants $(\epsilon_1, \epsilon_2, \epsilon_3)$ are (from left to right and then top to bottom) (i) $(2, 3, 4)$, (ii) $(2, 2.5, 3)$, (iii) $(2.25, 2.5, 2.75)$ and (iv) $(2.4, 2.5, 2.6)$.

Figure 3.15 shows an array of topological phase diagrams representing the Chern number by colour. In each case the biaxial cone semi-angle is stated above the plot. In each plot of figure 3.15, the two lines dividing the phase diagram represent the zero contour lines of $b_{\blacksquare_z}(\mathbf{k})$ at each of the two C-points. Although difficult to observe in figure 3.15, the stronger the biaxiality the larger the region of non-zero Chern numbers. This enlargement of the topologically non-trivial phase

results from the increased displacement of the C-point from the face centre of the Brillouin zone. This variation of the phase diagram is however no where near as pronounced as the corresponding variation for biaxial Faraday effect photonic crystals in subsection 3.5.3. The comparative stability in this case follows from the quadratic dependence of the B polynomial (2.32) on propagation direction for chirality as compared to the linear dependence for the Faraday effect (2.31).

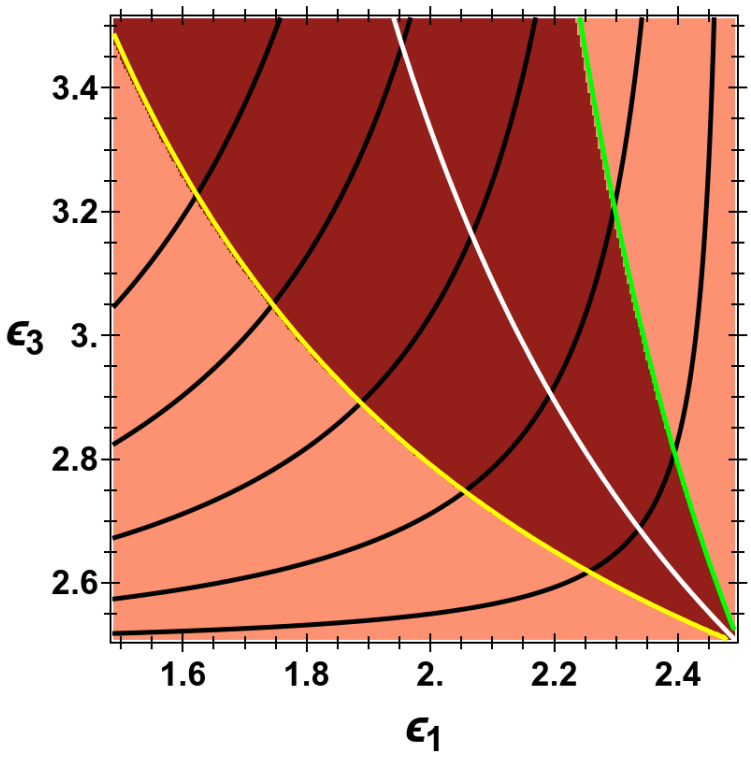

FIGURE 3.16: A phase diagram representing the Chern number by colour of a square patterned photonic crystal. The photonic crystal is composed of chiral biaxial material of sphenoidal or pedial type. This phase diagram examines the effect of continuously varying the degree of biaxiality. The median principal dielectric constant is fixed at $\epsilon_2 = 2.5$ and the other two principal refractive indices (ϵ_1, ϵ_3) are allowed to vary. The black contours are curves along which the biaxial cone semi-angle A is constant. The lowest of which has $A = 2^\circ$ and each subequent contour is 2° higher. The white contour represents the line $\alpha = \beta$, the yellow contour represents $\alpha = 2.4\beta$ while the green contour represents $\alpha = 0.4\beta$. The isotropic and anisotropic chiralities are $(\tilde{G}_i, \tilde{G}_a) = (-0.5, 0.55)$.

Figure 3.16 examines the effect on the topological phase diagram of the continuous variation of two of the principal dielectric constants with the median one held fixed. The black overlaid contours represent constant values of the biaxial cone semi-angle in 2° increments from bottom to top of the figure. From this figure we can see, much more directly than in figure 3.15, that the size of the topologically non-trivial phase increases with increasing strength of biaxiality. The boundary

between the phases, for this set of parameters, approximately follows the contours $\alpha = 2.4\beta$ (yellow) and $\alpha = 0.4\beta$ (green).

3.5.4 Variation of Topological Phase Diagrams with Lattice Spacing to Wavelength Ratio

The other parameter we vary is the lattice spacing to wavelength ratio. As before we study four snapshots of the topological phase diagram in the space of the isotropic chirality contribution $\tilde{G}_i$ and the anisotropic chirality contribution $\tilde{G}_a$. Each of these snapshots considers a different lattice spacing to wavelength ratio.

Figure 3.17 shows an array of topological phase diagrams representing the Chern number by colour. In each case the lattice spacing to wavelength ratio is stated above the plot. We see that the higher this ratio the smaller the region of non-zero Chern numbers. This diminishing of the topologically non-trivial phase results from the C-points being pushed towards the boundary of the Brillouin zone. This occurs because the iso-frequency surface dispersion becomes increasingly dominated by the linear terms as $\frac{a}{\lambda}$ increases. Beyond a critical $\frac{a}{\lambda}$ a second pair of C-points of opposite topological index emerge along the line $k_y = \frac{\pi}{a}$. This emergence takes place for $\frac{a}{\lambda} \simeq 1.3$. Above this value of $\frac{a}{\lambda}$ there are therefore four zero contour lines of $b_{\blacksquare z}(\mathbf{k})$, one for each of the C-points. These extra C-points therefore result in an extra feature in the topological phase diagrams. The extra feature resulting from this emergence is a thin region nearly abutting the previous topologically non-trivial area. The sign of the Chern number of the new feature is opposite to that produced by the original two C-points at the same value of $\tilde{G}_i$.

Figure 3.18 examines the effect on the topological phase diagram of the continuous variation of the lattice spacing to wavelength ratio. From this figure we can see the size of the topologically non-trivial phase contracts with increasing $\frac{a}{\lambda}$. For $\frac{a}{\lambda} \gtrsim 1.3$ we begin to see the effect of the extra two C-points on the topological phase diagram.

A possible criticism of the analysis offered on the phase diagrams of 2D photonic crystals composed of chiral biaxial dielectrics is that of hyper-tailoring of parameters. The chirality tensor $\underline{\underline{\tilde{G}}}$ cannot be externally varied, although if we were to have considered metamaterials it may be possible to pre-engineer it. However, we have chosen to focus solely on dielectric crystals. As such, when we plot the phase diagrams in the preceding subsections we are not referring to a particular chiral biaxial material over the whole plot but rather some hypothetical material which possesses the properties of a single point on the diagram but is distinct to the material represented by adjacent points. We have adopted this approach principally due to the incomplete knowledge of the components of the chirality tensor $\underline{\underline{\tilde{G}}}$, where

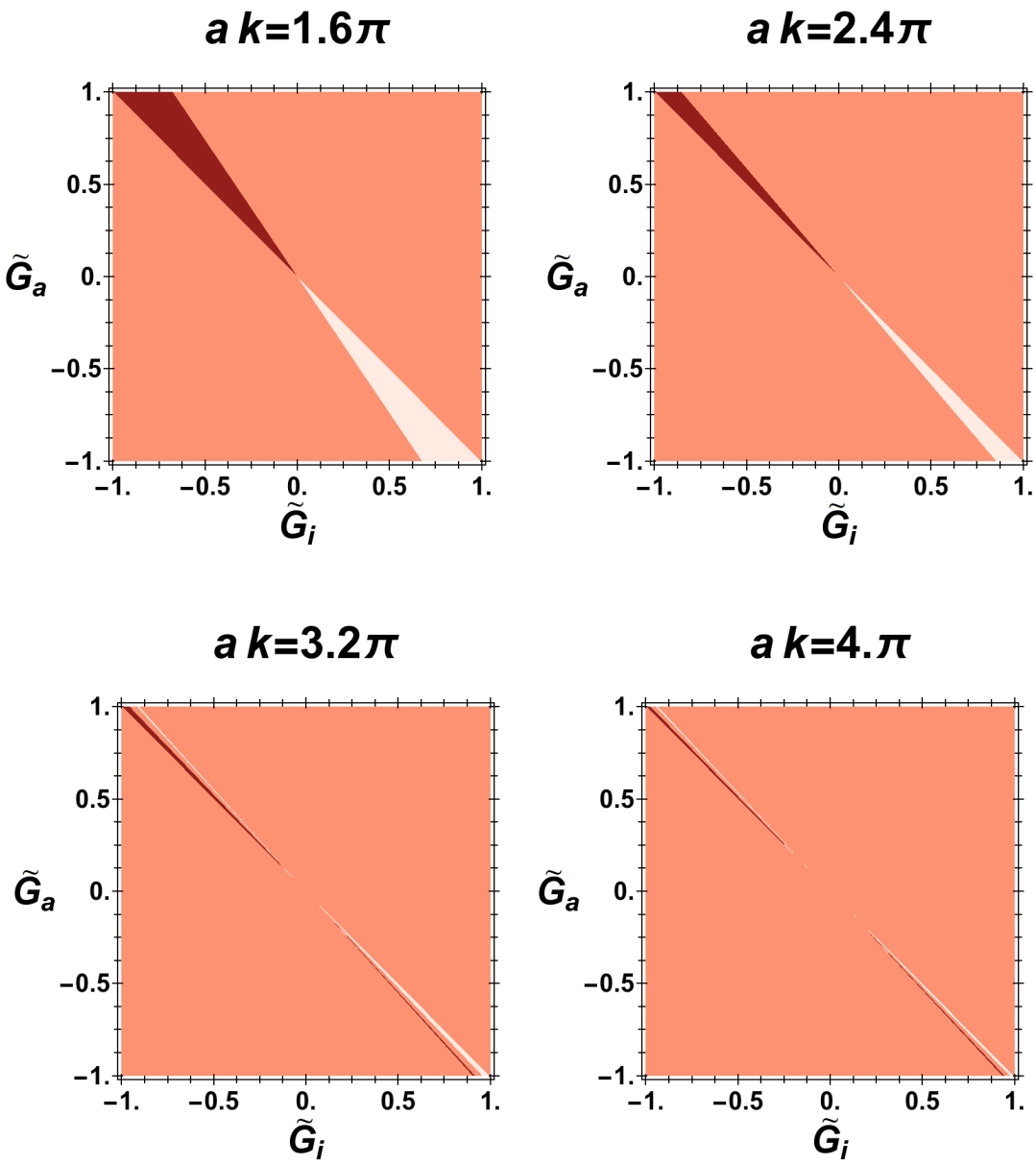

FIGURE 3.17: A panel of four phase diagrams representing the Chern number by colour of square patterned photonic crystals. The photonic crystals are composed of chiral biaxial materials of sphenoidal or pedial type. Each diagram in the panel is for a different lattice spacing to wavelength ratio. In each case the lattice spacing to wavelength ratio is stated above the diagram.

in many cases no more than one or two components are known, and to hopefully be able to say something global regarding photonic crystals composed of these types of materials. To mitigate the criticism of unrealistic tailoring of $\underline{\underline{\tilde{G}}}$ we have therefore considered the fraction of non-zero Chern numbers obtained over many random realisations of a pedial type chirality tensor.

Figure 3.19 looks at the fraction of topologically non-trivial photonic crystals of

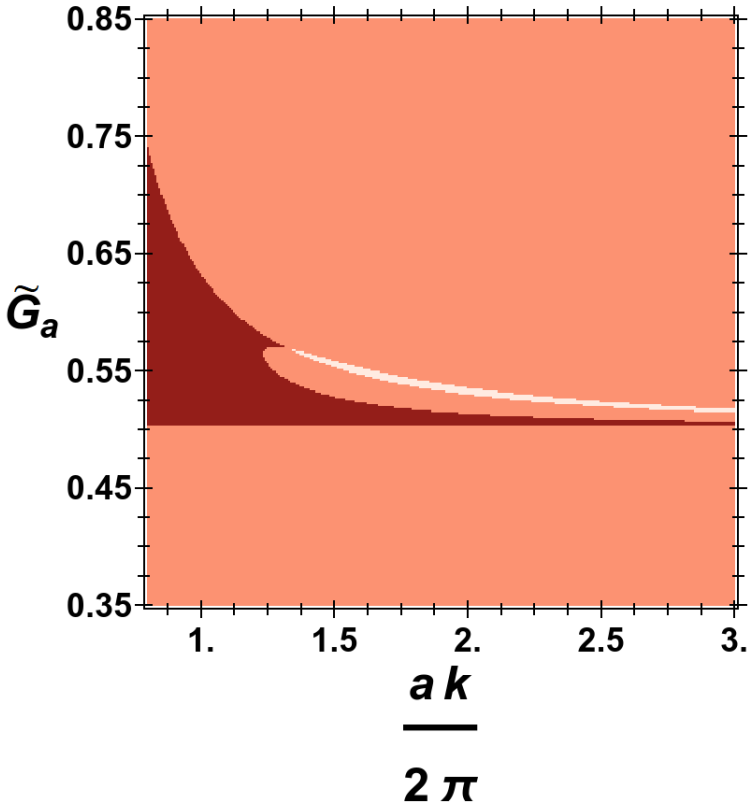

FIGURE 3.18: A phase diagram representing the Chern number by colour of a square patterned photonic crystal. The photonic crystal is composed of chiral biaxial material of sphenoidal or pedial type. The phase diagram examines the effect of continuously varying the lattice spacing to wavelength ratio of the photonic crystal. The strength of the isotropic chirality is held fixed at $\tilde{G}_i = -0.5$.

pedial materials with random chirality. In each of the 10000 realisations a random number is assigned to each of the chirality components. The running topologically non-trivial fraction is represented by the blue points with the one standard error either way represented by the red points. The long-term average tends to around 8% of realisations having a non-zero Chern number, which although not a huge proportion is still a significant fraction. This suggests that it should be possible to find a suitable biaxial crystal with pedial type chirality in order to produce a photonic crystal with a topological non-trivial iso-frequency surface.

We have now developed a picture of the topological phase diagram of square patterned photonic crystals composed of chiral biaxial dielectrics. This phase diagram can depend on up to eight parameters depending on the form of chirality considered. These parameters together fix the locations of the C-points and L-lines of the iso-frequency surfaces. The topological phase diagram is therefore a complicated hypersurface in the space of these parameters, nonetheless we have developed an understanding of these surfaces for each possible form of chirality. We discovered that, at least within the lattice Hamiltonian model, non-zero Chern

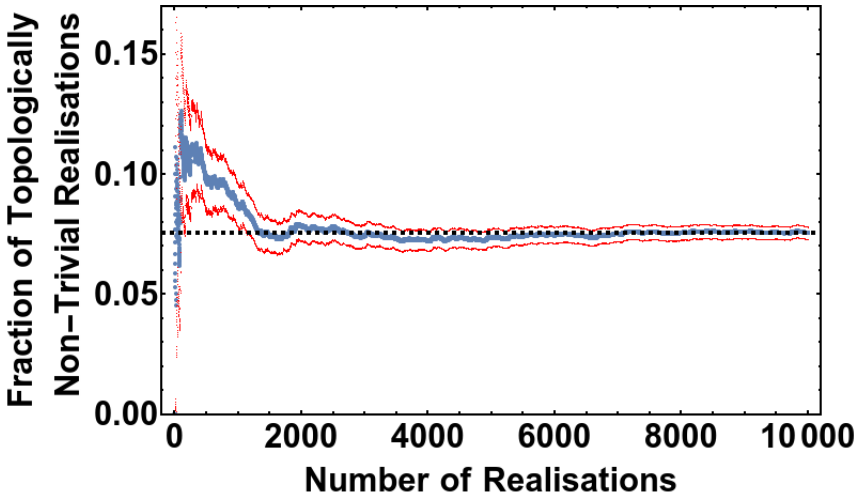

FIGURE 3.19: The fraction of topologically non-trivial systems of square photonic crystals composed of random chiral biaxial material of sphenoidal or pedial type. In each realisation we have assigned a random number $\in (-1, 1)$ to each non-zero component of the symmetric gyromagnetic tensor $\underline{\underline{\tilde{G}}}$. The blue points give the running fraction of topologically non-trivial systems while the red points indicate this running fraction plus or minus one standard error. The dashed black gridline gives the fraction after 10000 iterations.

numbers are only possible for dielectrics of the sphenoidal or pedial point groups. In these two instances the phase diagrams are hypersurfaces which vary in eight dimensions. To understand these surfaces we have examined representative $2D$ and $3D$ slices of the full $8D$ parameter space. The appearance of non-zero Chern number in this space occurs when the isotropic chirality contributions $\tilde{G}_i$ and the anisotropic chirality contributions $\tilde{G}_a$ are close to equal in magnitude but differ in sign. Once the presence of a topologically non-trivial surface in this hyperspace has been established we look at studying how the volume of that surface varies in different directions in parameter space. This analysis has led us to conclude that, with regard to maximising the size of the topologically non-trivial region, the biaxiality should be as strong as possible and the lattice spacing to wavelength ratio as small as possible.

3.5.5 Implications for Numerical Studies of Topological Invariants

All of the topological phase diagrams presented for photonic crystals composed of chiral biaxial materials followed from analysis of the lattice Hamiltonian $\underline{\underline{B}}_{\blacksquare}(\mathbf{k})$. However we saw in subsection 3.3.2 that in the regime of low lattice spacing to wavelength ratio, which has been considered for most of the phase diagrams, that there are two additional C-points in the numerical bandstructure calculations compared to the predictions of the lattice Hamiltonian. The effect of these additional C-points could be two-fold; they are likely to create richer phase diagrams for types of chirality that already allow non-zero Chern numbers and they could

allow non-zero Chern numbers for types of chirality for which analysis of the lattice Hamiltonian $B_{\blacksquare}(\mathbf{k})$ concluded that topological order would be difficult or impossible. Regarding the former, looking at figure 3.18 we see that following the emergence of the additional C-points there is a richer phase diagram. We therefore argue that the phase diagram of the numerical bandstructures will be more complicated compared to those of the lattice Hamiltonian. In the latter case it is possible that the numerical bandstructure calculations could show that non-zero Chern numbers are realisable for biaxial photonic crystals using chirality of rhombic disphenoidal form. This assessment is based on the lattice Hamiltonian showing that $b_{\blacksquare z}$ can change sign but that the zero contours of the C-points of opposite topological index are not appreciably displaced from each other. If the numerical calculations indicated that the zero contours became displaced then a non-zero Chern number would result. It is unlikely that non-zero Chern numbers would be possible for photonic crystals with either the rhombic pyramidal or domatic form of chirality.

3.6 Conclusion

In this chapter we were interested in the topological invariants of the iso-frequency surface of a square-patterned $2D$ photonic crystal composed of biaxial optically active materials. Our focus was on the two most paraxial polarisation-split bands of the iso-frequency surface, describing propagation largely perpendicular to the periodic plane of the photonic crystal. To describe such a system we have adapted the paraxial Hamiltonian eqs. (2.59) to (2.66) derived in section 2.6 to a square lattice geometry in section 3.2. To assess the fidelity of this adaptation we have compared the Hamiltonian to frequency-domain plane-wave simulations of corresponding systems. The comparison showed that the adapted paraxial Hamiltonian is a reasonable qualitative descriptor of these $2D$ photonic crystal structures. In particular, the adapted Hamiltonian captures the aspects critical to the topological characterisation of these systems, the presence and location of polarisation C-points in the first Brillouin zone, over most of the parameter range.

Since the lattice Hamiltonian gives a reasonable qualitative account of the singularity structure we can use it to determine the topological phase diagrams upon introduction of optical activity. In section 3.4 we considered the effect of optical activity due to the Faraday effect in a magnetic field. We found that, contrary to the case of a homogeneous material, it is possible to achieve a non-zero Chern number in certain parameter regimes. There are generally six parameters governing the value of the Chern number: the magnetic field direction, the three principal dielectric constants and the lattice spacing to wavelength ratio. To achieve a non-zero Chern number the magnetic field should be applied in any of a band of

directions, all of which are close to perpendicular to the optic axis direction. The width of this band is governed by the other four parameters. A more strongly biaxial material results in a wider band of directions as does a system with a lower lattice spacing to wavelength ratio.

The other form of optical activity that we considered is chirality. The nature of the chirality considered plays a decisive role in whether optical topological order is achievable at all. With reference to the lattice Hamiltonian model, it is only possible to achieve a non-zero Chern number with either dielectrics of sphenoidal or pedial form. For photonic crystals composed of these types of dielectrics a topologically non-trivial system is by no means guaranteed. Whether or not a non-zero Chern number results depends on the interplay of eight parameters: the four relevant components of the chirality tensor, the three principal dielectric constants and the lattice spacing to wavelength ratio. To achieve a non-zero Chern number the ratio of the diagonal components of the chirality tensor to each other should be close to positive unity while the ratio of each of the three diagonals to the relevant off-diagonal should be close to negative unity. When this is the case the range of tolerance close to unity for a non-zero Chern number is increased for a more strongly biaxial material and when the lattice spacing to wavelength ratio is lower.

In previous works on topologically non-trivial square patterned photonic crystals [31, 32, 118–121], degeneracies of the photonic band structure were inherited from the lattice symmetries rather than from the underlying dielectrics. These previous works additionally explicitly considered transverse magnetic modes, where the direction of propagation in the $2D$ Brillouin zone is decoupled from the polarisation state. In contrast, in the work presented in this chapter, the use of anisotropic dielectrics as well as the out-of-plane propagating geometry considered mean that such decoupling of propagation direction and polarisation does not occur.

The work in this chapter has instead presented an alternative framework within which to realise optical topological order. This framework is novel in that it does not rely on a specific lattice geometry to achieve Dirac points, but rather exploits the polarisation degeneracies of the index surfaces of anisotropic materials. We have shown that the effective optical spin-orbit coupling present in anisotropic and optically active materials allows topologically non-trivial iso-frequency surfaces of photonic crystals to be realised. A square lattice geometry is one of the simpler photonic crystal arrangements possible. It is likely that more complicated lattice geometries can produce richer topological phase diagrams. In chapter 4 we explore this possibility by examining the adaptation of the paraxial Hamiltonian eqs. (2.59) to (2.66) to a triangular lattice geometry.

Chapter 4

Triangularly Patterned Photonic Crystals

4.1 Introduction

In this chapter we study $2D$ photonic crystals composed of anisotropic optically active materials patterned in a triangular geometry. As in chapter 3 our primary interest is in realising non-zero topological invariants for the iso-frequency surfaces of these photonic crystals. As we are considering a periodic system we expect there to be net zero circulation of the linear-polarisation vector field over the first Brillouin zone, guaranteeing an equal number of singularities of each sign of topological index. This net-zero circulation is dictated by the underlying topology of the Brillouin zone. The geometry, however, dictates the local behaviour of the vector field and therefore will differ from the square geometry previously addressed. There may be a different total number of C-points in the first Brillouin zone and they will certainly occur at different locations in the first Brillouin zone. Correspondingly, the form of optical activity considered will also adapt to the triangular geometry in a different fashion to that seen for the square patterned case. In conjunction, these deviations will result in topological phase diagrams that differ from those of square patterned photonic crystals.

To assess these deviations we shall follow a similar procedure to that of chapter 3 by implementing the paraxial Hamiltonian derived in chapter 2 on a triangular grid. The adaptation of the Hamiltonian to a triangular geometry shall be detailed in section 4.2. The resulting Hamiltonian shall be analysed in section 4.3 with a particular focus on the number and locations of C-points. We then compare the predictions of the adapted Hamiltonian model to those of numerical simulations of corresponding structures. From there we turn to determining the topological phase diagrams of the iso-frequency surfaces of these triangular photonic crystals. The photonic crystals which we consider are composed of biaxial dielectrics featuring one of two separate types of optical activity. The forms of optical activity we consider are, respectively, the Faraday effect in section 4.4 and chirality in section 4.5. For each of these types of optical activity we compute the Chern number as

the relevant material parameters are allowed to vary. Through this approach we develop a thorough appreciation of the complicated topological phase diagrams. In section 4.6 we assess the geometry-enforced differences to the topological phase diagrams that we determined for square patterned photonic crystals. Finally in section 4.7 we offer conclusions and perspectives on the work presented in this chapter.

4.2 Triangular Photonic Crystal Geometry

As in chapter 3 we wish to adapt the paraxial Hamiltonian derived in chapter 2 to describe photonic crystals of the desired patterning geometry. The patterning geometry that we consider is that of a triangular lattice. The periodic triangularly patterned systems will be composed of anisotropic gyromagnetic dielectrics. The triangular patterning will be in the xy plane and the structures will be invariant along the z direction. The characteristic period in the xy plane is given by the lattice constant a and the triangular geometry of the lattice is captured by the two primitive lattice vectors $\mathbf{a}_1$ and $\mathbf{a}_2$:

$$\mathbf{a}_1 = a(1,0),\ \mathbf{a}_2 = \frac{a}{2}(1,\sqrt{3}). \tag{4.1}$$

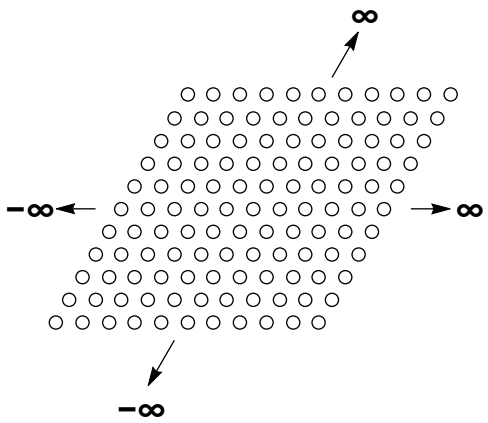

FIGURE 4.1: An illustration showing a section of the entrance face of a triangularly-patterned photonic crystal.

The geometry of the entrance face of the photonic crystal is illustrated in figure 4.1. The real space lattice depicted in this figure has a corresponding reciprocal space lattice arrangement which follows from the invariant translation vectors in wavevector space. These reciprocal lattice vectors $\mathbf{b}_1$ and $\mathbf{b}_2$ are

$$\mathbf{b}_1 = \frac{2\pi}{a}(1,-\frac{1}{\sqrt{3}}),\ \mathbf{b}_2 = \frac{2\pi}{a}(0,\frac{2}{\sqrt{3}}). \tag{4.2}$$

The primitive unit cell in reciprocal space is the first Brillouin zone. For a triangularly patterned photonic crystal this first Brillouin zone is a hexagon. In figure 4.2 we display the Brillouin zone as well as the coordinates of its high symmetry points. The labels for these high symmetry points that we shall adopt in this chapter are also displayed.

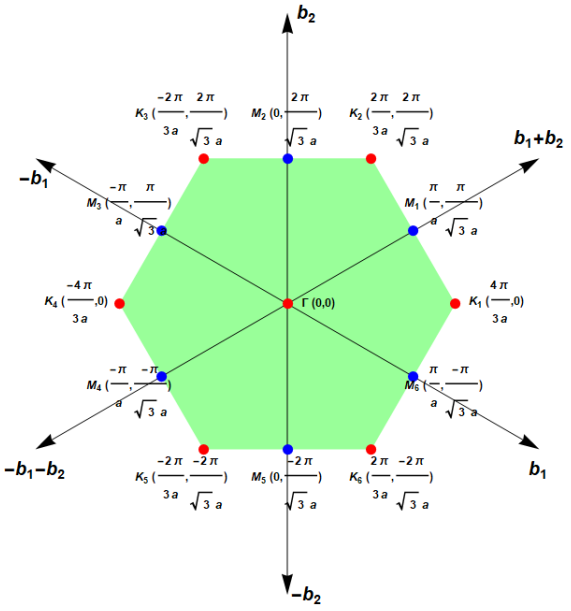

FIGURE 4.2: Nearest neighbour directions of the reciprocal lattice. The first Brillouin zone is the hexagon superposed in green. High symmetry points of the first Brillouin zone are marked and labelled.

As in chapter 3 we choose to orient the anisotropic dielectric materials with their optic axis along the z direction. Due to the anisotropy of the inclusions, the symmetry of the structure will be less than that of the triangular lattice itself.

Now that we have established the geometry of the problem we seek to adapt the Hamiltonian derived in chapter 2 to this geometry. We shall again seek a lattice regularisation of the Hamiltonian. In this case the desired lattice regularised Hamiltonian $\underline{\underline{B}}_{\blacktriangle}(\mathbf{k})$ is related to that of section 2.6 by the replacements [122, 123]

$$p_x = \frac{k_x}{k} \to \frac{2}{3ak}\left(\sin(ak_x) + \frac{1}{2}\left\{\sin\left[\frac{a}{2}(k_x + \sqrt{3}k_y)\right] + \sin\left[\frac{a}{2}(k_x - \sqrt{3}k_y)\right]\right\}\right), \tag{4.3}$$

$$p_y = \frac{k_y}{k} \to \frac{1}{\sqrt{3}ak}\left\{\sin\left[\frac{a}{2}(k_x + \sqrt{3}k_y)\right] - \sin\left[\frac{a}{2}(k_x - \sqrt{3}k_y)\right]\right\}, \tag{4.4}$$

$$p_x^2 = \frac{k_x^2}{k^2} \to \frac{2}{a^2k^2}\left[1 - \cos(ak_x)\right], \tag{4.5}$$

$$p_y^2 = \frac{k_y^2}{k^2} \rightarrow -\frac{2}{3a^2k^2}\left[1-\cos(ak_x)\right] + \frac{4}{3a^2k^2}\left(\left\{1-\cos\left[\frac{a}{2}(k_x+\sqrt{3}k_y)\right]\right\} + \left\{1-\cos\left[\frac{a}{2}(k_x-\sqrt{3}k_y)\right]\right\}\right). \tag{4.6}$$

The matrix $\underline{\underline{B}}_{\blacktriangle}(\mathbf{k})$ can be represented as

$$\underline{\underline{B}}_{\blacktriangle}(\mathbf{k}) = b_{\blacktriangle 0}(\mathbf{k})\underline{\underline{\mathbb{1}}} + \mathbf{b}_{\blacktriangle}(\mathbf{k})\cdot\underline{\underline{\boldsymbol{\sigma}}}. \tag{4.7}$$

The matrix $\underline{\underline{B}}_{\blacktriangle}(\mathbf{k})$ governs the propagation of light through triangularly patterned structures composed of biaxial optically active materials. This Hamiltonian matrix is one of the simplest lattice generalisations that both (i) reduces to the original paraxial Hamiltonian under small angle approximation of the trigonometric functions and (ii) is invariant under the addition of any integer number of reciprocal lattice vectors (4.2). The eigenvalues of the Hamiltonian $\underline{\underline{B}}_{\blacktriangle}(\mathbf{k})$ gives the two polarisation-split bands of highest propagation constant k_z for a triangular patterned photonic crystal composed of anisotropic gyromagnetic materials. In figure 4.3 we plot the eigenvalues of the Hamiltonian $\underline{\underline{B}}_{\blacktriangle}(\mathbf{k})$ over the first Brillouin zone for a biaxial photonic crystal lacking optical activity. The parameters used for this figure were $(\epsilon_1, \epsilon_2, \epsilon_3) = (2.25, 2.5, 2.75)$ and a lattice spacing to wavelength ratio of $\frac{a}{\lambda} = 0.8$ was chosen. These parameters are used throughout this chapter unless otherwise stated.

Although difficult to ascertain from figure 4.3, the introduction of periodicity has produced extra C-points in the iso-frequency band structures of the triangularly patterned photonic crystals. We shall now move to investigating the presence and locations of these C-points.

4.3 Degeneracy Structure of Triangular Photonic Crystals

We shall now examine the degeneracy structure of the iso-frequency surfaces of triangularly patterned photonic crystals. Initially we shall do this in a situation where there is no optical activity. Our first preliminary method of study is to use the derived lattice Hamiltonian model $\underline{\underline{B}}_{\blacktriangle}(\mathbf{k})$ to assess the C-points of the iso-frequency surfaces. This assessment will be primarily concerned with four factors (i) the number of C-points of the iso-frequency surfaces, (ii) their locations in the first Brillouin zone, (iii) their local circulation and (iv) their flow in reciprocal space as the lattice spacing to wavelength ratio is varied. We will then compare the predictions of the lattice Hamiltonian model $\underline{\underline{B}}_{\blacktriangle}(\mathbf{k})$ to those from a frequency-domain plane-wave simulation [117] of a corresponding structure.

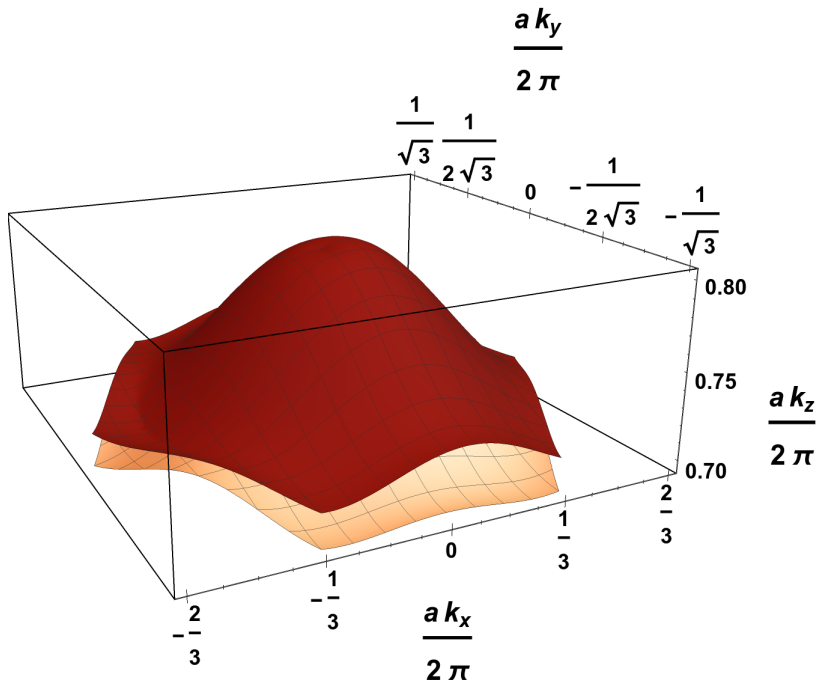

FIGURE 4.3: The iso-frequency surfaces of a triangularly-patterned photonic crystal composed of biaxial material. The plot is generated from the lattice Hamiltonian model. The surfaces are plotted over the first Brillouin zone and the parameters used were $(\epsilon_1, \epsilon_2, \epsilon_3) = (2.25, 2.5, 2.75)$ for the principal dielectric constants and a lattice spacing to wavelength ratio of $\frac{a}{\lambda} = 0.8$.

4.3.1 Degeneracy Structure from Lattice Hamiltonian

In the lattice Hamiltonian C-points are locations in reciprocal space $\mathbf{k}'$ where $\mathbf{b}_\blacktriangle(\mathbf{k}') = \mathbf{0}$. Since in the absence of optical activity $b_{\blacktriangle 3}(\mathbf{k}) = 0$ we need only focus on the zeroes of the functions $b_{\blacktriangle 1}(\mathbf{k})$ and $b_{\blacktriangle 2}(\mathbf{k})$. These zeroes follow contours in the first Brillouin zone, with the intersections of these contours representing C-point locations. We can visualise these locations graphically by looking at appropriate plots of the vector field $(b_{\blacktriangle 1}(\mathbf{k}), b_{\blacktriangle 2}(\mathbf{k}))$ over the first Brillouin zone.

Figure 4.4 shows the vector field $(b_{\blacktriangle 1}(\mathbf{k}), b_{\blacktriangle 2}(\mathbf{k}))$ along with the contours representing the zeroes of each of its components over an enlarged first Brillouin zone. The intersection of the turquoise and green contour lines represent C-points of the iso-frequency surfaces. We see that there are four C-points in the first Brillouin zone for this set of parameters. In addition to the C-point at Γ, which is that of the original Hamiltonian from section 2.6, there is an extra one along the $k_y = 0$ line near the K_4 boundary. The further two C-points appear along the line $k_x = -\frac{\pi}{a}$. By studying the overlaid vector field we can assess the local circulation of each of these C-points. On studying this vector field we note that there is a positive sense of circulation around each pair of points along the lines $k_y = 0$. Conversely there is a negative sense of circulation for each of the C-points along the line $k_x = -\frac{\pi}{a}$.

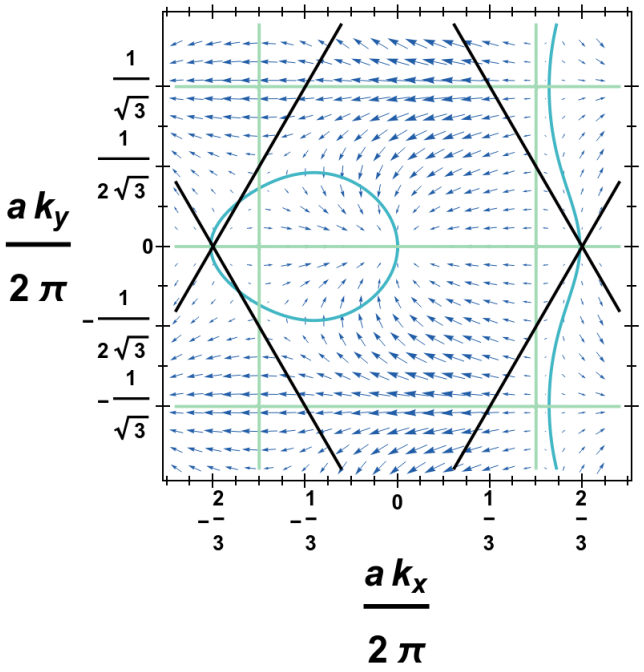

FIGURE 4.4: The zero contour lines of the polynomials $b_{\blacktriangle 1}(\mathbf{k})$ (turquoise) and $b_{\blacktriangle 2}(\mathbf{k})$ (green) over an enlarged area containing the first Brillouin zone. In the absence of a gyromagnetic perturbation, the intersection of the zero contour lines represent degeneracies of the iso-frequency bandstructure. The vector field $(b_{\blacktriangle 1}(\mathbf{k}), b_{\blacktriangle 2}(\mathbf{k}))$ is overlaid in blue.

The Berry flux corresponding to each of these singularities is $\pm\pi$, therefore upon introduction of optical activity the Chern number can be $C \in \{-2, -1, 0, 1, 2\}$.

As in the case of the square geometry the extra degeneracies occur, loosely speaking, towards the face centres and zone corners of the Brillouin zone. The topological indices are the same as that of the square geometry; positive for those at the zone centre and towards the zone corners and negative for those towards the face centres. The four C-points observed in figure 4.4 were for one particular set of parameters. To understand the topological phase diagram upon introduction of optical activity we need to understand the degeneracy structure in all relevant parameter regimes. The zeroes of the $b_{\blacktriangle 2}(\mathbf{k})$ component of the vector field occur along the high-symmetry lines $k_y = 0$, $\pm\frac{2\pi}{\sqrt{3}a}$ and $k_x = \pm\frac{\pi}{a}$ for all sets of parameters. The lines $k_y = -\frac{2\pi}{\sqrt{3}a}$ and $k_y = \frac{2\pi}{\sqrt{3}a}$ are related by a reciprocal lattice vector so we need only consider the degeneracy structure along one of these lines. We shall now examine the presence and flow of the degeneracies along each of these high-symmetry lines as the lattice spacing to wavelength ratio is varied.

We can see from figure 4.5 above that there are at least four C-points at all ratios of the lattice spacing to wavelength. These C-points occur in two pairs of two along the high symmetry lines $k_y = 0$ (top left) and $k_x = -\frac{\pi}{a}$ (top right). These four

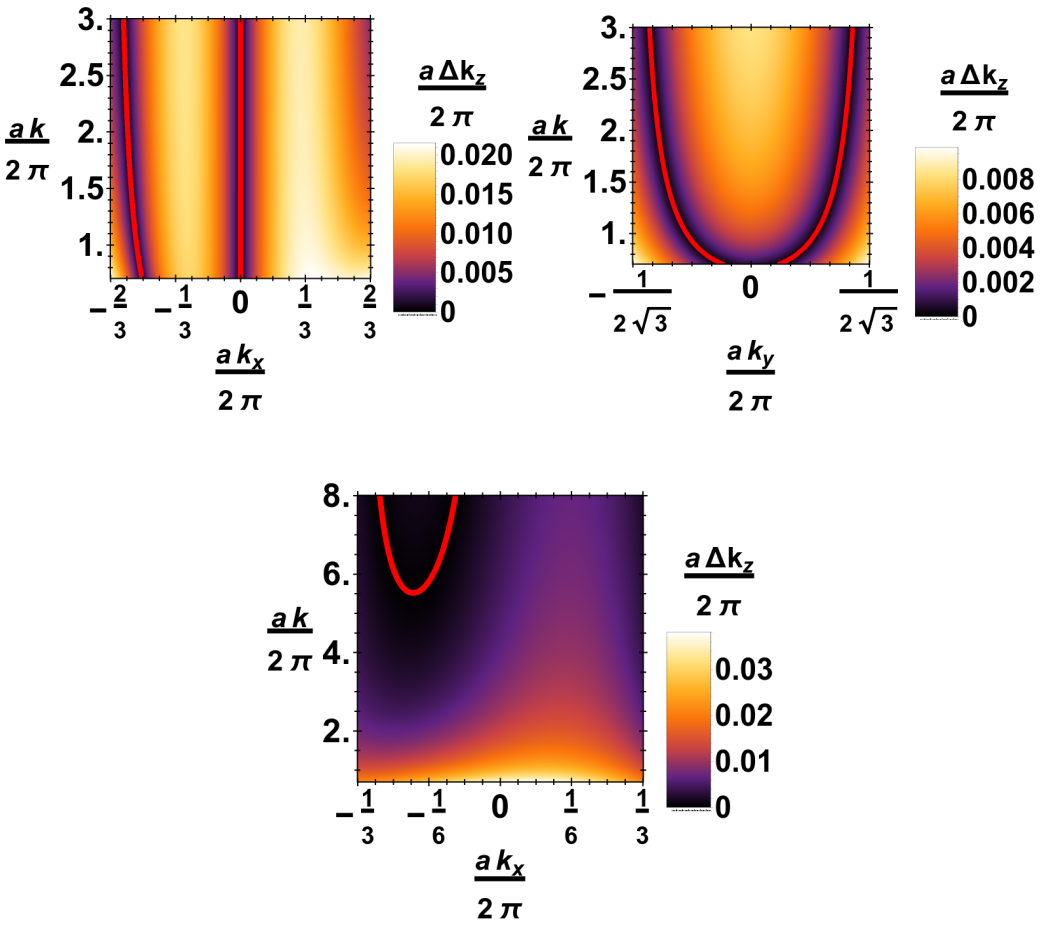

FIGURE 4.5: Three density plots representing the splitting of the bands of the iso-frequency surfaces. Each plot shows how the splitting of the bands varies with the lattice spacing to wavelength ratio. Each of these plots is along a high symmetry line of the first Brillouin zone. The high symmetry lines are $k_y = 0$ (top left), $k_x = -\frac{\pi}{a}$ (top right) and $k_y = \frac{2\pi}{\sqrt{3}a}$ (bottom). Contours representing C-points are superposed on each plot in red.

C-points are readily identifiable in figure 4.4. There is also an emergence of extra degeneracies along the line $k_y = \frac{2\pi}{\sqrt{3}a}$ (bottom) at high lattice spacing to wavelength ratio. We did not display the corresponding plot along the line $k_x = \frac{\pi}{a}$ as no degeneracies appear along this line. To assess what the topological indices of the emergent C-points are we can look at a plot of the vector field at a lattice spacing to wavelength ratio following their emergence.

In figure 4.6 we can see there are now six C-points in the first Brillouin zone. Looking at the vector field around each of the intersections along the line $k_y = \frac{2\pi}{\sqrt{3}a}$ allows us to determine the topological index of the extra degeneracies. The C-point closer to the K_3 zone corner has positive local circulation while the other one has negative local circulation. A clear picture of the degeneracy structure of these

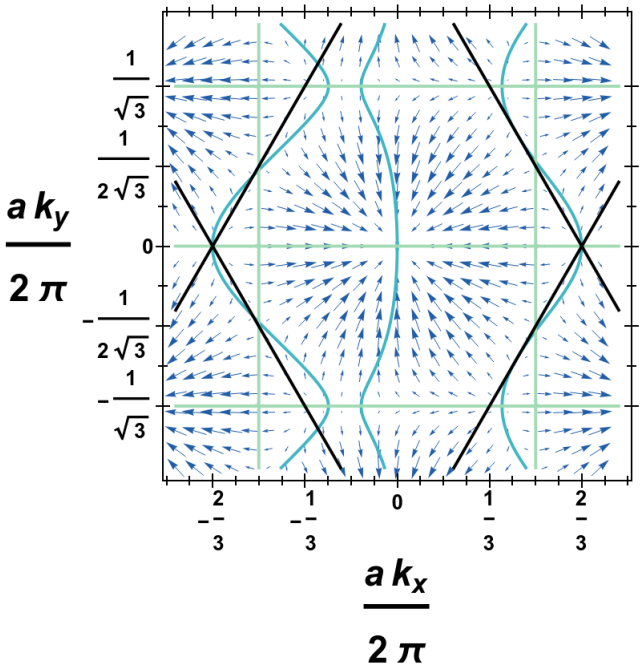

FIGURE 4.6: The emergence of extra structure in the highly paraxial regime. This extra structure is in the form of a pair of C-points along the $k_y = \frac{2\pi}{\sqrt{3}a}$ line. The lattice spacing to wavelength ratio considered is $a/\lambda = 7$.

triangular photonic crystal models has now been established. There are at most six C-points over this set of parameters of the lattice Hamiltonian. This means that the Chern number of this model is $C \in \{-3, -2, -1, 0, 1, 2, 3\}$. The ratio of the maximum number of degeneracies for triangular patterned photonic crystals compared to those of the square patterned crystals follows the ratio of the coordination number of the two lattices. We now turn to establishing whether this lattice Hamiltonian model is a qualitatively accurate descriptor of triangularly patterned photonic crystals.

4.3.2 Comparison to Simulations of Triangular Photonic Crystal Structures

To test the validity of the lattice Hamiltonian model $\underline{\underline{B}}_{\blacktriangle}(\mathbf{k})$ we shall compare its predictions to a numerical bandstructure calculation, using the frequency-domain plane-wave method [117]. We focus on the number and locations of degeneracies in the absence of optical activity as these are the crucial quantity for determining the Chern number once optical activity is introduced. We specifically consider a biaxial dielectric in which cylindrical air holes have been drilled to form a triangular lattice of the same form as in section 4.2.

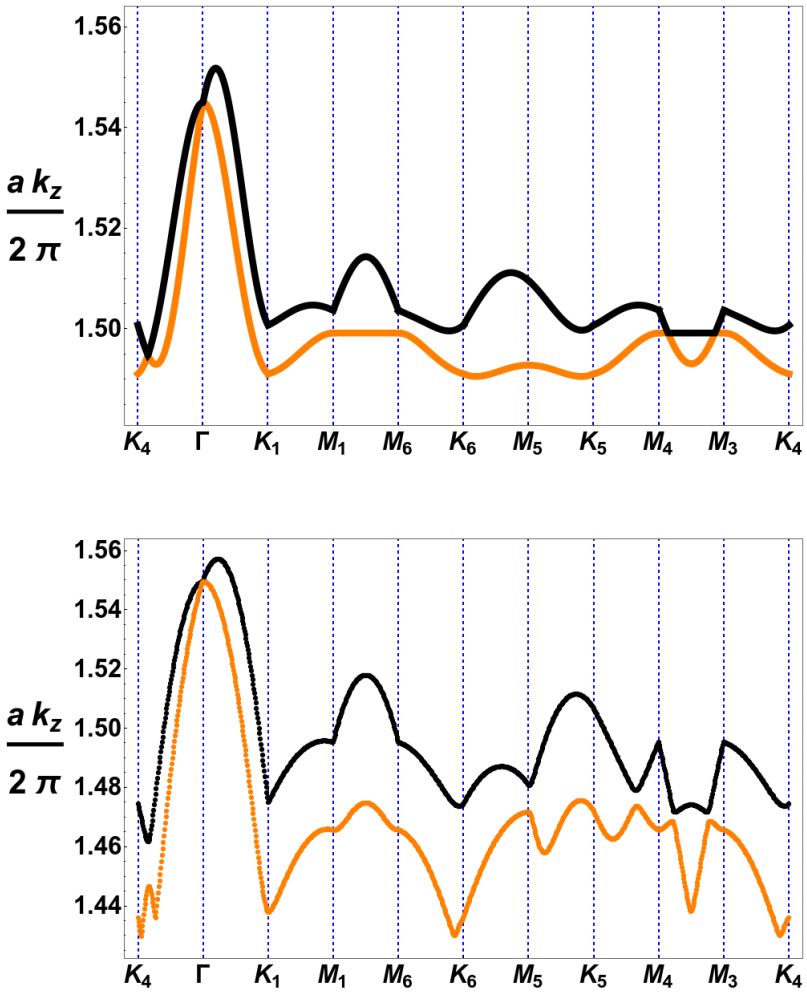

FIGURE 4.7: A comparison between the iso-frequency surfaces generated from the lattice Hamiltonian (top) and those generated from a frequency domain plane-wave simulation (bottom) for a triangular geometry. The iso-frequency surfaces are plotted as a path along high-symmetry lines of the first Brillouin zone is followed. These surfaces are compared at $ka \simeq 3.1\pi$. The plane-wave simulation has cylindrical air holes in the dielectric background. The radius of the air holes considered is $r = 0.15a$.

Figure 4.7 shows two iso-frequency surfaces plotted following a path along high symmetry lines of the first Brillouin zone. The top plot is that produced from the Hamiltonian $\underline{\underline{B}}_{\blacktriangle}(\mathbf{k})$, and the bottom plot is the result of the numerical simulation. These surfaces are compared at $ka \simeq 3.1\pi$ such that we are in a regime where the Hamiltonian $\underline{\underline{B}}_{\blacktriangle}(\mathbf{k})$ predicts that there is four C-points in the first Brillouin zone. Comparing the two plots we note the similarity in the overall morphology of the bands between each approach. As was the case for the square photonic crystals, the Hamiltonian approach underestimates the overall dispersion of the surfaces as well as the polarisation splitting of the bands. Potentially more significantly, however, is that the numerical simulation lacks the additional C-points along the high symmetry lines where their presence was predicted by the Hamiltonian model. We

therefore turn to examine the iso-frequency surfaces from the numerical simulation over the entire Brillouin zone. This will allow us to determine whether the expected C-points are completely absent or merely not confined to the high symmetry lines.

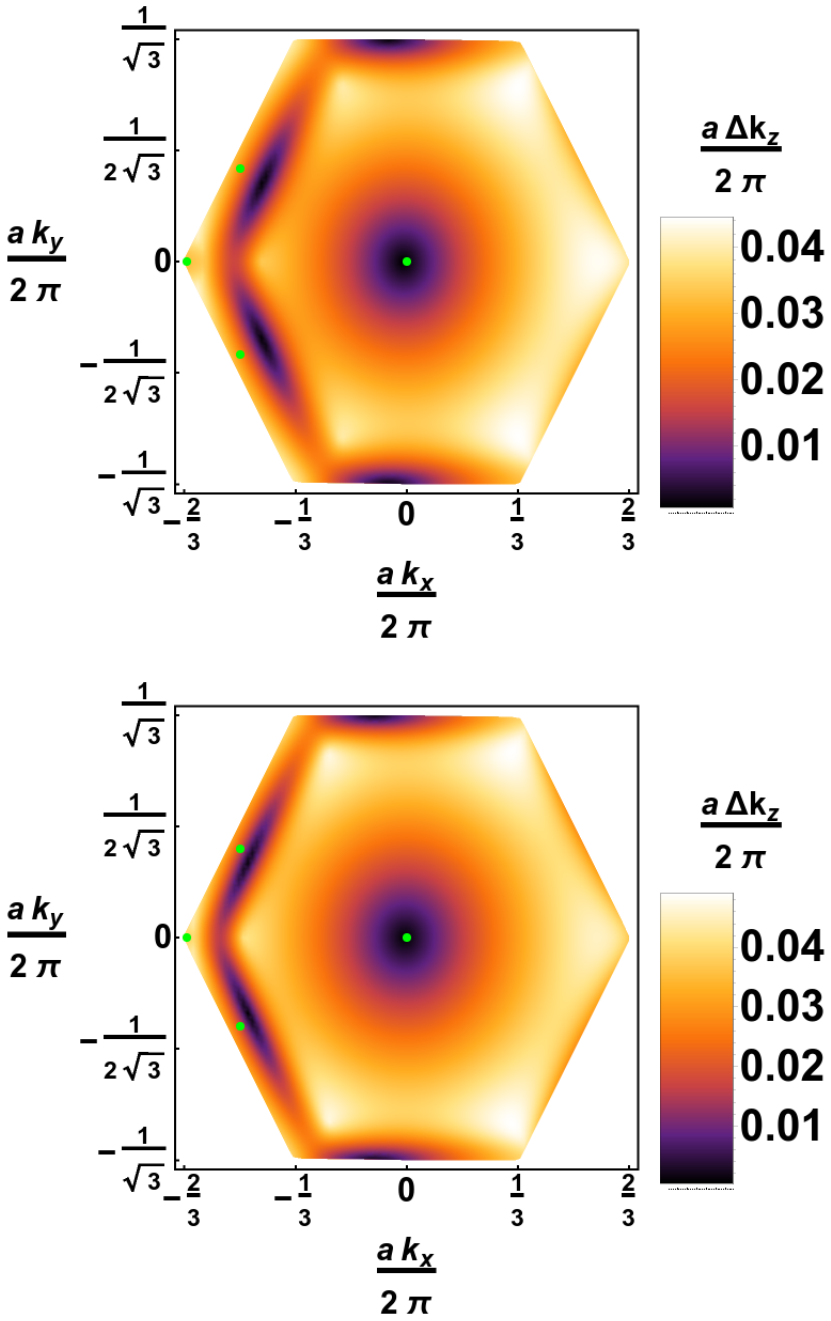

FIGURE 4.8: Two density plots showing the splitting of the two most paraxial bands of the iso-frequency surface computed from a frequency-domain plane-wave calculation. Each density plot considers a different frequency. The splittings are plotted over the hexagonal first Brillouin zone. The overlaid green points are the C-point locations at that frequency from the parxial theory.

Figure 4.8 shows two density plots where the splitting of the bands of the iso-frequency surfaces from the numerical simulations are represented. Each plot

considers a different frequency; in the top plot we considered $ka = 1.93854 \times 2\pi$ while in the bottom plot we choose $ka = 1.48397 \times 2\pi$. For each frequency we have marked the C-point locations predicted by the Hamiltonian $\underline{\underline{B}}_{\blacktriangle}(\mathbf{k})$ by green points. In each instance we observe what appears to be four degeneracies over the entire Brillouin zone. The numerical simulations feature one degeneracy at the zone centre, one near the top/bottom edge of the Brillouin zone and two more towards the M_3 and M_4 face centres. These two C-points close to the M_3 and M_4 face centres can be identified with those of the Hamiltonian which appeared along the $k_x = -\frac{\pi}{a}$ line. The difference in the C-point location between the final C-point of the Hamiltonian $\underline{\underline{B}}_{\blacktriangle}(\mathbf{k})$, which is close to K_4, and that of the numerical solution, which is close to the top/bottom edge of the Brillouin zone, appears substantial. We however note that the point K_4 is related to both K_2 and K_6 by reciprocal lattice vectors so that the location difference is actually much less significant. The numerical simulations clearly indicate that the C-points resist being pinned to high symmetry lines contrary to what the lattice Hamiltonian $\underline{\underline{B}}_{\blacktriangle}(\mathbf{k})$ predicted. We attribute this difference to the different treatment of scattering and the omission of higher order terms in the paraxial Hamiltonian of section 2.6. Nevertheless the model correctly predicts the number of C-points of the iso-frequency surfaces as well as the approximate locations of these C-points. We therefore argue that the Hamiltonian $\underline{\underline{B}}_{\blacktriangle}(\mathbf{k})$ will produce a similar topological phase diagram to that which a numerical simulation would produce. Hence we shall turn to using $\underline{\underline{B}}_{\blacktriangle}(\mathbf{k})$ to examine the topological phase diagram upon the introduction of one of two kinds of optical activity.

4.4 Photonic Crystals Composed of Biaxial Faraday Effect Materials

The first form of optical activity that we shall consider is the Faraday effect. Upon introduction of a non-zero magnetic field in a general direction, the degeneracies of the iso-frequency surfaces are lifted and the polarisation states of each surface become generally elliptical. Without loss of generality we shall assume that the maximum splitting due to the magnetic field occurs along the direction in which the field is applied. Depending on the orientation of the magnetic field, L-lines can appear in the first Brillouin zone. Due to periodicity these L-lines always appear in such a way that any reciprocal lattice vector translation crosses an even number of L-lines. These L-lines separate regions of one handedness of elliptical polarisation from regions which have the opposite handedness. If the magnetic field is such that odd number of L-lines separate C-points of different topological index then this is an orientation of the magnetic field which can result in a non-zero Chern number [89] as we now explore.

4.4.1 Examination of Topological Phase Diagrams

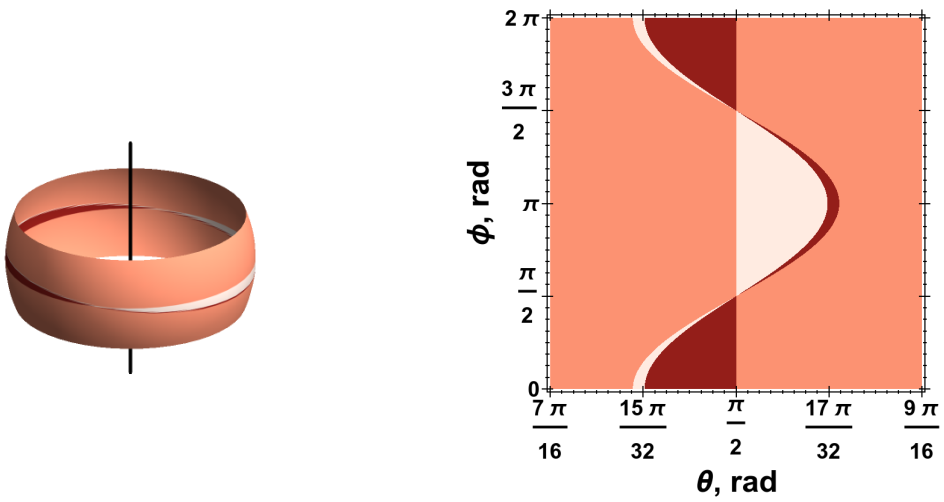

FIGURE 4.9: Phase diagrams representing the Chern number by colour of a triangularly patterned photonic crystal. The photonic crystal is composed of biaxial Faraday effect material. The phase diagram is plotted in the space of the external magnetic field application direction (θ, ϕ). The colours represent $C = 0$ (mid pink) and $C = \pm 1$ (dark or light pink). The figure on the left is a wrapping of the figure on the right onto a section of the surface of a sphere. The black line in the left figure represents the optic axis direction of the biaxial material.

In figure 4.9 we see two plots showing the Chern number by colour of a triangularly patterned photonic crystal composed of biaxial Faraday effect material. The plots are in the space of the direction of the externally applied magnetic field (θ, ϕ); where θ is measured from the optic axis direction of the homogeneous material, i.e. $\theta = \frac{\pi}{2}$ corresponds to applying the magnetic field in a plane perpendicular to the optic axis direction. In figure 4.9 we have calculated the Chern number using the method of Sticlet et al. [23]. We see that non-zero Chern numbers (light and dark pink) are achievable. These non-zero Chern numbers occur for a range of field application directions close to perpendicular to the optic axis. In these figures we have considered a lattice spacing to wavelength ratio $\frac{a}{\lambda} = 0.8$, for which there are four C-points. The bounding contours of these topological phases then represent the gap closing at each of these four lifted degeneracies. Each of these four contours are geodesics connecting the antipodal magnetic field application directions $(\theta, \phi) = (\frac{\pi}{2}, \frac{\pi}{2})$ and $(\theta, \phi) = (\frac{\pi}{2}, \frac{3\pi}{2})$. If the magnetic field is applied in either of these directions the gap closes at all of the C-points. These geodesics are each described by the equation (3.10) with suitable constants c_1 and c_2. The $\theta = \frac{\pi}{2}$ geodesic corresponds to the gap closing at the Γ point, the inner geodesic contour which weaves above and below the equator and separates the $C = \pm 1$ phases corresponds to the gap closing at both the C-points along the line $k_x = -\frac{\pi}{a}$ simultaneously. The outer geodesic contour represents the gap closing at the C-point

towards the K_4 zone corner. In comparison to the corresponding phase diagrams for square patterned photonic crystals (figure 3.9), there are several differences. Firstly, the range of permissible angles for triangular patterning is much larger than in the square patterned cases. Additionally the location of the non-zero regions have been reflected across the $\theta = \frac{\pi}{2}$ line and the sign of the Chern number has also changed. We shall examine these differences in greater detail in section 4.6.

We now wish to examine the evolution of these phase diagrams as the parameters of the photonic crystal are varied. We will consider variation of both the strength of biaxiality and the lattice spacing to wavelength ratio. For each of these variations the shrinking or increasing of the topologically non-trivial phase can be understood in the context of how the variation alters the ratio of c_2/c_1 in the geodesic equation (3.10).

4.4.2 Variation of Topological Phase Diagrams with Degree of Biaxiality

The first parameter we consider the variation of is the degree of biaxiality. Initially we shall examine four snapshots of the topological phase diagrams in the space of the magnetic field application direction. Each of these snapshots considers a different set of principal dielectric constants.

Figure 4.10 shows an array of topological phase diagrams representing the Chern number by colour. In each case the biaxial cone semi-angle, A, is stated above the plot. We see that the weaker the biaxiality the larger the region of non-zero Chern numbers. This is the opposite trend to that which was seen for square photonic crystals in figure 3.10 and is reflected by the decreasing magnitude of the ratio c_2/c_1 in the geodesic equation (3.10) with increasing biaxiality. To further assess this behaviour we shall now consider the effect on the phase diagram of the continuous variation of the degree of biaxiality.

Figure 4.11 examines the effect on the topological phase diagram of the continuous variation of two of the principal dielectric constants with the median one held fixed. The black overlaid contours represent constant values of the biaxial cone semi-angle in 2° increments from bottom to top of the figure. From this figure we can see the size of the topologically non-trivial phase exhibits a complicated expansion and contraction behaviour with increasing strength of biaxiality.

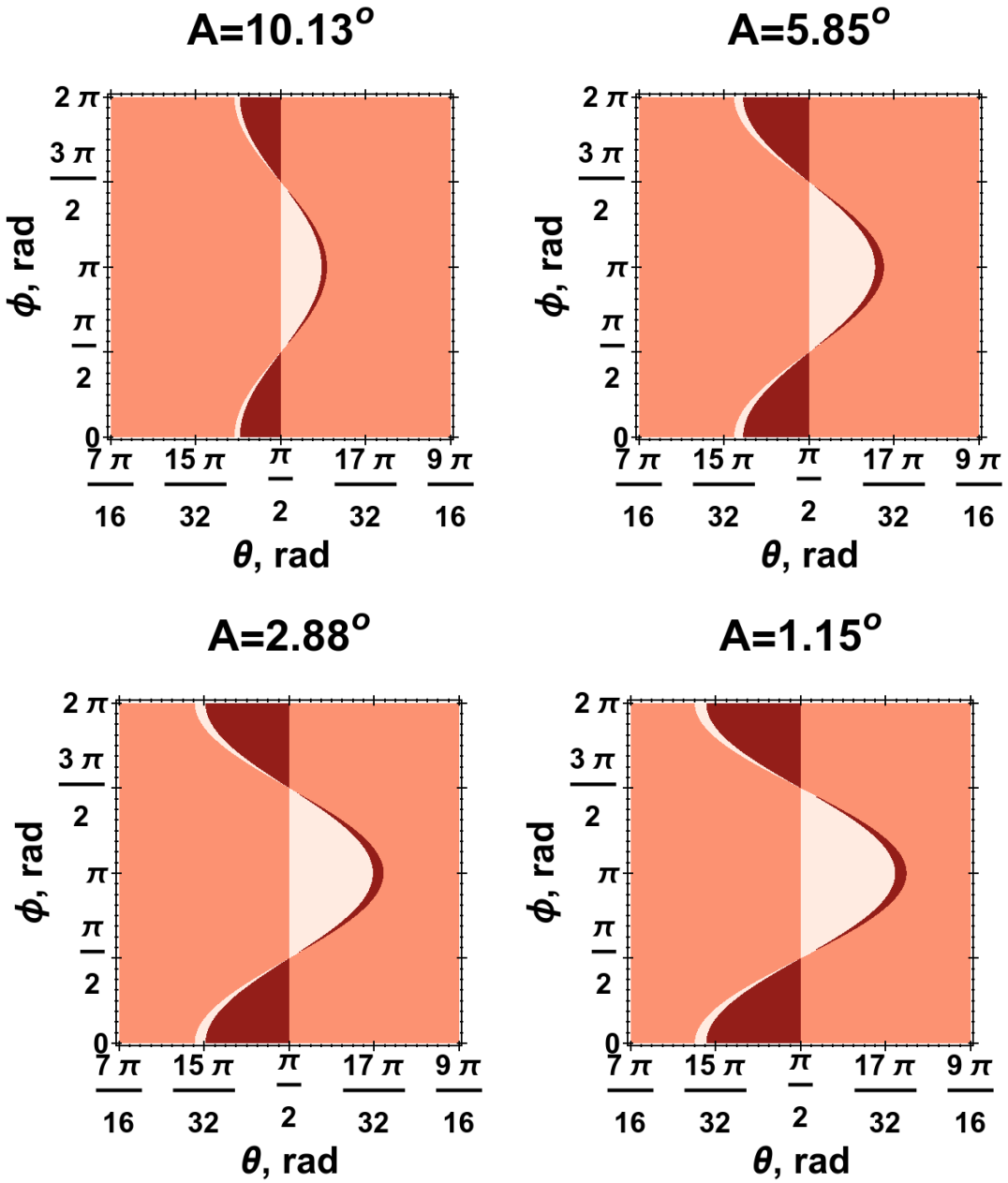

FIGURE 4.10: A panel of four phase diagrams representing the Chern number by colour of triangularly patterned photonic crystals. The photonic crystals are composed of biaxial Faraday effect material. Each diagram is for a different degree of biaxiality. In each case the biaxial cone semi-angle is stated above the diagram. The principal dielectric constants $(\epsilon_1, \epsilon_2, \epsilon_3)$ are (from left to right and then top to bottom) (i) $(2, 3, 4)$, (ii) $(2, 2.5, 3)$, (iii) $(2.25, 2.5, 2.75)$ and (iv) $(2.4, 2.5, 2.6)$.

4.4.3 Variation of Topological Phase Diagrams with Lattice Spacing to Wavelength Ratio

The other parameter we can vary is the lattice spacing to wavelength ratio of the photonic crystal. As before we study four snapshots of the topological phase diagram

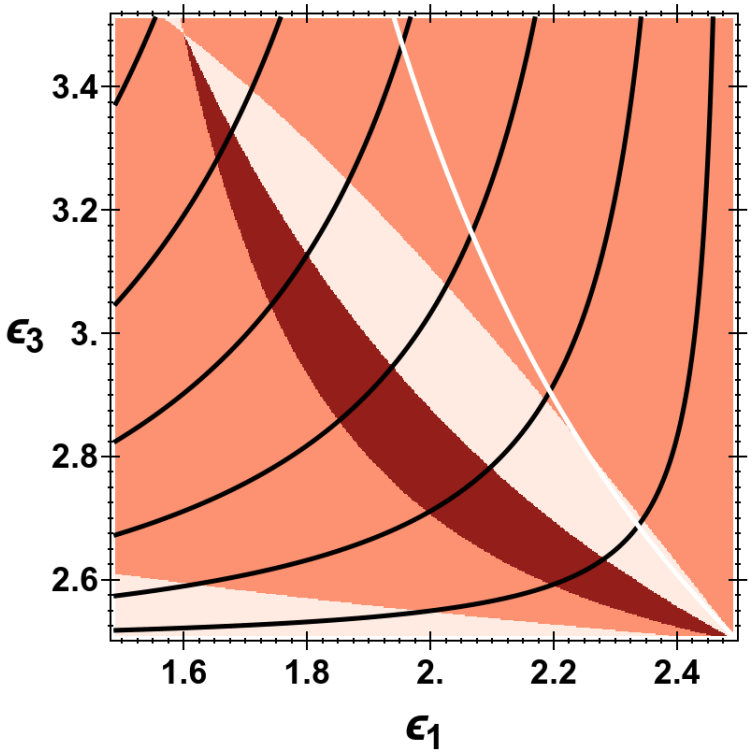

FIGURE 4.11: The Chern number at magnetic field application direction $(\theta, \phi) = (\frac{33\pi}{64}, \pi)$ of a triangularly patterned photonic crystal. The photonic crystal is composed of biaxial Faraday effect material. The black contour lines are lines of constant cone semi-angle A. The lowest of these contour lines is $A = 2^\circ$ and each higher one is 2° more. The white contour line is $\alpha = \beta$.

in the space of the magnetic field application direction. Each of these snapshots considers a different lattice spacing to wavelength ratio.

Figure 4.12 shows an array of topological phase diagrams representing the Chern number by colour. In each case the lattice spacing to wavelength ratio is stated above the plot. We see that the higher this ratio the smaller the region of non-zero Chern numbers. This is the same trend as was seen for square patterned photonic crystals. As in that case, the diminishing of the topologically non-trivial phase results from the decreasing magnitude of the ratio of c_2/c_1 in the geodesic equation for each of the C-points. This occurs because the iso-frequency surface dispersion becomes increasingly dominated by the lower-order terms as $\frac{a}{\lambda}$ increases. Additionally we observe that as $\frac{a}{\lambda}$ increases that a more equitable distribution of the $C = \pm 1$ phases on each side of the $\theta = \frac{\pi}{2}$ line results.

Figure 4.13 examines the effect on the topological phase diagram of the continuous variation of the lattice spacing to wavelength ratio. From this figure we can see the size of the topologically non-trivial phase contracts with increasing $\frac{a}{\lambda}$. We additionally see that the area of the topologically non-trivial phase closer to the

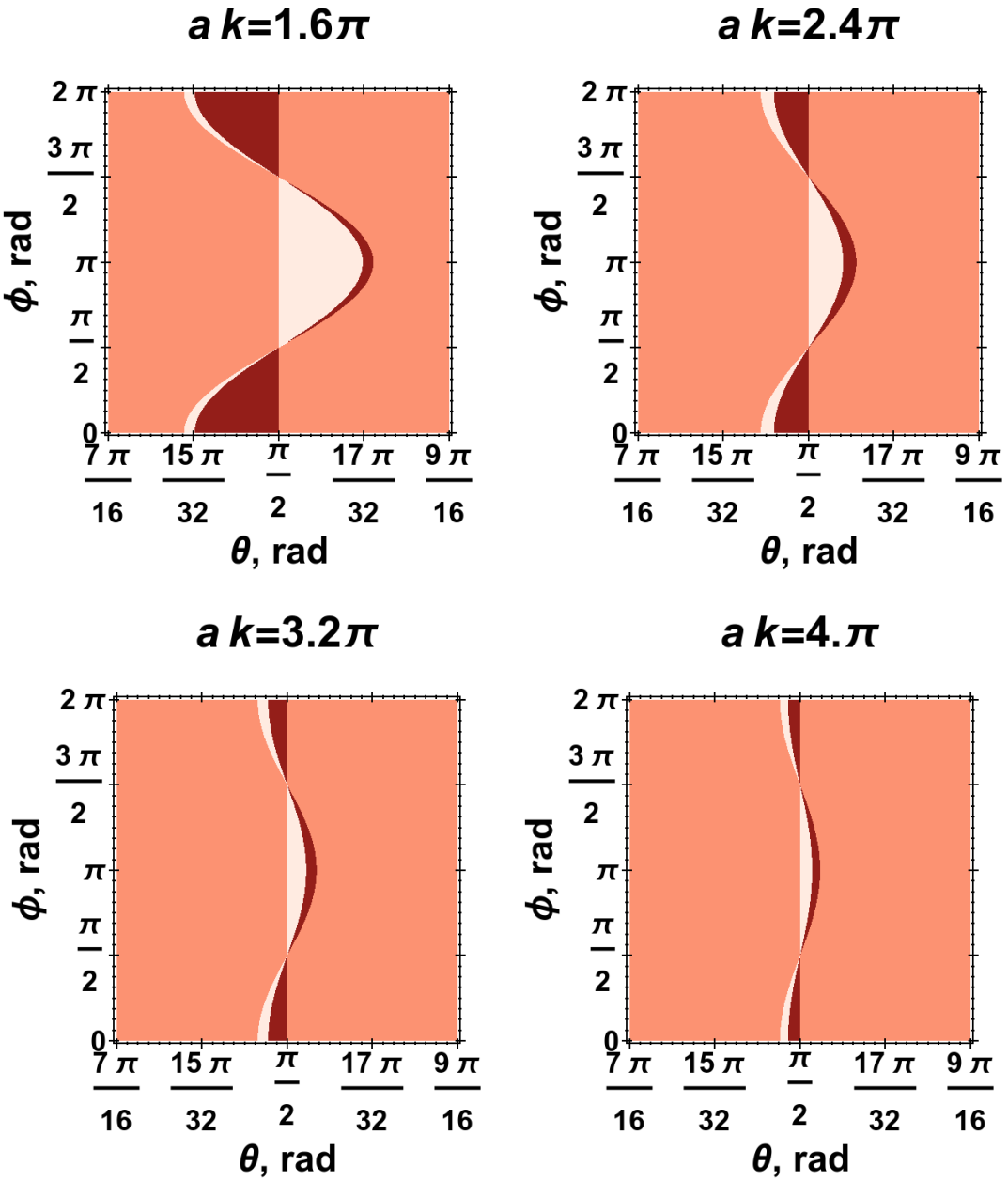

FIGURE 4.12: A panel of four phase diagrams representing the Chern number by colour of triangularly patterned photonic crystals. The photonic crystals are composed of biaxial Faraday effect material. Each diagram is for a different lattice spacing to wavelength ratio. In each case this ratio is stated above the diagram.

$\theta = \frac{\pi}{2}$ equator contracts at a faster rate compared to that of the opposite sign.

We have now developed a detailed understanding of the topological phase diagram of triangularly patterned photonic crystals composed of biaxial Faraday effect dielectrics. This phase diagram depends on six parameters which together fix the locations of the C-points and L-lines of the iso-frequency surfaces. The topological phase diagram is therefore a complicated hypersurface in the space of these parameters, nonetheless we have developed an understanding of it by examining

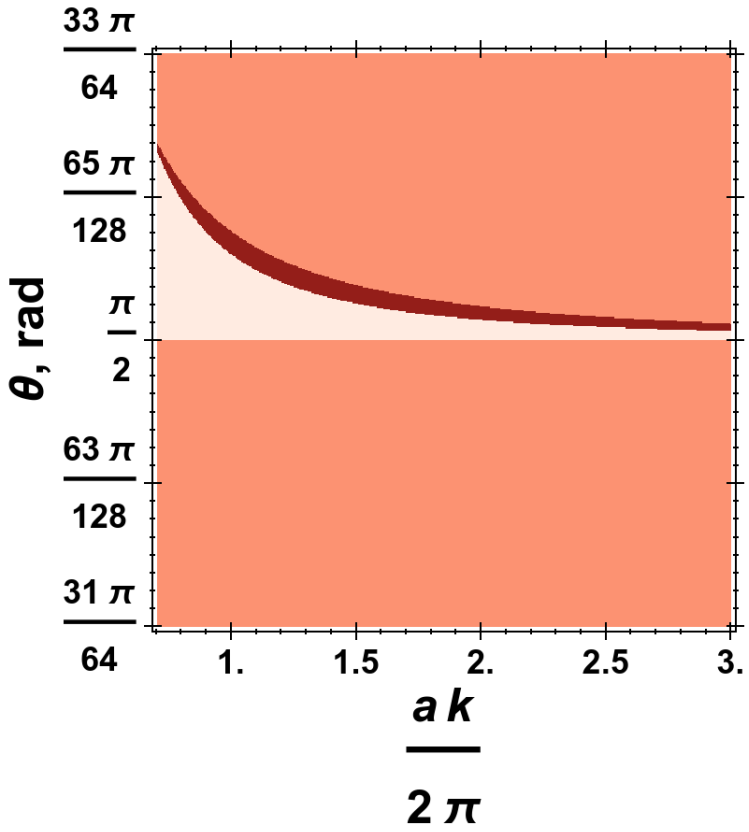

FIGURE 4.13: A phase diagram representing the Chern number by colour of a triangularly patterned photonic crystal. The photonic crystal is composed of biaxial Faraday effect material. The phase diagram examines the effect of continuous variation of the lattice spacing to wavelength ratio. The lattice spacing to wavelength ratio is plotted against the magnetic field direction θ with $\phi = \pi$ held fixed.

representative slices. The immediate conclusion, and one which differs completely from the result of the homogeneous material seen in subsection 2.4.3, is that one can achieve a non-zero Chern number. This non-zero Chern number occurs when the magnetic field is applied for a band of directions almost perpendicular to the optic axis direction. Once the presence of a topologically non-trivial surface in this hyperspace has been established, we study how the volume of that surface varies in different directions in parameter space. This analysis has led us to conclude that, with regard to maximising the size of the topologically non-trivial region, the lattice spacing to wavelength ratio should be as small as possible. The overall area of the topologically non-trivial parameter regimes are larger than that which was seen for the corresponding square patterned systems. Additionally, the topologically non-trivial areas of these triangularly patterned structures exhibited a complicated behaviour as the strength of the biaxial constituents was varied.

4.5 Photonic Crystals Composed of Chiral Biaxial Materials

We now consider chiral biaxial materials as the constituents of the triangularly patterned structures. The introduction of chirality has the potential to lift the degeneracies of the iso-frequency surfaces. If this proves to be the case the iso-frequency surfaces can be assigned a Chern number. Whether or not this invariant is non-zero depends on the parameters of the photonic crystal. Depending on the form of the chirality there are between five and ten parameters determining the Chern numbers of the iso-frequency surfaces. We shall initially focus on the simpler forms of chirality, those of the orthorhombic crystals, and then progress to those of increasing complexity.

Before examining the different forms of chirality though it will be helpful to determine which components of the chirality tensor are relevant to $b_{\blacktriangle z}$ at each of the C-points. As in chapter 3 we shall decompose the symmetric chirality tensor $\underline{\underline{G}}$ into $\underline{\underline{G}} = \gamma_C \underline{\underline{\tilde{G}}}$. For the two C-points which feature along the line $k_y = 0$ the only relevant components are $\tilde{G}_{11}$, $\tilde{G}_{13}$ and $\tilde{G}_{33}$. For the other two C-points, which appear along the line $k_x = -\frac{\pi}{a}$, the component $\tilde{G}_{22}$ is also relevant in determining $b_{\blacktriangle z}$. This means that the parameter space to be explored is potentially up to eight dimensions depending on the form of chirality. This corresponds with the square patterned photonic crystal case where the parameter space was also eight dimensional.

4.5.1 Forms of Chirality

Rhombic Pyramidal

For rhombic pyramidal dielectrics there is one non-zero component of the symmetric chirality tensor $\underline{\underline{\tilde{G}}}_{abc}$ featuring on the off-diagonal. This tensor is related to that in the principal axes frame $\underline{\underline{\tilde{G}}}_{123}$ by a permutation to appropriately match up the crystallographic axes and the principal dielectric axes. Considering photonic crystals formed from these materials, under any of the possible permutations of axes, the resulting Chern number is zero. There being only one non-zero component of $\underline{\underline{\tilde{G}}}$ simply does not give the flexibility to achieve different signs of $b_{\blacktriangle z}$ at the different C-points.

Rhombic Disphenoidal

For rhombic disphenoidal structures the chirality tensor is diagonal with distinct entries. Considering photonic crystals patterned out of rhombic disphenoidal materials, it is possible to achieve a non-zero Chern number for the iso-frequency surfaces. The three non-zero components of $\underline{\underline{\tilde{G}}}$, for this set of C-point locations are sufficient to achieve a topologically non-trivial result. This contrasts with the

corresponding result for the lattice Hamiltonian model of square patterned photonic crystals.

Domatic

For domatic materials the symmetric chirality tensor features two non-zero distinct entries on the off-diagonals. Considering photonic crystals patterned out of domatic materials, it is not possible to achieve a non-zero Chern number for the iso-frequency surfaces. The zero Chern number in this case is irrespective of which of the dielectric axes correspond to the b crystallographic axis. Since $\tilde{G}_{12}$ and $\tilde{G}_{23}$ do not contribute to $b_{\blacktriangle z}$ along the line $k_y = 0$ and $k_x = -\frac{\pi}{a}$ we are again effectively in a situation where only one component of $\underline{\underline{\tilde{G}}}$ is relevant. This case is then similar to that of chirality of the rhombic pyramidal form with one component of $\underline{\underline{\tilde{G}}}$ lacking the flexibility to achieve a non-zero Chern number.

Sphenoidal

For sphenoidal materials the symmetric chirality tensor features three distinct entries on the diagonal as well as one off-diagonal entry. Considering photonic crystals patterned out of sphenoidal materials, it is possible to achieve a non-zero Chern number for the iso-frequency surfaces. This is unsurprising as the possible rhombic disphenoidal chirality tensors are a subset of the sphenoidal ones. As such in the two instances where the 2 dielectric axis does not corresponds to the b crystallographic axis the topological phase diagrams are the same as for the rhombic dispehnoidal materials. For the other possible configuration, where the 2 dielectric axis and the b crystallographic axis correspond, the topological phase diagram will be richer than that of the rhombic disphenoidal as the effects of $\tilde{G}_{13}$ need to be considered.

Pedial

All the previous cases represent subsets of what can be seen in pedial crystal structures. Owing to this the possibility of a non-zero Chern number for the iso-frequency surfaces of triangularly patterned pedial materials follows from those of the rhombic disphenoidal and sphenoidal cases. In fact within the lattice Hamiltonian model the topological phase diagrams of the sphenoidal (in the latter configuration) and pedial cases will be the same.

Beyond the lattice model we expect these predictions to be a conservative estimate of the topological phase diagrams that are possible. As the C-point locations from the numerical simulations resisted pinning to high symmetry lines it is likely

that $\tilde{G}_{12}$ and $\tilde{G}_{23}$ would be relevant at at least some of the C-points. For this reason we would expect some domatic crystals could have non-zero Chern numbers also.

4.5.2 Examination of Topological Phase Diagrams

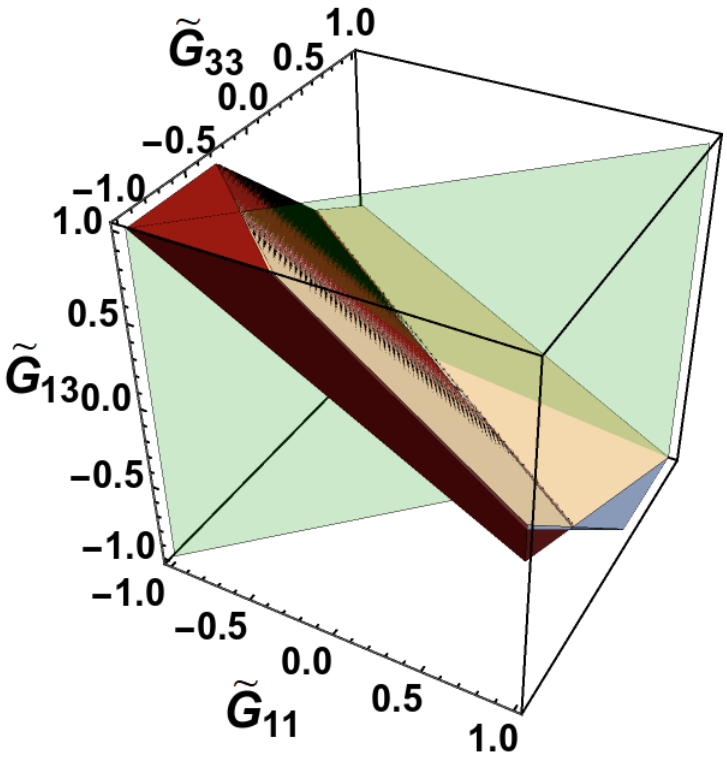

FIGURE 4.14: A 3D phase diagram representing the regions of non-zero Chern number by colour of a triangularly patterned photonic crystal. The photonic crystal is composed of chiral biaxial material. The form of chirality is either that of a sphenoidal or pedial structure. In the case of a sphenoidal material we have taken the b crystallographic axis and the 2 dielectric axis to coinceide. The darker (lighter) pink region represents a Chern number $C = 1$ ($C = -1$). The black and grey regions represent $C = \pm 2$. The region of zero Chern number is left transparent. We fix $\tilde{G}_{22} = \tilde{G}_{11}$ for this plot. The plane $\tilde{G}_{11} = \tilde{G}_{33}$ is shown in green.

Henceforth we will focus on dielectrics with either the sphenoidal or pedial point groups. For the sphenoidal cases we consider that the 2 dielectric axis corresponds with the b crystallographic axis. The handedness of the C-points is determined by the four chirality tensor components $\tilde{G}_{11}$, $\tilde{G}_{22}$, $\tilde{G}_{33}$ and $\tilde{G}_{13}$. With this in mind we can examine the Chern number in the space of three of these four components. While doing this we shall fix the fourth component $\tilde{G}_{22}$ to be the same value as $\tilde{G}_{11}$.

Figure 4.14 plots the regions of non-zero Chern number in the space of the three aforementioned chirality tensor components. We immediately see that the

possibility of a non-zero Chern number, which was theorised earlier, can be realised. This realisation occurs in regions where the two components $\tilde{G}_{11}$ and $\tilde{G}_{33}$ have the same sign as each other and a different sign to $\tilde{G}_{13}$. The locations and shapes of the topologically non-trivial parameter regimes is somewhat similar to that seen in the square case in figure 3.14 although the division lines within this region are different and in this case we also have regions of $C = \pm 2$ also.

We shall now turn to assessing the variation of the phase diagrams as the other parameters of the photonic crystal are changed. As in section 4.4 we consider the variation of the principal dielectric constants and the lattice spacing to wavelength ratio of the photonic crystal. To facilitate a more direct assessment of the effect of the parameter variation we shall consider the green $2D$ planar slice of the parameter space shown in figure 4.14. The slice we consider is therefore $\tilde{G}_{11} = \tilde{G}_{22} = \tilde{G}_{33} \equiv \tilde{G}_i$ which, although artificial, is likely the easiest to examine due to the observations that followed from the examination of figure 4.14 in the preceding paragraph. We additionally relabel $\tilde{G}_{13} \equiv \tilde{G}_a$.

4.5.3 Variation of Topological Phase Diagrams with Degree of Biaxiality

The first parameter that we consider the variation of is the degree of biaxiality. Initially we shall examine four snapshots of the topological phase diagrams in the space of the isotropic chirality tensor components $\tilde{G}_i$ and anisotropic chirality tensor components $\tilde{G}_a$. Each of these snapshots considers a different set of principal dielectric constants.

Figure 4.15 shows an array of topological phase diagrams representing the Chern number by colour. In each case the biaxial cone semi-angle is stated above the plot. Although difficult to observe in figure 4.15, the stronger the biaxiality the larger the region of non-zero Chern numbers. This enlargement of the topologically non-trivial phase results from the increased displacement of the C-points from the face centres and zone corners of the Brillouin zone. This variation of the phase diagram is no where near as complex as the variation for biaxial Faraday effect photonic crystals in subsection 4.5.3. The comparative stability in this case follows from the quadratic dependence of the B polynomial (2.43) on propagation direction for chirality as compared to the linear dependence for the Faraday effect (2.42).

Figure 4.16 examines the effect on the topological phase diagram of the continuous variation of two of the principal dielectric constants with the median one held fixed. The black overlaid contours represent constant values of the biaxial cone semi-angle, increasing in 2° increments from bottom to top of the figure. From this figure we can see, much more directly than in figure 4.15, that the size of the topologically non-trivial phase increases with increasing strength of biaxiality. One

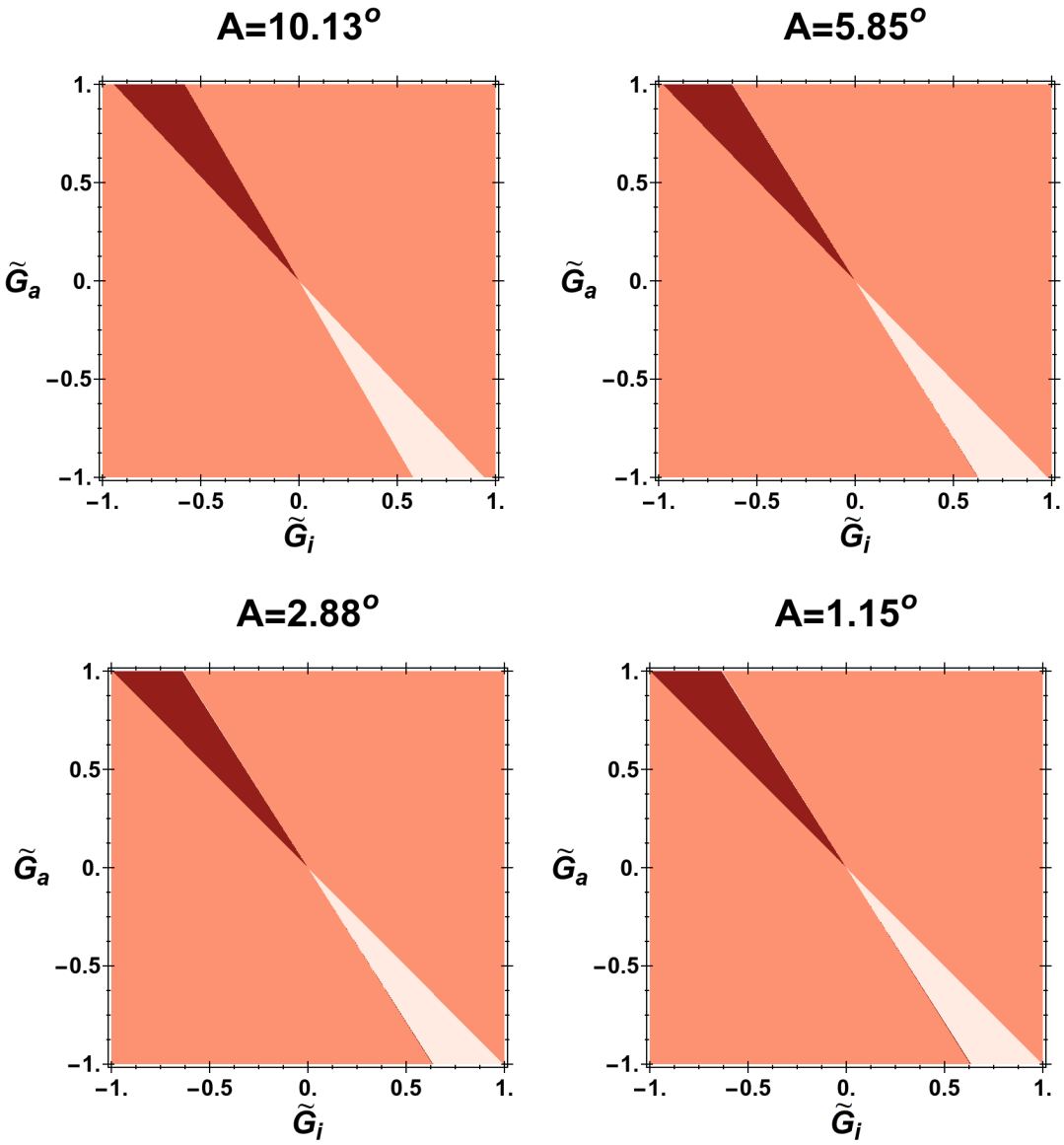

FIGURE 4.15: A panel of four phase diagrams representing the Chern number by colour of triangularly patterned photonic crystals. The photonic crystals are composed of chiral biaxial material. Each diagram is for a different degree of biaxiality. In each case the biaxial cone semi-angle is stated above the diagram. The principal dielectric constants $(\epsilon_1, \epsilon_2, \epsilon_3)$ are (from left to right and then top to bottom) (i) $(2, 3, 4)$, (ii) $(2, 2.5, 3)$, (iii) $(2.25, 2.5, 2.75)$ and (iv) $(2.4, 2.5, 2.6)$.

of the boundaries between the phases, for this set of parameters, approximately follows the yellow $\alpha = 3.5\beta$ contour line.

4.5.4 Variation of Topological Phase Diagrams with Lattice Spacing to Wavelength Ratio

The other parameter we vary is the lattice spacing to wavelength ratio. As before we study four snapshots of the topological phase diagram in the space of the isotropic

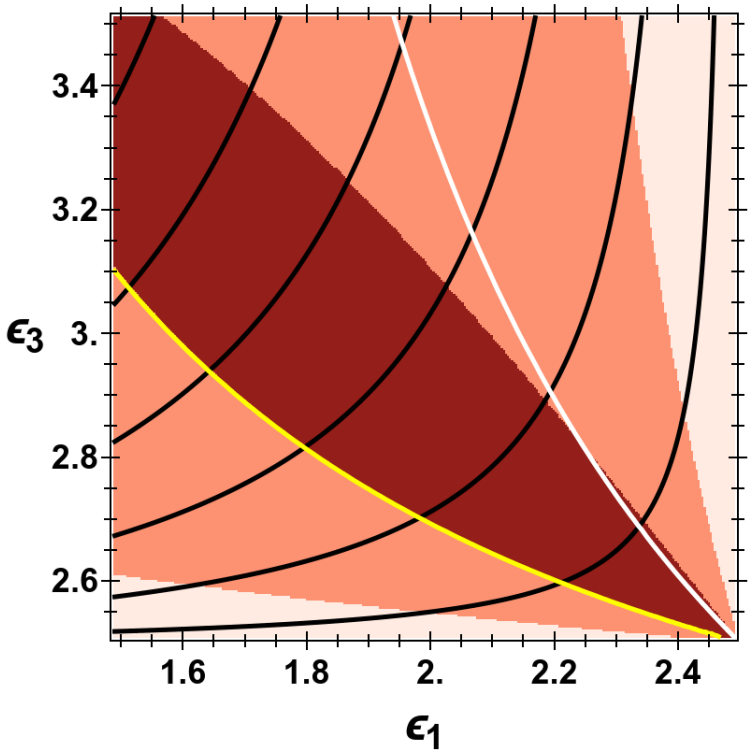

FIGURE 4.16: A phase diagram representing the Chern number by colour of a triangularly patterned photonic crystal. The photonic crystal is composed of chiral biaxial material of sphenoidal or pedial type. This phase diagram examines the effect of continuously varying the degree of biaxiality. The median principal dielectric constant is fixed at $\epsilon_2 = 2.5$ and the other two principal dielectric constants (ϵ_1, ϵ_3) are allowed to vary. The black contour lines are lines of constant cone semi-angle A. The lowest of these contour lines is $A = 2^\circ$ and each higher one is 2° more. The white contour line is $\alpha = \beta$ and the yellow one is $\alpha = 3.5\beta$. The isotropic and anisotropic chiralities are $(\tilde{G}_i, \tilde{G}_a) = (-0.5, 0.6)$.

chirality contribution $\tilde{G}_i$ and the anisotropic chirality contribution $\tilde{G}_a$. Each of these snapshots considers a different lattice spacing to wavelength ratio.

Figure 4.17 shows an array of topological phase diagrams representing the Chern number by colour. In each case the lattice spacing to wavelength ratio is stated above the plot. We see that the higher this ratio the smaller the region of non-zero Chern numbers. This diminishing of the topologically non-trivial phase results from the C-points being pushed towards the boundaries of the Brillouin zone. This occurs because the iso-frequency surface dispersion becomes increasingly dominated by the lower-order terms as $\frac{a}{\lambda}$ increases.

Figure 4.18 examines the effect on the topological phase diagram of the continuous variation of the lattice spacing to wavelength ratio. From this figure we can see the size of the topologically non-trivial phase contracts with increasing $\frac{a}{\lambda}$.

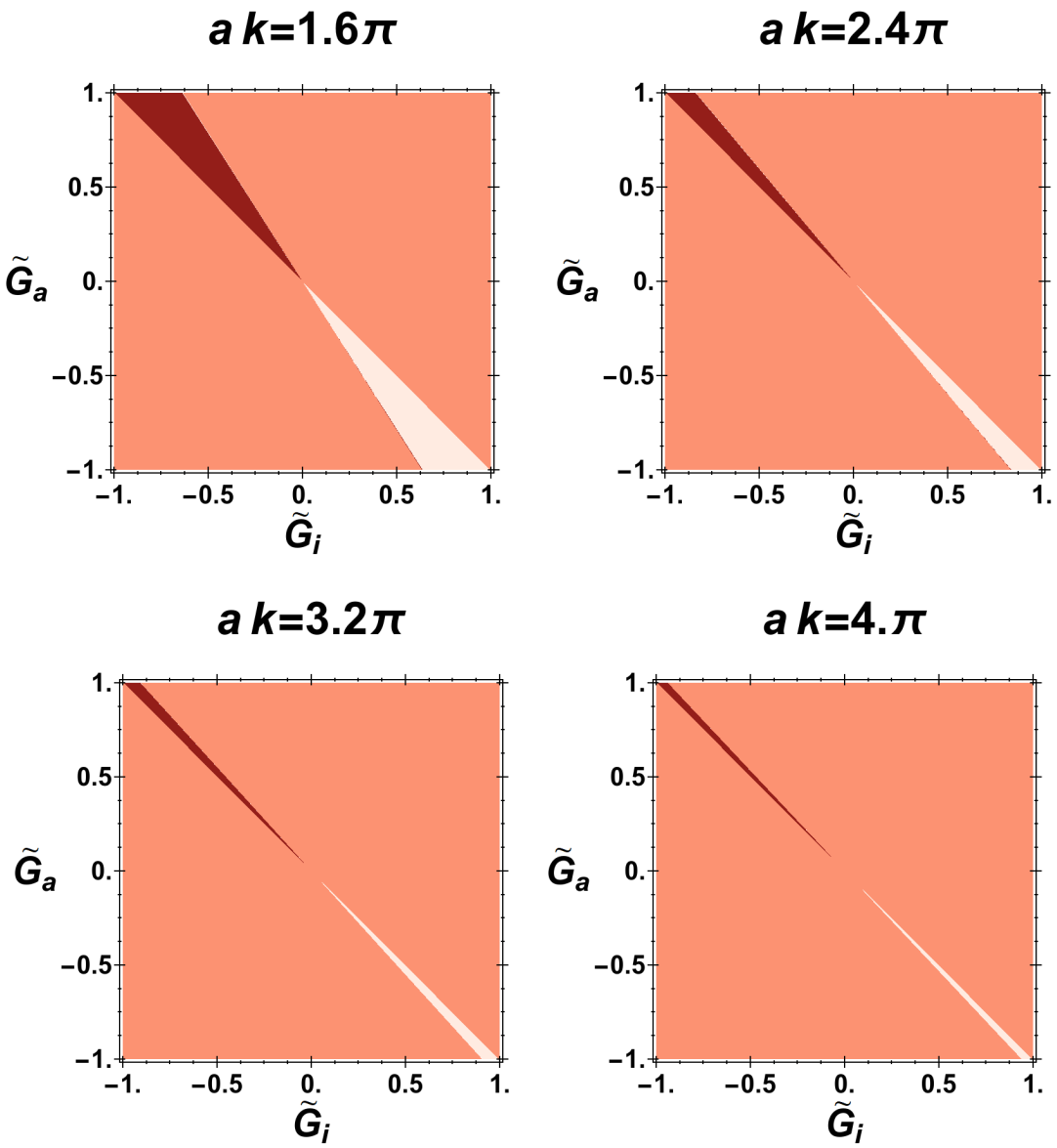

FIGURE 4.17: A panel of four phase diagrams representing the Chern number by colour of triangularly patterned photonic crystals. The photonic crystals are composed of chiral biaxial material. Each diagram is for a different lattice spacing to wavelength ratio. In each case this ratio is stated above the diagram.

We have now developed a detailed understanding of the topological phase diagram of triangularly patterned photonic crystals composed of chiral biaxial dielectrics. Within the lattice Hamiltonian model this phase diagram can depend on up to eight parameters depending on the form of chirality considered. These parameters together fix the locations of the C-points and L-lines of the iso-frequency surfaces. The topological phase diagram is therefore a complicated hypersurface in the space of these parameters. Nonetheless we have developed an understanding of these surfaces for each possible form of chirality. We discovered that, at least within the lattice model, non-zero Chern numbers are only possible for dielectrics of the

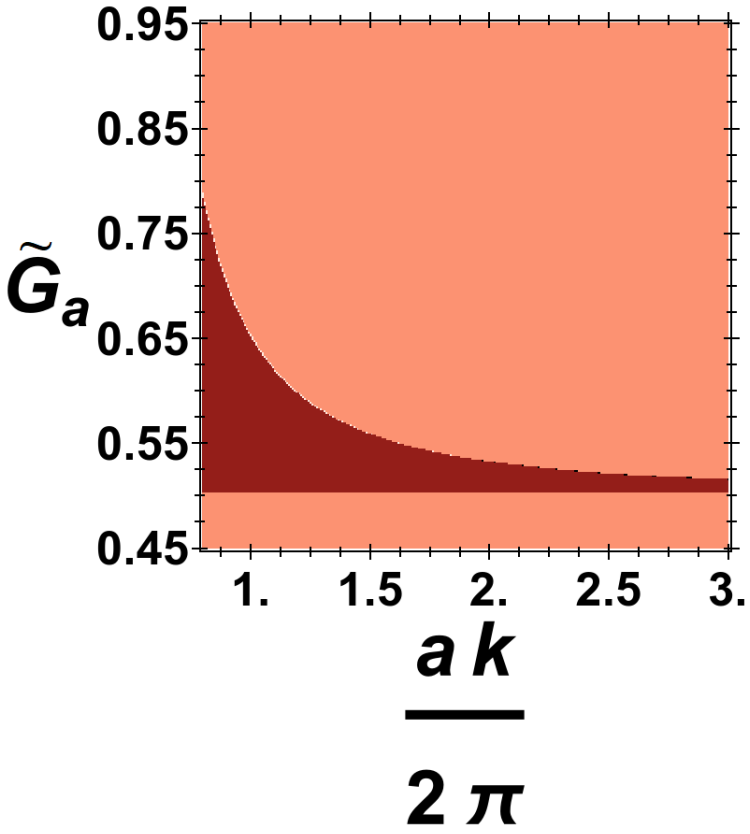

FIGURE 4.18: A phase diagram representing the Chern number by colour of a triangularly patterned photonic crystal. The photonic crystal is composed of chiral biaxial material. The phase diagram examines the effect of continuously varying the lattice spacing to wavelength ratio of the photonic crystal. The strength of the isotropic chirality is held fixed at $\tilde{G}_i = -0.5$.

rhombic dispenoidal, sphenoidal or pedial point groups. In the former instance the phase diagrams are hypersurfaces which vary in seven dimensions. This is also the case for two permutations of the sphenoidal point group structures. For the other permutation of the sphenoidal point group structure and for pedial type structures the phase diagrams depend on eight parameters. To understand these surfaces we have examined representative $2D$ and $3D$ slices of the full $8D$ parameter space. The appearance of non-zero Chern number in this space occurs when the isotropic chirality contributions $\tilde{G}_i$ and the anisotropic chirality contributions $\tilde{G}_a$ are close to equal in magnitude but differ in sign. Once the presence of a topologically non-trivial surface in this hyperspace has been established, we study how the volume of that surface varies in different directions in parameter space. This analysis has led us to conclude that, with regard to maximising the size of the topologically non-trivial region, the biaxiality should be as strong as possible and the lattice spacing to wavelength ratio as small as possible. In comparison to square patterned photonic crystals the realisation of non-zero Chern number regions for rhombic disphenoidal structures is unique to the triangular geometry, at least within

the lattice models. Additionally we saw that, for sphenoidal and pedial forms of chirality, although the location and shape of the topologically non-trivial area was somewhat similar to the square patterned cases, the boundaries within those areas were different. In the triangular geometry there were $C = \pm 2$ regions which were absent from the square patterned case. Beyond the lattice model it is likely the chirality tensor components $\tilde{G}_{12}$ and $\tilde{G}_{23}$ would be relevant and hence that domatic structures could also be topologically non-trivial, under the right conditions.

4.6 Comparison Between Square and Triangular Photonic Crystals

We shall now investigate the differences between the topological phase diagrams for triangularly patterned photonic crystals and those for square patterned photonic crystals in chapter 3. The deviations in the topological phase diagrams between the two geometries are much more pronounced when biaxial Faraday effect constituents are considered. The deviations for chiral biaxial materials are relatively minor so we shall only examine those for the biaxial Faraday effect materials.

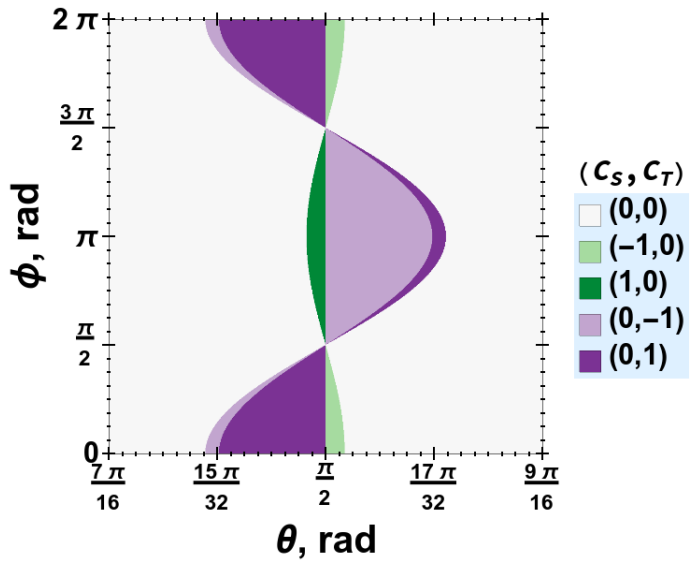

FIGURE 4.19: Comparison of the Chern numbers determined for two different photonic crystal lattice geometries. The two geometries considered are square and triangular. In each case we consider biaxial Faraday effect dielectrics as the photonic crystal constituents. The comparison considers how the Chern number depends on the direction (θ, ϕ) in which the magnetic field is applied. The colour scheme of the plot is given in the legend on the right.

In figure 4.19 we look at how the topologically ordered phases in the two geometries depend on the direction of the applied magnetic field. The Chern number

in the two geometries, C_S (square) and C_T (triangular), is displayed according to the legend of the figure. We can see that the topologically non-trivial regions for each of the geometries do not overlap at all. At any angle ϕ we see that the phases for each geometry occur on opposite sides of the $\theta = \frac{\pi}{2}$ equator. Mathematically, this is due to the ratios c_2/c_1 of the geodesic equations (3.10) for the C-points in each geometry having opposite signs. To investigate the physical cause of this difference between the two geometries we need to examine the two models more closely. In particular, we can look at plots of the zero contour lines of the polynomials $\mathbf{b}_{\blacksquare}(\mathbf{k})$ and $\mathbf{b}_{\blacktriangle}(\mathbf{k})$ over the relevant Brillouin zones to assess the origin of the differences.

In figure 4.20 we can see the cause of the discrepancy between the Chern numbers determined in the two geometries. The zero contour lines are broadly similar in both geometries, particularly in the central regions of each Brillouin zone. Closer to the zone boundaries we see how the geometry impacts the zero contour lines. There are three principal factors which acting in combination with the zero contours of $b_3(\mathbf{k})$ in each geometry explain the differences in Chern number. These three factors are the swapped sign of the topological index of the C-point towards the zone boundary along the $k_y = 0$ line, the increased displacement of this C-point from the boundary in the triangular geometry and the two extra C-points in the triangular geometry. The swap in sign of topological index has occurred as, in the triangular geometry, the C-point towards the boundary along the $k_y = 0$ line represents a zone corner C-point rather than a face centre C-point, which it is for the square geometry.

It is interesting that the Faraday effect is much more sensitive than chirality to these differences between the two geometries. This must be attributable to the different ways in which the two forms of optical activity depend on the propagation direction, which we saw in equations (2.42) and (2.43).

4.7 Conclusion

In this chapter we were interested in the topological invariants of the iso-frequency surface of triangularly-patterned 2D photonic crystals composed of biaxial optically active materials. Our focus was on the two most paraxial polarisation-split bands of the iso-frequency surface describing propagation largely perpendicular to the periodic plane of the photonic crystal. To describe such a system we have adapted the paraxial Hamiltonian derived in section 2.6 to a triangular lattice geometry in section 4.2. To assess the fidelity of this adaptation we have compared the lattice Hamiltonian to frequency-domain plane-wave simulations of corresponding systems. The comparison showed that the adapted Hamiltonian is a reasonable qualitative descriptor of these 2D photonic crystal structures. In particular, the

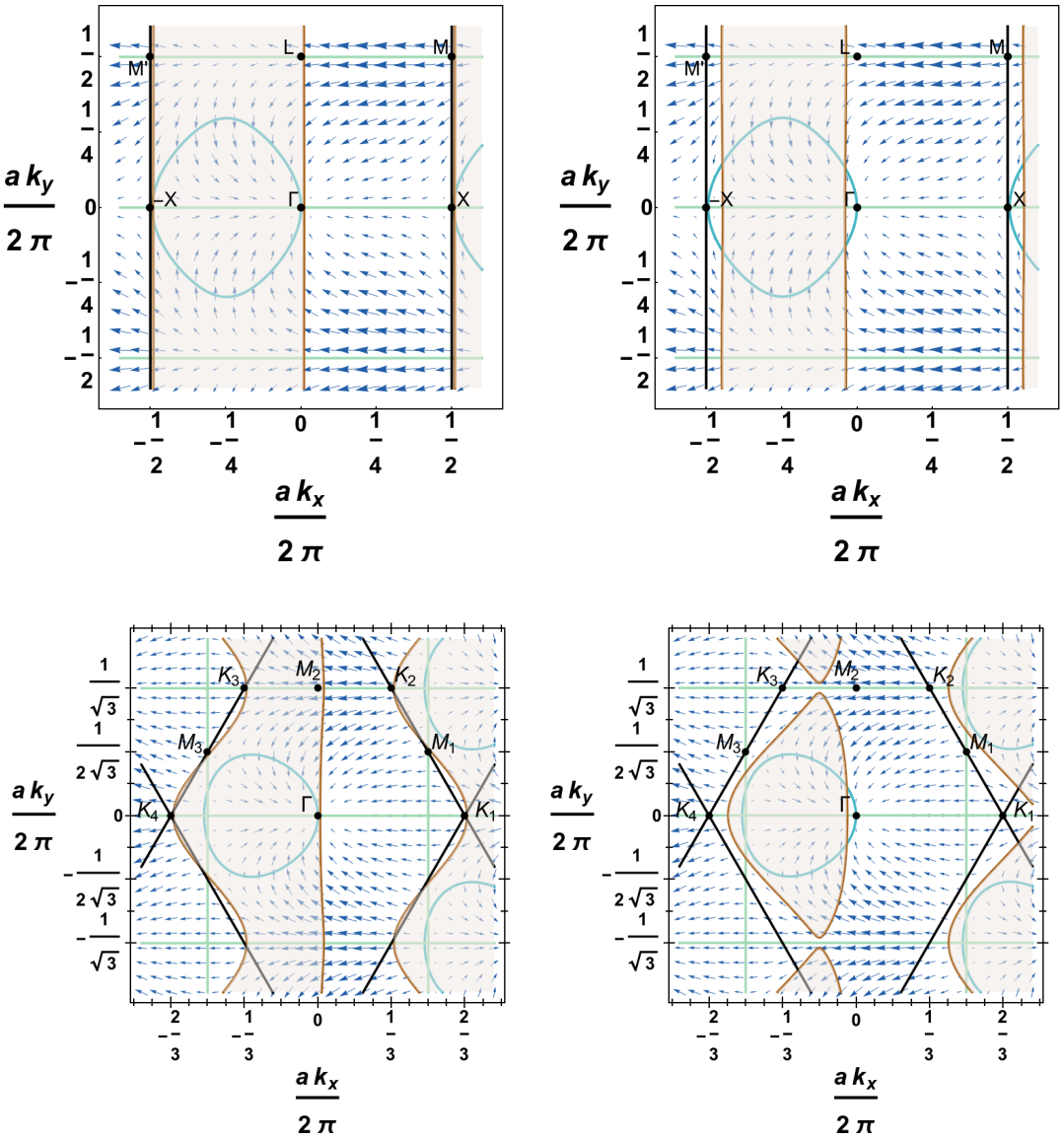

FIGURE 4.20: Four plots investigating the discrepancy in Chern numbers between the two geometries. The two geometries considered were (top row): square and (bottom row): triangular. For both geometries the photonic crystals are composed of biaxial Faraday effect materials. For both geometries the same two magnetic field application directions were used. In the left figures $(\theta, \phi) = (\frac{127\pi}{256}, \pi)$ and in the right figures $(\theta, \phi) = (\frac{33\pi}{64}, \pi)$.

adapted Hamiltonian captures the aspects most important to the topological characterisation of these systems, the number of polarisation C-points and their approximate locations in the first Brillouin zone.

Since the lattice Hamiltonian gives a reasonable qualitative account of the singularities in the iso-frequency surfaces we can use it to assess the topological phase diagrams of the iso-frequency surfaces of $2D$ anisotropic photonic crystals upon addition of optical activity. In section 4.4 we considered the addition of a Faraday effect exploiting magnetic field. We found that it is possible to achieve a non-zero

Chern number in certain parameter regimes. There are generally six parameters governing the value of the Chern number: the magnetic field direction, the three principal dielectric constants and the lattice spacing to wavelength ratio. To achieve a non-zero Chern number the magnetic field should be applied in any of a band of directions, all of which are close to perpendicular to the optic axis direction. The width of this band is governed by the other four parameters. A system with a lower lattice spacing to wavelength ratio has a wider band of directions. The width of the band of directions exhibits a complex dependence on the strength of biaxiality.

The other form of optical activity that we considered is chirality. The nature of the chirality considered plays a decisive role in whether optical topological order is achievable at all. With reference to the lattice Hamiltonian model, it is only possible to achieve a non-zero Chern number with either dielectrics of rhombic disphenoidal, sphenoidal or pedial form. For photonic crystals composed of these types of dielectrics a topologically non-trivial system is by no means guaranteed. Whether or not a non-zero Chern number results depends on the interplay of either seven or eight parameters: the three or four relevant components of the chirality tensor, the three principal dielectric constants and the lattice spacing to wavelength ratio. For the sphenoidal or pedial forms of chirality a non-zero Chern number is achieved when the ratio of the diagonal components of the chirality tensor to each other should be close to positive unity while the ratio of each of the three diagonals to the relevant off-diagonal should be close to negative unity. When this is the case the range of tolerance close to unity for a non-zero Chern number is increased for a more strongly biaxial material and when the lattice spacing to wavelength ratio is lower.

In previous works that have theorised and realised Chern insulators in trinagularly patterned photonic crystals [9, 10, 33, 88], degeneracies of the photonic band structure were inherited from the lattice symmetries rather than from the underlying dielectrics. These previous works additionally explicitly considered situations in which the propagation direction and polarisation state are de-coupled. In contrast, the consideration of anisotropic dielectrics in this chapter means that such a de-coupling does not occur.

The work presented in this chapter is therefore a parallel study to that presented in chapter 3 where square patterned photonic crystals were considered. Each of these approaches exploits the polarisation degeneracies of the index surfaces of homogeneous anisotropic materials to realise topologically non-trivial systems. The topological phase diagrams produced for the two geometries showed broad similarities in the topologically non-trivial parameter regimes. The different geometry caused only minor deviations in the size and small shifts in the locations of the topologically non-trivial parameter regimes. This confirms that, as we expected, the

dominant mechanism underpinning these topologically non-trivial iso-frequency surfaces is the anisotropic optically active materials rather than any special type of patterning. This suggests that the approach provides a general framework for the realisation of topological order in photonic crystals.

Chapter 5

Edge Theories of Topologically Non-Trivial Systems

5.1 Introduction

A possible physical manifestation of a non-zero topological invariant in a bulk system is the appearance of edge states at its boundary [6]. These states can appear when a topologically non-trivial system has an interface with a topologically trivial one. The nature of the edge states depends on what type of non-zero invariant is present [124]. In the case of a non-zero Chern number the edge states propagate chirally around the boundary, either clockwise or anti-clockwise [27]. The origin of the edge states states can be elucidated by imagining, rather than an abrupt interface, a smooth interpolation between the two materials in the direction perpendicular to the boundary. In this scenario it is clear that, since away from the boundary the value of the relevant topological invariant differs on each side, there must be a degeneracy of the band structure, separating the two phases. The region of the degeneracy of the band structure will then possess low-energy locally-bound states. For an abrupt boundary the edge states will persist provided that the scattering effects of the boundary do not mix the edge states with those of the bulk. Whether or not this mixing happens depends on the nature of the band gap of the system considered. These edge states, if they exist, are localised within a certain characteristic distance of the boundary [125]. The characteristic distance in turn sets a scale for the minimum system size in order to observe the edge states.

To assess whether edge states appear or not one has to study a finite geometry version of the bulk system Hamiltonian. Although there have been studies that have examined edge states by studying terminations of continuum Hamiltonians [126, 127] we will focus on terminating lattice theories. The introduction of a boundary to these bulk lattice Hamiltonians breaks translation invariance in the direction perpendicular to the wall. Owing to this, Bloch's theorem no longer applies in the direction perpendicular to the wall and consequently solutions which grow or decay in that direction are allowed. The wavevector parallel to the boundary remains a good quantum number, which characterises the solutions.

In chapters 3 and 4 we examined anisotropic photonic crystals whose iso-frequency surfaces can be described by a topologically non-trivial Hamiltonian. This Hamiltonian models the paraxial evolution of light propagating primarily out of the periodic plane of the photonic crystals. Edge states in this context would therefore be solutions which travel chirally around the xy boundary of the photonic crystal as they evolve along the z direction. In this chapter we will examine the prospect of edge states for the anisotropic photonic crystals of chapters 3 and 4.

To address this prospect it will be helpful to first recognise the differences between the theories of the preceding chapters and that of the idealised Chern insulator of section 1.3 where edge states emerged in a straightforward manner. The most immediate difference is that the idealised Chern insulator possesses a bulk band-gap over the entire Brillouin zone (see figure 1.3) whereas the photonic crystal models of chapters 3 and 4 do not (see figures 3.3 and 4.3). A second difference between the idealised Chern insulator and the photonic topological insulators of chapters 3 and 4 is that the latter have a lower degree of symmetry than the former. In particular the theories of chapters 3 and 4, due to the anisotropy of the dielectric materials, do not possess the $\frac{\pi}{4}$ and $\frac{\pi}{6}$ rotation symmetries of the respective lattices. We need therefore to explore two questions; what implications do the lack of a complete photonic band gap have on edge state formation, and, whether the reduced symmetry of the photonic crystal makes the edge theories dependent on the boundary orientation?

To explore the first question we must decide what manner of boundary condition to employ. In this work we shall employ two variants of boundary condition, an open boundary condition and a boundary condition which explicitly includes a description of the adjacent material. The open or hard wall boundary conditions are a mathematically convenient set of boundary conditions. These boundary conditions employ an infinite potential jump on the perimeter of the topologically non-trivial material. The infinite potential step means that the field must vanish on each boundary. An immediate consequence of the vanishing is that, for edge state formation, two decay length scales are required for each edge [128]. The first length scale is needed to make the field grow in the close vicinity of the wall and the second to make the field decay as one penetrates further into the bulk [129]. The question is then whether the two decay length scales are available to construct an edge state solution.

Though mathematically convenient the hard wall boundary conditions are not always realistic. In reality the field will not vanish on the boundary and will instead extend into the adjacent material. Owing to this it may be desirable to include a description of the adjacent topologically trivial material. The inclusion of the adjacent material in describing the whole system may circumvent the need for two

decay length scales for each edge which was required for the hard wall boundary conditions. As the field is finite on the boundary between the two materials we may only require a single decay length scale. This is perhaps suggested by the $1D$ Jackiw Rebbi model [130], which is a continuum model comprising Dirac fermions in each half-space separated by a boundary at the origin. The masses of the fermions are taken to differ in sign and magnitude. Each half space does not properly define an integer Chern number as there is not a proper lattice regularisation. Nevertheless, the interface between the two half-spaces can be regarded as one across which the Chern number changes by $|\Delta C| = 1$. There is therefore a solution bound to the interface between the two materials. This solution interestingly exhibits exponential decay with a single exponent in each material. On this basis we will explore whether a two-dimensional model featuring an interface between lattice systems of differing Chern number requires four decaying length scales to form edge states or if two are sufficient.

In this chapter we employ either a hard-wall boundary condition or one which includes the adjacent material. In each instance we investigate when edge state formation occurs, and for the second form of boundary condition, how many decaying length scales are required. The question of the number of available decaying length scales is related to the bulk band structure. In particular, the morphology of the bands and not just their topological invariants is relevant [131]. We therefore seek to understand edge state appearance through the analysis of bulk band structures. For a hard wall geometry this requires exclusive study of the band structure of the topologically non-trivial material, whereas when we include the adjacent material we must also consider its band structure.

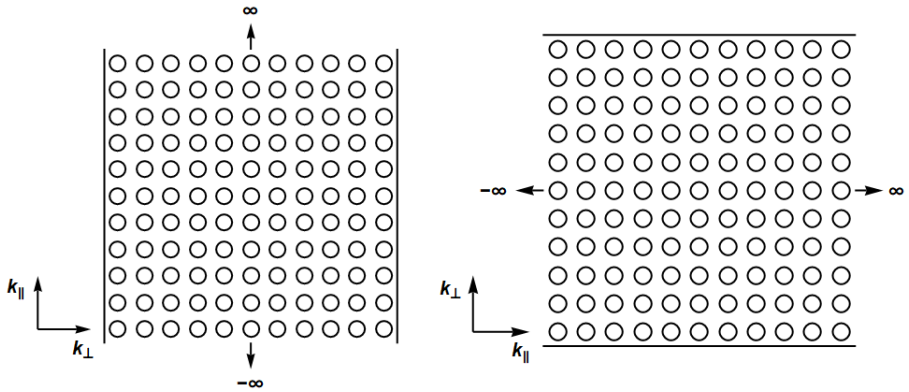

FIGURE 5.1: Two cartoons illustrating possible terminations to a structure one can consider in order to examine edge features. On the left we consider a system which is finite in x and infinite in y while on the right we have the converse.

As well as the form of the boundary conditions employed the orientation of the boundary can also affect the existence and characteristics of edge states

[132]. For a square lattice the two most natural terminations, which we shall consider throughout this chapter, are shown in figure 5.1. In this figure we consider introducing walls perpendicular to either of the two directions of patterning of the two-dimensional bulk material. The resulting Hamiltonian in each of these geometries, when diagonalised, need not produce corresponding edge theories. As the photonic crystal models of chapters 3 and 4 did not possess the symmetry of their respective lattices we shall explore whether and how this reduced symmetry manifests in the edge theories produced under each termination.

To this end we begin this work in section 5.2 by studying the formation of edge states for topologically non-trivial system using a hard-wall boundary condition. We do this by studying an adapted Chern insulator model. This study will help us understand how the bulk band structure affects both the available decay length scales and the possible termination orientations for edge state formation. In particular we shall study the fate of the edge states as the bulk band gap is closed. In section 5.3 we study the same adapted Chern insulator put into contact with a topologically trivial insulator. The trivial insulator we consider is a version of the Chern insulator but in a topologically trivial parameter regime. This allows us to study, for the compound system, whether the conditions necessary for edge state formation differ from those of the hard wall boundary conditions and in what ways. In section 5.4 we use some of our insights from section 5.2 to study the edge theories of the topologically non-trivial bulk systems of chapters 3 and 4. Finally in section 5.5 we offer some conclusions on the results of this chapter.

5.2 Topological Edge State Formation in a Hard Wall Geometry

To study the role of the boundary conditions on edge state formation for topologically non-trivial systems which lack a complete band gap we shall study an amended version of the Chern insulator model introduced in section 1.3. The amended version we consider is

$$\begin{aligned}\underline{\underline{H}} =& \big(\alpha_x(1-\cos k_x)+\alpha_y(1-\cos k_y)\big)\underline{\underline{\mathbb{1}}}+\\ &+(\sin k_x, \sin k_y, 2+m-\cos k_x-\cos k_y)\cdot\underline{\underline{\boldsymbol{\sigma}}}.\end{aligned} \tag{5.1}$$

The additional terms are those multiplying the identity matrix in equation (5.1). These terms will allow us to remove the complete bulk band gap in certain directions in k-space. As these additional terms are proportional to the identity matrix they do not affect the eigenvectors of the Hamiltonian. Consequently, since the additions do not affect the eigenvectors, the topological phase diagram is the same as in section 1.3. Throughout this section we shall work in the topologically

non-trivial regime $m = -1$ in which the Chern number $C = -1$. We saw in section 1.3 that when the additional terms are absent there is a complete bulk band gap. We also saw that when this bulk system is considered in a finite geometry with hard-wall boundary conditions that edge states are present. These edge states are reasonably extended in the wavevector parallel to the boundary and cross at $k_{\|} = 0$. In real space the edge states are well-localised in the direction perpendicular to the boundary. In this section we investigate the fate of these edge states as the complete bulk band gap vanishes.

With this in mind we study a finite geometry version of the Hamiltonian (5.1). We suppose that there is a termination of the structure in the y direction. This termination is similar to the right-hand illustration in figure 5.1 and leaves N sites in y between the two boundaries. The introduction of the terminations requires Fourier transforming the k_y terms in equation (5.1) back to real space, resulting in the desired finite geometry matrix. This matrix is a $2N \times 2N$ matrix which couples the two spin states on each y site to their nearest neighbours in the positive and negative y direction. The matrix can be thought of as a tri-diagonal one with each element itself a 2×2 block. There are therefore three non-zero distinct 2×2 blocks that feature on the tri-diagonals. One block describes the on-site Hamiltonian, which is on the main-diagonal, while the other two blocks describe the hopping up and down the chain which feature on the off-diagonals. The on-site block takes the form

$$\underline{\underline{\mathcal{M}}} = \begin{pmatrix} (\alpha_x + 1)(1 - \cos k_x) + \alpha_y & \sin k_x \\ \sin k_x & (\alpha_x - 1)(1 - \cos k_x) + \alpha_y \end{pmatrix}. \tag{5.2}$$

One of the inter-site hopping blocks is

$$\underline{\underline{\mathcal{T}}} = \begin{pmatrix} -\frac{1}{2}(\alpha_y + 1) & -\frac{1}{2} \\ \frac{1}{2} & -\frac{1}{2}(\alpha_y - 1). \end{pmatrix}. \tag{5.3}$$

The third block is the inter-site block that hops in the other direction and is the Hermitian conjugate of (5.3). For a given number of sites N and having chosen α_x and α_y the finite geometry band structure can then be determined by finding the eigenvalues of this large matrix as functions of k_x.

Rather than solving the eigenvalue equation for a given choice of parameters we will attempt to make some general conclusions about how the solutions depend on the parameters. To this end we note that, away from the ends of the chain, there is the same equation for each two-line block considered. This set of simultaneous equations is of the form

$$\underline{\underline{\mathcal{T}}}^{+} \boldsymbol{\psi_{n-1}}(k_x) + \underline{\underline{\mathcal{M}}} \boldsymbol{\psi_n}(k_x) + \underline{\underline{\mathcal{T}}} \boldsymbol{\psi_{n+1}}(k_x) = E \boldsymbol{\psi_n}(k_x), \tag{5.4}$$

where $\boldsymbol{\psi_n}(k_x)$ is a spinor on site n. As we are interested in the prospect of solutions

which grow or decay from site to site we shall propose a solution $\boldsymbol{\psi_n} = \lambda^n \boldsymbol{\phi}$. Inserting a solution of this form, dividing by λ^n and re-arranging produces the equation

$$\left[\underline{\underline{\mathcal{T}}}^{+} + \lambda(\underline{\underline{\mathcal{M}}} - E\underline{\underline{\mathbb{1}}}) + \lambda^2 \underline{\underline{\mathcal{T}}}\right]\boldsymbol{\phi} = 0. \tag{5.5}$$

Non-trivial solutions of the equation (5.5) follow from requiring that the determinant of the matrix within the square brackets vanishes. Solving the determinant equation in turn leads to, for a chosen set of parameters $(k_x, \alpha_x, \alpha_y)$, a quartic equation in λ. The quantity λ is the eigenvalue of the discrete translation operator along y. As such, it describes whether, and to what degree, solutions can grow or decay from site to site. If $|\lambda| = 1$ then only the phase of $\boldsymbol{\psi}$ changes between sites and not its amplitude. When $|\lambda| \neq 1$ growing and decaying solutions are allowed. Those with $|\lambda| > 1$ grow as n increases while those with $|\lambda| < 1$ decay with increasing n. Although the determinant equation is a quartic in λ the solutions actually come in two reciprocal pairs [132]. This reciprocity of solutions represents the reciprocity of hopping in opposite directions along the chain. When all four of the $|\lambda|$ differ from unity edge states can be constructed. As discussed in section 5.1, for hard wall boundary conditions each edge requires two non-unity $|\lambda|$ to construct an edge state. On the top edge, where $n = N$, we require the two $|\lambda| > 1$ solutions while on the bottom edge we require the two $|\lambda| < 1$ solutions. This method therefore allows us to examine how the band structure parameters $(k_x, \alpha_x, \alpha_y)$ impact the possibility of edge states.

In figure 5.2 we plot the absolute value of each of the four solutions for λ as a function of energy for three different sets of parameters. In each plot we have considered the solutions of the discriminant equation (5.5) for $k_x = 0$ as this is the value of the wavevector at which the edge states cross when $\alpha_x = 0 = \alpha_y$. In each of the plots we consider $\alpha_x = 0.25$. For each plot we consider a distinct value of α_y; in the top left plot we consider $\alpha_y = 0.25$, in the top right plot $\alpha_y = 0.8$ while in the bottom plot $\alpha_y = 1.1$. In each plot we mark the $|\lambda| = 1$ line with a dashed black horizontal gridline. Additionally in each of the three plots we mark the minimum and maximum energies of each band of the bulk band structure along the line $k_x = 0$. The extreme energies of the lower band are marked by green vertical gridlines while those of the upper band are represented by brown vertical gridlines. The area between these gridlines, which represents the extent of the bulk bands, is shaded accordingly.

In each of the plots we see that over the shaded energy intervals there are two $|\lambda| = 1$ solutions. These $|\lambda| = 1$ solutions are the bulk band structure solutions; those for which the amplitude of the solutions do not change from site to site along y. As the energy considered passes outside the extremes of the bulk band structure the values of $|\lambda|$ depart from unity in a way that maintains the reciprocity. In the

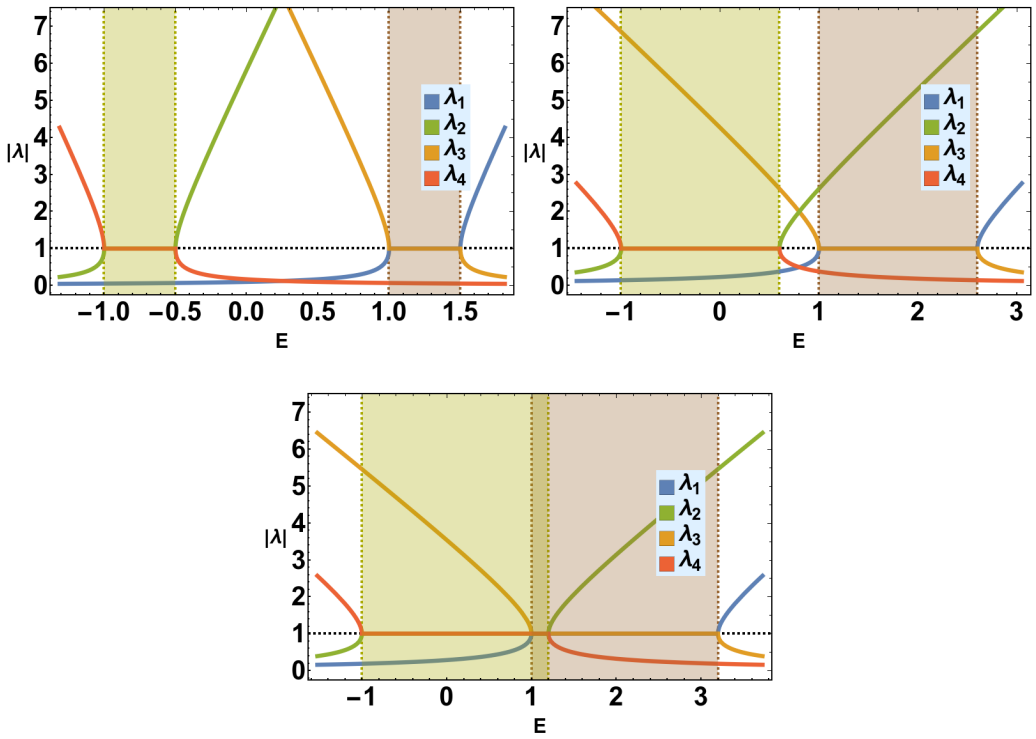

FIGURE 5.2: Absolute value of λ for three different values of the parameter α_y: $\alpha_y = 0.25$ (top left), $\alpha_y = 0.8$ (top right) and $\alpha_y = 1.1$ (bottom). In each case $\alpha_x = 0.25$. The horizontal gridline is the line $|\lambda| = 1$ and the the vertical gridlines are the minimum and maximum of the upper (brown) and lower (green) bands of the bulk band structure along the line $k_x = 0$. The area between the extreme values for each band is shaded in the corresponding colour.

top plots of figure 5.2 the shaded energy intervals of each band are non-overlapping representing a complete band-gap along the line $k_x = 0$. In this band-gap there are four $|\lambda| \neq 1$ solutions in both cases. Between the top left and top right plots of figure 5.2 we see that the width of the band-gap has decreased as α_y has increased between the top left and top right plot. In the lower plot of figure 5.2 the shaded energy intervals are now partially overlapping and the bulk band gap along $k_x = 0$ has disappeared. As the band-gap has disappeared we have also lost any energy interval between the energy extent of the bulk band structure for which there are four $|\lambda| \neq 1$ solutions. We therefore conclude that the regions for which at least two $|\lambda| = 1$ solutions exist correspond to the energy intervals of the bands of the bulk band structure. Consequently, when the bulk band structure lacks a complete band gap along the k_x considered there are never four $|\lambda| \neq 1$ solutions within those energy intervals.

How do these conclusions relate to the presence of edge states, and, if present, their characteristics? To address this question we shall move from the general to the specific by diagonalising the matrix from which the equation (5.4) followed. We diagonalise this matrix for each set of α_x and α_y considered in figure 5.2 at a desired

resolution in k_x and for a sufficient number of sites along y. This will enable us to relate the eigenvalues of the discrete translation operator with the edge states and their properties.

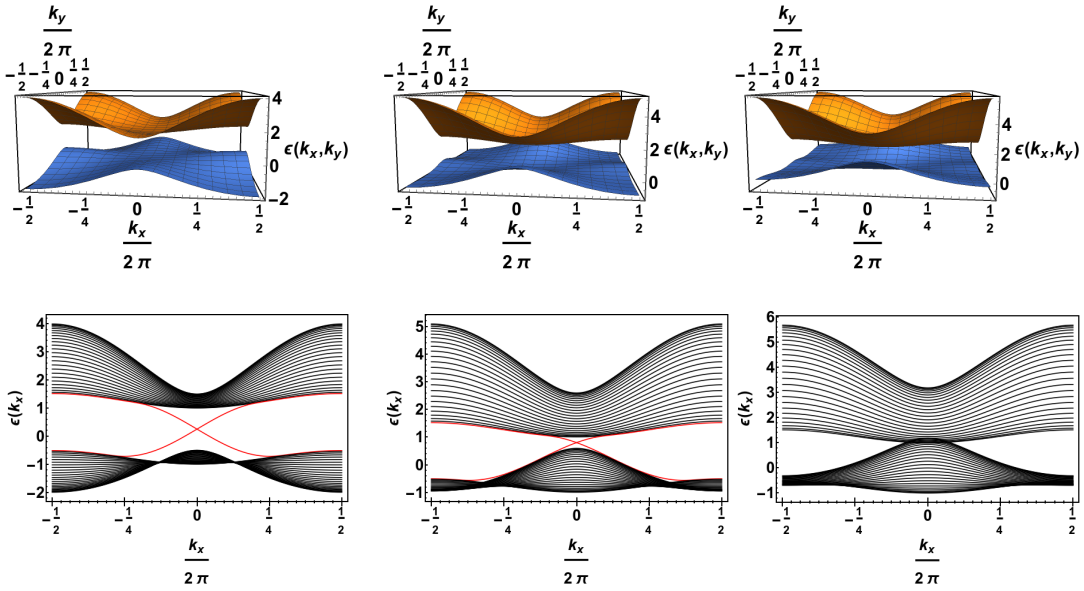

FIGURE 5.3: A grid of plots showing the bulk band structure (top row) and the corresponding finite geometry band structure (bottom row) under three different sets of parameters. In the left column $\alpha_y = 0.25$, in the central column $\alpha_y = 0.8$ and in the right column $\alpha_y = 1.1$. In all cases $\alpha_x = 0.25$. For the finite geometry band structures we consider 25 sites along the y direction.

In figure 5.3 we show a grid of plots depicting the bulk band structures (top row) and the corresponding finite geometry band structures (bottom row) for three different sets of parameters. Each column considers a separate set of parameters which are the same as were chosen for figure 5.2. In all of the figures $\alpha_x = 0.25$. In the leftmost column we consider $\alpha_y = 0.25$, in the central column $\alpha_y = 0.8$ and in the rightmost column $\alpha_y = 1.1$. In each instance we have considered a finite system with 25 sites along the y direction. In the two columns with the lowest α_y values we can see solutions resembling edge states crossing the gap between the two groups of mini-bands of each finite geometry band structure. In the $\alpha_y = 1.1$ finite geometry band structure the gap has disappeared and hence the question of edge states is more ambiguous. To illuminate this question we can examine the eigenvectors resulting from the diagonalisation of the finite geometry matrices.

In figure 5.4 we examine a grid showing plots of the spin-summed density of the eigenvectors of the supposed edge states from figure 5.3. Each column considers the same parameters as those of figure 5.3. The top row shows the edge state which should exist on the top edge and the bottom row shows the corresponding plots for the bottom edge. In the two cases with the lowest α_y we see well-localised edge states as expected. In the $\alpha_y = 0.8$ case we observe that there is less density

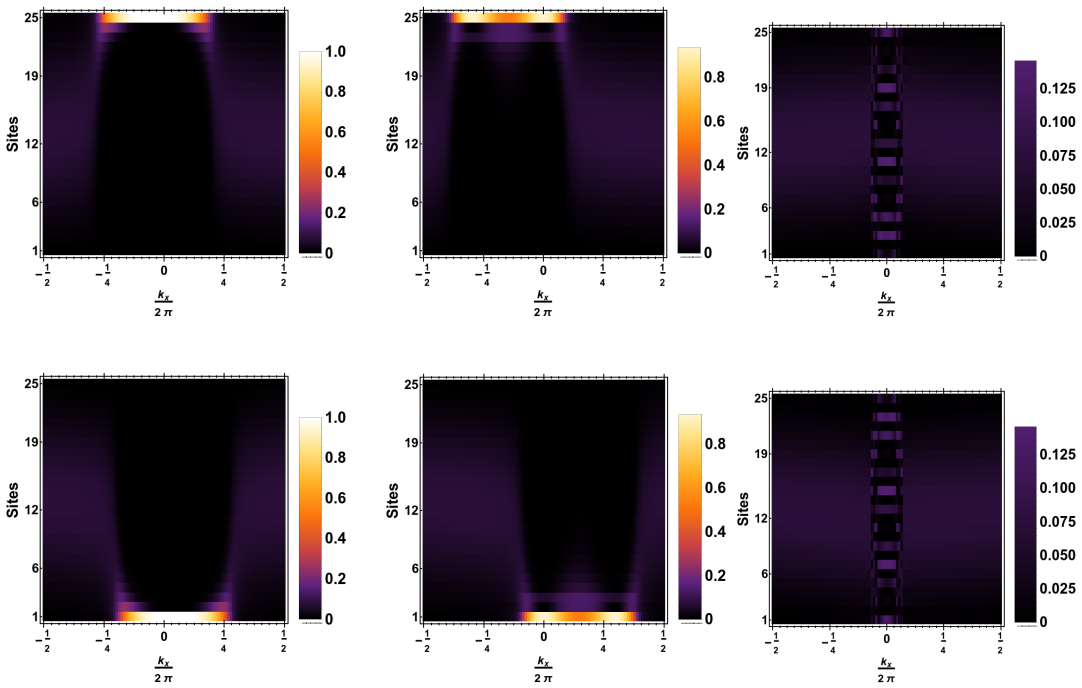

FIGURE 5.4: A grid of plots showing the spin-summed densities of the eigenvectors corresponding to the central eigenvalues in figure 5.3 under three different sets of parameters. In the left column $\alpha_y = 0.25$, in the central column $\alpha_y = 0.8$ and in the right column $\alpha_y = 1.1$. In all cases $\alpha_x = 0.25$. We consider 25 sites along the y direction in all cases.

overall on the outermost sites compared to the almost perfectly localised $\alpha_y = 0.25$ case. In the rightmost column where $\alpha_y = 1.1$ there are no edge state like features observable over any of the extent in wavevector space where these features existed in the other α_y cases. The absence of edge features could be attributable to not having considered a large enough system or examining the wrong mini-bands or both. However since this disappearance corresponds with the closing of the bulk band gap we contend that the transition from four to two non-unity eigenvalues of the discrete translation operator has stymied edge state formation completely. In regard to this perspective it does not matter how large a system one considers as the boundary conditions are incompatible with edge state formation. This perspective is supported by the work of Mao and Kuramoto [133]. Mao and Kuramoto [133] examined an alternative Chern insulator model and reached the same conclusion that the edge states disappear at all wavevectors as the band gap closes. So if it is the boundary conditions that are frustrating the edge state formation is it possible to realise edge states by considering either terminating the bulk structure along a different direction or a completely different set of boundary conditions entirely?

The preceding results suggest that the relevant property is the presence of a band gap in the wavevector direction perpendicular to the boundary at the value of the wavevector parallel to the boundary where edge states would be expected to cross. The presence of such a band gap assures four non-unity absolute values of

the discrete translation operator which in turn allows the formation of edge states in a hard wall geometry. We can consider terminating the structure in a different direction so as to achieve these four non-unity $|\lambda|$. In the cases where α_x and α_y differ we look at terminating the bulk structure in the x direction rather than the y direction previously considered. As the additional terms in the Hamiltonian (5.1) are the only ones which introduce asymmetry in the dispersion along the k_x and k_y we can, rather than terminating along the x direction, simply interchange α_x and α_y.

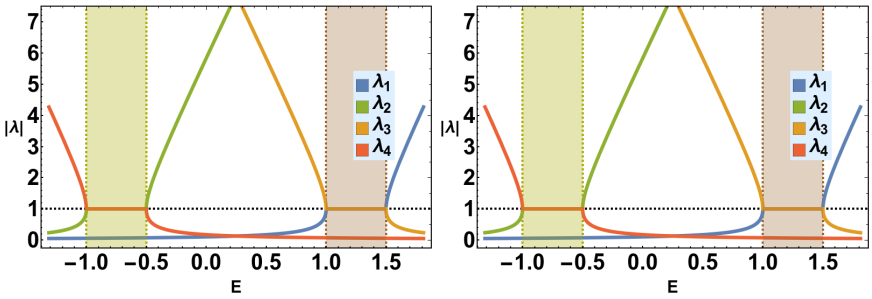

FIGURE 5.5: Absolute value of λ for two different values of the parameter α_x: $\alpha_x = 0.8$ (left) and $\alpha_x = 1.1$ (right). In each case $\alpha_y = 0.25$ The horizontal gridline is the line $|\lambda| = 1$ and the the vertical gridlines are the minimum and maximum of the upper (brown) and lower (green) bands of the bulk band structure along the line $k_x = 0$. The area between the extreme values for each band is shaded in the corresponding colour.

First of all, in figure 5.5, we focus on the absolute value of the eigenvalues of the discrete translation operator. In each case we fix $\alpha_y = 0.25$; in the left plot we have chosen $\alpha_x = 0.8$ while in the right plot $\alpha_x = 1.1$. We see that in each instance the energy extents of the bands of the bulk band structures are non-overlapping and hence there are four non-unity $|\lambda|$ in the energy region between the two bands. In fact the two plots are the same as the $|\lambda|$ only depend on the band structure in the direction perpendicular to the interface. Hence since α_y is the same in each instance the two plots are the same. This suggests that we should expect edge states to be present in both instances as we shall now investigate.

In figure 5.6 we show a grid of plots depicting the bulk band structures (top row) and the corresponding finite geometry band structures (bottom row) for the two sets of parameters considered in figure 5.5. In each instance we see clear evidence of edge states in the finite geometry band structures as expected from the examination of figure 5.5.

In figure 5.7 we examine the spin-summed density of the eigenvectors for each of the mini-bands in red in figure 5.6. In each instance we see that there are well-localised edge states on the top and bottom edges, and that these figures differ from the corresponding plots of figure 5.4 where the other termination was

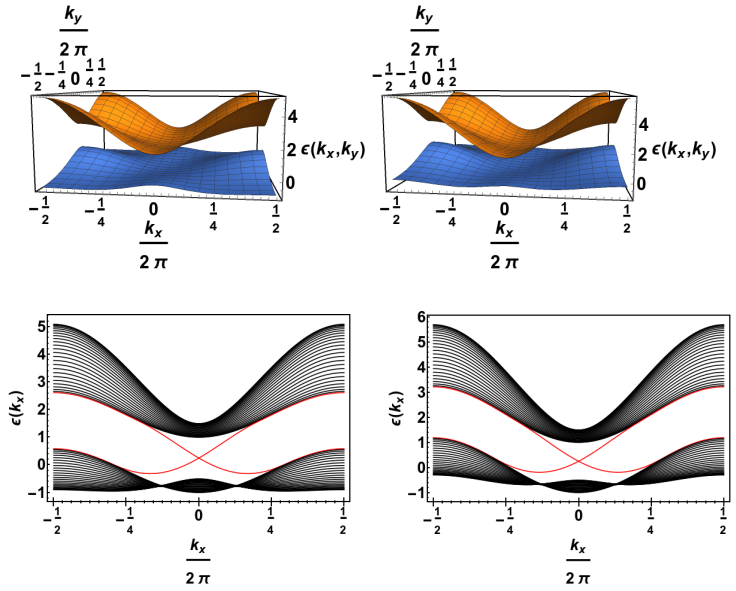

FIGURE 5.6: A grid of plots showing the bulk band structure (top row) and finite geometry band structure (bottom row) under two different sets of parameters. In the left column $\alpha_x = 0.8$ and in the right column $\alpha_x = 1.1$. In all cases $\alpha_y = 0.25$. For the finite geometry band structures we consider 25 sites along the y direction.

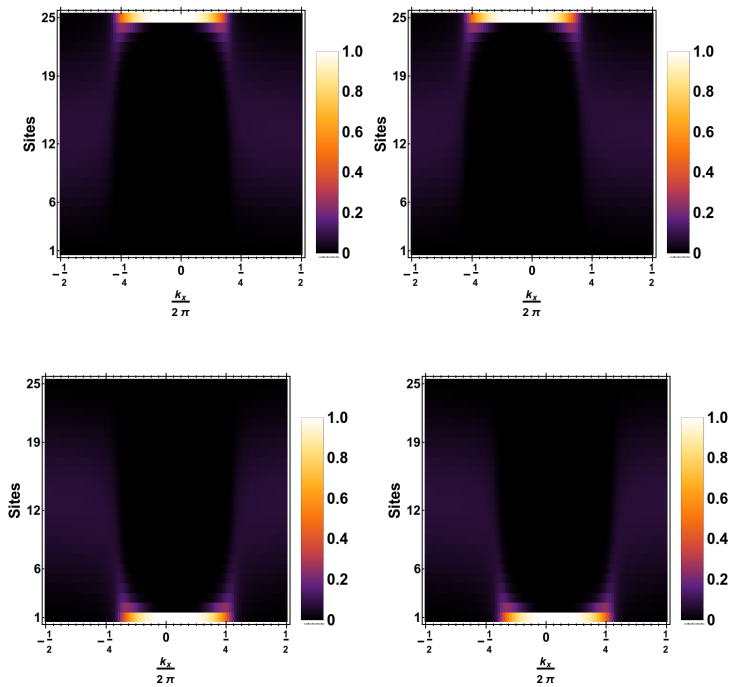

FIGURE 5.7: A grid of plots showing the spin-summed densities of the eigenvectors corresponding to the central eigenvalues in figure 5.6 under two different sets of parameters. In the left column $\alpha_x = 0.8$ and in the right column $\alpha_x = 1.1$. In both cases $\alpha_y = 0.25$. We consider 25 sites along the y direction in both cases.

considered. We therefore conclude that in cases where the bulk band structure is not symmetric under $\frac{\pi}{2}$ rotations different edge theories are produced when the

system is terminated along the different patterning directions. A consequence of this conclusion is that when the band structure lacks a complete band gap it may still be possible to achieve partial edge states by a judicious termination. This occurs if the bulk structure is terminated in a direction for which there is a band gap in $k_\perp$ to the interface along the $k_\parallel$ line at which the edge states would be expected to cross.

There is of course no requirement to terminate these structure along one of the directions of patterning of the underlying lattice. In the instance of an arbitrary termination, not along either direction of patterning, we expect the same general conclusion.

In section 5.4 we use the methods of analysis and the insights from this section to assess the possibility of full or partial edge states for a topologically non-trivial photonic crystal theory from chapter 3.

5.3 Topological Edge State Formation in Geometry Which Includes Abutting Material

We will now consider an alternative boundary condition. This alternative formulation will explicitly include an adjacent topologically trivial material. As in the previous section we wish to examine the fate of the edge states as the complete band-gap of the topologically non-trivial material is lost. We are particularly interested in establishing whether the edge states persist and if so whether their survival can be attributed to the requirement of, in this situation, fewer non-unity absolute value eigenvalues of the discrete translation operator.

The adjacent material we consider is of a similar form to the material in section 5.2 in that it will also be described by the Hamiltonian (5.1). For the adjacent material we shall fix $m = 1$ so that the Chern number $C = 0$. Additionally we shall fix α_x and α_y at the same values as in the topologically non-trivial material. To describe hopping across the interface between the two materials we shall make the approximation of using the matrix (5.3). To justify this approximation we note that the only difference that we are considering between the two materials is in the chosen values of m which does not feature at all in the intra-material hopping matrices.

There are two possible methods of performing the finite geometry calculations with both materials included. These two possibilities are either having a single interface between the two materials with hard walls at the other edges or having two interfaces between the materials. Figure 5.8 illustrates these two possibilities along with the hard wall boundary condition of section 5.2. In this section we shall

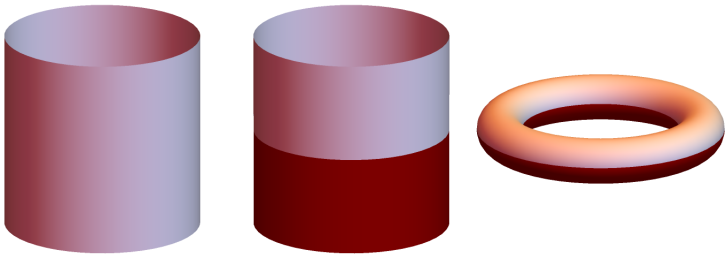

FIGURE 5.8: Three types of boundary condition employed in sections 5.2 and 5.3. In each case the lighter pink material is topologically non-trivial with a Chern number $C = -1$ while the darker pink material is topologically trivial with a Chern number $C = 0$. The leftmost illustration represents the hard-wall boundary condition while the central and rightmost illustrations represents two variants of boundary condition which include the adjacent material. In the central illustration we consider an interface between the two materials but with hard walls at the other ends of the materials. In the rightmost illustration we consider two interfaces between the two materials.

employ both the central and rightmost geometries of figure 5.8.

In either of the two geometries that include both materials we shall consider a compound system comprising 30 sites evenly shared between each material. In both cases we fix $(\alpha_x, \alpha_y) = (0.25, 1.1)$. In this parameter regime in the hard wall geometry the bulk band gap had closed along the line $k_x = 0$. As was shown in figure 5.4, this implies there are no edge states when the structure is terminated in the y direction. For each of the geometries considered in this section we shall use the same orientation, with the terminations and/or interfaces perpendicular to the y axis.

In figure 5.9 we look at the spin-summed eigenvectors of the two central eigenvalues (top and bottom rows) of the finite geometry calculations for each of the two geometries considered (left and right columns). We see that for each geometry some of the edge state density persists by the interface between the two materials, just inside the topologically non-trivial material. The geometry that features the hard wall boundary lacks this edge feature completely on that edge. As such, we can clearly see that the interface between the two materials is responsible for the survival of edge features. We shall now examine how this survival can be understood in the context of the two bulk materials.

Figure 5.10 shows the absolute value of the discrete translation operator λ for the parameters used in producing figure 5.9. For this figure we consider solving the determinant equation (5.5) at $k_x = \pi/5$ which is part of the region in which the edge state appeared in figure 5.9. In this figure we see that the extents of the energy bands are non-overlapping and hence there is a band-gap for these parameters. The edge state persisting is therefore not attributable to one only requiring two

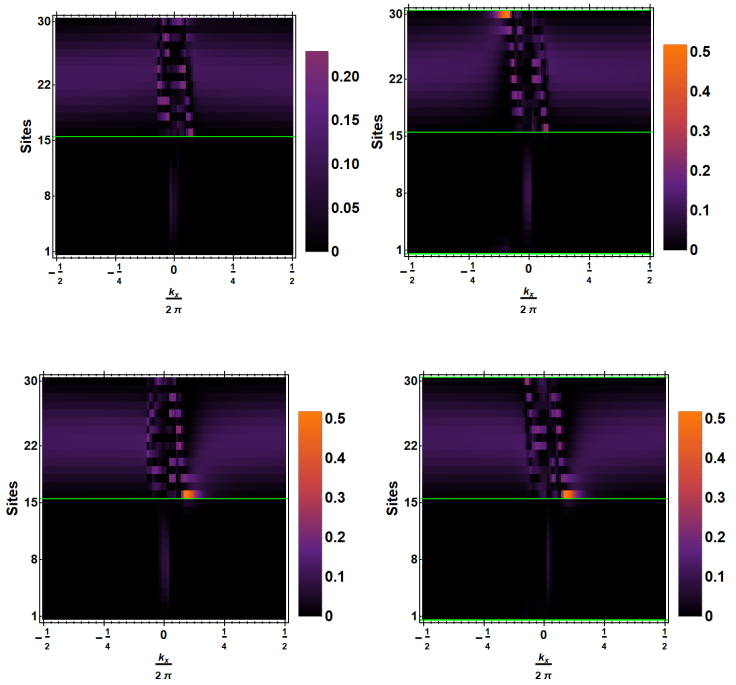

FIGURE 5.9: A grid of plots showing the spin-summed densities of the eigenvectors corresponding to the central eigenvalues for two different geometries. In the left column we consider the central geometry of figure 5.8 while in the right column we consider the rightmost geometry of that figure. In each case we consider 30 sites along y which are evenly distributed between the two materials. The material in the first 15 sites is the topologically trivial material with $m = 1$. The green lines in each case represent interfaces between the two materials. For the figures in the right column there is an interface between the 30th site and the 1st site. In both cases $(\alpha_x, \alpha_y) = (0.25, 1.1)$.

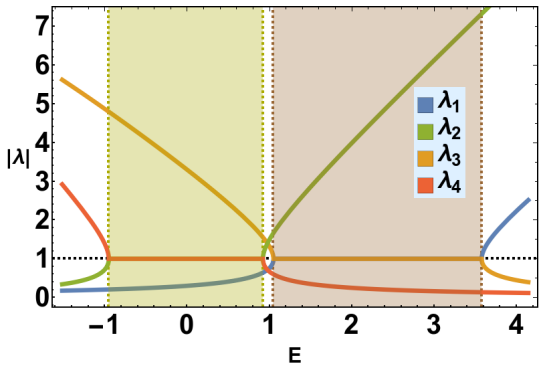

FIGURE 5.10: Absolute value of the eigenvalue λ of the discrete translation operator along y for the parameters $(\alpha_x, \alpha_y, k_x) = (0.25, 1.1, \pi/5)$.

non-unity $|\lambda|$ in this geometry but rather that the edge states persist over the range of the wavevector that supports four non-unity $|\lambda|$. Owing to this we would expect that if we increase α_y further that the edge states will disappear entirely once this range of wavevectors ceases to exist.

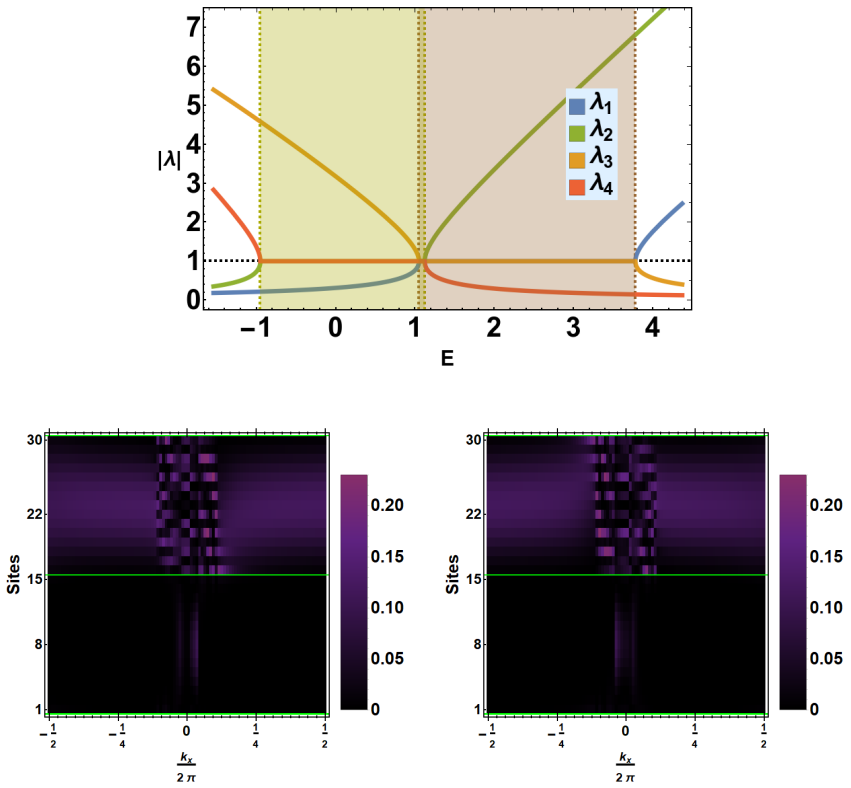

FIGURE 5.11: The top figure shows the absolute value of the eigenvalue λ of the discrete translation along y at the parameters $(\alpha_x, \alpha_y, k_x) = (0.25, 1.2, \pi/5)$. The bottom figures show the corresponding spin-summed densities of the eigenvectors associated with the central two eigenvalues. In each case we consider 30 sites along y which are evenly distributed between the two materials. The material in the first 15 sites is the topologically trivial material with $m = 1$. The green lines in each case represent interfaces between the two materials.

Figure 5.11 shows exactly this. Here we consider $\alpha_y = 1.2$ and see in the top plot that this adjustment leads to the reduction of the number of non unity $|\lambda|$ from four to two. Consequently when we look at the spin-summed eigenvectors of the central two eigenvalues in the lower figures we see that the edge features have disappeared completely.

We therefore conclude that boundary conditions which include the adjacent material may allow the edge states to persist beyond the closing of the bulk band gap over some wavevector ranges. These wavevector ranges are those for which there are still four non-unity $|\lambda|$. As the overall curvature of the bands in $k_\perp$ increases these wavevector ranges shrink and eventually disappear completely. This is in contrast to the hard wall boundary condition where we saw a binary present/absent transition of the edge states once the gap closed along the line $k_\parallel = 0$. So the inclusion of a sharp interface between the topologically non-trivial material and its topologically trivial neighbour does allow a comparatively modest extension of the parameter range for the observation of edge features but is still incompatible with

edge state formation beyond a certain threshold. The underlying mechanism that allows this dichotomy between the edge features for each of the boundary conditions considered remains an open question.

5.4 Appearance of Edge States in Photonic Crystal Models

In this section we shall seek to utilise the understanding we developed in section 5.2 regarding edge state formation in a hard wall geometry to one of the topologically non-trivial photonic models presented in chapter 3. We learned that the appearance of full or partial edge states is linked to the existence of four non-unity absolute value eigenvalues of the discrete translation operator in the direction perpendicular to the wall. The existence of such non-unity eigenvalues is in turn related to the band-gaps of the bulk band structure. We shall therefore study the iso-frequency band structure of the chiral biaxial photonic crystals of section 3.5 in order to determine the conditions necessary for full or partial edge states.

In section 3.5 we saw that the iso-frequency surfaces of square photonic crystals composed of chiral biaxial materials could be topologically non-trivial. In these systems, at least within the model studied, a non-zero Chern number can result when the chirality is of either sphenoidal or pedial form. For chirality of these two types the ratios of the non-zero components of the chirality tensor must be within given ranges to achieve a non-zero Chern number. The overall scale of the components did not, however, matter for determining the topological phase and only affected the size of the topologically non-trivial gap. The strength of the chirality, however, exerts significant agency over whether complete or partial band gaps are achievable and hence whether edge states are possible.

The strength of optical activity is captured by a quantity known as the optical specific rotation which we introduced in chapter 2. This quantity can be related to the components of the symmetric chirality tensor. In chapter 3 we chose to decompose the chirality tensor $\underline{\underline{G}}$ into two parts: a matrix $\underline{\underline{\tilde{G}}}$ with each non-zero entry allowed to vary between -1 and 1 and an overall multiplier γ_C related to the optical specific rotation ρ_C. In that chapter it was the matrix $\underline{\underline{\tilde{G}}}$ that determined the topological phase while, in this chapter, it will be the multiplier γ_C which determines the prospects for edge state formation. In chapter 2 we saw that the relation between the optical specific rotation and the chirality tensor components involved a conversion of the optical activity strength from being measured per meter to being measured per wavelength. This conversion will, for the first time, introduce a dependence on the operating wavelength of the photonic crystal individually rather than on the ratio of the lattice spacing to the operating wavelength. We need therefore to consider the possibility of edge states not only as depending on the strength of optical activity but also on the operating wavelength of the photonic

crystal.

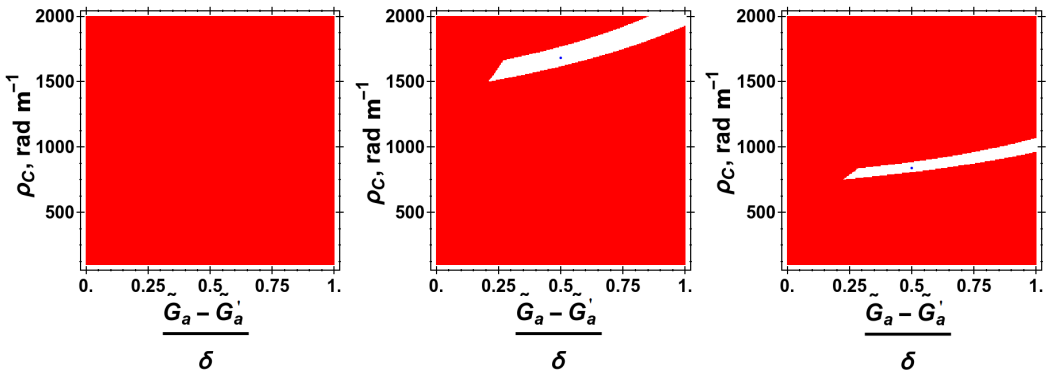

FIGURE 5.12: Three region plots examining the magnitude of the eigenvalues of the translation operator perpendicularly to the boundary. Each region plot considers a distinct value of the lattice spacing a of the structure. The lattice spacing considered are $a = 1 \times 10^{-4}$ m (left), $a = 5 \times 10^{-4}$ m (middle) and $a = 1 \times 10^{-3}$ m (right). In each case the lattice spacing to wavelength ratio $a/\lambda = 4/5$. The white regions are those in which there are four non-unity magnitude eigenvalues of the translation operator. The marked points in the middle and right plots are at $((\tilde{G}_a - \tilde{G}_a')/\delta, \rho_C) = (0.5, 1680)$ and $((\tilde{G}_a - \tilde{G}_a')/\delta, \rho_C) = (0.5, 840)$ respectively.

In figure 5.12 we display three plots examining the areas which support four non-unity absolute value eigenvalues of the discrete translation operator along the y-direction. Each plot considers a photonic crystal with a distinct lattice spacing and operating wavelength such that their ratio is constant at $\frac{a}{\lambda} = 0.8$. In the left plot we consider a lattice spacing $a = 100\mu$m, in the central plot $a = 500\mu$m while in the right plot $a = 1$mm. On the vertical axis of the plots is the optical specific rotation ρ_C while on the horizontal axis is a transformed coordinate related to the anisotropic chirality $\tilde{G}_a$ introduced in section 3.5. The transformed coordinate runs from 0 to 1 which are the endpoints of the topologically non-trivial parameter regime at $\tilde{G}_i = 1$. As such, the whole plot area corresponds to a $C = -1$ configuration. In line with the findings of section 5.2, in each case the value of k_x, i.e. $k_{\|}$, was chosen by examining where the edge states cross when the terms proportional to the identity matrix have been omitted. For the lattice Hamiltonian $\underline{\underline{B}}_{\blacksquare}(\mathbf{k})$, k_z is the analogue of the energy in section 5.2. The previously determined value of k_x allows us to determine the value of k_z at which to solve the determinant equation for the eigenvalues of the discrete translation operator. In particular, the value of k_z is set as $b_{\blacksquare 0}(k_x, 0)$. In the plots of figure 5.12 the white regions are those which support four non-unity absolute value λ while the red regions do not, and instead support either two or zero. From figure 5.12 we see that there are areas which have four decay length scales in the $a = 500\mu$m and $a = 1$ mm cases. We should therefore expect that edge states should exist for these parameters when a termination along y is introduced provided a

sufficiently large system is considered.

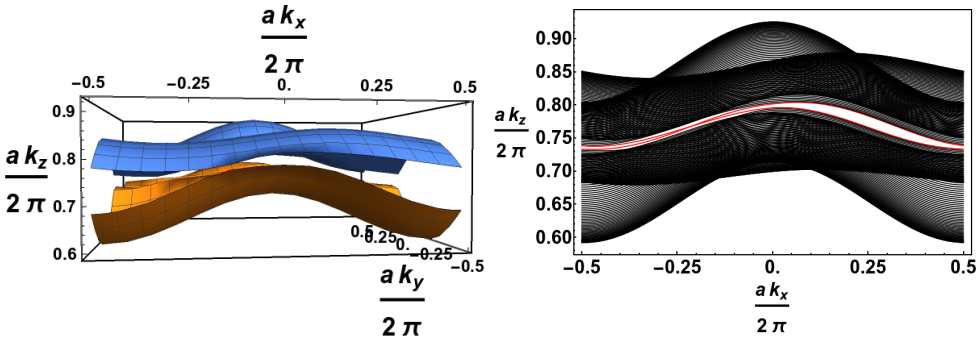

FIGURE 5.13: Bulk (left) and finite geometry (right) band structures of a photonic crystal composed of chiral biaxial material. The geometry considered is that of the right plot of figure 5.1, a boundary in the y direction. For this geometry we have considered 100 sites between the two walls. The parameters considered are such that both the Chern number is non-zero and there are four non-unity eigenvalues of the translation operator.

We now turn to examine the band structure of one of these photonic crystals in a region where there are four non-unity eigenvalues of the discrete translation operator. We shall consider the parameters indicated by the blue dot in the rightmost plot of figure 5.12. For these parameters we plot the bulk and finite geometry band structure in figure 5.13. The diagonalisation performed to produce the finite geometry band structure considered 100 sites in the y direction. In the finite geometry plot we see features (in red) which have an immediate and obvious resemblance to edge states. These appear to be similar to those of the bottom right plot of figure 5.6 in the sense that the states persist despite the lack of a complete band-gap in the wavevector parallel to the wall k_x. To verify the appraisal that these are indeed edge states we can examine the eigenvectors corresponding to these two red mini-bands. This will also allow us to establish the decay length of the edge states if that is indeed what they are.

In figure 5.14 we show two density plots of the polarisation-summed squared magnitude of the eigenvectors corresponding to the red mini-bands of figure 5.13. We see that these mini-bands do indeed represent edge states; in each case the maximum density is on the outermost sites and is centred around the wavevector at which the red mini-bands cross. These edge states are reasonably well localised to the boundary.

We must still confirm that these edge states are indeed topological. It is possible that they are instead a serendipitous appearance, unrelated to the bulk topological invariants, which has been enabled by the presence of four decay length scales. As the edge states cross each other in figure 5.13 it would suggest

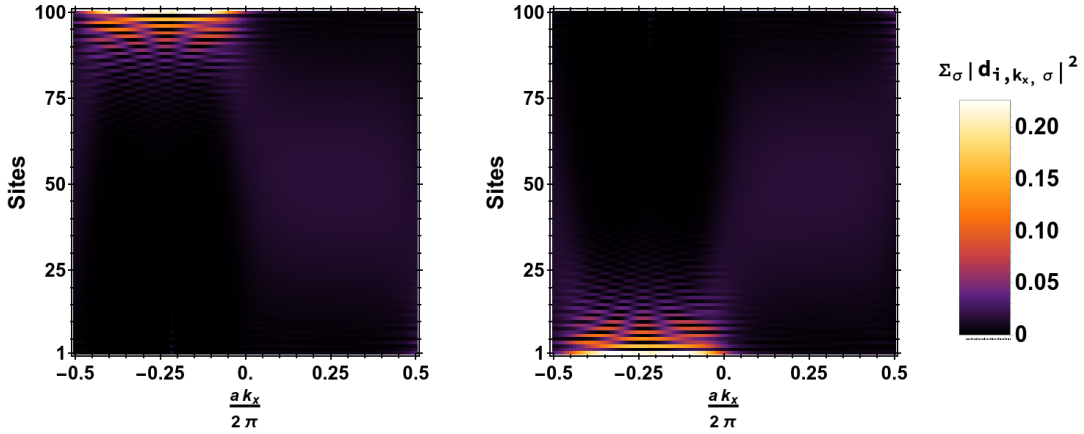

FIGURE 5.14: A density plot looking at the polarisation-summed squared magnitude of two of the normalised eigenvectors resulting from the diagonalisation which produced figure 5.13. The two eigenvectors considered are those mini-bands coloured in red in figure 5.13.

that they are topological. To definitively rule out the alternative explanation we shall consider a diagonalisation of one of these photonic crystals in a topologically trivial regime where four decay length scales exist. In particular we choose a point, $(\tilde{G}_a, \rho_C) = (-0.9, 1100)$, just off the right hand side of the plot area of the right plot of figure 5.12. At these parameters there are four decay length scales and the Chern number $C = 0$.

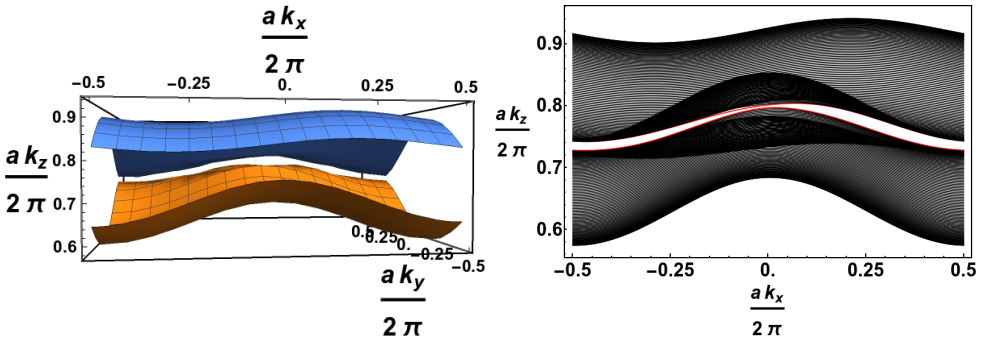

FIGURE 5.15: Bulk (left) and finite geometry (right) band structures of a square patterned photonic crystal composed of chiral biaxial materials. The parameters are chosen such that both the Chern number $C = 0$ and there are four decay length scales available. The finite geometry calculation considered 100 sites along the y direction.

In figure 5.15 we examine the bulk and finite geometry band structures of the topologically trivial photonic crystal discussed in the previous paragraph. We see that there are features in red which depart from the bulk band structure and therefore resemble edge states. Unlike as in figure 5.13 these edge states do not cross. This is a reflection of the now trivial Chern number. Hence we conclude that

the edge states of figure 5.13 were indeed topological in nature.

We can see in figure 5.13 that although there are edge states they are only partial ones as there is no complete band gap in k_x. This is indicative of a general trend - it is difficult to find parameter regimes where simultaneously a complete bulk band gap exists and the Chern number is non-zero. In the investigations we have carried out we have yet to come across such regions. This is largely attributable to the weakness of the polarisation splitting in comparison to the overall dispersion. To readily achieve complete band gaps requires both exceedingly strongly biaxial materials as well as artificially large optical activity. In this section we assumed that the specific rotation is a static quantity when, in reality, it exhibits chromatic behaviour, meaning that the values of rotation considered for figure 5.12 are unnaturally large. This would therefore make the fabrication of a photonic crystal with these properties a difficult prospect. There are, however, many possible optimisations that could be made to this type of scheme, for instance the model through which we conducted much of this analysis did not include the lower refractive index material at all. As such, there are possible optimisations involving varying any of the lattice spacing to wavelength ratio, the type of lower index material, the geometric profile of these inclusions or the filling factor of the inclusions individually, or all of these factors in combination [134–139]. Additionally we only considered the orientation of these photonic crystals where an optic axis lay along the invariant direction of the structure. The consideration of other orientations of the optic axes may ameliorate the question of band gaps, making them more readily achievable [134, 135]. In these alternative orientations, it is certain that the degeneracy structure would be different and hence the topological phase diagrams would be different also. We speculate that there are parameter regimes that show a greater prospect of partial or complete band gaps. Determining if and where they overlap with the topologically non-trivial parameter regimes should be the pertinent thing to consider from the offset if adopting systems of this type. This question is, however, beyond what we have considered in this thesis and represents a possible future direction of exploration.

This analysis could equally have considered any of the other three theories of topologically non-trivial photonic crystals developed in chapter 3 and 4. We would expect that had this been done the results would have been largely similar.

5.5 Conclusion

In this chapter we have studied the bulk-boundary correspondence of topologically non-trivial materials. The nature of this correspondence in each material needs to be independently investigated. In systems that have a complete bulk band-gap,

the corresponding edge theory emerges in a straightforward fashion for myriad boundary conditions. In materials that lack such a complete gap, however, the situation is somewhat more complicated. In these cases the boundary conditions can allow only partial edge states or frustrate edge state appearance entirely. Regarding the former, these partial edge state solutions are localised in one of the directions but extended in the perpendicular direction. The appearance of edge states is therefore dependent on the orientation of the termination considered.

In section 5.2 we investigated the importance of the termination orientation as well as the presence or absence of a complete bulk band-gap on edge state formation in the case of a hard wall boundary condition. To do this, we considered an adapted Chern insulator model with parameters that can close the bulk band-gap in either the x or y directions without altering the topological phase. By using a transfer-matrix type approach we discovered that, as the band-gap closed along the line at which the edge states previously crossed, there is a present/absent transition of the edge states over the entire relevant wavevector range. When, instead, the bulk band gap closes in the perpendicular direction, we see that the edge states persist. This means that partial edge states are possible when a complete bulk band-gap is absent.

We then, in section 5.3, considered an alternative geometry - one that includes the adjacent topologically trivial material explicitly. The adjacent material we considered was a Chern insulator of a similar form to that of the preceding section but in a topologically trivial parameter regime. In this geometry we observed that the abrupt present/absent transition of the edge states was replaced by a continuous shrinkage of their wavevector extent and their eventual complete disappearance as the overall curvature was increased.

In section 5.4 we used the insights from section 5.2 to examine the prospect of edge states for the bulk photonic crystal models of chapters 3 and 4. As a representative case we considered the square patterned photonic crystals composed of chiral biaxial materials with a hard wall boundary. For these systems, the strength of the optical activity is the critical determiner of whether partial or complete band-gaps exist. Consequently, the strength of the optical specific rotation determines whether edge states are possible in this geometry. We found that in some parameter regimes partial edge states are possible. By examining the corresponding finite geometry band structures, as well as the polarisation-summed eigenvector densities, we verified the existence of these predicted edge states. We further confirmed that these edge states are topological in nature by comparison with the finite geometry band structure and eigenvectors in the topologically trivial regime. These partial edge states exist in parameter regimes representing artificially large optical activity such that producing a photonic crystal with the necessary properties would be challenging. Nevertheless, there are myriad possible optimisations to the design of

these optical systems which could reduce the need for such large optical activity somewhat.

Chapter 6

Magneto Exciton Polaritons in Bulk Semiconductors

6.1 Introduction

In this chapter we are interested in the topological features of the solutions to the wave equation, for light propagating through a bulk semiconductor in a magnetic field. In these semiconductors the electronic band structure features a set of valence bands energetically separated from a set of conduction bands. The electronic band structure dictates the dielectric behaviour of the semiconductor which around the band edge is heavily frequency dependent [92].

The zero temperature electronic ground state of a semiconductor can be envisaged as an arrangement of electrons completely filling a set of valence bands leaving the conduction bands completely unoccupied. This ground state configuration can be optically excited resulting in the transfer of a valence band electron to the conduction band [140]. The resulting state differs from the ground state by the presence of the excited electron in the conduction band and the absence of the electron in the valence band. This electronic absence in the valence band can be viewed as a hole possessing the opposite properties (charge, spin, etc.) to those of the missing electron. The viewpoint of conduction band electrons and valence band holes enables one to think of the ground state of the semiconductor as being one with no particles and the first excited state as featuring one of each [141]. These are however not free particles but rather emergent excitations of multi-particle electron systems [18]. These excitations have some similar properties to the corresponding free particle, but in other ways show significant deviance.

This view of the electronic ground state and the first excited state of semiconductors allows a perspective on the dielectric behaviour. The electronic contribution to the dielectric behaviour arises from transitions between one arrangement of electrons and another. In this picture the frequency difference between the individual electrons in each configuration determines the frequency at which that transition contributes to the dielectric function [142]. Following this logic we would

expect that the dielectric function will have an abrupt feature at the frequency corresponding to the onset of transitions, i.e. the band gap frequency. Although this description is useful as an introductory tool, the near band-edge dielectric behaviour of real semiconductors is more complex [18]. In particular, in the first excited state described above, the conduction electron and valence hole interact with each other via the Coulomb force as well as an exchange interaction [141], and more complex correlation effects. The Coulomb force allows the formation of a bound state known as an exciton. The exciton has a series of bound energy levels below the conduction band edge. Above the conduction band edge the conduction electron and valence hole are unbound but nonetheless interacting [93]. The bound exciton states and the unbound Coulomb interacting conduction electron and valence hole, rather than the free electrons and holes, are what determine the optical response of realistic semiconductors.

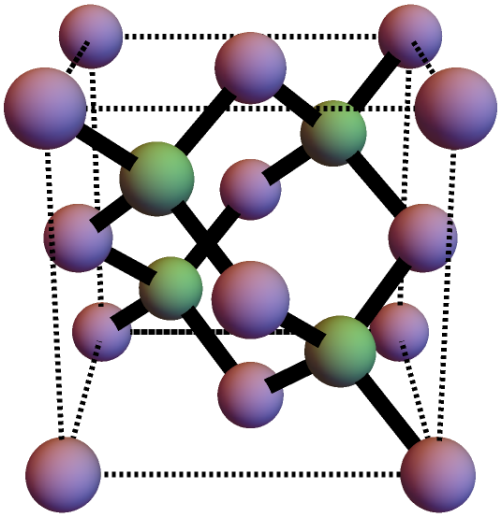

FIGURE 6.1: Illustration showing the real space unit cell composition of a zincblende lattice structure. The different coloured inclusions represent atoms of two distinct species.

The dielectric behaviour close to the band edge will be dominated by exciton effects, but how do we determine the nature of the excitons and how their coupling to light emerges? To do this we must return to the electronic band structure of the semiconductor. For this chapter we focus on direct band-gap zincblende semiconductors. The zincblende structure, shown in figure 6.1, consists of two inter-penetrating face centred cubic lattices of two distinct atomic species. The two species are typically group III and group V elements or group II and group VI elements. For either type of constituent pair, the valence band structure of the semiconductor is similar. The valence bands of these systems are made from p-like atomic orbitals with orbital angular momentum $l = 1$ [143]. When the orbital motion is coupled to the electronic spin, as occurs in semiconductors, the total angular momentum states $\mathbf{J} = \mathbf{L} + \mathbf{S}$ result. In this instance there are $j = \frac{3}{2}$ and

$j = \frac{1}{2}$ states [142]. The spin-orbit interaction of the semiconductor differentiates between the two **J** states typically displacing the $j = \frac{1}{2}$ downward in energy [144]. The valence bands with $j = \frac{3}{2}$ are themselves split for non-zero **k** according to the projection of **J** along **k**. The bands with $j_z = \frac{3}{2}$ are termed the heavy hole valence bands and those with $j_z = \frac{1}{2}$ are known as the light hole bands due to their differing inverse curvatures. The conduction band $\mathbf{k} = 0$ state is composed of s-type atomic orbitals with $l = 0$. The total angular momentum of the conduction band states including spin is thus $\sigma = \frac{1}{2}$. Figure 6.2 shows an illustration of the band structure of the semiconductors which we consider.

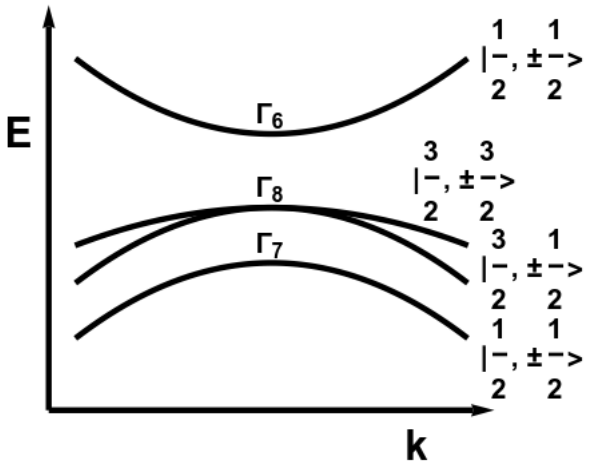

FIGURE 6.2: An illustration of the typical form of electronic band structure of a zincblende semiconductor. The bands are labelled on the right by their total angular momentum and z-projection $|j, j_z\rangle$. The labelling of each band at the centre correspond to the transformation properties of the $k = 0$ wavefunctions.

To describe the excitons formed in a semiconductor possessing a band structure similar to that seen in figure 6.2, we must take proper account of the degeneracy and anisotropy of the valence bands. We must also consider the strength of the Coulomb interaction between the electron and hole. In this regard there are two extreme situations; the tightly-bound exciton case where the electron and hole are separated by at most a few unit cells and the weakly-bound exciton case where the electron and hole are separated by many unit cells [18]. In the latter case the Coulomb interaction is screened by the dielectric constant which, due to the averaging over many cells, can be approximated by its static value [141]. In this chapter we shall be concerned with weakly-bound excitons. The framework within which to describe the weakly-bound excitons is the effective mass approximation. This approach leads to a two-particle Schrödinger type equation in which the kinetic energy terms are appropriate to the band structure of the semiconductor including anisotropy and degeneracy. The exchange interaction of the electrons and holes can also be included within this framework. Furthermore it is possible to include magnetic fields through a minimal coupling substitution. The solution of this two-particle

equation for the exciton energies and wavefunction allows the optical response of magneto-excitons in bulk semiconductors to be determined.

The solutions of the wave equation close to the electron hole pair resonances of the dielectric function are known as polaritons [17]. These polaritons are superpositions of photons and excitons which form from the strong light-matter coupling in semiconductors. The coupling of the light and matter modifies the individual dispersions of the photon and exciton as shown in figure 6.3 [17]. In this figure we have considered an idealised isotropic semiconductor with a single conduction and valence band. In such a semiconductor the exciton spectrum is that of an hydrogen atom and the optical response is known [145, 146]. As the anisotropy and degeneracy of the valence bands of a realistic semiconductor are included, the polariton dispersion will become more complex. The introduction of a magnetic field further complicates things, resulting in a still richer polariton dispersion relation. The examination of these magneto-exciton-polariton dispersion relations are the ultimate goal of this chapter.

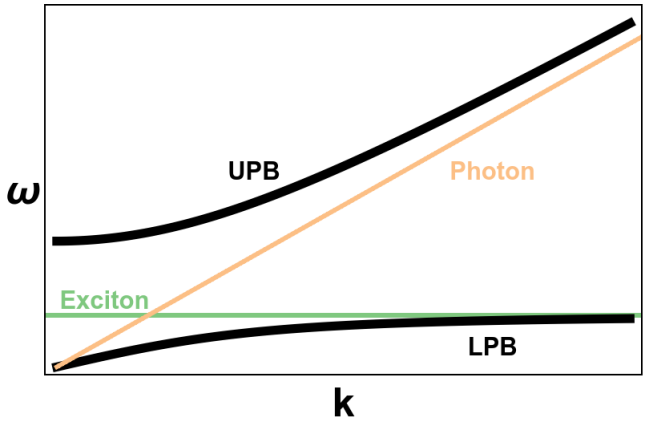

FIGURE 6.3: An illustration of the dispersion relation of a polariton resulting from the coupling of light to excitons in a semiconductor. The exciton (green) and photon (orange) dispersions anti-cross resulting in a lower and upper polariton branch (LPB and UPB).

To calculate these magneto-exciton-polariton dispersion relations we must go through a couple of preliminary stages. The first stage is to calculate the exciton spectrum in bulk semiconductors subjected to a magnetic field. In section 6.2 we calculate the exciton ground state of direct band-gap zincblende semiconductors using the Hamiltonian derived in Cho et al. [147]. This effective Hamiltonian includes the electron-hole exchange interaction, the static magnetic field, and the degeneracy and anisotropy of the valence bands. The next stage, which we carry out in section 6.3, is to derive the contribution of the exciton ground state to the dielectric susceptibility. We derive the optical response within linear response theory, resulting in an anisotropic and multiply-resonant dielectric function. In section 6.4 we explore the polariton solutions of the wave equation for this kind

of dielectric function. Initially we focus on setting up the polariton equation in subsection 6.4.1 where we introduce a 2×2 matrix approach for determining the transverse-polariton solutions. In subsections 6.4.2 and 6.4.3 we solve the polariton equation in the absence and presence of dissipation, respectively. In each situation we examine the polarisation structure of the polaritons with a particular focus on the degeneracies of the polariton dispersion relation. Finally, in section 6.5, we offer conclusions on the magneto-exciton-polaritons in bulk semiconductors.

6.2 Effective Mass Equations for Electron-Hole Pairs in Bulk Semiconductors

6.2.1 Setting up the Effective Mass Equations

The description of the loosely-bound exciton states in bulk semiconductors generally follows from the solution of a set of coupled differential equations known as the effective mass equations [141]. These equations are a form of two-particle Schrödinger equation describing conduction electrons and valence holes. The Hamiltonian which gives rise to excitons includes two types of contributions: the kinetic energy of the electrons and holes and the potential energy describing the interaction between them (and possibly also the interactions of the electron and hole with external fields). Luttinger and Kohn [148] showed how the effective mass equations for holes in semiconductors with degenerate spin-orbit coupled valence bands subjected to a magnetic field could be deduced. A similar approach has been utilised to determine the corresponding equations for excitons resulting from the Coulomb interaction between electrons and holes [149].

We are interested in determining the exciton ground state through the effective mass equations for valence band holes with Γ_8 symmetry and conduction band electrons with Γ_6 symmetry. The four-fold and two-fold degeneracies of the respective bands can be treated using the effective angular momentum operators $\underline{\underline{\mathbf{J}}}$ and $\underline{\underline{\boldsymbol{\sigma}}}$ through the method of Luttinger [150]. The $\underline{\underline{\mathbf{J}}}$ operators act only on the valence band states with $j_z = \pm\frac{3}{2}, \pm\frac{1}{2}$, while the $\underline{\underline{\boldsymbol{\sigma}}}$ operator acts only on the conduction band states with $\sigma_z = \pm\frac{1}{2}$. In each of these subspaces an arbitrary matrix can be expressed in terms of sums of independent matrices formed from $\underline{\underline{\mathbf{J}}}$ and $\underline{\underline{\boldsymbol{\sigma}}}$ respectively. In the case of the valence holes the independent matrices are

$$\begin{aligned} &\underline{\underline{\mathbb{1}}}_4,\ \underline{\underline{J}}_x,\ \underline{\underline{J}}_y,\ \underline{\underline{J}}_z,\ \underline{\underline{J}}_x^2,\ \underline{\underline{J}}_y^2,\ \{\underline{\underline{J}}_x,\underline{\underline{J}}_y\},\ \{\underline{\underline{J}}_y,\underline{\underline{J}}_z\}\ ,\ \{\underline{\underline{J}}_z,\underline{\underline{J}}_x\},\ \{(\underline{\underline{J}}_y^2-\underline{\underline{J}}_z^2),\underline{\underline{J}}_x\},\\ &\{(\underline{\underline{J}}_z^2-\underline{\underline{J}}_x^2),\underline{\underline{J}}_y\},\ \{(\underline{\underline{J}}_x^2-\underline{\underline{J}}_y^2),\underline{\underline{J}}_z\},\ \underline{\underline{J}}_x^3,\ \underline{\underline{J}}_y^3,\ \underline{\underline{J}}_z^3,\ \underline{\underline{J}}_x\underline{\underline{J}}_y\underline{\underline{J}}_z+\underline{\underline{J}}_z\underline{\underline{J}}_y\underline{\underline{J}}_x, \end{aligned} \tag{6.1}$$

where $\{\underline{\underline{A}}, \underline{\underline{B}}\} = (\underline{\underline{A}}\ \underline{\underline{B}} + \underline{\underline{B}}\ \underline{\underline{A}})/2$. For the conduction electrons the independent matrices are

$$\underline{\underline{\mathbb{1}}}_2, \ \underline{\underline{\sigma}}_x, \ \underline{\underline{\sigma}}_y, \ \underline{\underline{\sigma}}_z. \tag{6.2}$$

The independent matrices of the overall 8×8 exciton Hamiltonian are the direct products of the independent matrices of the hole and electron subspaces (6.1) and (6.2). The allowed terms in the exciton Hamiltonian are those products of powers of $\mathbf{k}$ with the matrix products that in combination have the appropriate symmetries of the Zincblende structures [151, 152]. When these combinations have been determined the system of equations describing the relative electron hole motion can be written generally as

$$\sum_{c'=1}^{2}\sum_{v'=1}^{4}\underbrace{\left[\underline{\underline{H}}^e_{cc'}(-i\boldsymbol{\nabla}_e)\otimes\underline{\underline{\delta}}_{vv'} - \underline{\underline{\delta}}_{cc'}\otimes\underline{\underline{H}}^h_{vv'}(-i\boldsymbol{\nabla}_h) - \frac{e^2}{4\pi\epsilon_0\epsilon|\mathbf{r}|}\underline{\underline{\delta}}_{cc'}\otimes\underline{\underline{\delta}}_{vv'} + \underline{\underline{H}}_{\text{exch}}\right]}_{\underline{\underline{H}}}\times$$
$$\times\,\mathbf{F}_{c'v'}(\mathbf{r}) = E\mathbf{F}_{cv}(\mathbf{r}). \tag{6.3}$$

In the above equation $\mathbf{F}_{cv}(\mathbf{r})$ is the real space envelope function of the electron-hole pair, $\underline{\underline{H}}^e$ is the Hamiltonian governing the kinetic energy contributions of the conduction electrons, $\underline{\underline{H}}^h$ is the Hamiltonian governing the kinetic energy contributions of the holes and $\underline{\underline{H}}_{\text{exch}}$ is the electron-hole exchange. The third term is the Coulomb interaction between the electrons and holes. In this term $\mathbf{r} = \mathbf{r}_e - \mathbf{r}_h$ is the separation of the electron and hole and ϵ is the static dielectric constant, taking account of the screening due to the electronic and lattice polarisation. Individually the electron, hole and exchange Hamiltonians $\underline{\underline{H}}^e$, $\underline{\underline{H}}^h$ and $\underline{\underline{H}}_{\text{exch}}$ are [152]

$$\underline{\underline{H}}^e_{cc'}(-i\boldsymbol{\nabla}_e) = \underline{\underline{H}}^e_{cc'}(\mathbf{k}_e) = \underline{\underline{H}}^e_{cc'}(\mathbf{k}) = \frac{\hbar^2k^2}{2mm^*_e}\underline{\underline{\mathbb{1}}}_2, \tag{6.4}$$

$$-\underline{\underline{H}}^h_{vv'}(-i\boldsymbol{\nabla}_h) = -H^h_{vv'}(\mathbf{k}_h) = -H^h_{vv'}(-\mathbf{k}) = \frac{\hbar^2}{2m}\Big((\gamma_1+\frac{5}{2}\gamma_2)k^2\underline{\underline{\mathbb{1}}}_4 - 2\gamma_2(k_x^2\underline{\underline{J}}^2_x +$$
$$+\,k_y^2\underline{\underline{J}}^2_y + k_z^2\underline{\underline{J}}^2_z) - 4\gamma_3(k_xk_y\{\underline{\underline{J}}_x,\underline{\underline{J}}_y\} + k_yk_z\{\underline{\underline{J}}_y,\underline{\underline{J}}_z\} + k_zk_x\{\underline{\underline{J}}_z,\underline{\underline{J}}_x\})\Big), \tag{6.5}$$

$$\underline{\underline{H}}_{\text{exch}} = \Delta_0\underline{\underline{\mathbb{1}}} + \Delta_1(\underline{\underline{\boldsymbol{\sigma}}}\cdot\underline{\underline{\mathbf{J}}}) + \Delta_2(\underline{\underline{\boldsymbol{\sigma}}}\cdot\underline{\underline{\mathbf{J}}}^3). \tag{6.6}$$

In equations (6.4) and (6.5), the penultimate equality comes from the consideration of vertical transitions to excitons with wave vector $\mathbf{K} = k_e + k_h \simeq 0$ [140]. The set of parameters $(m^*_e, \gamma_1, \gamma_2, \gamma_3)$ represent the conduction band effective mass and the three Luttinger parameters respectively [150]. They are typically set from experimental values and describe the curvature of the conduction and valence bands as well as the anisotropy of the valence bands of the semiconductor in question. The parameters $(\Delta_0, \Delta_1, \Delta_2)$ describe the overall energy shift due to the

exchange interaction, the isotropic exchange shift and the anisotropic exchange shift. In the above equation we have omitted the small k-linear terms in the valence Hamiltonian $\underline{\underline{H}}^h$. This omission is justified in work by Baldereschi and Lipari [153]. The system of equations for the envelope functions $\mathbf{F}_{cv}(\mathbf{r})$ describe the excitons formed in bulk semiconductors with realistic valence bands.

The effect of an external magnetic field $\mathbf{B}$ on the relative electron hole motion in a semiconductor can be included by the addition of the new invariant forms which result from combinations of $\mathbf{B}$, $\mathbf{k}$ and the products of the matrices (6.1) and (6.2). Together these additional contributions describe the Zeeman effect of the conduction electrons and valence holes as well as the orbital diamagnetism. The inclusions of both of these effects can be achieved by the replacements [154]

$$\underline{\underline{H}}^e(\mathbf{k}) \to \underline{\underline{H}}^e(\mathbf{k} + e\mathbf{A}) + g^*\mathbf{B} \cdot \underline{\underline{\boldsymbol{\sigma}}} \tag{6.7}$$

and

$$\underline{\underline{H}}^h(-\mathbf{k}) \to \underline{\underline{H}}^h(-\mathbf{k} + e\mathbf{A}) + \kappa\mathbf{B} \cdot \underline{\underline{\mathbf{J}}} + q\mathbf{B} \cdot \underline{\underline{\mathbf{J}}}^3 \tag{6.8}$$

in the original Hamiltonians $\underline{\underline{H}}^e$ and $\underline{\underline{H}}^h$. In the equations (6.7) and (6.8) above $\mathbf{A}$ is the vector potential of the external field. The inclusion of a magnetic field has introduced an additional three parameters (g^*, κ, q) to the electron-hole relative motion Hamiltonian. These new parameters describe the effective magnetic moment of the conduction electrons, the effective magnetic moment of the valence holes and the anisotropic g-factor of the valence holes respectively [150]. Solution of the set of equations (6.3) with the replacements (6.7) and (6.8) therefore determines the energy spectrum of well-separated electron-hole pairs in bulk semiconductors subjected to a magnetic field. The solution of these equations is not however a straightforward proposition, as we now discuss.

6.2.2 Solving the Effective Mass Equations

The solution of the exciton effective mass equations is not in general possible and instead one must resort to approximate methods. One of these approximate methods is to use a variational approach [155], in which the ground state energy of the system is minimised within a class of trial solutions [156–159]. Another method is to adopt a perturbation theory approach [153, 160–163]. This approach is tractable as the exciton effective mass equations are sufficiently close to that of a hydrogen atom with modified mass and dielectric constant. The "hydrogen atom" in this instance is formed from the Coulomb binding between the conduction electrons and the isotropic part of the valence hole $\underline{\underline{H}}_0 = (\frac{p^2}{2\mu_0} - \frac{e^2}{4\pi\epsilon_0\epsilon|\mathbf{r}|})\underline{\underline{\mathbb{1}}}_8$. The reduced mass μ_0 of the electron and hole is

$$\frac{1}{\mu_0} = \frac{1}{m}\left(\frac{1}{m_e^*} + \gamma_1\right) \tag{6.9}$$

and hence the exciton Rydberg energy and exciton Bohr radius are

$$R_0 = \frac{\mu_0 e^4}{32\pi\epsilon_0\epsilon\hbar^2} \ , \ a_0 = \frac{4\pi\epsilon_0\epsilon\hbar^2}{e^2\mu_0}. \tag{6.10}$$

The unperturbed 1s exciton ground state is eightfold degenerate at energy $E = E_g - R_0$, where E_g is the band-gap energy. The usage of the effective mass formalism can be self-consistently justified by comparing a_0 to the lattice constant a of the material considered. If $a_0 >> a$ then the average separation of the electron and hole is many lattice sites and the effective mass equation framework was warranted.

In the absence of a magnetic field the remaining part of the exciton Hamiltonian $\underline{\underline{H}} - \underline{\underline{H}}_0$ features the d-like operators $\underline{\underline{H}}_d$ (i.e. those which when expressed in terms of spherical harmonics exclusively feature terms with $l = 2$ [153]) as well as the exchange interaction $\underline{\underline{H}}_{\text{exch}}$. The introduction of a magnetic field introduces additional perturbative parts, $\underline{\underline{H}}_l$ and $\underline{\underline{H}}_q$, which are linear and quardatic in the magnetic field. In first order degenerate perturbation theory $\underline{\underline{H}}_l$, $\underline{\underline{H}}_q$ and $\underline{\underline{H}}_{\text{exch}}$ give non-vanishing contributions [162, 163]. To second order, the nd hydrogenic states contribute through $\underline{\underline{H}}_d$, $\underline{\underline{H}}_l$ and $\underline{\underline{H}}_q$ as well as the ns states through $\underline{\underline{H}}_q$ [154]. The work of Cho et al. [147] showed that an effective Hamiltonian describing the 1s exciton ground state could be derived using this perturbative approach. The 1s exciton Hamiltonian takes the form

$$\begin{aligned}\underline{\underline{H}} =& E_B \underline{\underline{\mathbb{1}}}_8 + \tilde{\Delta}_1 \underline{\underline{\boldsymbol{\sigma}}} \cdot \underline{\underline{\mathbf{J}}} + \tilde{\Delta}_2 \underline{\underline{\boldsymbol{\sigma}}} \cdot \underline{\underline{\mathbf{J}}}^3 + \tilde{g}_c \mu_B \mathbf{B} \cdot \underline{\underline{\boldsymbol{\sigma}}} \otimes \underline{\underline{\mathbb{1}}}_4 - 2\mu_B \underline{\underline{\mathbb{1}}}_2 \otimes \left[\tilde{\kappa}\mathbf{B} \cdot \underline{\underline{\mathbf{J}}} + \tilde{q}\mathbf{B} \cdot \underline{\underline{\mathbf{J}}}^3\right] \\ &+ \left(\frac{ea_0}{2c}\right)^2 \frac{1}{\mu_0} \underline{\underline{\mathbb{1}}}_2 \otimes \left[c_1 B^2 \underline{\underline{\mathbb{1}}}_4 + c^2 (\mathbf{B} \cdot \underline{\underline{\mathbf{J}}})^2 + c_3 (B_x B_y \{\underline{\underline{J}}_x, \underline{\underline{J}}_y\} + B_y B_z \{\underline{\underline{J}}_y, \underline{\underline{J}}_z\} \right. \\ &\left. + B_z B_x \{\underline{\underline{J}}_z, \underline{\underline{J}}_x\})\right]\end{aligned} \tag{6.11}$$

The coefficients in (6.11) are expressible in terms of the material parameters of the Hamiltonian eqs. (6.4) to (6.8):

$$E_B = E_g - R_0 + \Delta_0 - b_1, \tag{6.12}$$

$$\tilde{\Delta}_1 = \Delta_1, \tag{6.13}$$

$$\tilde{\Delta}_2 = \Delta_2, \tag{6.14}$$

$$\tilde{g}_c = g, \tag{6.15}$$

$$\tilde{\kappa} = \kappa - d - \frac{13}{6} d(\tau - 1), \tag{6.16}$$

$$\tilde{q} = q + \frac{2}{3} d(\tau - 1), \tag{6.17}$$

$$c_1 = 1 - \nu - \frac{5}{4}\delta', \tag{6.18}$$

$$c_2 = \delta', \tag{6.19}$$

$$c_3 = 2\delta'\left(\frac{1}{\tau} - 1\right). \tag{6.20}$$

In the equation (6.12) the b_1 addition to E_B comes from the second order degenerate perturbation theory contribution of $\underline{\underline{H}}_d^2$. The additions in $\tilde{\kappa}$, equation (6.16), and $\tilde{q}$, equation (6.17), arise from the second order $\underline{\underline{H}}_d\underline{\underline{H}}_l$ perturbation. The extra terms in equation (6.18) arise from the second order contributions of $\underline{\underline{H}}_l^2$ and $\underline{\underline{H}}_d\underline{\underline{H}}_q$ with the former also contributing to equations (6.19) and (6.20). The parameters $(b_1, d, \tau, \nu, \delta')$ are related to the Luttinger parameters by:

$$\begin{aligned}
b_1 &= \frac{1}{R_0 a_0^4}\frac{\hbar^4}{5m^2}(2\gamma_2^2 + 3\gamma_3^2)S_1, \\
d &= \frac{32}{5}\frac{\mu_0}{m}\gamma_3^2 M, \\
\tau &= \frac{\gamma_2}{\gamma_3}, \\
\nu &= \frac{16}{15}\left(\frac{\mu_0\gamma_2}{m}\right)^2\left(2 + \frac{3}{\tau^2}\right)(3N + W), \\
\delta' &= \left(1 + \frac{16}{15}W\right)\frac{\mu_0\gamma_2}{m}.
\end{aligned} \tag{6.21}$$

The constants S_1, M, N and W come from dimensionless sums over intermediate states and are given by:

$$\begin{aligned}
S_1 &= 0.2246, \\
M &= 0.281, \\
N &= 0.469, \\
W &= 0.719.
\end{aligned} \tag{6.22}$$

The derived Hamiltonian (6.11) is valid in the low magnetic field region. This region is defined by the condition that the exciton Rydberg R_0 and the cyclotron energy $\hbar\omega_c$ satisfy [154]

$$\gamma \equiv \frac{1}{2}\frac{\hbar\omega_c}{R_0} = \frac{e\hbar|\mathbf{B}|}{2\mu_0 R_0} \leq 0.4. \tag{6.23}$$

The condition (6.23) distinguishes the regime $\gamma \leq 0.4$ where we can think of the Zeeman splitting of hydrogenic excitons from the regime $\gamma >> 1$ where the Coulomb interaction is a perturbation on the electron and hole Landau levels. We shall henceforth focus on the regime $\gamma \leq 0.4$ where perturbation theory is applicable.

At zero magnetic field, and assuming $\Delta_2 = 0$, the eigenstates of the Hamiltonian (6.11) are those of total angular momentum $\mathbf{I} = \mathbf{J} + \boldsymbol{\sigma}$. These states diagonalise the Δ_1 exchange interaction and result in an exciton spectrum where the $i = 2$ states are five-fold degenerate and the $i = 1$ states are three-fold degenerate.

The effect of the magnetic field, barring any hyper-tailored sets of parameters, is to lift the degeneracies of the exciton ground state. As this degeneracy is lifted, the magnetic field contribution competes with the exchange interaction to determine the nature of the solutions of equation (6.11). At zero field the states are eigenstates of i and i_z, while as the magnetic field increases the states tend increasingly towards being eigenstates of j_z and σ_z. As the boundary of the perturbative regime is reached ($\gamma = 0.4$) the latter description is the more relevant way of thinking of the exciton solutions.

The energy ordering of the excitons upon introduction of a magnetic field is particular to each semiconductor. To describe the exciton ground state in any material we need data on the previously mentioned semiconductor parameters. We have chosen to make use of the data provided by Winkler [164], which is reproduced in table 6.1 below for convenience. The exchange parameters Δ_1 were taken from Fu et al. [165], where in the cases for which the authors had not calculated the isotropic exchange parameter we have used their interpolation formula.

Material		GaAs	InSb	InAs	InP	CdTe	ZnSe
E_g	eV	1.519	0.237	0.418	1.423	1.606	2.82
P	eVÅ	10.493	9.641	9.197	8.85	9.496	10.628
Q	eVÅ	8.165	8.13	8.331	7.216	7.873	9.845
m^*		0.0665	0.0139	0.0229	0.0803	0.09	0.16
g^*		-0.44	-51.56	-14.9	1.26	-1.77	1.06
γ_1		6.85	37.1	20.4	4.95	5.3	4.3
γ_2		2.1	16.5	8.3	1.65	1.7	1.14
γ_3		2.9	17.7	9.1	2.35	2.	1.84
κ		1.2	15.6	7.6	0.97	0.61	0.2
q		0.01	0.39	0.39	0.	0.04	0.
Δ_1	μeV	-9.61	0	-0.29	-18.5	-23.02	-117.82
ϵ_b		12.5	16.8	11.8	12.1	9.7	8.7

TABLE 6.1: Material parameters of direct band gap semiconductors considered in this work. The data is taken from Winkler [164] and Fu et al. [165].

In addition to the parameters in table 6.1, we will consider $\Delta_0 = 0$ and $\Delta_2 = 0$ throughout. The former simplification amounts to omitting an overall uniform energy shift, while the latter is a comparably small effect. The data in table 6.1 allows us to describe the exciton species in each of the semiconductors considered by diagonalising the Hamiltonian (6.11). Before this, however, we shall examine the basic derived exciton descriptors for each semiconductor from this set of data. This will allow us to examine the justification of an effective mass treatment for each semiconductor.

Material		GaAs	InSb	InAs	InP	CdTe	ZnSe
R_0	meV	4.061	0.391	1.001	5.108	8.124	15.507
a_0	nm	14.285	102.73	49.233	11.358	8.745	5.075
$\frac{a_0}{a}$		25.269	158.559	81.267	19.353	13.488	8.967
$B_{\max}$	T	1.286	0.025	0.108	2.035	3.432	10.191

TABLE 6.2: Derived exciton parameters of direct band gap semiconductors considered in this work.

Table 6.2 gives the exciton Rydberg energy R_0, the exciton Bohr radius a_0, the ratio of the Bohr radius a_0 to the lattice constant a and the magnetic field $B_{\max}$ such that $\gamma = 0.4$ for each of the semiconductors of table 6.1. We see that in each case the effective mass formalism is justified, the case of ZnSe is the most marginal but still has an average separation of $\simeq 9$ lattice constants. The maximum allowed magnetic field depends linearly on the exciton Rydberg energy, as such those with the largest binding energy have the largest allowed magnetic field. The extreme values of the magnetic field $B_{\max}$ for each semiconductor such that the perturbative approach is still valid are the points at which there will be maximum splitting of the electron hole pairs, within this framework at least. We now examine the dependence of the exciton ground state on the magnetic field.

Figure 6.4 shows the splitting of exciton ground state of bulk semiconductors as a magnetic field is introduced. Each panel of figure 6.4 considers one of the six semiconductors from table 6.1. Each panel considers a magnetic field along the z-axis and is plotted over the range $B_z \in [0, B_{\max}]$. In each figure, the exciton is labelled and coloured according to the polarisation of light that excites that exciton. Strictly speaking we have coloured the excitons on the basis of their character at $B_z = B_{\max}$ as at zero magnetic field only the three $i = 1$ excitons couple to light [152]. At $B_z = B_{\max}$ the excitons are effectively electron hole pairs and hence six of them are optically active. The basis for the individual colourings will be addressed in the section to come. By considering each panel we see that there is generally no particular pattern to the energy ordering of the excitons between each semiconductor.

Our interest is in establishing the optical response of these magneto-excitons with a view to examining the behaviour of the polaritons that propagate in these bulk magnetically biased semiconductors. In examining the optical response due to excitons, the nomenclature of hydrogenic states is typically adopted. The allowed optical transitions are to the s-like excitonic states. In most cases it is difficult to see excitonic features in the optical response for $n \geq 2$ as the hydrogen-like levels become closer spaced and rapidly approach the band edge [140]. Additionally, as the principal quantum number n increases the optical transition strengths of each of the exciton levels decreases roughly like n^{-3} [17]. In conjunction, the closer spaced

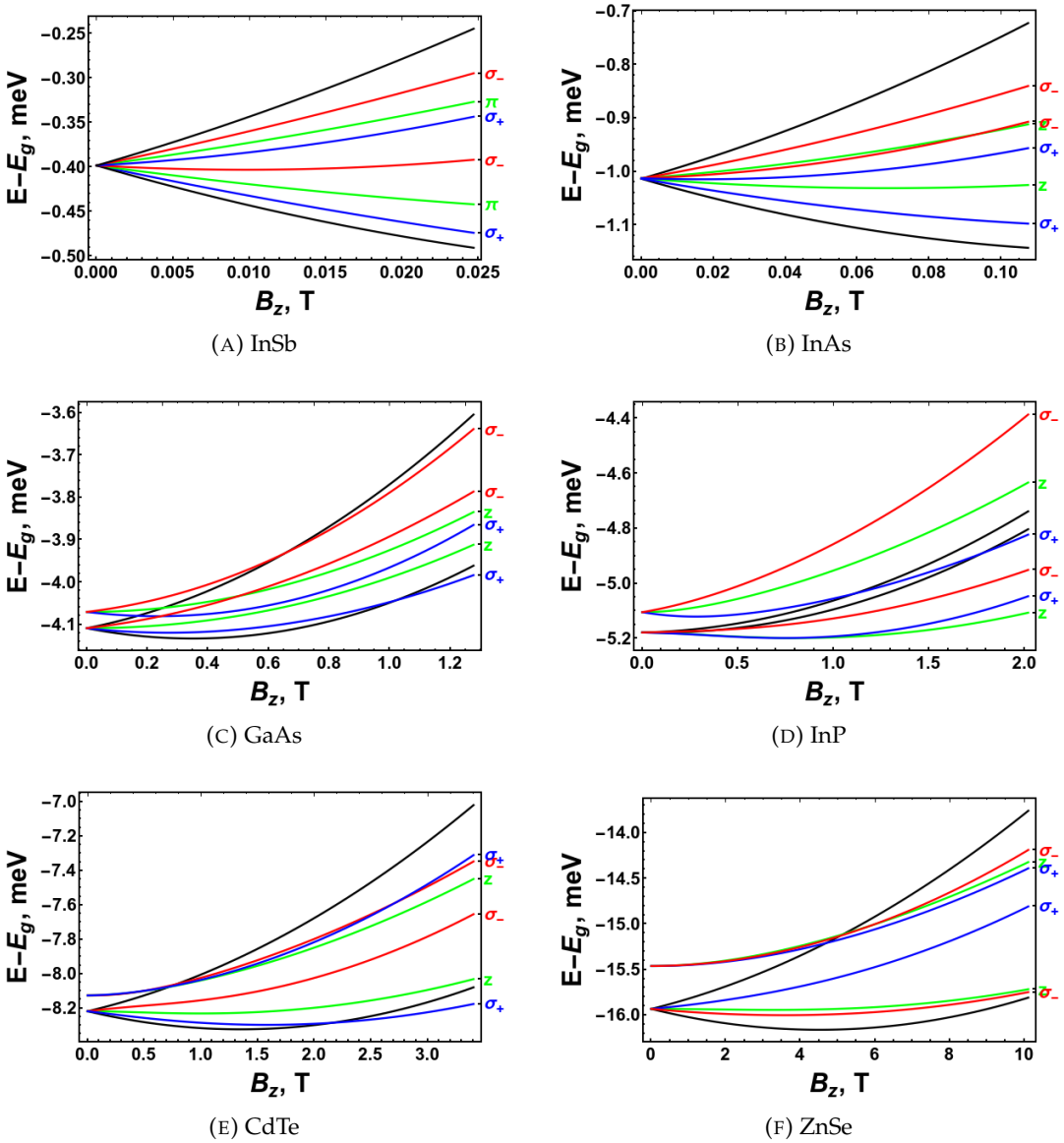

(A) InSb (B) InAs

(C) GaAs (D) InP

(E) CdTe (F) ZnSe

FIGURE 6.4: Dependence of the 1s exciton binding energy on magnetic field for the six direct band-gap zincblende semiconductors in table 6.1. In each case the material is labelled underneath the plot. The 1s exciton energies are plotted in the range of magnetic fields for which $B_z \leq B_{\text{max}}$ (see table 6.2). The excitons are coloured according to the polarisation of light to which they couple which are given at the right border of each plot. The excitons coloured in black are optically dark.

exciton levels and the weaker transition strengths mean that the $n = 1$ exciton levels give the most important contribution to the optical response below the band edge. This is of course an idealisation, in which the exciton energy levels are perfectly hydrogenic, however given that the departures of the magneto-excitons from the hydrogenic solutions are small, the perturbed 1s exciton ground state remain the dominant contribution to the optical response.

6.3 Optical Response of Bulk Magneto-Excitons

We now turn to assessing how the $1s$ magneto-exciton ground state couples to light. We are particularly interested in how the polarisation structure of the allowed optical transitions emerges. Our goal for this section is therefore to derive the dielectric function of general magnetically-biased zincblende semiconductors close to their conduction band edge. We expect the dielectric function to be anisotropic and heavily frequency dependent close to the electron-hole pair resonances.

To achieve this goal we shall use the framework of independent particle linear response theory to express the optical susceptibility due to transitions between the semiconductor ground state $|0\rangle$ and the one exciton state which is expressed as

$$\begin{aligned} X &= \sum_{c=1}^{2}\sum_{v=1}^{4}\sum_{\mathbf{k}_e,\mathbf{k}_h} \mathbf{A}_{c,v}(\mathbf{k}_e,\mathbf{k}_h)\psi_{c,\mathbf{k}_e}(\mathbf{r}_e)\psi_{v,\mathbf{k}_h}(\mathbf{r}_h) \\ &= \sum_{q=1}^{8} \mathbf{X}_q(\mathbf{r}_e,\mathbf{r}_h). \end{aligned} \tag{6.24}$$

In equation (6.24) above, ψ_c and ψ_v are respectively the Bloch functions of the allotted conduction band and valence band. $\mathbf{A}_{c,v}$ is the wavevector space envelope function, which is the Fourier transform of the solution of the effective mass equation $\mathbf{F}_{c,v}$. $\mathbf{X}_q$ is the q-th excitonic state where $q \in [1,4]$ corresponds to all $c = 1$ parts and $q \in [5,8]$ to all possible $c = 2$ parts. The optical susceptibility is calculated by taking matrix elements of the electric dipole operator, $e\mathbf{r}$, between the crystal ground state and the exciton states [166]. The matrix elements of the dipole operator are then weighted by an energy denominator, which specifies the position of the relevant electron hole pair resonances. The susceptibility is

$$\epsilon_0\chi_{ij} = e^2\sum_{X_q}\left[\frac{\langle X_q|r_i|0\rangle\langle 0|r_j|X_q\rangle}{E+(E_{X_q}-E_0)+i\Gamma_{X_q0}} - \frac{\langle X_q|r_j|0\rangle\langle 0|r_i|X_q\rangle}{E-(E_{X_q}-E_0)+i\Gamma_{X_q0}}\right]. \tag{6.25}$$

In the equation for the optical susceptibility, the Γ_{X_q0} which appear in the denominators, represent the effect of dissipative processes which broaden a particular electron hole pair resonance. In equation (6.25) E_0 represents the energy of the maximum of the valence bands which we shall choose as our zero energy henceforth. The difficulty in determining the susceptibility is then exclusively the evaluation of the position matrix elements in equation (6.25). To achieve this evaluation we express the position matrix elements in terms of the corresponding momentum matrix elements, which are known. This is accomplished by taking matrix elements of the relation [142]

$$[H_0,\mathbf{r}] = \frac{i\hbar}{m}\boldsymbol{\pi} \tag{6.26}$$

between the crystal ground state and the one exciton state. In the relation (6.26)

above $\boldsymbol{\pi}$ differs from $\mathbf{p}$ by additional terms from relativistic effects and external fields. Provided that the magnetic field splitting of the valence and conduction bands are small compared with the band gap, which is the case for all magnetic field strengths considered, the additional terms are small and can be neglected [140]. Re-expressing for the position matrix elements establishes the desired relationship

$$\langle 0|\mathbf{r}|X_q\rangle = \frac{-i\hbar}{mE_{X_q}}\langle 0|\mathbf{p}|X_q\rangle. \tag{6.27}$$

Equation (6.27) allows us to express the susceptibility (6.25) as

$$\epsilon_0\chi_{ij} = \frac{e^2\hbar^2}{m^2}\sum_q \frac{1}{(E_{X_q}-E_0)^2}\left[\frac{\langle X_q|p_i|0\rangle\langle 0|p_j|X_q\rangle}{E+E_{X_q}+i\Gamma_{X_q0}} - \frac{\langle X_q|p_j|0\rangle\langle 0|p_i|X_q\rangle}{E-E_{X_q}+i\Gamma_{X_q0}}\right]. \tag{6.28}$$

Given that, at the maximum allowed field strength, the excitons are exceedingly close to being electron-hole pairs from a single pair of valence and conduction bands, we will make the approximation of treating them as such. This approximation allows a more direct computation of the dielectric behaviour. To maintain the validity of this approximation we shall therefore fix the magnetic field at its maximum allowed value. The susceptibility is then determined by evaluating the momentum matrix elements between the crystal ground state and each possible pair of excited electron hole pairs. These eight matrix elements can be calculated by exploiting the atomic s and p-like symmetries of the $k = 0$ Bloch wavefunctions. This allows us to write each of the matrix elements in terms of the Kane parameter P of the chosen semiconductor and the hydrogenic $1s$ exciton real space envelope function F_q [18, 140, 167]

$$\begin{aligned}
\langle X_1|\mathbf{p}|0\rangle &= \mathbf{0},\\
\langle X_2|\mathbf{p}|0\rangle &= F_2^*(0)\left(\frac{m}{\hbar}\right)|P|\left(\frac{i}{\sqrt{6}},\frac{1}{\sqrt{6}},0\right),\\
\langle X_3|\mathbf{p}|0\rangle &= F_3^*(0)\left(\frac{m}{\hbar}\right)|P|\left(0,0,\sqrt{\frac{2}{3}}i\right),\\
\langle X_4|\mathbf{p}|0\rangle &= F_4^*(0)\left(\frac{m}{\hbar}\right)|P|\left(\frac{-i}{\sqrt{2}},\frac{1}{\sqrt{2}},0\right),\\
\langle X_5|\mathbf{p}|0\rangle &= F_5^*(0)\left(\frac{m}{\hbar}\right)|P|\left(\frac{i}{\sqrt{2}},\frac{1}{\sqrt{2}},0\right),\\
\langle X_6|\mathbf{p}|0\rangle &= F_6^*(0)\left(\frac{m}{\hbar}\right)|P|\left(0,0,\sqrt{\frac{2}{3}}i\right),\\
\langle X_7|\mathbf{p}|0\rangle &= F_7^*(0)\left(\frac{m}{\hbar}\right)|P|\left(\frac{-i}{\sqrt{6}},\frac{1}{\sqrt{6}},0\right),\\
\langle X_8|\mathbf{p}|0\rangle &= \mathbf{0}.
\end{aligned} \tag{6.29}$$

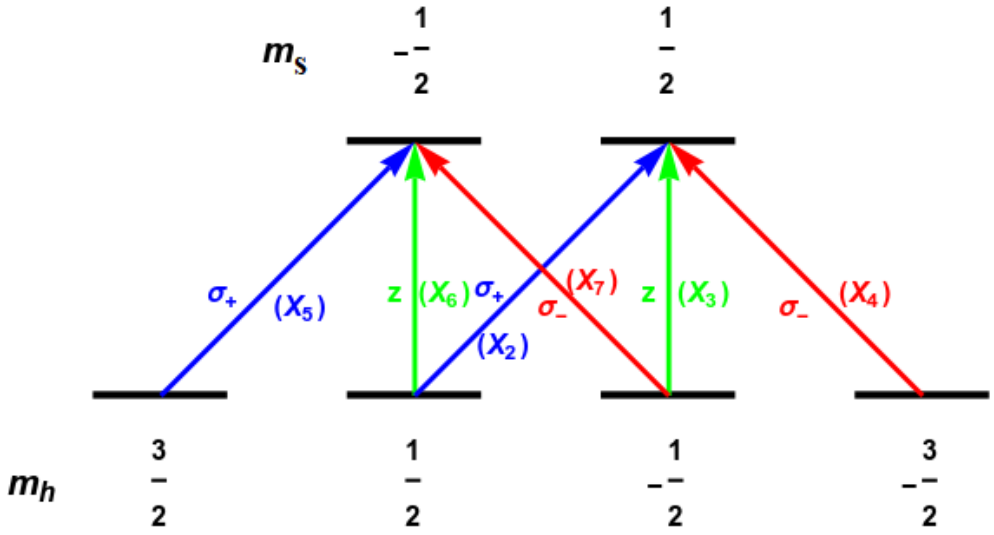

FIGURE 6.5: Optical transition structure between the crystal ground state and the eight possible first excited states for $\mathbf{B} \parallel \mathbf{z}$. These eight possible excited states consist of every possible pair of the two types of conduction electrons and four types of valence holes. Six of these eight transitions are optically allowed and are represented by coloured arrows. The colour of these arrows represents the necessary polarisation of light to induce this transition and the associated electron-hole pair is indicated in parentheses.

The real space envelope factors F_q can be approximated by the unperturbed hydrogenic result

$$|F_q(0)|^2 \simeq \frac{1}{\pi a_0^3} \ \forall \, q. \tag{6.30}$$

If one wished to go beyond this approximation one would have to account for the small mixing in of d states from the perturbations. This would likely introduce a dependence of the oscillator strengths on the exchange interaction as in the work of Ekardt et al. [168], and possibly also on the magnetic field, as is the case for quantum well excitons in microcavities [169, 170]. Neglecting the mixing in of d-states will marginally change the oscillator strengths of each of the transitions but not materially affect the results of the susceptibility calculation. If one wished to include the mixing, the perturbed wavefunctions are available in the work of Świerkowski [171]. Focusing on the vector structure of the momentum matrix elements (6.29), the polarisation structure of the allowed transitions can be read off. Figure 6.5 exemplifies this optical transition structure.

By examining the non-zero momentum matrix elements of (6.29), we see that the optically allowed transitions are those for which there is either zero or one unit change in the angular momentum along the z direction. The two disallowed transitions, those for which the matrix element is zero, correspond to cases where the change in angular momentum is two units. These cases are consequently known as dark excitons. In figure 6.5 we see the structure of the optically allowed

transitions. Each of the optically allowed transitions, indicated by an arrow, is coloured according to the corresponding change in angular momentum along the z direction. The blue and red transitions correspond to changes of plus and minus one unit respectively, while the green transitions correspond to an unchanged angular momentum along z. This means that the blue transitions are induced by left circularly polarised light for $\mathbf{k} \parallel \hat{\mathbf{z}}$, represented by the notation σ_+, the red transitions by right circularly polarised light for $\mathbf{k} \parallel \hat{\mathbf{z}}$, represented by σ_- and the green transitions by light which is linearly polarised along $\hat{\mathbf{z}}$, represented by Z.

Finally using equations (6.29), the susceptibility (6.28) can be re-written as a sum over poles in the form

$$\underline{\underline{\chi}}(\omega) = \sum_{q=1}^{8} \left[\frac{\underline{\underline{A}}_q}{\hbar\omega + (E_{X_q} - E_0) + i\Gamma_q} - \frac{\underline{\underline{A}}_q^*}{\hbar\omega - (E_{X_q} - E_0) + i\Gamma_q} \right]. \tag{6.31}$$

Each pole of equation (6.31) is weighted by the appropriate oscillator strength matrix $\underline{\underline{A}}_q$. The matrix structure of these $\underline{\underline{A}}_q$ enforce the optical selection rules. The dielectric function of the semiconductor close to these resonance can then be written as

$$\underline{\underline{\epsilon}}(\omega) = \epsilon_b \underline{\underline{\mathbb{1}}}_3 + \underline{\underline{\chi}}(\omega). \tag{6.32}$$

The background dielectric ϵ_b in the above equation (6.32) accounts for all the other charged components of the semiconductor which oscillate in response to the applied electric field.

The preceding analysis suggests that the natural basis for the dielectric function, that in which it is diagonal, is the LRZ basis, rather than the XYZ one. This transformation can be enacted by the matrix $\underline{\underline{S}}$ according to:

$$\underline{\underline{\epsilon}}_{LRZ} = \underline{\underline{S}}\, \underline{\underline{\epsilon}}_{XYZ} \underline{\underline{S}}^+ \tag{6.33}$$

where the matrix $\underline{\underline{S}}$ is given by

$$\underline{\underline{S}} = \begin{pmatrix} \frac{1}{\sqrt{2}} & -\frac{i}{\sqrt{2}} & 0 \\ \frac{1}{\sqrt{2}} & \frac{i}{\sqrt{2}} & 0 \\ 0 & 0 & 1 \end{pmatrix}. \tag{6.34}$$

The transformation (6.33) does indeed diagonalise the dielectric tensor. The goal of this section, to determine the dielectric function close to the 1s magneto-exciton resonances, is now complete. We shall now turn to examining the result of this derivation. Henceforth we shall focus on the case of GaAs, although the results of this section apply to any of the semiconductors considered in table 6.1. We expect that, although the fine details of the dielectric behaviour of each semiconductor will be different, the functions will be qualitatively similar. Owing to this narrowing our

focus to exclusively consider GaAs should not necessarily narrow the scope of the observations that shall be made.

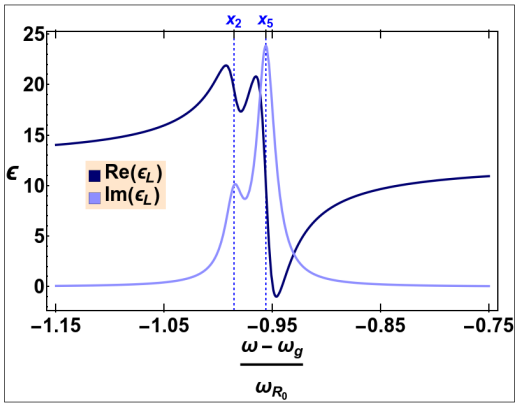

(A) ϵ_L, $\Gamma = 0.01R_0$

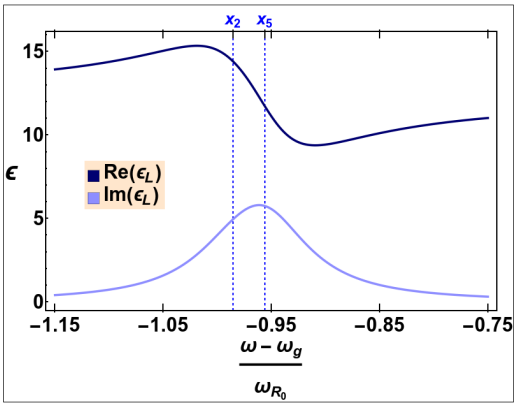

(B) ϵ_L, $\Gamma = 0.05R_0$

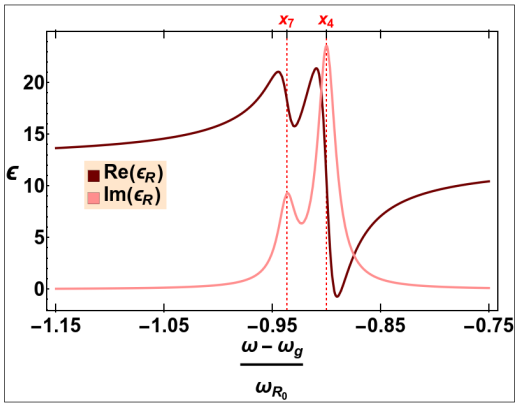

(C) ϵ_R, $\Gamma = 0.01R_0$

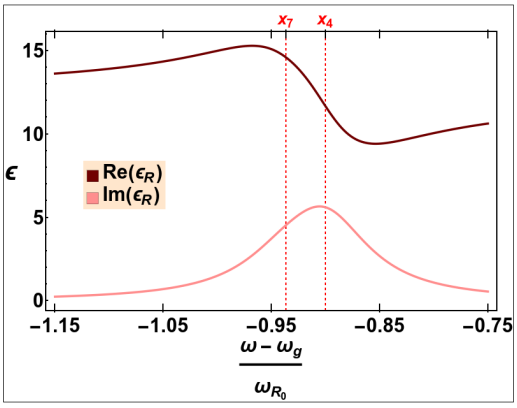

(D) ϵ_R, $\Gamma = 0.05R_0$

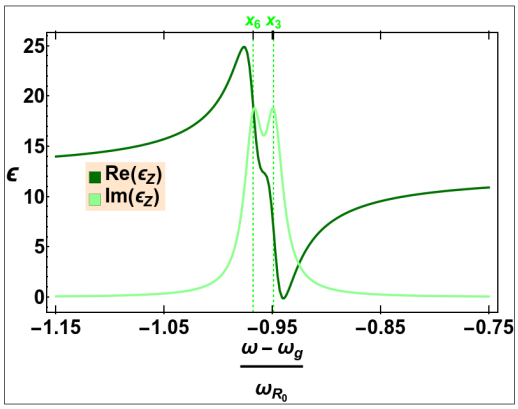

(E) ϵ_Z, $\Gamma = 0.01R_0$

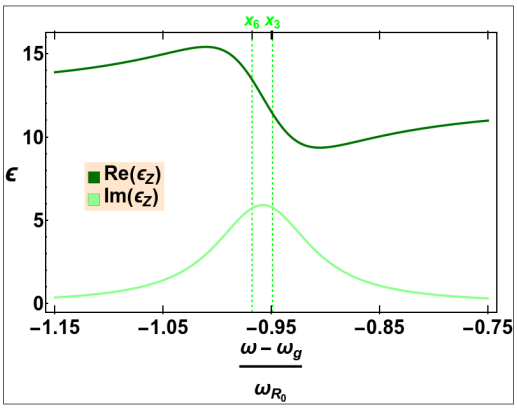

(F) ϵ_Z, $\Gamma = 0.05R_0$

FIGURE 6.6: Frequency dependence of the three non-zero components of the dielectric tensor of GaAs arising from the transitions to 1s exciton states. The three components are ϵ_L (top row), ϵ_R (middle row) and ϵ_Z (bottom row). Each column represents a different strength of damping Γ of each of the poles. The left column is for a damping $\Gamma = 0.01R_0$ and the right considers $\Gamma = 0.05R_0$.

Figure 6.6 shows the frequency dependence of the real and imaginary parts of

the dielectric function in the LRZ basis. Each of these plots considers a frequency interval close to the relevant resonances, i.e. just below the band-gap frequency. Frequency is measured relative to the band gap frequency ω_g and in units of the exciton Rydberg frequency ω_{R_0}. Each column of figure 6.6 considers a distinct constant damping common to each of the resonances. The left column considers a damping $\Gamma = 0.01R_0$ while the right column considers a damping of $\Gamma = 0.05R_0$. Each row considers a different component of the dielectric function. The top row shows the ϵ_L component of the dielectric function, the middle row shows the ϵ_R component and the bottom row shows the ϵ_Z component. Each of these plots can be understood in terms of a Lorentz oscillator model susceptibility, except in this case there are two resonances. It is easy to see these two resonances for each of the components and the relative oscillator strengths of each of the transitions. In particular, we can see the asymmetry of the oscillator strengths for the two transitions involved in ϵ_L and for the two transitions relevant to ϵ_R. Each of the poles contributing to ϵ_Z have similar oscillator strength. We further note that, as expected, the dielectric function is anisotropic, resulting from the differing frequencies of each of the six pertinent resonances.

The derivation of the dielectric function of magnetically biased bulk semiconductors is not the primary result of the chapter but rather a transitional one. We intend to use the derived dielectric functions to assess the magneto-exciton-polaritons of bulk semiconductors. The anisotropy and multi-resonant nature of the dielectric function promises richly structured polariton dispersion relations which we shall now investigate.

6.4 Magneto-Exciton Polaritons

In this section we focus on utilising the dielectric function derived in section 6.3 to determine and analyse the dispersion relation of bulk magneto-exciton-polaritons. This will first involve, in subsection 6.4.1, looking for plane-wave solutions of the wave equation when considering the anisotropic and multi-resonant dielectric functions of bulk magnetically biased semiconductors. This is facilitated by introducing a 2×2 matrix equation formalism which will better accommodate the determination of the transverse polariton solutions.

The matrix equation framework will then be used repeatedly, to examine the polariton dispersion relations in many different regimes. We will search for these polariton solutions in the frequency interval between $\omega \in [\omega_g - 1.15\omega_{R_0}, \omega_g - 0.75\omega_{R_0}]$ which contains all of the perturbed $1s$ electron hole pairs and is thus the relevant range for examining polariton effects. In subsection 6.4.2 we conduct this search in the situation where there are no dissipative effects included in the dielectric

function, whereas in subsection 6.4.3 we solve the polariton dispersion equation in a situation where there is a non-zero and variable amount of dissipation. In either situation we focus on the anisotropy of the magneto-exciton-polariton-dispersion as well as the degenerate features present therein.

6.4.1 Setting up and Solving the Magneto-Exciton Polariton Equation

In a simple cubic semiconductor the dielectric function $\underline{\underline{\epsilon}}(\omega)$ is isotropic, and exhibits a single resonance in a frequency window around the exciton Rydberg energy. Looking for plane-wave solutions to the wave equation for this material, a scalar equation emerges: $\frac{c^2k^2}{\omega^2} = \epsilon(\omega)$. This equation gives the polariton dispersion relation which is isotropic, two-branched and polarisation degenerate. However, when the dielectric function is anisotropic, the vector wave-equation has to be addressed instead. The plane-wave solutions of the wave equation in this case result in the following equation to be solved for the polariton dispersion relation:

$$-\mathbf{k}\times\mathbf{k}\times\mathbf{E} = \frac{\omega^2}{c^2}\underline{\underline{\epsilon}}(\omega)\mathbf{E}. \tag{6.35}$$

This is the vector generalisation of the equation $\left(\frac{c^2k^2}{\omega^2} = \epsilon(\omega)\right)$, giving the polariton dispersion relation, and applies to semiconductors with anisotropic dielectric functions. The equation (6.35) is similar to equation (2.17) in chapter 2 except in this case the equation is formulated in terms of the electric field **E** rather than the displacement field **D**.

Our objective is therefore to solve the equation (6.35) for the allowed $(\mathbf{k},\omega)$ of the polaritons. There are two forms of solutions to equation (6.35): longitudinal solutions with $\mathbf{k} \parallel \mathbf{E}$ and transverse solutions with $\mathbf{k} \perp \mathbf{E}$. The frequencies of the longitudinal polaritons satisfy $\hat{\mathbf{k}}^T\underline{\underline{\epsilon}}(\omega)\hat{\mathbf{k}} = 0$ for a given propagation direction $\hat{\mathbf{k}}$. To obtain the transverse polariton solutions we can simplify equation (6.35) by taking matrix elements with every combination of two unit vectors orthogonal to $\hat{\mathbf{k}}$. We shall take these two unit vectors $\hat{\mathbf{k}}_\theta$ and $\hat{\mathbf{k}}_\phi$ as

$$\begin{aligned}\hat{\mathbf{k}}_\theta &= (\cos\theta\cos\phi, \cos\theta\sin\phi, -\sin\theta)^T,\\ \hat{\mathbf{k}}_\phi &= (-\sin\phi, \cos\phi, 0)^T.\end{aligned} \tag{6.36}$$

This procedure eliminates the longitudinal polariton solutions producing a 2×2 matrix problem for the transverse polariton solutions

$$k^2\underline{\underline{\mathbb{1}}}_2\mathbf{E}_\perp = \left[\frac{\omega^2}{c^2}\epsilon_b\underline{\underline{\mathbb{1}}}_2 + \frac{\omega^2}{c^2}\begin{pmatrix}\hat{\mathbf{k}}_\theta^T\underline{\underline{\chi}}(\omega)\hat{\mathbf{k}}_\theta & \hat{\mathbf{k}}_\theta^T\underline{\underline{\chi}}(\omega)\hat{\mathbf{k}}_\phi\\ \hat{\mathbf{k}}_\phi^T\underline{\underline{\chi}}(\omega)\hat{\mathbf{k}}_\theta & \hat{\mathbf{k}}_\phi^T\underline{\underline{\chi}}(\omega)\hat{\mathbf{k}}_\phi\end{pmatrix}\right]\mathbf{E}_\perp. \tag{6.37}$$

The non-identity part of the matrix equation (6.37) contains information regarding the polarisation structure of the exciton-polaritons. This matrix can be re-written as follows:

$$\begin{aligned}\underline{\underline{\tilde{\chi}}}(\omega) &= \begin{pmatrix} \hat{\mathbf{k}}_\theta^T \underline{\underline{\chi}}(\omega)\hat{\mathbf{k}}_\theta & \hat{\mathbf{k}}_\theta^T \underline{\underline{\chi}}(\omega)\hat{\mathbf{k}}_\phi \\ \hat{\mathbf{k}}_\phi^T \underline{\underline{\chi}}(\omega)\hat{\mathbf{k}}_\theta & \hat{\mathbf{k}}_\phi^T \underline{\underline{\chi}}(\omega)\hat{\mathbf{k}}_\phi \end{pmatrix}, \\ &\equiv \sum_{q=1}^{8} \left[\frac{\underline{\underline{\tilde{A}}}_q}{\hbar\omega + (E_{X_q} - E_0) + i\Gamma} - \frac{\underline{\underline{\tilde{A}}}_q^*}{\hbar\omega - (E_{X_q} - E_0) + i\Gamma} \right].\end{aligned} \tag{6.38}$$

In equation (6.38), we have introduced the directionally dependent oscillator strength matrices $\underline{\underline{\tilde{A}}}_q$

$$\underline{\underline{\tilde{A}}}_q = \begin{pmatrix} A_{q;11}\cos^2\theta + A_{q;33}\sin^2\theta & -iA_{q;11}\cos\theta \\ iA_{q;11}\cos\theta & A_{q;11} \end{pmatrix}. \tag{6.39}$$

It should be noted that these $\underline{\underline{\tilde{A}}}_q$ matrices do not depend on ϕ at all. This is to be expected as the only privileged direction in the problem is the direction of the magnetic field along the z-axis ($\theta = 0$). Non-trivial transverse solutions to the polariton equation in a specified direction (θ, ϕ) are obtained by finding the (k, ω) which solve the equation

$$\det\left[(1 - \frac{c^2k^2}{\omega^2\epsilon_b})\mathbb{1} + \frac{1}{\epsilon_b}\sum_{q=1}^{8}\left[\frac{\underline{\underline{\tilde{A}}}_q}{\hbar\omega + (E_{X_q} - E_0) + i\Gamma} - \frac{\underline{\underline{\tilde{A}}}_q^*}{\hbar\omega - (E_{X_q} - E_0) + i\Gamma} \right] \right] = 0. \tag{6.40}$$

The combination of the form of equation (6.40) with that of the matrices (6.39) imposes an additional symmetry between the solutions at θ and those at $\pi - \theta$. The combination of this symmetry with the ϕ independence of the matrices (6.39) means that all the unique solutions of the polariton equation can be found in the interval $\theta \in [0, \frac{\pi}{2}]$.

To solve equation (6.40) there are two possible approaches: either 1) solve for k at a specified ω or 2) solve for ω at a specified k. Of the two approaches the former is preferable as it results in a fourth order polynomial in k to be solved (in fact a quadratic in k^2) rather than (in a low symmetry direction) a sixteenth order polynomial in ω. The order of these polynomials in either k or ω is not arbitrary; it reflects either the two allowed polarisation states $\perp$ to $\hat{\mathbf{k}}$ (for positive k) or the maximum number of allowed polariton branches for ω.

The solution of the determinant equation (6.40) for the transverse polariton dispersion relation is now our focus. To examine these solutions we shall use a combination of two approaches. The first approach shall be to examine plots of the polariton dispersion relations. These plots can be produced by solving equation (6.40) for k at a sufficient resolution in the frequency interval $\omega \in [\omega_g - 1.15\omega_{R_0}, \omega_g - 0.75\omega_{R_0}]$. The second approach is to characterise the possible solutions that are to be expected by algebraic analysis of equation (6.40). To conduct this analysis we note that for any specified ω we are solving an equation of the form

$$a(\theta, \omega, \Gamma)k^4 + b(\theta, \omega, \Gamma)k^2 + c(\theta, \omega, \Gamma) = 0, \tag{6.41}$$

which as previously mentioned is a quadratic in k^2. As such, we can analyse the nature of the solutions by studying the discriminant

$$\Delta(\theta, \omega, \Gamma) = b(\theta, \omega, \Gamma)^2 - 4a(\theta, \omega, \Gamma)c(\theta, \omega, \Gamma). \tag{6.42}$$

Note that the discriminant has dimensions of $[\Delta] = m^4$, so a typical scale for the discriminant would be $\Delta \simeq (10^{-7})^4\ \mathrm{m}^4 = 10^{-28}\ \mathrm{m}^4$. These two approaches shall be used to study the polariton dispersion relation, in the aforementioned frequency interval, for all unique θ and under varying levels of dissipation Γ.

6.4.2 Magneto-Exciton Polariton Dispersion Relation in Absence of Resonance Damping

The first solutions of the determinant equation (6.40) that we seek are when there is no dissipation considered in the dielectric function, i.e. when $\Gamma = 0$. To develop our expectations of what type of polariton solutions are possible in this regime we shall first study the discriminant $\Delta(\theta, \omega, 0)$. In the situation of no dissipation the coefficients $a(\theta, \omega, 0)$, $b(\theta, \omega, 0)$ and $c(\theta, \omega, 0)$ are all real. Since the coefficients of the quartic equation (6.41) are all real this means that the discriminant is real. Additionally, over the parameter regime $\theta \in [0, \frac{\pi}{2}]$ and $\omega \in [\omega_g - 1.15\omega_{R_0}, \omega_g - 0.75\omega_{R_0}]$ the coefficients are such that the discriminant is non-negative. This means that the solutions for k^2 are either real positive or real negative. The solutions for k are therefore either entirely real or imaginary but not generally complex. Of the four solutions for k we shall restrict ourselves to the two of those which have either positive real or positive imaginary part.

Analysis of the discriminant also allows us to scrutinize the polariton dispersion relation for degeneracies. The degeneracies are points where two polaritons have a common (k, ω). These special points in the dispersion relation can be determined by solving $\Delta(\theta, \omega, 0) = 0$.

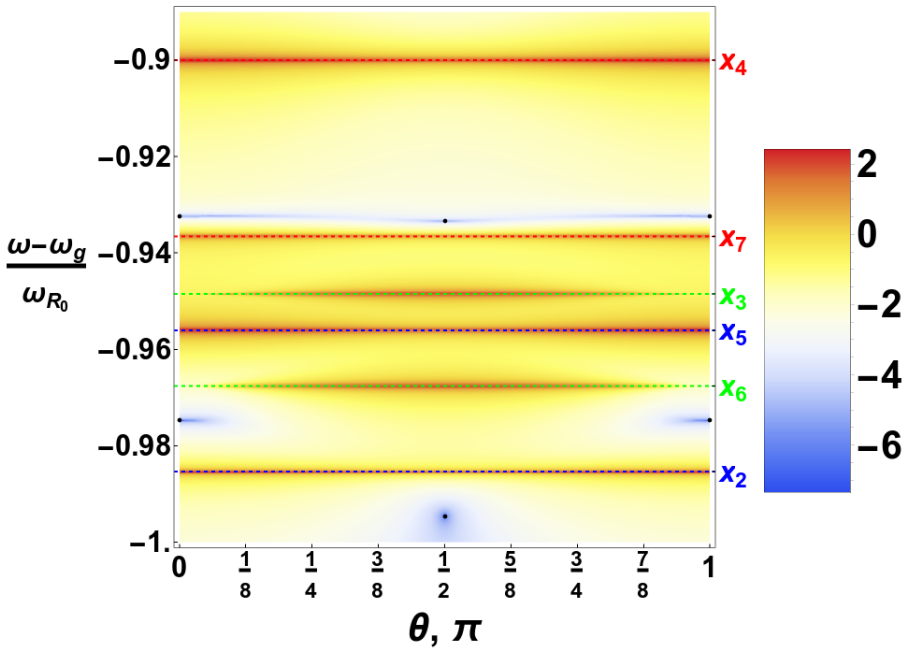

FIGURE 6.7: A density plot of $\log_{10}\left(\frac{\Delta(\theta,\omega,0)}{10^{-28}\ \mathrm{m}^4}\right)$ as a function of the frequency ω and the polar angle θ. The black points are those at which the discriminant $\Delta = 0$.

In figure 6.7 we examine the discriminant over relevant intervals of (θ, ω). Solutions of the degeneracy equation, indicated by black points, could only be found for two distinct values of θ, $\theta = 0$, corresponding to propagation in the Faraday geometry where $(\mathbf{k} \parallel \mathbf{B})$ and $\theta = \frac{\pi}{2}$, corresponding to propagation in the Voigt geometry where $(\mathbf{k} \perp \mathbf{B})$. In both cases there are two degeneracies. For propagation perpendicular to the magnetic field, the degeneracies are extended ring degeneracies owing to the ϕ invariance of the solutions of equation (6.40). Analysis of the discriminant can not however tell us anything further about these degeneracies, in order to further characterise them we now turn to examining plots of the polariton dispersion relations. The degeneracies are features in the four dimensional space $(\mathbf{k}, \omega)$ so they can not be directly visualised, however, studying them in the three dimensional space (k_x, k_z, ω) shall be sufficient owing to the aforementioned ϕ invariance. We shall make extensive use of this type of three dimensional visualisation of the polariton dispersion relation, as well as studying two dimensional plots of the magnitude of k versus ω in a specified direction $(\theta, 0)$. In combination these figure variants will allow us to study the degeneracies of the polariton dispersion relation.

Magneto-Exciton Polariton Dispersion for $\hat{\mathbf{k}} \parallel \mathbf{B}$

We shall now move to visually assessing the dispersion relation of bulk magneto-exciton-polaritons. We shall begin by examining the dispersion relation for propagation along the magnetic field direction. Considering light incident along the direction $(\theta = 0, \phi = 0)$, we can see from equations (6.29) and (6.39) that the two

excitons which couple to z-polarised light, x_3 and x_6, will both have zero oscillator strength. We hence expect that the order of the equation (6.40) in ω to reduce by four leaving a twelfth order polynomial having six positive frequency solutions.

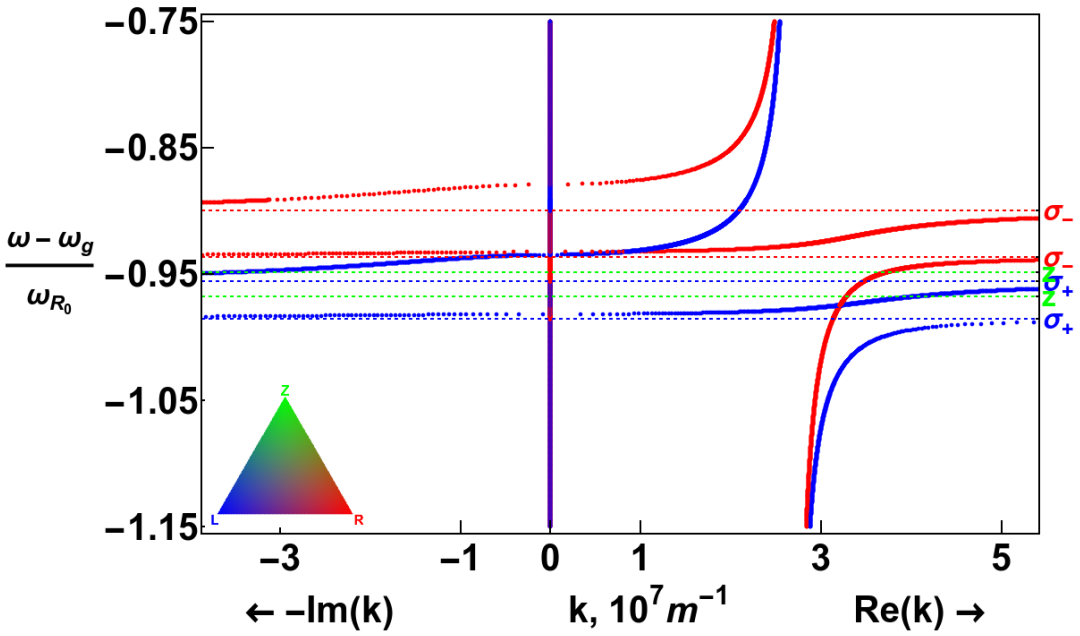

FIGURE 6.8: Transverse polariton dispersion relation of bulk GaAs for light propagating parallel to the magnetic field direction $\hat{\mathbf{z}}$, i.e. $(\theta, \phi) = (0, 0)$. In this figure we have considered no damping of any of the excitonic resonances, i.e. $\Gamma_q = 0 \; \forall q$. The branches of the polariton dispersion relation are coloured according to their polarisation with the colouring scheme provided in the colour triangle in the lower left of the figure.

Figure 6.8 shows the magneto-exciton polariton dispersion for light propagating along the z-direction. The branches of the dispersion relation are coloured according to their polarisation (see inset colour triangle in figure). In this arrangement the polarisation states are left (blue) and right (red) circularly polarised in the $x - y$ plane. There are three branches for each of these polarisations. Well below the lowest electronic resonances the lower polariton branch for each polarisation increases in a linear fashion. As the lower branches approach the relevant resonance (x_7 for right circularly polarised light and x_5 for left circularly polarised light) the dispersion starts to flatten out and asymptote horizontally. As these resonances are approached the splitting of the branches increases significantly. Between the first and the second electronic resonance for each polarisation, there is an intermediate polariton branch. This intermediate branch starts as purely imaginary k, i.e. a decaying state, before becoming purely real and oscillatory as ω increases. Above the second electronic resonance for each polarisation there is an upper polariton branch. The upper polariton branch starts as a decaying solution before becoming

oscillatory. The upper branches then start to curve upwards and recover the linear photonic dispersion. Our primary interest is in the degeneracies in these polariton dispersion relation which we shall now discuss.

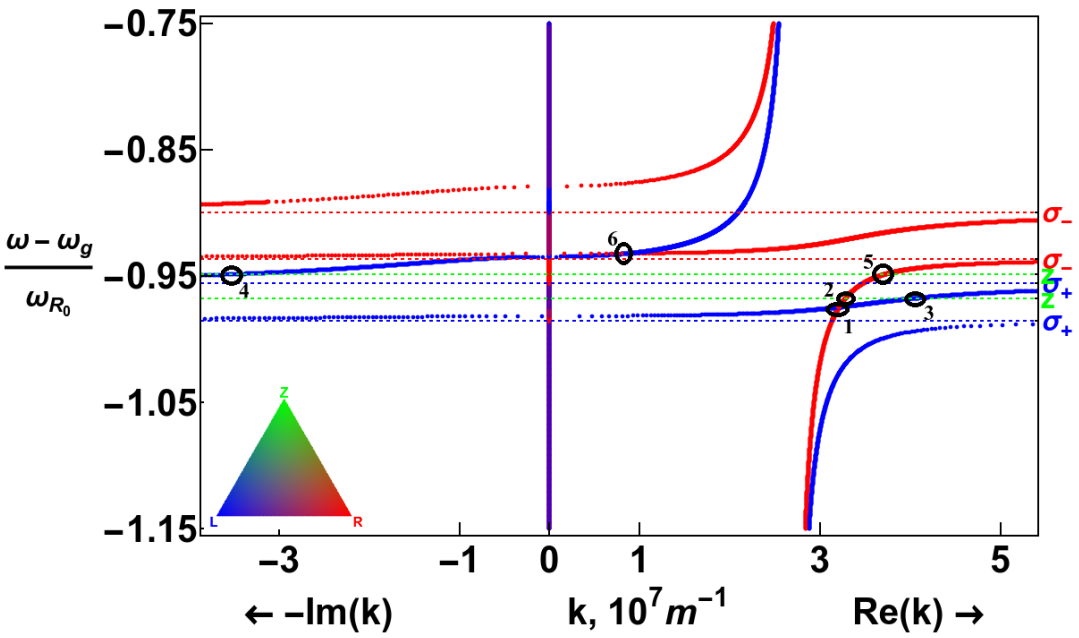

FIGURE 6.9: Polariton dispersion relation of bulk GaAs for $\hat{\mathbf{k}} \parallel \hat{\mathbf{z}}$ as in figure 6.8 with the degeneracies encircled and numbered.

In figure 6.9 we have reproduced figure 6.8 with the noteworthy features encircled and numbered to facilitate referencing. It is clear to see that the features 1 and 6 are the previously mentioned degeneracies of the dispersion relation, where the left and right circularly polarised polaritons cross. These are the two degeneracies predicted in figure 6.7. The features $2-5$ represent the intersections between each of the left and right circularly polarised polaritons and the two Z-polarised longitudinal polaritons at the x_3 and x_6 exciton resonances. Away from $\theta = 0$ the oscillator strength of the Z electron-hole transitions becomes non-zero, and the longitudinal polaritons become transverse solutions that exhibit dispersion. The Hopfield coefficients [172], which give the content of each of the excitons and each polarisation of light in the polariton branch, indicate that the exciton constituency of the relevant polariton branches locally mix in a way that suggests these intersections are topological. We will now pay individual attention to each of the features numbered $1-6$, in particular we will assess whether these degeneracies are isolated or extended by looking at the polariton solutions at nearby θ.

In figure 6.10 we study the local dispersion of feature 1 in figure 6.9. The local dispersion is examined in the $k_y = 0$ hyper-plane. Each of the surfaces is coloured according to the polarisation of the solution at that configuration in parameter

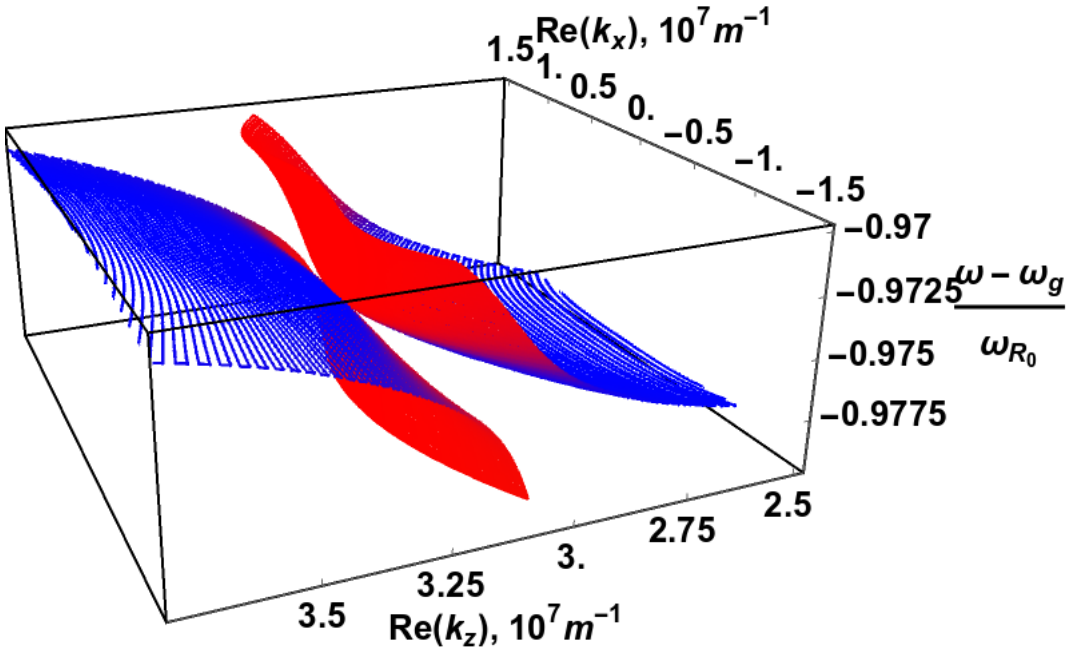

FIGURE 6.10: Local dispersion around the first feature of figure 6.9. We consider the dispersion in the $k_y = 0$ plane.

space. Feature 1 is the first polarisation degeneracy of the $\theta = 0$ polariton dispersion relation. As expected from the discriminant analysis this is an isolated degeneracy. We now turn to assess the local splitting of the two branches. From figure 6.8 we have seen that in the $k_x = k_y = 0$ plane the intersection of the two polariton branches is linear. By examining figure 6.10 it appears that the splitting of the branches in k_x is quadratic.

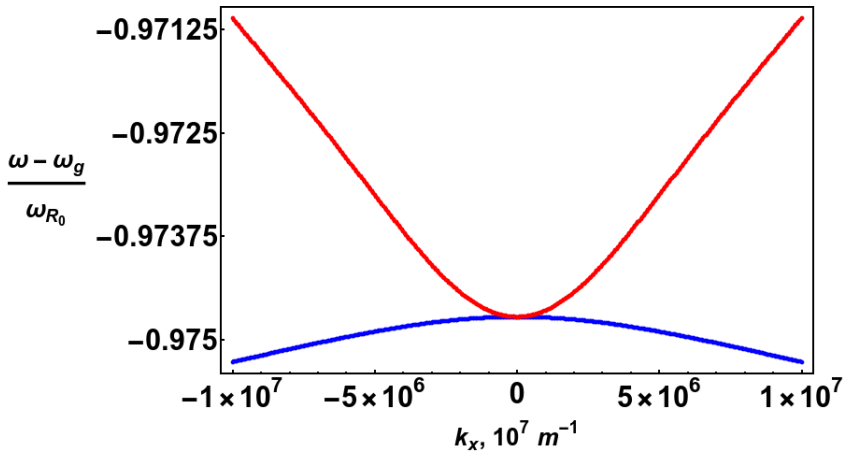

FIGURE 6.11: Local dispersion in transverse direction k_x through the first feature of figure 6.9.

Figure 6.11 examines the local dispersion in k_x of the two polariton branches relevant to feature 1 of figure 6.9. In the figure 6.11 we fix the k_z component of the wavevector at that of the lower frequency intersection in the $\theta = 0$ polariton dispersion relation. In this figure we again see only evidence for a quadratic intersection of

the polariton branches in k_x (and hence also in k_y). We can not definitively rule out the possibility that sufficiently close to the degeneracy there may be a predominantly linear dispersion in k_x. Our analysis has however not generated such behaviour so, to the best of our knowledge, we conclude that this feature is an isolated degeneracy of mixed dispersion. The degeneracy is therefore a generalisation of a Weyl point, with linear splitting of the branches in the $k_x = k_y = 0$ plane and quadratic splitting in k_x and k_y. Since the dispersion has to have a ϕ symmetry, the simplest low energy behaviour of this degeneracy would be of the form

$$\propto a_1(k_x^2 \underline{\underline{\sigma}}_x + k_y^2 \underline{\underline{\sigma}}_y) + b_1(k_z - k_z^{(I)})\underline{\underline{\sigma}}_z, \tag{6.43}$$

where $k_z^{(I)}$ is the intersection point of the two polariton dispersions. Topologically, this degeneracy is distinct from that of a Weyl point and, correspondingly, the local polarisation behaviour is different. The topological charge of this degeneracy can be calculated using the approach given in the appendix of an article by Chang and Yang [173]. In this case the topological charge is zero. We now move on to the next features highlighted in figure 6.9.

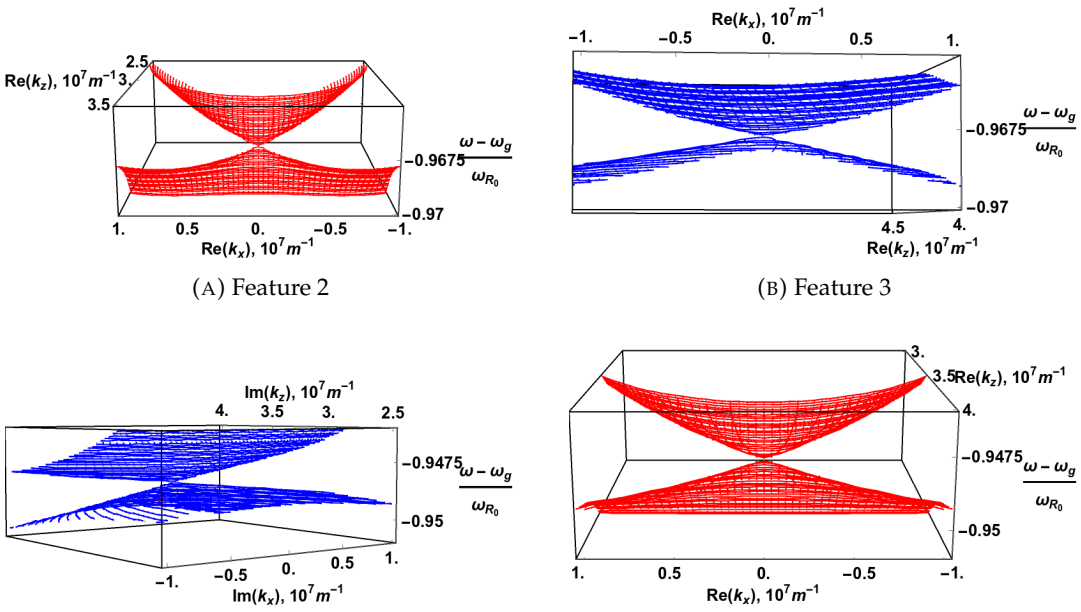

(A) Feature 2 (B) Feature 3

(C) Feature 4 (D) Feature 5

FIGURE 6.12: Local dispersion around each of features $2-5$ in the $\hat{\mathbf{k}} \parallel \hat{\mathbf{z}}$ polariton dispersion relation. In each case we have considered the $k_y = 0$ plane and have coloured the surfaces according to the polarisation.

In figure 6.12 we have studied features $2-5$ of figure 6.9. Each of these four features is centred, in frequency, around the frequency of either of the Z-polarised electron hole pairs. The top row of figure 6.12 is centred around the frequency of the x_6 resonance while the bottom row is centred around the frequency of the x_3

resonance. Each of the four plots comprising figure 6.12 features a two-sheeted surface constricting to an isolated common point at the centred frequency. These isolated common degeneracies are Weyl points with a linear splitting of the surfaces in all directions. These Weyl points have a topological charge of ± 1 and appear in positive and negative topological charge pairs. The cause of these points is the emergence of two extra transverse polariton branches away from the $k_x = k_y = 0$ plane. When off z-axis propagation is considered, the oscillator strength of the Z polarised transitions become non-zero and consequently extra transverse polariton branches emerge. Locally to each of these Weyl points there is a mixing of the exciton content of each branch with Z excitons being mixed with the L or R excitons of each branch.

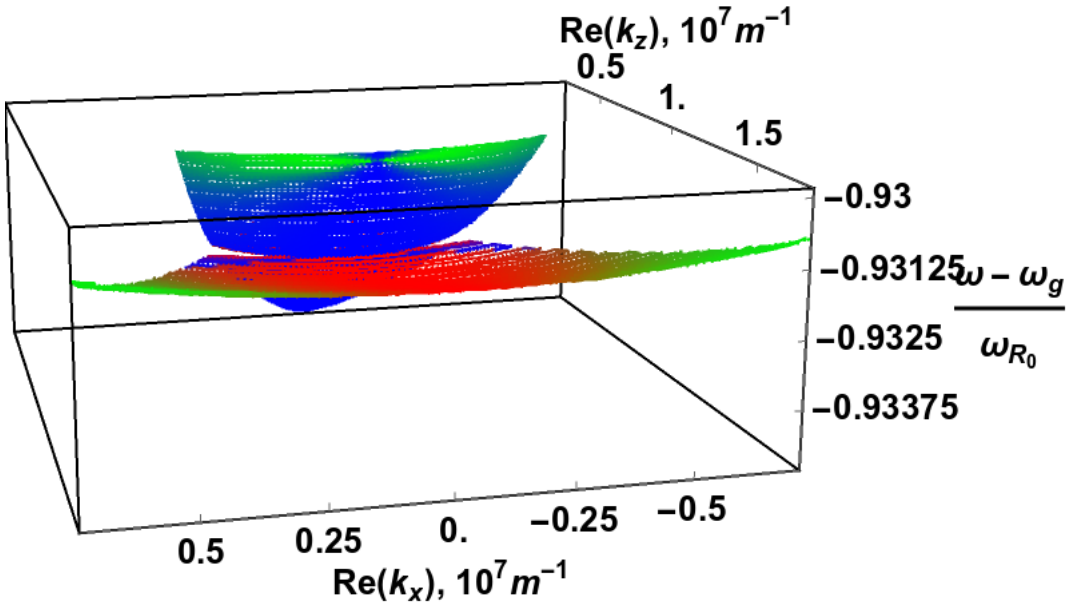

FIGURE 6.13: Local dispersion around the sixth feature of figure 6.9. We consider the dispersion in the $k_y = 0$ plane.

In figure 6.13 we study the final feature of the $\theta = 0$ polariton dispersion relation; feature 6 of figure 6.9. Similar to feature 1, feature 6 is a degeneracy of the L and R polariton branches. The discriminant analysis indicated that this is an isolated degeneracy. As for feature 1 we are interested in the local splitting of the sheets of this surface in all directions. From figure 6.8 it is evident that the splitting in the $k_x = k_y = 0$ direction is linear. Figure 6.13 suggests that the splitting in the other directions is quadratic.

Figure 6.14 allows us to better assess the dispersion of this polarisation degeneracy in k_x. In the figure 6.14 we fix the k_z component of the wavevector at that of the higher frequency intersection in the $\theta = 0$ polariton dispersion relation. Figure 6.14 seems to confirm that the splitting in the other directions is quadratic. As for feature 1 we can not definitively rule out predominantly linear splitting sufficiently close to

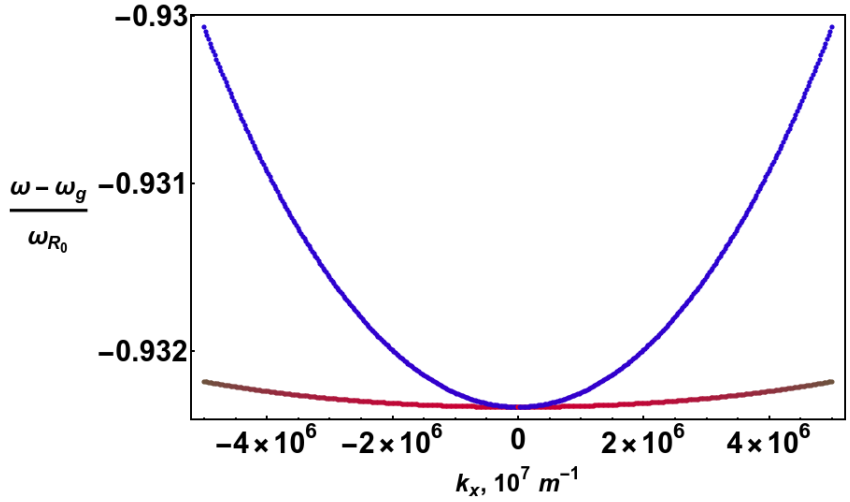

FIGURE 6.14: Local dispersion in transverse direction k_x through the sixth feature of figure 6.9.

the degeneracy however we have not observed such behaviour. Therefore, as was the case for feature 1 we concluded that this feature is a generalised Weyl point with linear dispersion in the z direction and quadratic splitting in the other directions. The low energy dispersion around this point is therefore of the form

$$\propto a_2(k_x^2 \underline{\underline{\sigma}}_x + k_y^2 \underline{\underline{\sigma}}_y) + b_2(k_z - k_z^{(II)})\underline{\underline{\sigma}}_z, \tag{6.44}$$

where $k_z^{(II)}$ is the intersection point of the two polariton branches. As was the case with the first degeneracy, this is a quadratic Weyl node with zero topological charge.

The examination of the six features of the $\theta = 0$ polariton dispersion relation of figure 6.9 has now been carried out. We now move to consider the polaritons formed for light propagating in the other special configuration, that of the Voigt geometry where $\mathbf{k} \perp \mathbf{B}$.

Magneto-Exciton Polariton Dispersion for $\hat{\mathbf{k}} \perp \mathbf{B}$

In the Voigt geometry one of the polarisations of light couples exclusively to the x_3 and x_6 electron hole pairs. The other polarisation of light will couple, to some degree, with each of the other four optically allowed transitions.

Figure 6.15 shows the resulting polariton dispersion relation in the Voigt geometry. Similarly to figure 6.8 the coupling of a polarisation of light to the two Z-polarised electron hole pairs results in three polariton branches of fixed polarisation. The other polarisation of light couples to each of the remaining four electron hole pairs, resulting in five polariton branches. We see in figure 6.15 that the colouring of these five polariton branches is not constant as in the case of figure

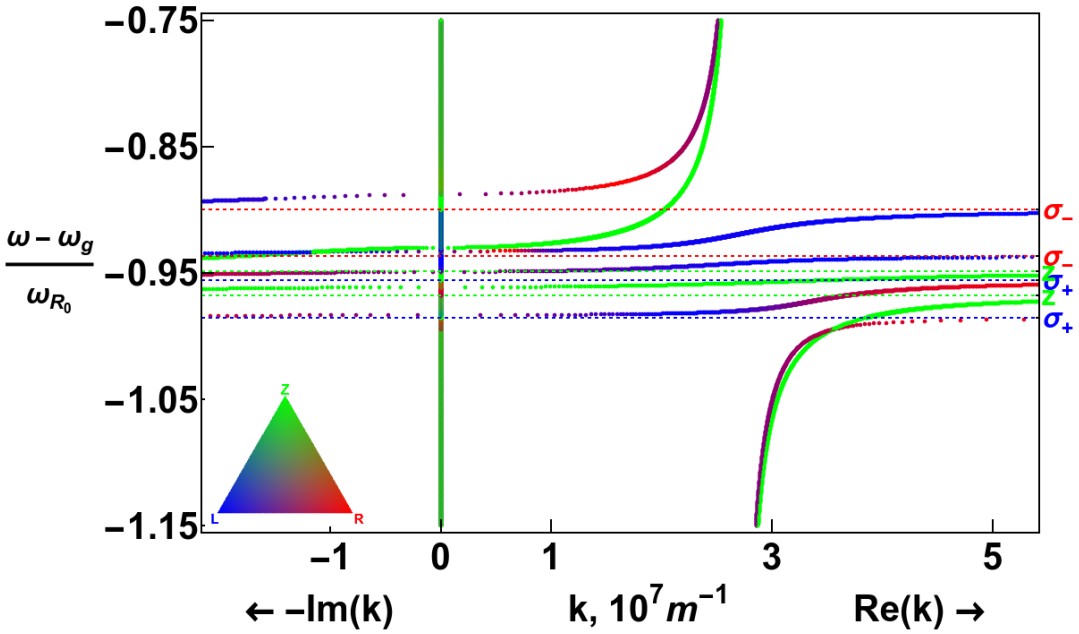

FIGURE 6.15: Polariton dispersion relation of bulk GaAs for light propagating perpendicularly to the magnetic field direction $\hat{\mathbf{z}}$, i.e. $(\theta, \phi) = (\frac{\pi}{2}, 0)$. In this figure we have considered no damping of any of the excitonic resonances, i.e. $\Gamma_q = 0 \; \forall q$.

6.8 or for the other three branches in figure 6.15. In this instance the degree of mixture of red and blue represents a variation of the relative weighting of left and right circularly polarised light in the $x - y$ plane. This inconstancy of polarisation profile of a polariton branch is, in fact, the norm for these dispersion relations. For light propagating in a general direction, not orthogonal to the planes of vibration of any of the electron hole resonances, the polarisation profile of each of the eight polariton branches varies continuously.

The two degeneracies of the polariton dispersion relation in the Voigt geometry are labelled in figure 6.16. Analysis of the discriminant (6.42) has suggested that these two polarisation degeneracies are extended around the $k_z = 0$ plane and split apart as $k_z \neq 0$ solutions are considered. We shall now examine each of these two degeneracies.

Figure 6.17 is a panel of figures that examines the local dispersion relation of each of the degeneracies of figure 6.16 in two different hyper-planes. The two hyper-planes considered are, in the left column, the $k_z = 0$ hyper plane, and, in the right column, the $k_y = 0$ hyper-plane. For each of the figures we observe that the degeneracy is extended in the $k_z = 0$ hyper-plane while each of the surfaces split as $k_z \neq 0$ solutions are included.

We have now developed a complete picture of the degeneracies of the polariton

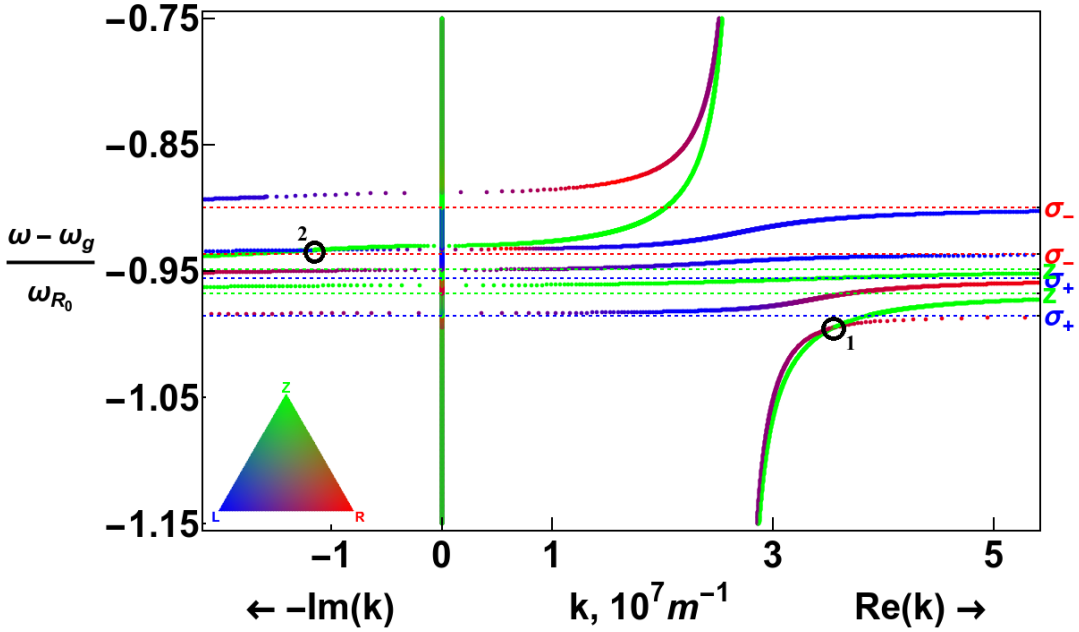

FIGURE 6.16: Polariton dispersion relation of bulk GaAs for $\hat{\mathbf{k}} \parallel \hat{\mathbf{x}}$ as in figure 6.15 with the degeneracies encircled and numbered.

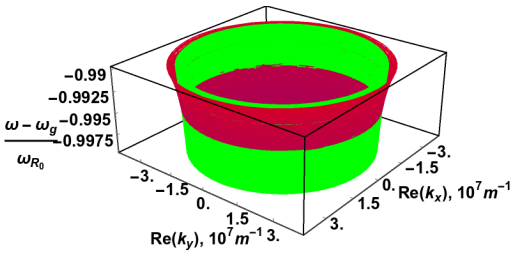

(A) 1st Degeneracy, $k_z = 0$

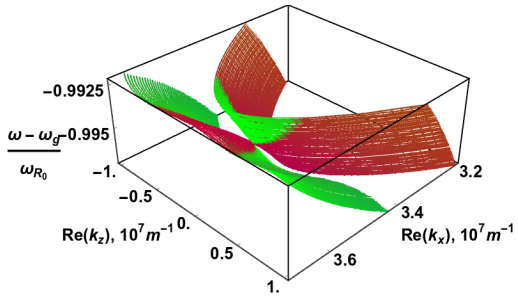

(B) 1st Degeneracy, $k_y = 0$

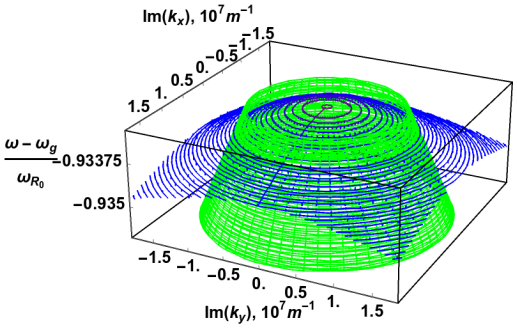

(C) 2nd Degeneracy, $k_z = 0$

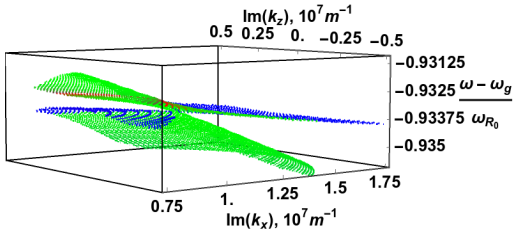

(D) 2nd Degeneracy, $k_y = 0$

FIGURE 6.17: Local dispersion of the each of the degeneracies in figure 6.16. The top row considers the first degeneracy of figure 6.16 and the bottom row the second degeneracy. For each of the degeneracies we consider the dispersion in two different hyper-planes. In the left column we have considered $k_z = 0$ while in the right column we have considered $k_y = 0$.

dispersion relations in the absence of dissipation. There are two special relative orientations specifying the relationship between the magnetic field direction and the direction of propagation $\mathbf{k}$. These relative orientations are the Faraday configuration ($\mathbf{k} \parallel \mathbf{B}$) and the Voigt configuration ($\mathbf{k} \perp \mathbf{B}$). In the former case, there are six polariton branches, three of each of left and right handed circular polarisation. These six branches intersect at two points, which are isolated degeneracies that are generalisations of Weyl points. Additionally, there are degeneracies between each of the transverse polariton modes and the longitudinal modes resulting in four Weyl points with topological charges of ± 1. For light propagating in the Voigt geometry there are now eight polariton branches as the oscillator strength of each dipole-allowed transition is non-zero. These eight branches divide into three of fixed z polarisation and five of variable mixture of left and right handed circular polarisation. There are two intersections of these set of branches, which are extended degeneracies in the $k_z = 0$ hyper plane but which split apart as $k_z \neq 0$ solutions are considered.

We now focus on the evolution of these polariton dispersions as dissipative processes are included. Rather than model each of the myriad processes that contribute to the overall dissipation individually, we choose to introduce a uniform broadening to each of the electron hole pair resonances. Although this uniform broadening is an idealisation, we do not believe that the inclusion of different damping for the different excitons would qualitatively affect our results.

6.4.3 Magneto-Exciton Polariton Dispersion Relation with Resonance Damping

The consideration of resonance damping opens the possibility of interesting non-Hermitian effects. In crystal optics it has been shown that the introduction of absorption (a non-Hermitian effect) has changed the nature of the degeneracies which were present in the Hermitian case [91]. In more general optical systems absorption has also allowed myriad interesting topological phenomena [75]. In our case, when damping of the electron hole pair resonances is included, the nature of equation (6.40) is altered and, hence, so is the discriminant equation (6.42). With this inclusion the quartic coefficients of equation (6.41) become complex and therefore so does the discriminant. Owing to the complexity of the discriminant, the solutions for the polariton dispersion at a given real ω will produce generally complex k. Similarly, the solution of $\Delta(\theta, \omega, \Gamma) = 0$ now constitutes the simultaneous solution of two equations, $\mathrm{Re}(\Delta(\theta, \omega, \Gamma)) = 0$ and $\mathrm{Im}(\Delta(\theta, \omega, \Gamma)) = 0$. Although in isolation the solution of either of these equations does not have a direct physical consequence, the simultaneous solution indicates the presence of an exceptional point [75, 174, 175]. Exceptional points are degeneracies where the real and imaginary parts of k are degenerate at a given frequency ω. The presence of exceptional points and their

fate as the strength of dissipation is varied is our primary focus in this section.

Prior to addressing the question of exceptional points, it will be beneficial to examine the effect of dissipation on the polariton dispersion relation in a general sense. We would expect that, when dissipation is included, the asymptotes of the polariton dispersion seen in subsection 6.4.2 would disappear. This disappearance is achieved by the joining of the branches of the polariton dispersion above and below each resonance.

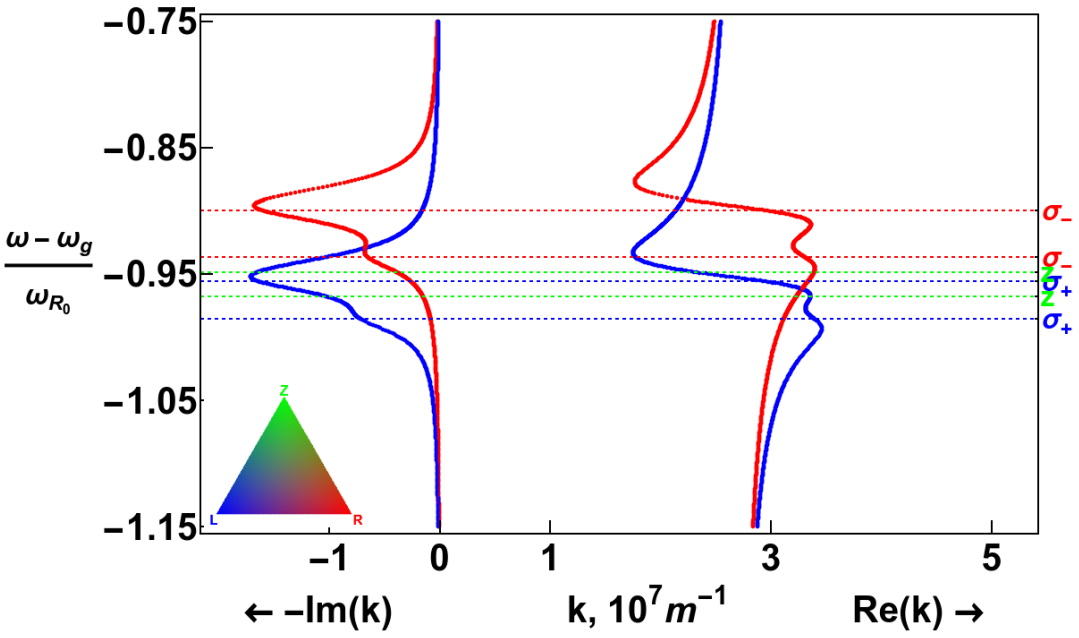

FIGURE 6.18: GaAs polariton dispersion relation for light propagating along the magnetic field direction $\hat{\mathbf{z}}$. In this figure we have considered a broadening of each of the electron-hole pair resonances $\Gamma = 0.015R_0$.

Figure 6.18 shows the polariton dispersion relation in the Faraday configuration where dissipation has been included. We should thus compare this dispersion relation to the corresponding one without dissipation in figure 6.8. For this figure we have considered a uniform broadening of $\Gamma = 0.015R_0$ for each of the electron hole pair resonances. As expected the solutions are now generally complex k. The real and imaginary parts of k of each polarisation are both continuous functions; the asymptotes have disappeared. At this level of dissipation we can see the bi-resonant structure of the ϵ_L and ϵ_R dielectric components by looking at the imaginary parts of k for each polarisation. The imaginary part of k also reveals the asymmetry of the oscillator strengths for each resonance. As the strength of damping is further increased the presence of individual resonances will first become indiscernible ($\Gamma \gtrsim 0.03R_0$), then the presence of any resonance will be difficult to observe ($\Gamma \gtrsim 0.25R_0$). We note that in figure 6.18 there are two degeneracies of the

real parts of k and one degeneracy of the imaginary parts of k. As the frequency of the imaginary degeneracy does not match either of the frequencies of the real degeneracies, this is not a polariton dispersion that exhibits an exceptional point. To assess the appearance of exceptional points we will use discriminant analysis rather than plotting individual polariton dispersion relations.

Degeneracy Structure of Dispersion Relations with Resonance Broadening

We now look at solving $\Delta(\theta, \omega, \Gamma) = 0$ at chosen non-zero values of Γ. We will solve this simultaneous equation numerically by root-finding techniques and will use a graphical representation of the solutions to elucidate the behaviour of the solutions as Γ is varied.

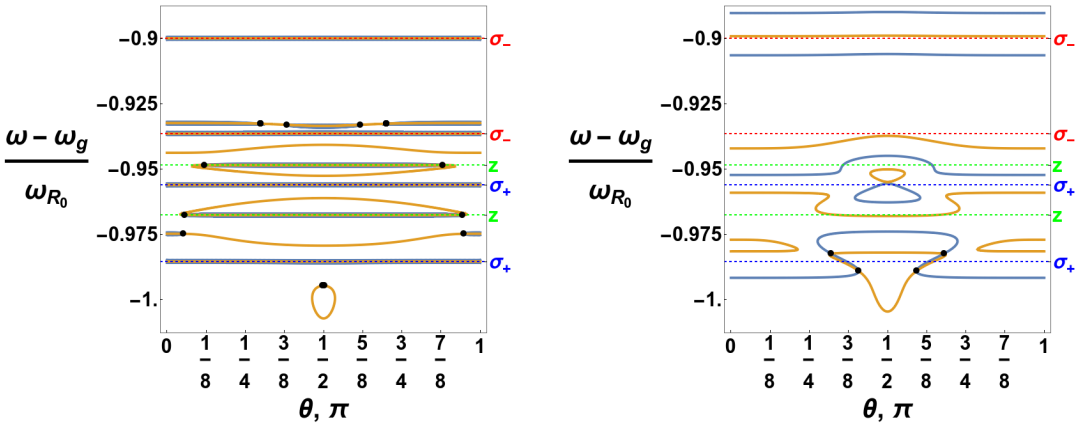

(A) $\Gamma = 0.0005R_0$. (B) $\Gamma = 0.008R_0$.

FIGURE 6.19: Two plots showing the zero contour lines of the real (blue) and imaginary (orange) parts of the discriminant Δ. In each plot we have considered a distinct resonance broadening Γ for each of the electron-hole pair resonances. In the left figure $\Gamma = 0.0005R_0$ while in the right figure $\Gamma = 0.008R_0$. Intersections of the zero contour lines, marked with black dots, represent points at which $\Delta = 0$.

Figure 6.19 represents the solutions of the equation $\Delta(\theta, \omega, \Gamma) = 0$ for two different amounts of dissipation. In the left plot of figure 6.19 we have chosen $\Gamma = 0.0005R_0$ while in the right plot $\Gamma = 0.008R_0$. In each plot we have used blue and orange curves which display the zero contour lines of $\mathrm{Re}(\Delta(\theta, \omega, \Gamma))$ and $\mathrm{Im}(\Delta(\theta, \omega, \Gamma))$ respectively. The intersection of these contour lines are then exceptional points where $\Delta(\theta, \omega, \Gamma) = 0$. In the left plot of figure 6.19 we see a number of exceptional points. Comparing the left plot of figure 6.19 to the discriminant analysis when $\Gamma = 0$ presented in figure 6.7 allows us to better understand some of the exceptional points. The presence of these points can be understood as the extension of the $\Gamma = 0$ degeneracies to the case of complex solutions. As non-zero dissipation is introduced the four distinct frequency $\theta = 0$ degeneracies of figure 6.9 and the two $\theta = \frac{\pi}{2}$ degeneracies of figure 6.16 become exceptional points. All of the exceptional

points of the polariton dispersion relation become itinerant as Γ is allowed to vary, moving in the (θ, ω) space. As Γ is increased some of these exceptional points can meet and annihilate. This is what has occurred in between the left plot of figure 6.19 and the right plot where we see fewer exceptional points. The locations of the exceptional points in figure 6.19 are all at non-zero θ. Hence, owing to the ϕ invariance of solutions, the exceptional points are not isolated but are instead rings of exceptional points.

Rings of Exceptional Points

We can examine the local dispersion around the exceptional points predicted from the discriminant analysis. We will focus on the highest frequency exceptional point of figure 6.19b, which is a solution of the equation $\Delta(\theta, \omega, 0.008R_0) = 0$. This solution occurs for light propagating in a direction $\theta_\star$ (or by symmetry of solutions $\pi - \theta_\star$). To begin with, we will look at a $2D$ plot of the polariton dispersion relation for light propagating in the direction $\theta = \theta_\star$ before examining $3D$ plots of the real and imaginary parts of the polariton dispersion around the exceptional point.

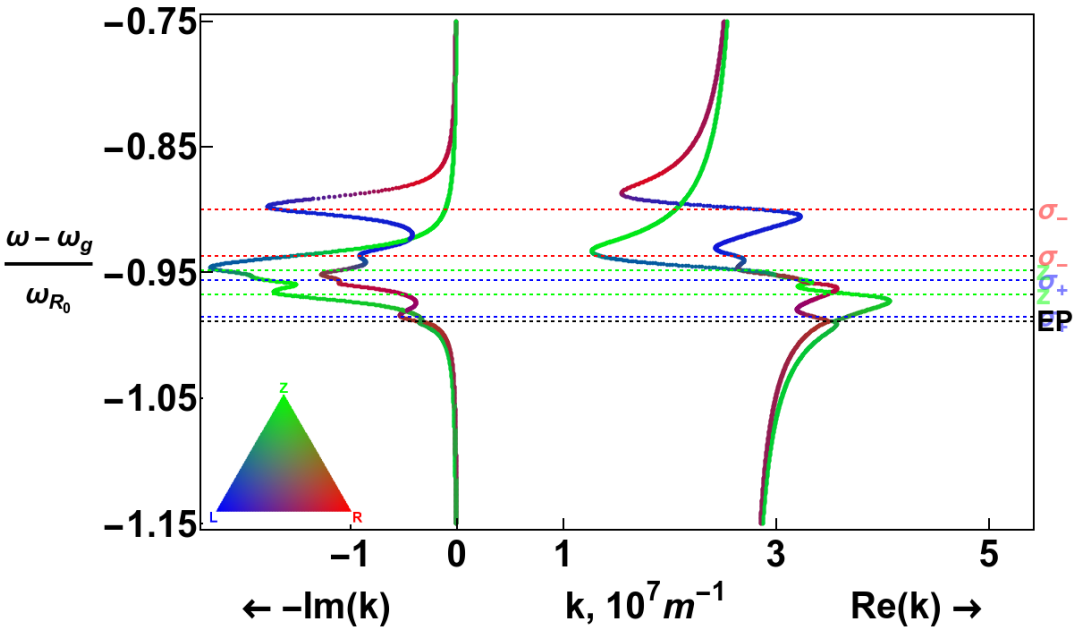

FIGURE 6.20: The polariton dispersion relation for light propagating in a direction $(\theta, \phi) = (\theta_\star, 0)$, where $\theta_\star$ has been determined from figure 6.19. We consider $\Gamma = 0.008R_0$.

In figure 6.20, we see a polariton dispersion relation that exhibits an exceptional point. In this figure, we have considered a damping of $\Gamma = 0.008R_0$ and light propagating in a direction $(\theta, \phi) = (\theta_\star, 0)$. The exceptional point occurs at the frequency marked by the black dashed gridline labelled EP in figure 6.20. We clearly see that, at this frequency, there is degeneracy in both the real and imaginary parts

of k.

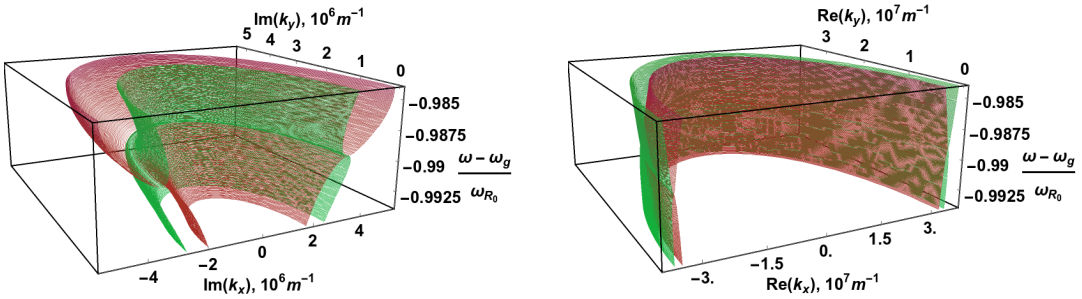

(A) Imaginary Part (B) Real Part

FIGURE 6.21: Two figures showing the imaginary (left) and real (right) parts of the polariton dispersion relation in the $k_z = \cos(\theta_\star)$ plane for a resonance broadening $\Gamma = 0.008R_0$. For each of these plots we show the section of the ring from $\phi = 0$ to $\phi = \pi$.

Figure 6.21 shows one half of the ring of exceptional points of the polariton dispersion relation for light propagating in a direction $\theta_\star$ in a material with damping $\Gamma = 0.008R_0$. We show both the real and imaginary parts of the polariton dispersion relation. For each part, we plot the ring of exceptional points for $\phi \in [0, \pi]$. The key observation from figure 6.21 is that the degeneracy in the real and imaginary parts of $\mathbf{k}$ are present over all ϕ, as expected. The exceptional point for light propagating in a direction $\theta_\star$ is, therefore, in fact, a ring of exceptional points.

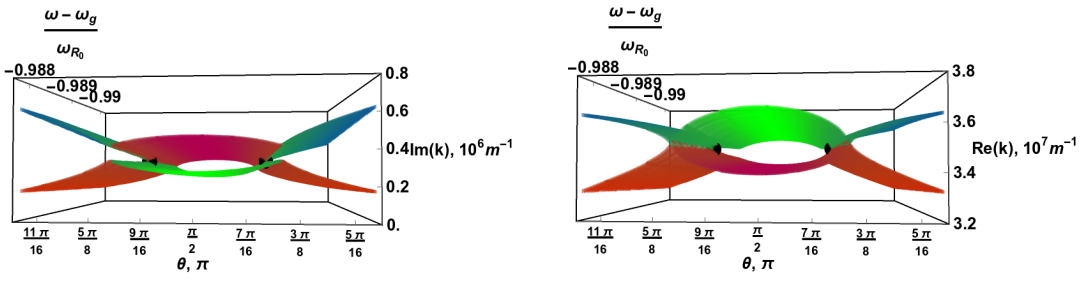

(A) Imaginary Part (B) Real Part

FIGURE 6.22: Two figures showing the imaginary (left) and real (right) parts of the local dispersion around the exceptional points at $\theta_1 = \theta_\star$ and $\theta_2 = \pi - \theta_\star$. Here we are looking at the dispersion in the plane $k_y = 0$.

Figure 6.22 shows the two exceptional points located at $\theta_\star$ and $\pi - \theta_\star$. In this figure, we display the real and imaginary k parts of the polariton dispersion relation. For each of the real and imaginary parts, there are extended degeneracies. These extended degeneracies in real and imaginary k are non-overlapping except at their end points which are the exceptional point locations.

Beyond the level of dissipation considered in the right plot of figure 6.19 ($\Gamma = 0.008R_0$), the exceptional points continue to move. As the dissipation is

increased, each of the remaining pairs meet and annihilate.

The observations which have been made in this chapter apply to a regime of low damping, where, in the case of GaAs, the dissipation is on the scale of tens of μeV. The strength of the dissipation in a bulk semiconductor is determined by many inter-related factors. A significant one of these factors is the purity of the crystal. The dissipation can additionally be tuned somewhat by varying the temperature. For the features described to be observed we would likely require a highly pure semiconductor crystal in a low temperature environment. The relevant scale to compare the dissipation Γ to is the Rabi splitting energy. It may be easier to probe the low damping regime for other semiconductors in table 6.1. This may be the case as, due to the precise energies of the six optically excitable exciton transitions, the rings of exceptional points are naturally more robust and persist to higher strengths of dissipation.

6.5 Conclusion

In this chapter we have studied the magneto-exciton-polaritons of bulk magnetically-biased semiconductors. This began with our adoption of a methodology to describe the interaction of electrons and holes in a bulk semiconductor under a static external magnetic field. For weakly bound excitons, the requisite framework is the set of effective mass equations for relevant combinations of valence and conduction bands. In zincblende semiconductors, where the spin-orbit spliting of the $j = \frac{1}{2}$ valence band from the $j = \frac{3}{2}$ valence band is sufficiently strong, the relevant bands are the four $j = \frac{3}{2}$ valence bands and the two $j = \frac{1}{2}$ conduction bands. The set of effective mass equations is thus a system of eight equations to be solved for the magneto-exciton energies and wavefunctions. The exact solution of the effective mass equations is not generally possible and instead we must resort to approximate methods. One such method is the effective Hamiltonian derived by Cho et al. [147] which utilises the perturbative approach of Altarelli and Lipari [154] as well as including the exchange interaction. This effective Hamiltonian describes the magneto-exciton ground state of bulk semiconductors in the low magnetic field regime. We used this effective Hamiltonian in order to determine the optical response of the exciton ground state.

We described the optical susceptibility due to the 1s-like magneto-excitons within the non-interacting linear response framework. In this framework, the optical susceptibility and hence the dielectric function can be expressed in terms of expectation values of the dipole operator between the crystal ground state and the one exciton state. To calculate the dielectric function we made use of several relations to express the position matrix elements in terms of known momentum

matrix elements. The structure of these momentum matrix elements enforces the optical selection rules, dictating which of the electron hole pairs is relevant to the dielectric function for light of a given polarisation. We considered a magnetic field at the extreme bounds of the allowable regime for the effective Hamiltonian. At this magnetic field strength, six of the eight excitons contribute to the dielectric function overall. In its diagonal basis, each component of the dielectric function is determined by transitions to a distinct pair of the dipole allowed excitons. The energies of each of these six electron hole pairs then determines whether there is anisotropy of the dielectric function. For non-zero magnetic field, the dielectric function is anisotropic.

The magneto-exciton-polaritons of bulk semiconductors were described by solving the wave equation incorporating the derived dielectric function. This vector equation is a generalised polariton equation relevant to an anisotropic dielectric. We recast the polariton equation as a 2×2 matrix equation for the transverse polariton solutions, which we then determined numerically.

The solutions of the polariton equation were studied for light propagating in special configurations and at varying levels of dissipation. A particular focus of this study was on degeneracies in the polariton dispersion relation. In the absence of damping there are several forms of degeneracies present, all appearing for light propagating in two particular configurations. For light propagating in the Faraday configuration there are two generalised quadratic Weyl points between the transverse polariton modes. These quadratic Weyl nodes have a topological charge of zero. Additionally in this configuration there are four Weyl points between each of the transverse polariton solutions and the longitudinal polariton solutions. These Weyl points have a topological charge of ± 1. For light propagating in the Voigt configuration there are two degeneracies between the transverse polariton solutions. These degeneracies are extended rings in the $k_z = 0$ plane. When dissipative effects are included, we found that the $\Gamma = 0$ degeneracies become exceptional points which move in (θ, ω) space as Γ is varied. Since these itinerant degeneracies occur at non-zero θ they are necessarily rings of exceptional points. The largest amount of exceptional rings occurs in a very low damping regime and as the strength of damping is increased pairs of exceptional rings come together and annihilate. Above a certain threshold of dissipation, all of the rings of exceptional points disappear.

Chapter 7

Conclusions and Future Directions

In this thesis, we have discussed several topological aspects of photonic systems that can be realised by exploiting optical anisotropy. Here we provide a brief summary of the work, put the work in the context of the wider field of topological photonics and suggest some possible future directions to be explored.

As a first study, we characterised closed surfaces in wavevector space by a topological invariant called a Chern number. The materials which we considered were biaxial, optically active dielectrics which were either homogeneous or periodically patterned. We showed that these materials can possess gapped, i.e. non-degenerate, and topologically non-trivial index surfaces. This approach is novel as it does not rely on a specific form of lattice geometry, but rather on the conical intersections generically present in the index surfaces of biaxial materials.

These theories of topologically non-trivial optical systems concerned photonic semi-metals with topological bands, rather than photonic insulators, which possess a complete band-gap. As such, the question of the bulk-boundary correspondence for these photonic semi-metals is somewhat more complicated. We therefore chose to study the effect that the closing of the band-gap has on edge state formation in systems which have abrupt terminations and/or interfaces. The insights from this analysis allowed a parameter regime where partial edge states of a photonic crystal model to be identified.

Our final investigation concerned the quasi-particles resulting from the strong-coupling of light to matter excitations in bulk semiconductors. When a magnetic field is applied to a bulk direct-gap zincblende semiconductor, the magneto-exciton-polariton dispersion relations which follow are rich in topological features. In the absence of dissipative processes, these dispersions display isolated Weyl point degeneracies as well as extended ring degeneracies. When dissipation is introduced, these degeneracies become rings of exceptional points.

The promise of optical anisotropy in realising topologically non-trivial photonic systems is considerable. Here, we have addressed several diverse systems with

the common theme that being able to control and manipulate the propagation and polarisation characteristics of incoming light using anisotropy can have significant topological implications. Elements of this work should be considered as tools in a larger toolbox that allows the implementation of everything from effective spin-orbit coupling to synthetic magnetic field for photons, in order to explore myriad forms of topological order.

There are many possible extensions to the work presented in this thesis. An interesting extension to the studies carried out in chapter 2 would be to derive the propagator Hamiltonian of section 2.6 without using any of the approximations adopted in this thesis. Preliminary work in this regard has suggested that the resulting Hamiltonian, despite possessing real eigenvalues, is non-Hermitian. If this is indeed the case, then it would be interesting to assess whether signatures of this non-Hermitian Hamiltonian would have observable consequences for the propagation of light.

Our work in chapters 3 and 4 has shown that anisotropic photonic crystals have the potential to produce topologically non-trivial bandstructures. In chapter 5 we discovered that despite being topologically non-trivial the theories of chapters 3 and 4 were not particularly well suited to displaying edge features. This limitation was due to the theories lacking a complete photonic band-gap in the topologically non-trivial parameter regime. We therefore suggest that future theories concerning the topological invariants of the bandstructures of anisotropic photonic crystals should focus on both the topological invariants and realising a complete band-gap from the offset.

A worthwhile avenue of exploration to extend the work of chapter 6 is to investigate the topological phases of bulk magneto-exciton-polaritons subjected to a periodic potential. Various $2D$ or $3D$ effective periodic potentials could be implemented, opening up new possibilities. In the case of $2D$ effective potentials, owing to the extra features of bulk dispersion relations, it may be possible to achieve richer topological phase diagrams than those of microcavity systems [34–36, 176]. These diagrams could be richer in the sense that they have higher values of topological invariants which have already been realised in microcavity settings, or open the possibility of non-zero invariants as yet unrealised in $2D$. For $3D$ effective periodic potentials, we may focus on intrinsically three-dimensional topological effects. The bulk may, therefore, provide the platform for $3D$ topological insulators, Weyl semi-metal phases or open Fermi arcs in momentum space for polaritonic bandstructures.

In a more general sense, topological photonics has many interesting pathways to explore. Beyond utilising anisotropy alone the incorporation of absorption and/or

non-linearity could allow myriad intriguing possibilities.

Bibliography

[1] D. J. Thouless, M. Kohmoto, M. P. Nightingale, and M. den Nijs, Phys. Rev. Lett. **49**, 405 (1982).

[2] C. L. Kane and E. J. Mele, Phys. Rev. Lett. **95**, 146802 (2005).

[3] K. v. Klitzing, G. Dorda, and M. Pepper, Phys. Rev. Lett. **45**, 494 (1980).

[4] J. E. Avron, D. Osadchy, and R. Seiler, Physics Today **56**, 38 (2003).

[5] B. I. Halperin, Phys. Rev. B **25**, 2185 (1982).

[6] B. A. Bernevig and T. L. Hughes, *Topological insulators and topological superconductors*, 1st ed. (Princeton University Press, Princeton NJ, 2013).

[7] J. E. Avron, R. Seiler, and B. Simon, Phys. Rev. Lett. **51**, 51 (1983).

[8] C. Kittel, *Introduction to solid state physics*, 6th ed. (John Wiley & Sons, Hoboken NJ, 1953).

[9] S. Raghu and F. D. M. Haldane, Phys. Rev. A **78**, 033834 (2008).

[10] F. D. M. Haldane and S. Raghu, Phys. Rev. Lett. **100**, 013904 (2008).

[11] Z. Yang, F. Gao, X. Shi, X. Lin, Z. Gao, Y. Chong, and B. Zhang, Phys. Rev. Lett. **114**, 114301 (2015).

[12] P. Wang, L. Lu, and K. Bertoldi, Phys. Rev. Lett. **115**, 104302 (2015).

[13] M. Born and E. Wolf, *Principles of optics*, 7th ed. (Cambridge University Press, Cambridge, 1959).

[14] B. Guenther, *Modern optics*, 2nd ed. (Oxford University Press, Oxford, 1990).

[15] J. D. Joannopoulos, S. G. Johnson, J. N. Winn, and R. D. Meade, *Photonic crystals: molding the flow of light*, 2nd ed. (Princeton University Press, Princeton NJ, 2008).

[16] J.-M. Lourtioz, H. Benisty, V. Berger, J.-M. Gerard, D. Maystre, and A. Tchelnokov, *Photonic crystals: towards nanoscale photonic devices*, 1st ed. (Springer, Berlin/Heidelberg, 2005).

[17] C. Klingshirn, *Semiconductor optics*, 1st ed. (Springer, Berlin/Heidelberg, 1995).

[18] P. Basu, *Theory of optical processes in semiconductors*, 1st ed. (Clarendon Press, Oxford, 1997).

[19] M. V. Berry, Proc. Royal Soc. A **392**, 45 (1984).

[20] B. Simon, Phys. Rev. Lett. **51**, 2167 (1983).

[21] M. Kohmoto, Ann. Phys. **160**, 343 (1985).

[22] T. Fukui, Y. Hatsugai, and H. Suzuki, J. Phys. Soc. Jpn. **74**, 1674 (2005).

[23] D. Sticlet, F. Piéchon, J.-N. Fuchs, P. Kalugin, and P. Simon, Phys. Rev. B **85**, 165456 (2012).

[24] P. Renteln, *Manifolds, tensors and forms: an introduction for mathematicians and physicists*, 1st ed. (Cambridge University Press, Cambridge, 2014).

[25] Y. Hatsugai, Phys. Rev. Lett. **71**, 3697 (1993).

[26] Y. Hatsugai, Phys. Rev. B **48**, 11851 (1993).

[27] M. Z. Hasan and C. L. Kane, Rev. Mod. Phys. **82**, 3045 (2010).

[28] F. D. M. Haldane, Phys. Rev. Lett. **61**, 2015 (1988).

[29] G. W. Semenoff, Phys. Rev. Lett. **53**, 2449 (1984).

[30] T. Ochiai and M. Onoda, Phys. Rev. B **80**, 155103 (2009).

[31] Z. Wang, Y. D. Chong, J. D. Joannopoulos, and M. Solja či ć, Phys. Rev. Lett. **100**, 013905 (2008).

[32] Z. Wang, Y. Chong, J. D. Joannopoulos, and M. Soljacic, Nature **461**, 772 (2009).

[33] Y. Poo, R.-x. Wu, Z. Lin, Y. Yang, and C. T. Chan, Phys. Rev. Lett. **106**, 093903 (2011).

[34] C.-E. Bardyn, T. Karzig, G. Refael, and T. C. H. Liew, Phys. Rev. B **91**, 161413 (2015).

[35] K. Yi and T. Karzig, Phys. Rev. B **93**, 104303 (2016).

[36] A. V. Nalitov, D. D. Solnyshkov, and G. Malpuech, Phys. Rev. Lett. **114**, 116401 (2015).

[37] A. Mook, J. Henk, and I. Mertig, Phys. Rev. B **90**, 024412 (2014).

[38] L. M. Nash, D. Kleckner, A. Read, V. Vitelli, A. M. Turner, and W. T. M. Irvine, en, Proc. Natl. Acad. Sci. U.S.A **112**, 14495 (2015).

[39] C. L. Kane and E. J. Mele, Phys. Rev. Lett. **95**, 226801 (2005).

[40] B. A. Bernevig, T. L. Hughes, and S.-C. Zhang, Science **314**, 1757 (2006).

[41] M. König, S. Wiedmann, C. Brüne, A. Roth, H. Buhmann, L. W. Molenkamp, X.-L. Qi, and S.-C. Zhang, en, Science **318**, 766 (2007).

[42] A. B. Khanikaev, S. Hossein Mousavi, W.-K. Tse, M. Kargarian, A. H. MacDonald, and G. Shvets, Nat. Mater. **12**, 233 (2013).

[43] W.-J. Chen, S.-J. Jiang, X.-D. Chen, B. Zhu, L. Zhou, J.-W. Dong, and C. T. Chan, Nat. Commun. **5**, 5782 (2014).

[44] L. Fu, C. L. Kane, and E. J. Mele, Phys. Rev. Lett. **98**, 106803 (2007).

[45] J. E. Moore and L. Balents, Phys. Rev. B **75**, 121306 (2007).

[46] R. Roy, Phys. Rev. B **79**, 195322 (2009).

[47] A. A. Burkov, en, Nat. Mater. **15**, 1145 (2016).

[48] C. Fang, H. Weng, X. Dai, and Z. Fang, en, Chin. Phys. B **25**, 117106 (2016).

[49] L. Fu and C. L. Kane, Phys. Rev. B **76**, 045302 (2007).

[50] H. Zhang, C.-X. Liu, X.-L. Qi, X. Dai, Z. Fang, and S.-C. Zhang, en, Nat. Phys. **5**, 438 (2009).

[51] D. Hsieh, D. Qian, L. Wray, Y. Xia, Y. S. Hor, R. J. Cava, and M. Z. Hasan, en, Nature **452**, 970 (2008).

[52] Y. Xia, D. Qian, D. Hsieh, L. Wray, A. Pal, H. Lin, A. Bansil, D. Grauer, Y. S. Hor, R. J. Cava, and M. Z. Hasan, en, Nat. Phys. **5**, 398 (2009).

[53] A. Slobozhanyuk, H. S. Mousavi, X. Ni, D. Smirnova, Y. S. Kivshar, and A. B. Khanikaev, Nat. Photonics **11** (2016).

[54] A. P. Slobozhanyuk, A. B. Khanikaev, D. S. Filonov, D. A. Smirnova, A. E. Miroshnichenko, and Y. S. Kivshar, en, Sci. Rep. **6**, 22270 (2016).

[55] N. P. Armitage, E. J. Mele, and A. Vishwanath, Rev. Mod. Phys. **90**, 015001 (2018).

[56] X. Wan, A. M. Turner, A. Vishwanath, and S. Y. Savrasov, Phys. Rev. B **83**, 205101 (2011).

[57] Z. Wang, Y. Sun, X.-Q. Chen, C. Franchini, G. Xu, H. Weng, X. Dai, and Z. Fang, Phys. Rev. B **85**, 195320 (2012).

[58] S. M. Young, S. Zaheer, J. C. Y. Teo, C. L. Kane, E. J. Mele, and A. M. Rappe, Phys. Rev. Lett. **108**, 140405 (2012).

[59] S.-Y. Xu, I. Belopolski, N. Alidoust, M. Neupane, G. Bian, C. Zhang, R. Sankar, G. Chang, Z. Yuan, C.-C. Lee, S.-M. Huang, H. Zheng, J. Ma, D. S. Sanchez, B. Wang, A. Bansil, F. Chou, P. P. Shibayev, H. Lin, S. Jia, and M. Z. Hasan, en, Science **349**, 613 (2015).

[60] B. Q. Lv, H. M. Weng, B. B. Fu, X. P. Wang, H. Miao, J. Ma, P. Richard, X. C. Huang, L. X. Zhao, G. F. Chen, Z. Fang, X. Dai, T. Qian, and H. Ding, Phys. Rev. X **5**, 031013 (2015).

[61] S. Borisenko, Q. Gibson, D. Evtushinsky, V. Zabolotnyy, B. Büchner, and R. J. Cava, Phys. Rev. Lett. **113**, 027603 (2014).

[62] M. Neupane, I. Belopolski, M. M. Hosen, D. S. Sanchez, R. Sankar, M. Szlawska, S.-Y. Xu, K. Dimitri, N. Dhakal, P. Maldonado, P. M. Oppeneer, D. Kaczorowski, F. Chou, M. Z. Hasan, and T. Durakiewicz, Phys. Rev. B **93**, 201104 (2016).

[63] L. Lu, L. Fu, J. D. Joannopoulos, and M. Soljacic, Nat. Photonics **7**, 294 (2013).

[64] L. Lu, Z. Wang, D. Ye, L. Ran, L. Fu, J. D. Joannopoulos, and M. Soljačić, Science **349**, 622 (2015).

[65] J. Noh, S. Huang, D. Leykam, Y. D. Chong, K. P. Chen, and M. C. Rechtsman, Nat. Phys. **13**, 611 (2017).

[66] B. Yang, Q. Guo, B. Tremain, R. Liu, L. E. Barr, Q. Yan, W. Gao, H. Liu, Y. Xiang, J. Chen, C. Fang, A. Hibbins, L. Lu, and S. Zhang, Science (2018).

[67] W.-J. Chen, M. Xiao, and C. T. Chan, en, Nat. Commun. **7**, 13038 (2016).

[68] J. Noh, S. Huang, D. Leykam, Y. D. Chong, K. P. Chen, and M. C. Rechtsman, Nat. Phys. **13**, 611 (2017).

[69] M. Xiao, W.-J. Chen, W.-Y. He, and C. T. Chan, en, Nat. Phys. **11**, 920 (2015).

[70] Z. Yang and B. Zhang, Phys. Rev. Lett. **117**, 224301 (2016).

[71] F. Li, X. Huang, J. Lu, J. Ma, and Z. Liu, Nat. Phys. **14**, 30 (2018).

[72] P. Delplace, J. Li, and D. Carpentier, en, EPL **97**, 67004 (2012).

[73] C. M. Bender and S. Boettcher, Phys. Rev. Lett. **80**, 5243 (1998).

[74] C. M. Bender, en, Rep. Prog. Phys. **70**, 947 (2007).

[75] Ş. K. Özdemir, S. Rotter, F. Nori, and L. Yang, en, Nat. Mater. **18**, 783 (2019).

[76] J.-W. Ryu, S.-Y. Lee, and S. W. Kim, Phys. Rev. A **79**, 053858 (2009).

[77] T. Gao, E. Estrecho, K. Bliokh, T. Liew, M. Fraser, S. Brodbeck, M. Kamp, C. Schneider, S. Höfling, Y. Yamamoto, et al., Nature **526**, 554 (2015).

[78] R. Uzdin, A. Mailybaev, and N. Moiseyev, en, J. Phys. A **44**, 435302 (2011).

[79] M. V. Berry and R. Uzdin, en, J. Phys. A **44**, 435303 (2011).

[80] T. J. Milburn, J. Doppler, C. A. Holmes, S. Portolan, S. Rotter, and P. Rabl, Phys. Rev. A **92**, 052124 (2015).

[81] D. Leykam, K. Y. Bliokh, C. Huang, Y. D. Chong, and F. Nori, Phys. Rev. Lett. **118**, 040401 (2017).

[82] C. E. Rüter, K. G. Makris, R. El-Ganainy, D. N. Christodoulides, M. Segev, and D. Kip, en, Nat. Phys. **6**, 192 (2010).

[83] S.-B. Lee, J. Yang, S. Moon, S.-Y. Lee, J.-B. Shim, S. W. Kim, J.-H. Lee, and K. An, Phys. Rev. Lett. **103**, 134101 (2009).

[84] B. Peng, Ş. K. Özdemir, M. Liertzer, W. Chen, J. Kramer, H. Yılmaz, J. Wiersig, S. Rotter, and L. Yang, en, Proc. Natl. Acad. Sci. U.S.A **113**, 6845 (2016).

[85] M. Liertzer, L. Ge, A. Cerjan, A. D. Stone, H. E. Türeci, and S. Rotter, Phys. Rev. Lett. **108**, 173901 (2012).

[86] J. Doppler, A. A. Mailybaev, J. Böhm, U. Kuhl, A. Girschik, F. Libisch, T. J. Milburn, P. Rabl, N. Moiseyev, and S. Rotter, en, Nature **537**, 76 (2016).

[87] W. Gao, M. Lawrence, B. Yang, F. Liu, F. Fang, B. Béri, J. Li, and S. Zhang, Phys. Rev. Lett. **114**, 037402 (2015).

[88] M. C. Rechtsman, J. M. Zeuner, Y. Plotnik, Y. Lumer, D. Podolsky, F. Dreisow, S. Nolte, M. Segev, and A. Szameit, Nature **496**, 196 (2013).

[89] T. Fösel, V. Peano, and F. Marquardt, New J. Phys. **19**, 115013 (2017).

[90] G. Gbur, *Singular optics*, 1st ed. (CRC Press, Boca Raton FL, 2016).

[91] M. V. Berry and M. R. Dennis, Proc. Royal Soc. A **459**, 1261 (2003).

[92] P. Yu and M. Cardona, *Fundamentals of semiconductors: physics and materials properties*, 1st ed. (Springer, Berlin/Heidelberg, 1995).

[93] S. Chuang, *Physics of optoelectronic devices*, 1st ed. (John Wiley & Sons, Hoboken NJ, 1995).

[94] J. Kasprzak, M. Richard, S. Kundermann, A. Baas, P. Jeambrun, J. M. J. Keeling, F. M. Marchetti, M. H. Szymańska, R. André, J. L. Staehli, V. Savona, P. B. Littlewood, B. Deveaud, and L. S. Dang, en, Nature **443**, 409 (2006).

[95] H. Deng, G. Weihs, C. Santori, J. Bloch, and Y. Yamamoto, en, Science **298**, 199 (2002).

[96] S. Klembt, T. H. Harder, O. A. Egorov, K. Winkler, R. Ge, M. A. Bandres, M. Emmerling, L. Worschech, T. C. H. Liew, M. Segev, C. Schneider, and S. Höfling, En, Nature **562**, 552 (2018).

[97] L. Landau, E. Lifshitz, and L. Pitaevskii, *Electrodynamics of continuous media*, 2nd ed., Vol. 8 (Pergamon Press, Oxford, 1984).

[98] M. Jeffrey, "Conical diffraction: complexifying Hamilton's diabolical legacy", PhD thesis (University of Bristol, 2007).

[99] A. Lakhtakia and T. Mackay, *Electromagnetic anisotropy and bianisotropy - a field guide*, 1st ed. (World Scientific Publishing, Singapore, 2010).

[100] G. Kaye and T. Laby, *Tables of physical and chemical constants*, 16th ed. (Longman, Harlow, 1995).

[101] J. Nye, *Physical properties of crystals*, 1st ed. (Oxford Science Publications, Oxford, 1985).

[102] J. Anthony, R. Bideaux, K. Bladh, and M. Nichols, *Handbook of mineralogy* (Mineralogical Society of America, Chantilly VA, 2019).

[103] W. R. Hamilton, Trans. R. Irish. Acad., 1 (1837).

[104] H. Lloyd, Phil. Mag., 112 (1833).

[105] M. V. Berry and M. R. Jeffrey, J. Opt. **8**, 363 (2006).

[106] Berry M.V, Proc. Royal Soc. A **461**, 2071 (2005).

[107] M. A. M. Marte and S. Stenholm, Phys. Rev. A **56**, 2940 (1997).

[108] M. V. Berry, M. R. Jeffrey, and M. Mansuripur, J. Opt. **7**, 685 (2005).

[109] M. V. Berry, J. Opt. **6**, 289 (2004).

[110] K. Sakoda, *Optical properties of photonic crystals*, 1st ed. (Springer, Berlin/Heidelberg, 2001).

[111] L. Lu, J. D. Joannopoulos, and M. Soljacic, Nat. Photonics **8**, Review, 821 (2014).

[112] G. Alagappan, X. W. Sun, and H. D. Sun, Phys. Rev. B **77**, 195117 (2008).

[113] I. A. Khromova and L. A. Melnikov, Opt. Commun. **281**, 5458 (2008).

[114] G. Alagappan, X. W. Sun, P. Shum, M. B. Yu, and D. den Engelsen, J. Opt. Soc. Am. A **23**, 2002 (2006).

[115] S. Shen, *Topological insulators*, 1st ed. (Springer, Berlin/Heidelberg, 2012).

[116] H. B. Nielsen and M. Ninomiya, Phys. Lett. **B105**, 219 (1981).

[117] S. G. Johnson and J. D. Joannopoulos, Opt. Express **8**, 173 (2001).

[118] J.-X. Fu, R.-J. Liu, and Z.-Y. Li, Appl. Phys. Lett. **97**, 041112 (2010).

[119] J.-X. Fu, R.-J. Liu, and Z.-Y. Li, en, EPL **89**, 64003 (2010).

[120] S. A. Skirlo, L. Lu, and M. Soljačić, Phys. Rev. Lett. **113**, 113904 (2014).

[121] S. A. Skirlo, L. Lu, Y. Igarashi, Q. Yan, J. Joannopoulos, and M. Soljačić, Phys. Rev. Lett. **115**, 253901 (2015).

[122] D. W. Zingg and H. Lomax, J. Comput. Phys. **108**, 306 (1993).

[123] L. Collatz, *The numerical treatment of differential equations*, 3rd ed. (Springer, Berlin/Heidelberg, 1966).

[124] M. König, H. Buhmann, L. Molenkamp, T. Hughes, C.-X. Liu, X.-L. Qi, and S.-C. Zheng, J. Phys. Soc. Jpn. **77**, 031007 (2008).

[125] M. Wada, S. Murakami, F. Freimuth, and G. Bihlmayer, Phys. Rev. B **83**, 121310 (2011).

[126] B. Zhou, H.-Z. Lu, R.-L. Chu, S.-Q. Shen, and Q. Niu, Phys. Rev. Lett. **101**, 246807 (2008).

[127] P. Michetti, P. H. Penteado, J. C. Egues, and P. Recher, Semicond. Sci. Technol **27**, 124007 (2012).

[128] S. Mao, Y. Kuramoto, K.-I. Imura, and A. Yamakage, en, J. Phys. Soc. Jpn. **79**, 124709 (2010).

[129] S. Murakami, J. Phys. Conf. Ser. **302**, 012019 (2011).

[130] R. Jackiw and C. Rebbi, Phys. Rev. D **13**, 3398 (1976).

[131] F. Lu, Y. Zhou, J. An, and C.-D. Gong, EPL **98**, 17004 (2012).

[132] K.-I. Imura, A. Yamakage, S. Mao, A. Hotta, and Y. Kuramoto, Phys. Rev. B **82**, 085118 (2010).

[133] S. Mao and Y. Kuramoto, Phys. Rev. B **83**, 085114 (2011).

[134] T. F. Khalkhali, B. Rezaei, and M. Kalafi, Opt. Commun. **284**, 3315 (2011).

[135] Z.-Y. Li, B.-Y. Gu, and G.-Z. Yang, en, Eur. Phys. J. B **11**, 65 (1999).

[136] I. A. Khromova and L. A. Melnikov, Opt. Commun. **281**, 5458 (2008).

[137] Z.-Y. Li, B.-Y. Gu, and G.-Z. Yang, Phys. Rev. Lett. **81**, 2574 (1998).

[138] S. Feng, Y. Yang, C. Lan, Z. Bai, and Y. Wang, en, Sci. China G **53**, 1788 (2010).

[139] T. Trifonov, L. F. Marsal, A. Rodríguez, J. Pallarès, and R. Alcubilla, Phys. Rev. B **69**, 235112 (2004).

[140] R. Willardson and A. Beer, *Semiconductors and semimetals*, 1st ed., Vol. 3 (Academic Press, Cambridge MA, 1967).

[141] F. Bassani and G. Pastori Parravicini, *Electronic states and optical transitions in solids*, 1st ed. (Pergamon Press, Oxford, 1975).

[142] H. Haug and S. Koch, *Quantum theory of the optical and electronic properties of semiconductors*, 4th ed. (World Scientific Publishing, Singapore, 2004).

[143] R. Willardson and A. Beer, *Semiconductors and semimetals*, 1st ed., Vol. 1 (Academic Press, Cambridge MA, 1966).

[144] M. I. Dyakonov, "Basics of semiconductor and spin physics", in *Spin physics in semiconductors*, Vol. 157, Springer Series in Solid-State Sciences (2008).

[145] R. J. Elliott, Phys. Rev. **108**, 1384 (1957).

[146] C. Tanguy, Phys. Rev. Lett. **75**, 4090 (1995).

[147] K. Cho, S. Suga, W. Dreybrodt, and F. Willmann, Phys. Rev. B **11**, 1512 (1975).

[148] J. M. Luttinger and W. Kohn, en, Phys. Rev. **97**, 869 (1955).

[149] G. Dresselhaus, J. Phys. Chem. Solids **1**, 14 (1956).

[150] J. M. Luttinger, en, Phys. Rev. **102**, 1030 (1956).

[151] K. Cho, Phys. Rev. B **14**, 4463 (1976).

[152] K. Cho, S. Suga, W. Dreybrodt, and F. Willmann, Phys. Rev. B **11**, 1512 (1975).

[153] A. Baldereschi and N. O. Lipari, Phys. Rev. B **3**, 439 (1971).

[154] M. Altarelli and N. O. Lipari, Phys. Rev. B **7**, 3798 (1973).

[155] W. Kohn and D. Schechter, Phys. Rev. **99**, 1903 (1955).

[156] T. P. McLean and R. Loudon, J. Phys. Chem. Solids **13**, 1 (1960).

[157] Y. Abe, J. Phys. Soc. Jpn. **19**, 818 (1964).

[158] A. Baldereschi and N. O. Lipari, Phys. Rev. B **8**, 2697 (1973).

[159] A. Baldereschi and N. O. Lipari, Phys. Rev. B **9**, 1525 (1974).

[160] N. O. Lipari and A. Baldereschi, Phys. Rev. B **3**, 2497 (1971).

[161] N. O. Lipari and A. Baldereschi, Phys. Rev. B **6**, 3764 (1972).

[162] L. Świerkowski, Phys. Rev. B **10**, 3311 (1974).

[163] L. Świerkowski, en, Il Nuovo Cimento B (1971-1996) **29**, 340 (1975).

[164] R. Winkler, *Spin–orbit coupling effects in two-dimensional electron and hole systems*, 1st ed. (Springer, Berlin/Heidelberg, 2003).

[165] H. Fu, L.-W. Wang, and A. Zunger, Phys. Rev. B **59**, 5568 (1999).

[166] Y. Shen, *The principles of nonlinear optics*, 1st ed. (John Wiley & Sons, Hoboken NJ, 1984).

[167] L. Świerkowski, Il Nuovo Cimento B (1971-1996) **29**, 340 (1975).

[168] W. Ekardt, K. Lösch, and D. Bimberg, Phys. Rev. B **20**, 3303 (1979).

[169] A. Armitage, T. A. Fisher, M. S. Skolnick, D. M. Whittaker, P. Kinsler, and J. S. Roberts, Phys. Rev. B **55**, 16395 (1997).

[170] J. D. Berger, O. Lyngnes, H. M. Gibbs, G. Khitrova, T. R. Nelson, E. K. Lindmark, A. V. Kavokin, M. A. Kaliteevski, and V. V. Zapasskii, Phys. Rev. B **54**, 1975 (1996).

[171] L. Świerkowski, Phys. Rev. B **10**, 3311 (1974).

[172] J. J. Hopfield, Phys. Rev. **112**, 1555 (1958).

[173] M.-C. Chang and M.-F. Yang, Phys. Rev. B **92**, 205201 (2015).

[174] J. Doppler, A. A. Mailybaev, J. Böhm, U. Kuhl, A. Girschik, F. Libisch, T. J. Milburn, P. Rabl, N. Moiseyev, and S. Rotter, en, Nature **537**, 76 (2016).

[175] B. Zhen, C. W. Hsu, Y. Igarashi, L. Lu, I. Kaminer, A. Pick, S.-L. Chua, J. D. Joannopoulos, and M. Soljačić, Nature **525**, 354 (2015).

[176] T. Karzig, C.-E. Bardyn, N. H. Lindner, and G. Refael, Phys. Rev. X **5**, 031001 (2015).